

MAGNETOM Flash

Issue Number 84 · 2/2023

ISMRM Edition

siemens-healthineers.com/magnetom-world

Page 4

Editorial Comment: Expanding Boundaries

Roderic I. Pettigrew

Page 9

The Role of 7T MRI in Cerebral Small Vessel Disease

Zihao Zhang, et al.

Page 44

Deep Learning MRI Sequences: The Present and the Future

Saif Afat, et al.

Page 73

Exploring the Potential of Low-Field Musculoskeletal MRI at 0.55T

Hanns-Christian Breit, et al.

Page 78

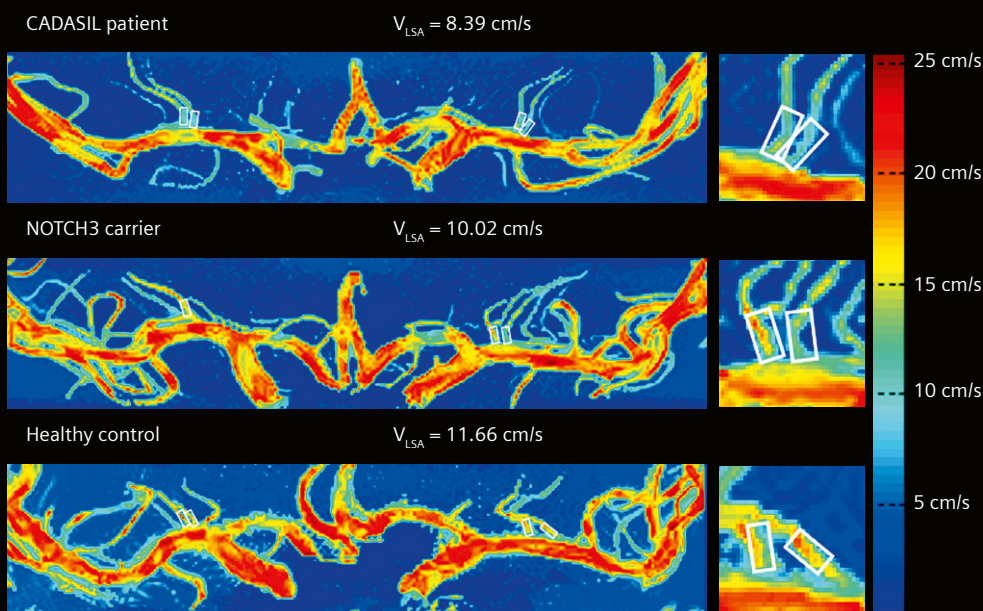
Fetal Low Field MRI – the First 150 Cases

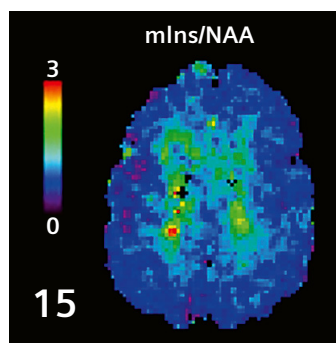
Jana Hutter, et al.

Page 96

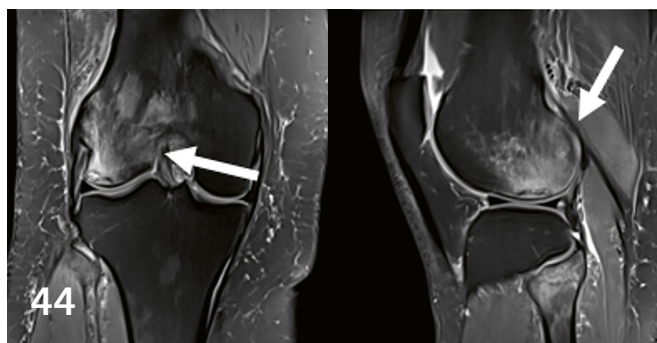
How to Deal with Arrhythmia in Cardiac MRI

Christian Houbois, et al.

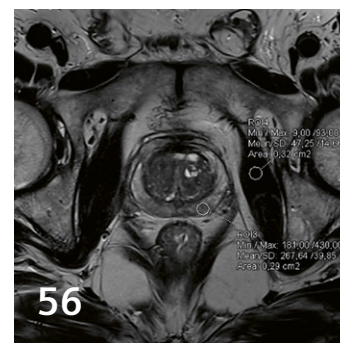




7T MRSI of mIns and NAA
in multiple sclerosis



DL-reconstructed PD TSE



Deep learning reconstruction
in prostate MRI

Editorial Comment

4 Expanding Boundaries¹

Roderic I. Pettigrew
Texas A&M University and Houston Methodist Hospital,
Houston, TX, USA

Neurological Imaging

9 The Increasing Role of 7T MRI in the Neuro-imaging of Cerebral Small Vessel Disease

Zihao Zhang, et al.
Chinese Academy of Sciences, Beijing, China

15 Milestones and Applications of High-Resolution 7T MRSI¹

Gilbert Hangel, et al.
High Field MR Centre, Medical University Vienna, Austria

26 Optimizing EPI Image Quality Beyond Linear Phase Corrections with Dual-Polarity GRAPPA¹

André Fischer, et al.
Siemens Healthineers, Erlangen, Germany

32 Retrospective Motion Correction for Brain MRI: A Technical Description of SAMER¹

Daniel Polak, et al.
Siemens Healthineers, Erlangen, Germany

36 Diffusion-Weighted Imaging of the Brain with Isotropic Resolution using syngo RESOLVE with GRAPPA and SMS

Thomas Illigen and Christian Söldner
Siemens Healthineers, Erlangen, Germany

Spotlight

44 Deep Learning MRI Sequences: The Present and the Future

Saif Afat, et al.
Eberhard Karls University Tuebingen, Germany

50 Deep Resolve Boost (DRB) and Sharp (DRS) for Diffusion: ADC Phantom Evaluation

Hyun-Soo Lee, et al.
Siemens Healthineers, Seoul, Republic of Korea

Men's Health

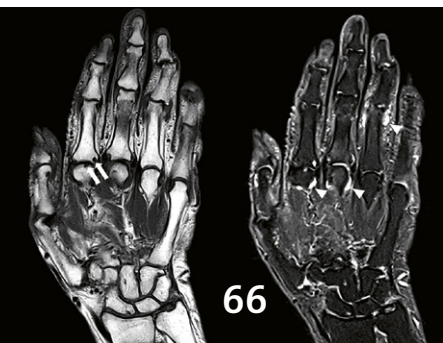
56 The Expanding Role of Deep Learning Reconstruction in Prostate MRI

Paulo Gil Agostinho, et al.
Hospital da Luz, Coimbra, Portugal

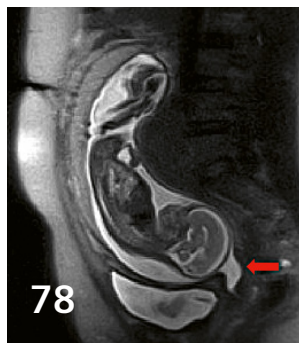
Expert Insights

64 My favourite feature: Append Table Positioning Strategy

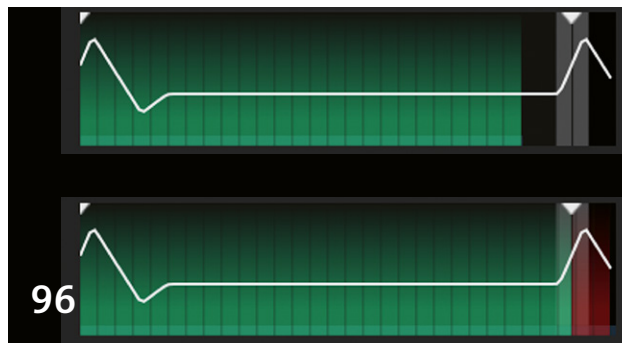
Cristiana Araújo
Siemens Healthineers, Porto, Portugal



0.55T MRI of a patient with rheumatoid arthritis



Fetal low field MRI³



How to deal with arrhythmia in cardiac MRI

Musculoskeletal Imaging

66 Imaging of the Musculoskeletal System Using 0.55T MRI

Tobias Pogarell and Rafael Heiss
Institute of Radiology, University Hospital Erlangen, Germany

73 Exploring the Potential of Low-Field Musculoskeletal MRI at 0.55T: Preliminary Results in Patients with Large Metal Implants²

Hanns-Christian Breit, et al.
University Hospital Basel, Switzerland

Fetal Imaging

78 Fetal³ Low Field MRI – the First 150 Cases

Jana Hutter, et al.
School of Biomedical Engineering, King's College London, UK

Cardiovascular Imaging

85 Cardiac MRI on the MAGNETOM Free.Max

Orlando P. Simonetti, et al.
The Ohio State University, Columbus, OH, USA

96 How to Deal with Arrhythmia in Cardiac MRI

Christian Houbois, et al.
University of Toronto and Sunnybrook Health Sciences Centre, Toronto, ON, Canada

106 Skip the Electrodes, But Not A Beat: The Engineering Behind the Beat Sensor

Peter Speier and Mario Bacher
Siemens Healthineers, Erlangen, Germany

Meet Siemens Healthineers

118 Introducing Katie Grant

Senior Director for MR Marketing and Sales Operations in North America, Minneapolis, MN, USA

119 Introducing Tom Hilbert

Quantitative Imaging Enthusiast & Acquisition and Reconstruction Expert at the Swiss Innovation Hub, Lausanne, Switzerland

¹Work in progress. The product is still under development and not commercially available. Its future availability cannot be ensured.

²The MRI restrictions (if any) of the metal implant must be considered prior to patient undergoing MRI exam. MR imaging of patients with metallic implants brings specific risks. However, certain implants are approved by the governing regulatory bodies to be MR conditionally safe. For such implants, the previously mentioned warning may not be applicable. Please contact the implant manufacturer for the specific conditional information. The conditions for MR safety are the responsibility of the implant manufacturer, not of Siemens Healthineers.

³MR scanning has not been established as safe for imaging fetuses and infants less than two years of age. The responsible physician must evaluate the benefits of the MR examination compared to those of other imaging procedures.



Roderic I. Pettigrew, PhD, MD, serves as chief executive officer (CEO) of Engineering Health (EnHealth) and inaugural dean, School of Engineering Medicine at Texas A&M University, which offers the ENMED (ENGINEERING MEDICINE) program in partnership with Houston Methodist Hospital. Dr. Pettigrew also holds the endowed Robert A. Welch Chair in Medicine. EnHealth is the nation's first comprehensive educational program to fully integrate engineering into all health-related disciplines. ENMED is the first constituent program focused on medicine.

An internationally recognized leader in biomedical imaging and bioengineering, Dr. Pettigrew served for 15 years as the founding director for the National Institute of Biomedical Imaging and Bioengineering (NIBIB) at National Institutes of Health (NIH). Prior to his appointment at the NIH, he joined Emory University School of Medicine as professor of radiology and medicine (cardiology) and Georgia Institute of Technology as professor of bioengineering. He is known for pioneering work in four-dimensional imaging of the cardiovascular system using magnetic resonance imaging (MRI).

Dr. Pettigrew has been elected to membership in the National Academy of Medicine, the National Academy of Engineering (NAE), the National Academy of Inventors, the American Academy of Arts and Sciences, and the National Academy of Sciences, India. His awards include gold medals from the Academy of Radiology Research and the Radiological Society of North America, the Arthur M. Bueche Award from the NAE and the Vannevar Bush Award from the National Science Board.

Expanding Boundaries

A lady approached Michael Faraday after one of his lectures on electromagnetism at the Royal Institution, and asked, "But, Professor Faraday, even if the effect you explained was obtained, what is the use of it?". According to Sir Richard Gregory, Faraday replied with Benjamin Franklin's aphorism: "Madam, will you tell me the use of a newborn child?" [1]

Sir Richard Gregory: Discovery, the spirit of science (London, 1916)

Pushing the envelope

In the last three decades, MRI has not only fulfilled its initial promise as a non-invasive imaging modality that can yield images with exquisite soft-tissue contrast in an impressive fashion; it has also become a versatile imaging tool that can provide insights into tissue in terms of its structure, function, and metabolism, and its magnetic, electrical, thermal, and mechanical properties. While the feasibility and demonstration of many advanced MR imaging methodologies often stem from academic settings, the engineering and technological refinements necessary for widespread clinical adoption require close collaboration between academics and industry partners. The fact that MRI systems are arguably among the most technologically and methodologically complex medical equipment you will find *routinely* used by clinicians around the world – with operational equipment specifications often prescribed in units of parts per million (ppm) – is a testament to the effective

collaboration between scientists in academia and industry. Just in the last two decades, this collaboration has contributed to impressive performance boosts in nearly every aspect of MRI hardware. There have been significant advances in main field strength, gradient performance, multi-channel radio-frequency coil arrays, and software – acquisition methodologies and reconstruction – to further our understanding of human health. It is worth noting that such impressive progress is not a mere byproduct of the technological advances that are bound to occur with time but advances that had to reckon with the bounds imposed by the biological effects due to exposure to electromagnetic fields. These span six or more orders of magnitude both in terms of amplitude (from several Tesla for static magnetic fields to μT for RF fields) and frequency (from gradient field oscillations at a few kHz to the RF field variations on the order of hundreds of MHz

that are characteristic of an MR experiment). Regulatory bodies and the MR community prescribed conservative limits for RF exposure, such as specific absorption ratio (SAR) or peripheral nerve stimulation (PNS), to minimize any potential harm. The MR community – both in academia and industry – has pushed the envelope far beyond what was once considered possible in nearly every aspect of MRI. For example, in 1979, based on theoretical models of dielectric and inductive losses in a human sample, it was suggested that: “...frequency of operation of the spectrometer with the human samples should be less than about 10 MHz” ($\sim 0.25T$) [2]. A mere few years later, in 1983, the first whole-body MRI scanners with field strengths of 1.5T that were capable of scanning the human head were introduced. Since that time, the strength of the main magnetic field of MRI scanners has increased five fold [3, 4]. The challenges of increased SAR and B_1^+ field inhomogeneity intrinsic to imaging at ultra-high fields are being met by methodological advances, such as techniques to lower the RF exposure while preserving tissue contrast and technological advances such as multi-array transmit solutions to minimize B_1^+ field homogeneity [5–7]. The SNR gains at ultra-high fields, as well as the increased sensitivity and specificity of the BOLD signal at ultra-high fields, have made it possible to image at resolutions capable of probing the columnar and laminar structures – believed to be the cortical processing units (CPU) – of the cortex [8]. This has also made it possible to couple blood flow dynamics in micro vessels of the brain to function [9], and to improve functional and structural images of the brain stem. From a clinical perspective, the increased sensitivity at ultra-high field imaging has broadened the range of potential applications: e.g., brain imaging with high spatial and contrast resolution to visualize various intracranial pathologies, to resolve metabolites hitherto undetectable at lower field strengths [10], measure pH in vivo, and evaluate neurovascular pathologies which may be contributing factors in many neurodegenerative [11] and demyelinating diseases [12, 13].

High-performance gradients for brain imaging: the lesson therein

Along the same lines, the potential to probe tissue micro-structure via diffusion-weighted imaging (DWI) accelerated the quest to develop high-performance gradients with high peak gradient strengths (G_{\max}) to impart sufficient diffusion sensitivity in relatively short times, and high slew rates (SR) to rapidly encode the diffusion-weighted signal with an echo-planar readout. At present, the commercial *whole-body* gradient systems available on the market can reach peak gradient amplitudes of around 80 mT/m and a maximum slew rate of 200 T/m/s [14]. Increasing the gradient performance of whole-body MR systems beyond this level

has been recognized as a significant challenge. With increasing coil radius (r), the coil inductance increases dramatically (by a factor of r^5), necessitating substantial power to drive the gradient coil (and mechanisms to dissipate the concomitant thermal load effectively). In addition, PNS thresholds decrease with increased imaging volume thereby restricting the range of G_{\max} /SR accessible for imaging. Many research MRI systems boast gradient inserts that cover a small region, e.g., an adult head, that can outperform whole-body gradient systems by a factor of four or more. Nearly a decade ago, the Human Connectome Project (HCP, funded by the National Institutes of Health) pushed the boundaries of DWI by customizing the gradient coil and gradient power amplifiers of commercial whole-body 3T scanners from Siemens Healthineers. The aim was to increase the maximum gradient strength from 40 mT/m to 100 mT/m [15] early on, with an even bolder version built as academically proposed with a maximum gradient strength of 300 mT/m [16]. Both systems boast a clean inner bore size of 56 cm with linearity of the gradient field (about 5% at 20 cm FOV) to image an adult head. It is no exaggeration to say that the technological and methodological advancements with the HCP have transformed the field of mapping connections within the brain and have yielded unprecedented insights into how the brain circuitry changes with aging and in disease. A more advanced version of the high-performance gradient system (dubbed Connectome 2.0¹), with a G_{\max} of 500 mT/m, a maximum SR of 600 T/m/s, and a slightly smaller inner diameter of 44 cm, is being developed [17] to study the functional architecture of the brain at multiple scales – from probing cellular geometries at microscopic levels to improving the robustness of estimates of fiber connectivity at macroscopic levels. Dedicated head-only systems with impressive gradient performance have now been demonstrated by several groups [18–22]. Overall, high-performance gradient systems have a high likelihood of becoming the new standard for neuro imaging, not just in research and academic settings but also in routine clinical practice.

High-performance gradients for whole-body imaging: what the future may hold

Indeed, the advent of high-performance gradients has contributed to opening new vistas of scientific inquiry to probe brain structure and function with unprecedented spatial and contrast resolutions. However, the role of high-performance gradients in body imaging has remained somewhat stagnant due to the inherent challenges of attaining sufficient gradient linearity over a large FOV, lower thresholds for PNS, and possible cardiac stimulation. However, the methodological improvements and technological expertise gained with high-performance gradients in neuroimaging can open new frontiers in the study of

structures outside the brain in the body. Several years ago, I advocated for developing high-performance gradients suitable for whole-body imaging and proposed what led to the creation of the 3T MAGNETOM Cima.X system¹, which will attain a gradient strength of 200 mT/m with a slew rate of 200 T/m/s. Compared to neuroimaging, the body-imaging challenges imposed by physiologic motion from cardiac pulsation, respiration, and blood flow, and by the substantial air-tissue interfaces in the thorax that introduce field inhomogeneities are substantial. Nonetheless there are several compelling reasons to investigate the role of high-performance gradients in the body.

First, as in neuroimaging, *even small reductions in TE* to attain a prescribed diffusion weighting may significantly mitigate the confounding effects of tissue motion and artifacts arising at susceptibility interfaces. Several clinical applications may immediately benefit from the availability of high-performance whole-body gradient systems. Multi-parametric MRI of the prostate – the recommended initial diagnostic test for men with suspected prostate cancer – would benefit where imaging guidelines prescribe that diffusion MRI at b-values $\sim 1400 \text{ s/mm}^2$ be obtained to improve the diagnostic confidence [23]. A concern, however, is that the presence of air in the bowels can substantially degrade the quality of prostate diffusion-weighted MRI. In our preliminary experience with human volunteers on the MAGNETOM Cima.X platform¹ [24], we successfully tested and demonstrated the feasibility of obtaining diffusion weighting $> 2400 \text{ s/mm}^2$ (TE $\sim 55 \text{ ms}$). The reduction in TE provides higher SNR for imaging and helps minimize the impact of T2 weighting in DWI.

Second, unlike neuroimaging, tissue motion – bulk motion as well as deformation – within the thoracoabdominal cavity is on the order of several millimeters of displacement. This is four or more orders of magnitude higher than the diffusive motion (micrometers) of water molecules and can result in a substantial signal loss if not treated appropriately. So, broader application of DWI in the body should consider the specific motion characteristics of the organ under investigation. One approach to increase the motion resilience is to design the diffusion-encoding gradient waveforms to be velocity (M_1) and acceleration (M_2) compensated at the cost of prolonged TE [25–28]. This cost could be partly mitigated with the availability of high-performance gradient systems. The feasibility of such M_1/M_2 -compensated diffusion-encoding gradient waveforms has been demonstrated, e.g., in cardiac DWI in systems with gradient strengths of 80 mT/m. It reasonably follows that these methods could directly benefit from the availability of systems capable of delivering higher gradient performance.

In the heart, diffusion tensor imaging (DTI) can map myofibrillar disarray in patients with hypertrophic cardiomyopathy, manifested as a reduction in fractional anisotropy (FA) [29]. Fractional anisotropy is also diminished in patients with dilated cardiomyopathy compared to normal controls [30]. Cardiac DWI/DTI has shown promise in evaluating myocardial infarction in acute and chronic settings, which could offer a non-contrast alternative or complement to the widely used delayed enhancement MRI [31, 32]. The availability of increased gradient performance should improve the robustness of these methods and offer wider clinical application.

Third, diffuse pathologic changes in tissue can subtly alter the underlying tissue microstructure and microcirculation that are not evident in conventional MRI. Despite the promise of the intra-voxel incoherent model of diffusion to yield information about tissue microstructure as well as microcirculation (perfusion) from a single experiment, accurate estimation of perfusion-related parameters – perfusion fraction (f) and pseudo-diffusion coefficient (D^*) – has been challenging. The reported values for a given organ system vary widely, as longer TEs associated with diffusion weighting encode relaxation-dependent effects in addition to diffusion [33]. Even modest reductions in TE with high-performance whole-body gradient systems can increase the robustness of estimating these parameters (particularly f) to yield imaging-based metrics that can help study such diffuse disease processes. For example, high-performance gradients could facilitate the development of diffusion-based non-contrast alternative metrics to extra-cellular volume fraction (ECV), a marker of diffuse fibrosis and in infiltrative cardiovascular pathologies such as cardiac amyloidosis, that is currently assessed with T1 measurements before and after the administration of an extracellular contrast agent [34]. Despite its promise, early DWI in the body has not found widespread clinical acceptance in the evaluation of diffuse disease processes. The improvements that come with high-performance gradient systems may increase the robustness of these measures enough to permit clinical adoption.

Fourth, the scale of endogenous tissue motion within the human body spans several orders of magnitude – from microscopic diffusive motion to rapid flow in large vessels that reaches many tens of cm/s. MRI scanners equipped with whole-body, high-performance gradient systems can enhance our ability to measure small tissue displacements, e.g., myocardial tissue velocities, vessel wall motion associated with cardiac pulsation, lymphatic drainage and cerebrospinal flow. The availability of (exceptionally) high gradient strengths can enhance the evaluation of microscopic externally imparted motion, e.g., to measure tissue motion caused by the acoustic radiation force at the focus of high-intensity ultrasound, or microscopic movement of

¹Work in progress. The product is still under development and not commercially available. Its future availability cannot be ensured.

tissue imparted by external transducers as in the case of MR elastography [35, 36].

Finally, the advantages of having seamless access to high-gradient performance on a whole-body clinical 3T scanner herald new vistas. It is true that the full hardware capabilities of the MAGNETOM Cima.X system¹ are expected to exceed what can be clinically used in some anatomies while staying within the current PNS limits – a condition analogous to the state of brain imaging when Connectom gradients were initially delivered. We have observed that in the last 15 years, the introduction of high-performance gradient systems for neuroimaging has revolutionized our understanding of brain structure and function. The MR community has developed MR methods and solutions to problems that seemed insurmountable at the time. Similar progress should happen in the body. New approaches are being developed to include PNS models in the design of gradient hardware and more tailored gradient waveforms that can be safely used for imaging. Perhaps the day is near when patient-specific limits for PNS will be determined at the beginning of an MRI scan, similar to what is done in modern CT scanners

to reduce radiation dose by modulating tube current as a function of patient body habitus. We hope the era of whole-body high-performance gradient systems will pave the way for a greater understanding of human health, earlier detection of disease, a greater opportunity for preventive intervention and thus improved delivery of healthcare.

Acknowledgments

This work significantly benefited from many conversations with and substantial editorial contributions by Raja Muthupillai, Ph.D., Visiting Research Professor at the School of Engineering Medicine / ENMED, Texas A&M University and Live Healthy Imaging, Houston.



Roderic I. Pettigrew

References

- Cohen IB. Faraday and Franklin's "Newborn Baby." *Proc Am Philos Soc.* 1987;131(2):177-182.
- Hoult DI, Lauterbur PC. The sensitivity of the zeugmatographic experiment involving human samples. *J Magn Reson.* 1979;34(2):425-433.
- Bottomley PA, Hart HR, Edelstein WA, Schenck JF, Smith LS, Leue WM, et al. NMR imaging/spectroscopy system to study both anatomy and metabolism. *Lancet.* 1983;2(8344):273-4.
- Uğurbil K. Imaging at ultrahigh magnetic fields: History, challenges, and solutions. *Neuroimage.* 2018;168:7-32.
- Padormo F, Beqiri A, Hajnal JV, Malik SJ. Parallel transmission for ultrahigh-field imaging. *NMR Biomed.* 2016;29(9):1145-1161.
- Katscher U, Börnert P. Parallel RF transmission in MRI. *NMR Biomed.* 2006;19(3):393-400.
- Zhu Y. Parallel excitation with an array of transmit coils. *Magn Reson Med.* 2004;51(4):775-784.
- Dumoulin SO, Fracasso A, van der Zwaag W, Siero JCW, Petridou N. Ultra-high field MRI: Advancing systems neuroscience towards mesoscopic human brain function. *Neuroimage.* 2018;168:345-357.
- Park CA, Kang CK, Kim YB, Cho ZH. Advances in MR angiography with 7T MRI: From microvascular imaging to functional angiography. *Neuroimage.* 2018;168:269-278.
- Nassirpour S, Chang P, Henning A. High and ultra-high resolution metabolite mapping of the human brain using 1 H FID MRSI at 9.4T. *Neuroimage.* 2018;168:211-221.
- McKiernan EF, O'Brien JT. 7T MRI for neurodegenerative dementias in vivo: a systematic review of the literature. *J Neurol Neurosurg Psychiatry.* 2017;88(7):564-574.
- Ineichen BV, Beck ES, Piccirelli M, Reich DS. New Prospects for Ultra-High-Field Magnetic Resonance Imaging in Multiple Sclerosis. *Invest Radiol.* 2021;56(11):773-784.
- Sati P. Diagnosis of multiple sclerosis through the lens of ultra-high-field MRI. *J Magn Reson.* 2018;291:101-109.
- Gudino N, Littin S. Advancements in Gradient System Performance for Clinical and Research MRI. *J Magn Reson Imaging.* 2023;57(1):57-70.
- Van Essen DC, Smith SM, Barch DM, Behrens TEJ, Yacoub E, Ugurbil K. The WU-Minn Human Connectome Project: an overview. *Neuroimage.* 2013;80:62-79.
- Setsompop K, Kimmlingen R, Eberlein E, Witzel T, Cohen-Adad J, McNab JA, et al. Pushing the limits of in vivo diffusion MRI for the Human Connectome Project. *Neuroimage.* 2013 Oct 15;80:220-33.
- Huang SY, Witzel T, Keil B, Scholz A, Davids M, Dietz P, et al. Connectome 2.0: Developing the next-generation ultra-high gradient strength human MRI scanner for bridging studies of the micro-, meso- and macro-connectome. *Neuroimage.* 2021;243:118530.
- Zhang B, Yen YF, Chronik BA, McKinnon GC, Schaefer DJ, Rutt BK. Peripheral nerve stimulation properties of head and body gradient coils of various sizes. *Magn Reson Med.* 2003;50(1):50-58.
- Chronik BA, Alejski A, Rutt BK. Design and fabrication of a three-axis edge ROU head and neck gradient coil. *Magn Reson Med.* 2000;44(6):955-963.
- Weiger M, Overweg J, Rösler MB, Froidevaux R, Hennel F, Wilm BJ, et al. A high-performance gradient insert for rapid and short-T₂ imaging at full duty cycle. *Magn Reson Med.* 2018;79(6):3256-3266.
- Foo TKF, Tan ET, Vermilyea ME, Hua Y, Fiveland EW, Piel JE, et al. Highly efficient head-only magnetic field insert gradient coil for achieving simultaneous high gradient amplitude and slew rate at 3.0T (MAGNUS) for brain microstructure imaging. *Magn Reson Med.* 2020;83(6):2356-2369.

- 22 Foo TKF, Laskaris E, Vermilyea M, Xu M, Thompson P, Conte G, et al. Lightweight, compact, and high-performance 3T MR system for imaging the brain and extremities. *Magn Reson Med*. 2018;80(5):2232-2245.
- 23 Beyer T, Schlemmer HP, Weber MA, Thierfelder KM. PI-RADS 2.1 – Image Interpretation: The Most Important Updates and Their Clinical Implications. *Rofo*. 2021;193(7):787-796. English, German.
- 24 Pettigrew RI, Muthupillai R, Buko E, Martin M, Fischer A. New high-performance whole-body gradients to clarify intravoxel incoherent motion DWI based multi-parametric MRI of the prostate: Initial results. Presented at: ISMRM & ISMRT Annual Meeting & Exhibition, 2023; Toronto, Canada.
- 25 Szczepankiewicz F, Sjölund J, Dall'Armellina E, Plein S, Schneider JE, Teh I, et al. Motion-compensated gradient waveforms for tensor-valued diffusion encoding by constrained numerical optimization. *Magn Reson Med*. 2021;85(4):2117-2126.
- 26 van Gorkum RJH, Guenther C, Koethe A, Stoeck CT, Kozerke S. Characterization and correction of diffusion gradient-induced eddy currents in second-order motion-compensated echo-planar and spiral cardiac DTI. *Magn Reson Med*. 2022;88(6):2378-2394.
- 27 Aliotta E, Moulin K, Magrath P, Ennis DB. Quantifying precision in cardiac diffusion tensor imaging with second-order motion-compensated convex optimized diffusion encoding. *Magn Reson Med*. 2018;80(3):1074-1087.
- 28 Moulin K, Croisille P, Feiweier T, Delattre BM, Wei H, Robert B, et al. In vivo free-breathing DTI and IVIM of the whole human heart using a real-time slice-followed SE-EPI navigator-based sequence: A reproducibility study in healthy volunteers. *Magn Reson Med*. 2016;76(1):70-82.
- 29 Tseng WYI, Dou J, Reese TG, Wedeen VJ. Imaging myocardial fiber disarray and intramural strain hypokinesis in hypertrophic cardiomyopathy with MRI. *J Magn Reson Imaging*. 2006;23(1):1-8.
- 30 von Deuster C, Sammut E, Asner L, Nordsletten D, Lamata P, Stoeck CT, et al. Studying Dynamic Myofiber Aggregate Reorientation in Dilated Cardiomyopathy Using In Vivo Magnetic Resonance Diffusion Tensor Imaging. *Circ Cardiovasc Imaging*. 2016;9(10):e005018.
- 31 NIELLES-VALLESPIN S, SCOTT A, FERREIRA P, KHALIQUE Z, PENNELL D, FIRMIN D. Cardiac Diffusion: Technique and Practical Applications. *J Magn Reson Imaging*. 2020;52(2):348-368.
- 32 Khalique Z, Ferreira PF, Scott AD, NIELLES-VALLESPIN S, FIRMIN DN, PENNELL DJ. Diffusion Tensor Cardiovascular Magnetic Resonance Imaging: A Clinical Perspective. *JACC: Cardiovasc Imaging*. 2020;13(5):1235-1255. Epub 2019 Oct 11.
- 33 Li YT, Cercueil JP, Yuan J, Chen W, Loffroy R, Wáng YXJ. Liver intravoxel incoherent motion (IVIM) magnetic resonance imaging: a comprehensive review of published data on normal values and applications for fibrosis and tumor evaluation. *Quant Imaging Med Surg*. 2017;7(1):59-78.
- 34 Messroghli DR, Moon JC, Ferreira VM, Grosse-Wortmann L, He T, Kellman P, et al. Clinical recommendations for cardiovascular magnetic resonance mapping of T1, T2, T2* and extracellular volume: A consensus statement by the Society for Cardiovascular Magnetic Resonance (SCMR) endorsed by the European Association for Cardiovascular Imaging (EACVI). *J Cardiovasc Magn Reson*. 2017;19(1):75.
- 35 Muthupillai R, Lomas DJ, Rossman PJ, Greenleaf JF, Manduca A, Ehman RL. Magnetic resonance elastography by direct visualization of propagating acoustic strain waves. *Science*. 1995;269(5232):1854-1857.
- 36 Ehman RL. Magnetic resonance elastography: from invention to standard of care. *Abdom Radiol (NY)*. 2022;47(9):3028-3036.

We appreciate your comments.

Please contact us at magnetomworld.team@siemens-healthineers.com

Editorial Board



Antje Hellwich
Editor-in-chief



Rebecca Ramb, Ph.D.
Vice President of MR
Research & Clinical Translation



Kathrin El Nemer, M.D.
MR Medical Officer



Wellesley Were
MR Business Development
Manager Australia and
New Zealand



Jane Kilkenny
Vice President of MR
Malvern, PA, USA



Heiko Meyer, Ph.D.
Head of Neuro Applications

Review Board

André Fischer, Ph.D.
Global Segment Manager Neurology,
Cardiovascular, and Pediatric MRI

Daniel Fischer
Head of Clinical and
Scientific Marketing

Christian Geppert, Ph.D.
Head of Cardiovascular Applications

Zahra Hosseini, Ph.D.
Global Product Marketing Manager
Free. Platform

Felix Müller-Witt
Global Head of Product Marketing

Gregor Thörmer, Ph.D.
Head of Oncological Applications

The Increasing Role of 7T MRI in the Neuroimaging of Cerebral Small Vessel Disease

Yue Wu^{1,2}; Rong Xue^{1,2}; Yan Zhuo^{1,2}; Zihao Zhang^{1,2,3}

¹State Key Laboratory of Brain and Cognitive Science, Institute of Biophysics, Chinese Academy of Sciences, Beijing, China

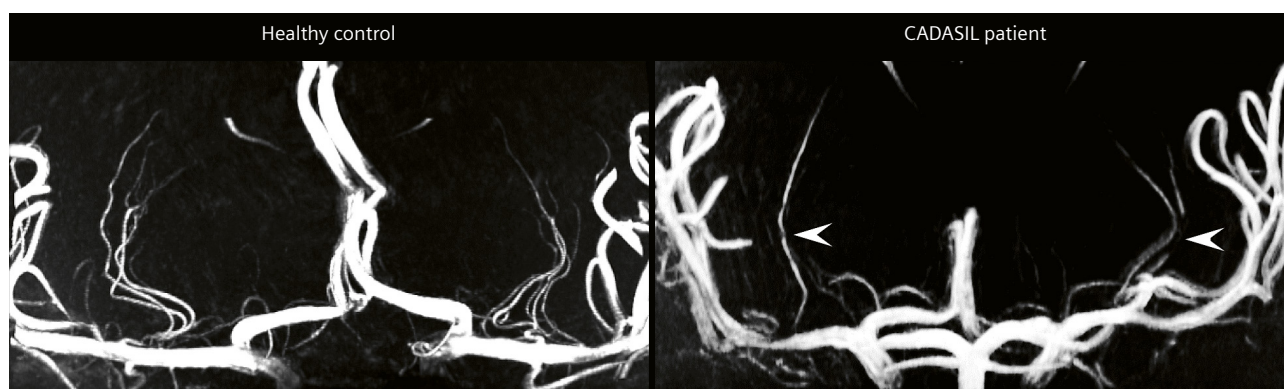
²University of Chinese Academy of Sciences, Beijing, China

³Institute of Artificial Intelligence, Hefei Comprehensive National Science Center, Hefei, China

Introduction

Cerebral small vessel disease (cSVD) is the most common, chronic, and progressive vascular disease [1]. cSVD causes acute symptoms, such as lacunar infarct and intracranial hemorrhage, accounting for 20% of symptomatic strokes. The patients also experience chronic insidious onset, for example, the high prevalence of cSVD in the elderly population was proven to be associated with an increased risk for dementia [2]. Previously, the STandards for Reporting Vascular changes on nEuroimaging (STRIVE) was proposed to guide the scientific reporting of changes related to cSVD on neuroimaging [3]. It manifests as recent small subcortical infarct, lacune of presumed vascular origin, white matter hyperintensity of presumed vascular origin, perivascular space, cerebral microbleed, and brain atrophy. However, these imaging features were summarized from clinically available 3T and 1.5T MRI scanners. The structure and function of cerebral small vessels, which are directly related to cSVD, could so far not be fully characterized at 3T and lower field strengths. Tiny parenchymal lesions such as cortical microinfarcts are also more difficult to detect at 3T and lower field strength, as spatial resolution can only be pushed to a certain extent in clinical scan times.

In recent years, ultra-high-field (UHF) MRI at 7T has been shown to be effective in diagnosing various neurovascular diseases. Since the signal-to-noise ratio (SNR) of MRI is approximately proportional to the field strength, 7T MRI provides an intrinsic signal-to-noise ratio (SNR) of approximately 2.3 times that of 3T and 4.7 times that of 1.5T, if a linear dependency of SNR to the field strength is assumed. However, literature indicates a supralinear correlation, proportional to $B_0^{1.65}$ [4]. Higher SNR supports using higher spatial resolution in the acquisition and enabling the visualization of small vessels and tiny lesions on the brain. On the other hand, relaxation times change as the field strength increases (T1 gets longer and T2 gets shorter), which allows MRI techniques such as angiography based on flow-related enhancement to achieve higher contrast-to-noise ratios (CNRs). Additionally, sequences sensitive to susceptibility effects, such as T2*-weighted imaging and quantitative susceptibility mapping (QSM)¹, benefit from increased susceptibility at 7T, enabling better visualization of venules and microbleeds. These advantages of 7T MRI provide an opportunity to directly evaluate the structure and function of cerebral small vessels.



1 Coronal maximum intensity projection of 7T TOF-MRA of a healthy control and a CADASIL patient. The arrowheads point to flow deficits in the lenticulostriate arteries.

¹Work in progress. The application is currently under development and is not for sale in the U.S. and in other countries. Its future availability cannot be ensured.

Angiography

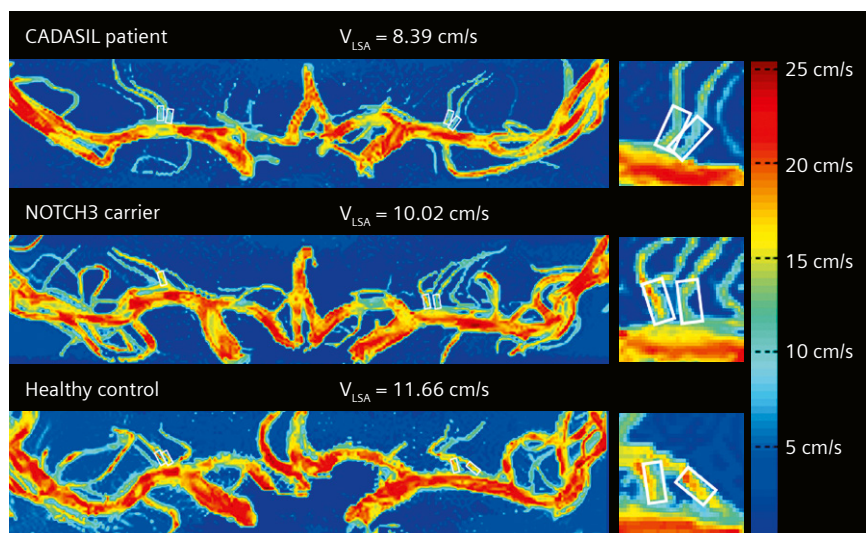
The CNR of TOF-MRA was reported 83% higher at 7T compared to that obtained at 3T [5]. The improved CNR highlighted smaller peripheral vessels, which can be clearly seen at images with high resolution. This in turn allows to e.g. detect stenosis and occlusion in rather small vessels like the lenticulostriate artery (LSA) using 7T TOF-MRA. This finding is a prone cause of cSVD in deep cerebral infarction [6]. On the other hand, the angiography of LSA can be used to assess the establishment of collateral circulation [7]. The vascular density of LSA visualized by 7T TOF-MRA was reported to be comparable to DSA, and significantly superior to 3T TOF-MRA [8].

The visualization of intracranial perforating arteries such as LSA by 7T TOF-MRA expands the horizon for *in vivo* imaging studies of cSVD. In patients with hypertension, the number of stems and branches of LSAs was significantly lower than that in healthy controls, while no difference was found in the curvature and tortuosity of LSA. In a genetic cSVD, called CADASIL (cerebral autosomal dominant arteriopathy with subcortical infarcts and leukoencephalopathy), the correlation between the number of LSA branches and the Mini-Mental State Examination (MMSE) score was confirmed. Meanwhile, an increased proportion of discontinuous flow of LSAs was reported in CADASIL patients [9]. LSAs are also a frequent source of lacunar infarcts. With segmentation and modeling, the culprit LSAs that may cause the lacunar infarct can be identified [10]. In addition, morphological changes in LSA were observed in the early progression of subcortical vascular dementia (SVaD). Lower number of branches and enlarged radius of LSA were found in SVaD patients [11]. These studies confirm that 7T TOF-MRA is an effective and non-invasive method to evaluate the morphological changes of perforating arteries in cSVD.

Flow velocity

By using velocity encoding (VENC) gradients, the flow velocity of blood vessels can be quantified by phase-contrast (PC) MRI. Time-resolved PC-MRI has been validated in measuring blood flow velocity of the aorta, carotid arteries and the circle of Willis (CoW) [12]. Due to the available SNR at 3T, the spatial resolution of PC-MRI cannot measure the flow velocity of arterioles very well. Another reason is that the partial volume effects lead to an underestimation of the flow velocity and miscalculate the flow direction [13]. The increased SNR and flow-related enhancement at 7T breaks down the barrier to measuring the velocity of perforating arteries. The velocity mapping of cerebral small vessels was firstly obtained with a non-time-resolved PC-MRA [14]. A VENC value of 15 cm/s was used to measure the velocity and direction of small arteries on the CoW, including LSA, posterior communicating artery and anterior choroidal artery. In patients with CADASIL, the flow velocity of LSA can be measured in the proximal segments [15]. The velocity was found to be decreasing with progression of the disease and correlated with aging, functional dependence, cognitive impairment and mood disturbance.

When scanned with a single slice technique, the time-resolved PC MRI enables dynamic assessment of flow pulsatility in perforating arteries. The temporal resolution can be set to 57-156 ms with an in-plane resolution of 0.3 mm [16]. In this manner, the flow velocities of LSAs can be measured at two planes: the basal ganglia (BG) and centrum semiovale (CSO). The range of changes in flow velocity within a cardiac cycle can be calculated as the pulsatility index (PI) [17], which represented the arteriole hemodynamics. In patients with cSVD-related stroke, the PIs of LSAs were found to be elevated in both BG and CSO [18]. Nevertheless, a higher PI was also correlated with age



2 The flow velocities of proximal lenticulostriate arteries measured by 7T PC-MRA. The velocity decreased with the progression of cerebral small vessel disease. CADASIL is a form of hereditary stroke disorder and is thought to be caused by mutations in the NOTCH3 gene.

in healthy individuals. The boundary between pathological and physiological changes of PI in cerebral small vessels remains to be clarified in future studies.

Susceptibility imaging

Susceptibility refers to the extent to which a substance becomes magnetized when it is placed in an external magnetic field. Susceptibility weighted imaging (SWI) is a commonly used imaging method reflecting susceptibility contrast, while quantitative susceptibility mapping (QSM) serves as the quantification method. The susceptibility-induced field inhomogeneity is more prone to be detected at UHF, which makes it an ideal choice for SWI and QSM [19]. Deoxyhemoglobin, hemosiderin, and ferritin are rich in iron, which makes the signal of venous blood, cerebral microbleeds, and subcortical nuclei prominent on susceptibility imaging.

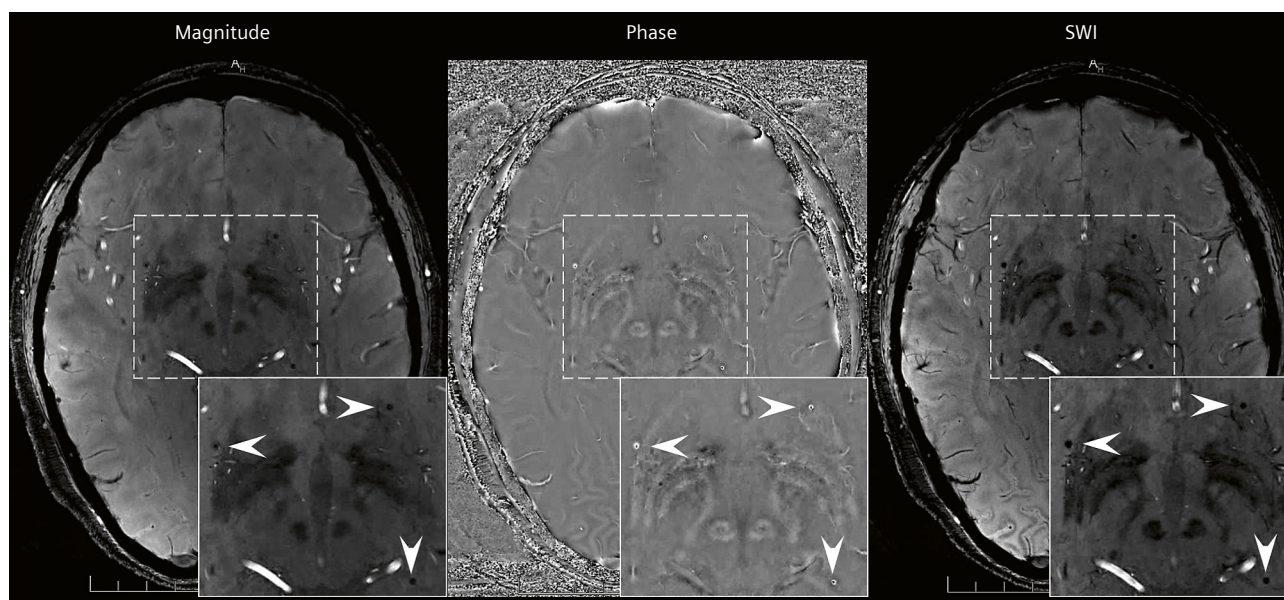
Cerebral veins with small calibers can be clearly displayed by 7T SWI, such as the deep medullary veins (DMVs). An automated algorithm to segment and quantify the DMV on 7T SWI was developed [20]. Using this method, the morphology of the DMV was analyzed in dementia likely caused by cSVD [21]. The number and vascular density were similar between patients and healthy controls, while more tortuous DMVs were found in the patient group. The curved DMVs were also more frequently to be found in sporadic cSVD [22]. The impaired integrity of the DMV was reported in CADASIL patients, which may occur before the appearance of white matter hyperintensities (WMH) [23]. The morphology of DMV on 7T SWI may play an important role in the diagnosis and research of cSVD.

The enhanced susceptibility effects at 7T makes QSM highly sensitive to magnetic susceptibility differences between components. Along with the increased SNR, the spatial resolution of QSM can be boosted at 7T. For instance, the higher susceptibility of superficial veins associated with disease progression was reported in CADASIL patients [24]. This increased susceptibility likely reflected decreased venous oxygen saturation. It was also related to the clinical phenotype and the STRIVE imaging features of cSVD.

Cerebral microbleeds (CMBs) are one of the conventional neuroimaging markers of cSVD. It can be detected with a higher sensitivity at 7T than at lower field strengths [25]. Considering the high detection rate of CMBs by 7T MRI, an automated postprocessing tool is needed for a reliable and reproducible detection. The increased CMBs and iron deposits caused by the dysfunction of blood-brain barrier in cSVD can be quantified using 7T QSM [26, 27].

Perivascular space

Perivascular spaces (PVS) are fluid-filled spaces that surround small arterioles, capillaries and venules in the brain. Enlarged PVS are considered one of the MR imaging hallmarks of cSVD and are associated with older age as well as the presence of lacunar infarcts and white matter lesions [28]. Using the increased CNR and spatial resolution, T2-weighted images at 7T were able to show not only the enlarged PVS, but also the physiological PVS in normal states [29]. The feasibility of imaging and quantifying PVS at 7T was first demonstrated in patients with Alzheimer's disease (AD). PVS was spatially correlated to LSA in BG



3 Cerebral microbleeds on susceptibility weighted imaging of a CADASIL patient. Arrowheads indicate the microbleeds in the thalamus.

and CSO, but not with veins [30]. Another study described the characteristics of PVS in BG, thalamus, midbrain, and white matter regions in 45 healthy subjects [31]. The number and volume fraction of PVS at BG were shown to increase with age, and largely varied among individuals. Interestingly, the study reported that inhalation of carbon dioxide significantly increased the volume fraction of PVS at BG and white matter, suggesting an association between vasodilation and PVS. The correlation between PVS and other imaging markers related to cSVD was then investigated in 50 community-dwelling individuals over 40 years old [32]. The number of PVS was found to correlate with the presence of CMBs, rather than age or vascular risk factors. Advanced post-processing methods were also developed to improve the visualization and quantification of PVS based on filtering and neural networks [33, 34]. In summary, PVS could be used as an imaging marker to reflect the progression of cSVD. However, the discrimination between physiological and pathological PVS must be answered by cohort studies in larger populations.

Cortical microinfarcts

Cerebral cortical microinfarcts (CMI) are a novel MRI marker of vascular brain injury and need a high spatial resolution to be detected. Using 7T MRI and histopathology on *ex vivo* tissue, cerebral microinfarcts greater than 1–2 mm in the cortical gray matter can be detected by 7T FLAIR with 0.80 mm isotropic resolution [35–37]. In another study, CMIs were also visible on 3T images, but the detection rate of these lesions was only 2% that of 7T [38]. Apart from the field strength, the sensitivity of CMI detection also depends on the imaging parameters and analysis methods: images should be acquired using 3D T1-weighted and 3D FLAIR (or T2-weighted) sequences

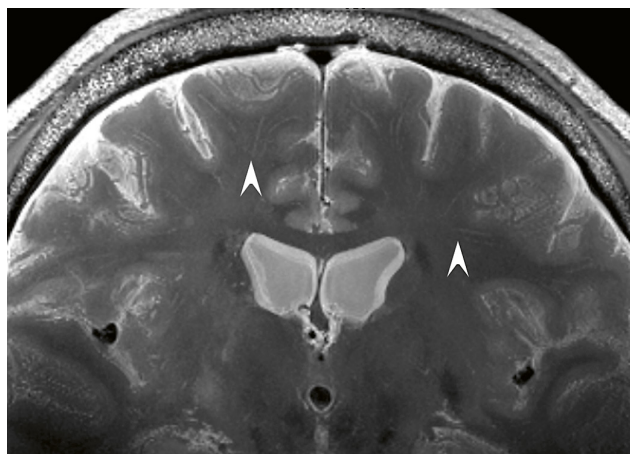
with isotropic voxels less than 1 mm to avoid missing tiny lesions, preferably with additional T2*-weighted or hemorrhage-sensitive sequences such as SWI to rule out confounding imaging features such as CMBs. Most clinical *in vivo* studies have focused on the detection of intracortical microinfarcts, i.e., CMI, because it has been difficult to distinguish microinfarcts from other lesions in subcortical regions (e.g., WMH, lacunar infarcts, and enlarged PVS). For example, histopathologic examination of juxtacortical regions demonstrated that lesions suspected to be microinfarcts were usually enlarged PVS [36]. Therefore, the consensus was reached that punctate subcortical lesions cannot be classified as cerebral microinfarcts without confirmation by DWI [39].

The high detection rate of CMIs using high resolution structural imaging at 7T should have theoretically promoted the study of CMIs. However, controversy still exists on the prevalence of CMI due to the limited sample size of existing studies. For instance, a higher number of CMIs was found in 14 patients with AD compared with 18 healthy controls, while the incidence of CMI was similar between the two groups [40]. In another study, no difference in the incidence and number of CMI was found between 29 patients with early AD and 22 healthy controls [41]. Further multicenter clinical trials with large populations and definitive diagnosis of cSVD could provide more convincing results on the incidence, etiology, and role of CMIs in cSVD.

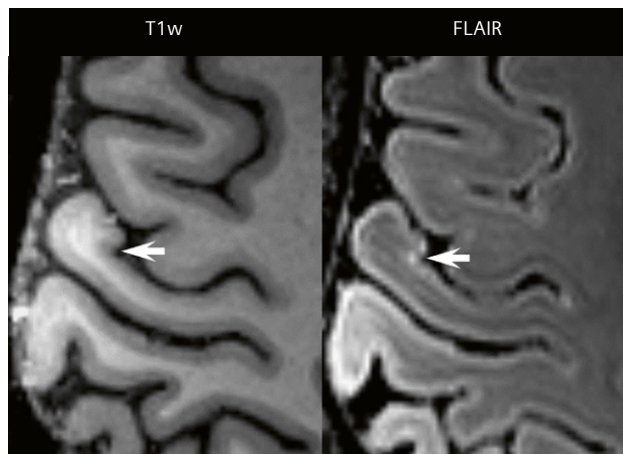
Future directions

Technical development

Both the hardware and software of 7T MRI were significantly improved over the recent years. The use of parallel transmitter coils (pTx)¹ has improved the field homogeneity significantly while still allowing simultaneous multiple slice



4 Perivascular spaces on a 7T T2-weighted image of a patient with subcortical vascular dementia.



5 The cortical microinfarct on the T1-weighted and FLAIR images of a CADASIL patient.

(SMS) acquisition. The development of new receive coils¹ including combined head and neck coils will allow neurovascular imaging with head-and-neck coverage with higher SNR. The use of compressed sensing, machine learning¹ and Wave-CAIPI acceleration techniques will reduce the scan time or increase resolution further at 7T.

Broader clinical application

With more and more 7T human MRI scanners installed each year in both research centers and hospitals, and more 7T scanners released for clinical use, it is expected that an increasing number of clinical and research studies will be performed at 7T. So far, there were only a few small sampled studies directly comparing between 3T and 7T for different neurovascular diseases. In the near future, it is critical to perform larger scale comparison studies to demonstrate the unique advantage of 7T over 3T. To demonstrate the clinical value of 7T MRI, future large scale multi-center studies are required. Strong collaboration between 7T sites and standardization of techniques across sites and scanners using phantoms are needed to enable such multi center studies.

Conclusion

UHF MRI, especially 7T MRI, has demonstrated its great value in the diagnosis and research of cSVD. Benefiting from the higher SNR and contrast, multi-modality high-resolution imaging methods at 7T, especially those based on the angiography and susceptibility contrasts, reveal various structural and functional changes of cerebral small vessels in cSVD. In the future, large cohort studies are needed to verify the diagnostic power of these imaging features, and determine the thresholds differentiating the physiological and pathological states. Nevertheless, the relative scarcity of 7T MRI scanners, as well as the physical challenges of UHF imaging, still hinder the broad application of 7T MRI in clinical environments. The combination of technology development and clinical research will bring new advances of 7T MRI to neurologists.

References

- Chojdak-Lukasiewicz J, Dziadkowiak E, Zimny A, Paradowski B. Cerebral small vessel disease: A review. *Adv Clin Exp Med*. 2021;30(3):349-356.
- Gorelick PB, Scuteri A, Black SE, Decarli C, Greenberg SM, Iadecola C, et al. American Heart Association Stroke Council, Council on Epidemiology and Prevention, Council on Cardiovascular Nursing, Council on Cardiovascular Radiology and Intervention, and Council on Cardiovascular Surgery and Anesthesia. Vascular contributions to cognitive impairment and dementia: a statement for healthcare professionals from the american heart association/american stroke association. *Stroke*. 2011;42(9):2672-2713.
- Wardlaw JM, Smith EE, Biessels GJ, Cordonnier C, Fazekas F, Frayne R, et al. Standards for Reporting Vascular changes on nEuroimaging (STRIVE v1). *Neuroimaging standards for research into small vessel disease and its contribution to ageing and neurodegeneration*. *Lancet Neurol*. 2013;12(8):822-838.
- Pohmann R, Speck O, Scheffler K. Signal-to-noise ratio and MR tissue parameters in human brain imaging at 3, 7, and 9.4 tesla using current receive coil arrays. *Magn Reson Med*. 2016 Feb;75(2):801-809.
- von Morze C, Xu D, Purcell DD, Hess CP, Mukherjee P, Saloner D, et al. Intracranial time-of-flight MR angiography at 7T with comparison to 3T. *J Magn Reson Imaging*. 2007;26(4):900-904.
- Kang CK, Park CA, Park CW, Lee YB, Cho ZH, Kim YB. Lenticulostriate arteries in chronic stroke patients visualised by 7 T magnetic resonance angiography. *Int J Stroke*. 2010;5(5):374-380.
- Lee YB, Kang CK, Kim KT, Park CA, Kim YB, Cho ZH. A non-invasive technique for visualization of microvessels in asymptomatic patients with middle cerebral artery steno-occlusion. *Vasc Med*. 2013;18(5):314-317.
- Cho ZH, Lee YB, Kang CK, Yang JW, Jung IH, Park CA, et al. Microvascular imaging of asymptomatic MCA steno-occlusive patients using ultra-high-field 7T MRI. *J Neurol*. 2013;260(1):144-150.
- Ling C, Fang X, Kong Q, Sun Y, Wang B, Zhuo Y, et al. Lenticulostriate Arteries and Basal Ganglia Changes in Cerebral Autosomal Dominant Arteriopathy With Subcortical Infarcts and Leukoencephalopathy, a High-Field MRI Study. *Front Neurol*. 2019;10:870.
- Kang CK, Wörz S, Liao W, Park CA, Kim YB, Park CW, et al. Three dimensional model-based analysis of the lenticulostriate arteries and identification of the vessels correlated to the infarct area: preliminary results. *Int J Stroke*. 2012;7(7):558-563.
- Seo SW, Kang CK, Kim SH, Yoon DS, Liao W, Wörz S, et al. Measurements of lenticulostriate arteries using 7T MRI: new imaging markers for subcortical vascular dementia. *J Neurol Sci*. 2012;322(1-2):200-205.
- Schneiders JJ, Ferns SP, van Ooij P, Siebes M, Nederveen AJ, van den Berg R, et al. Comparison of phase-contrast MR imaging and endovascular sonography for intracranial blood flow velocity measurements. *AJNR Am J Neuroradiol*. 2012;33(9):1786-1790.
- Hofman MB, Visser FC, van Rossum AC, Vink QM, Sprenger M, Westerhof N. In vivo validation of magnetic resonance blood volume flow measurements with limited spatial resolution in small vessels. *Magn Reson Med*. 1995;33(6):778-784.
- Kang CK, Park CA, Lee DS, Lee YB, Park CW, Kim YB, et al. Velocity measurement of microvessels using phase-contrast magnetic resonance angiography at 7 Tesla MRI. *Magn Reson Med*. 2016;75(4):1640-1646.
- Sun C, Wu Y, Ling C, Xie Z, Sun Y, Xie Z, et al. Reduced blood flow velocity in lenticulostriate arteries of patients with CADASIL assessed by PC-MRA at 7T. *J Neurol Neurosurg Psychiatry*. 2022;93(4):451-452.

¹Work in progress. The application is currently under development and is not for sale in the U.S. and in other countries. Its future availability cannot be ensured.

- 16 Bouvy WH, Geurts LJ, Kuijff HJ, Luijten PR, Kappelle LJ, Biessels GJ, et al. Assessment of blood flow velocity and pulsatility in cerebral perforating arteries with 7-T quantitative flow MRI. *NMR Biomed*. 2016;29(9):1295-1304.
- 17 Geurts L, Biessels GJ, Luijten P, Zwanenburg J. Better and faster velocity pulsatility assessment in cerebral white matter perforating arteries with 7T quantitative flow MRI through improved slice profile, acquisition scheme, and postprocessing. *Magn Reson Med*. 2018;79(3):1473-1482.
- 18 Geurts LJ, Zwanenburg JJM, Klijn CJM, Luijten PR, Biessels GJ. Higher Pulsatility in Cerebral Perforating Arteries in Patients With Small Vessel Disease Related Stroke, a 7T MRI Study. *Stroke*. 2018 Dec 11;50(1):62-68.
- 19 Ugurbil K. Magnetic resonance imaging at ultrahigh fields. *IEEE Trans Biomed Eng*. 2014;61(5):1364-1379.
- 20 Kuijff HJ, Bouvy WH, Zwanenburg JJ, Razoux Schultz TB, Viergever MA, et al. Quantification of deep medullary veins at 7 T brain MRI. *Eur Radiol*. 2016;26(10):3412-3418.
- 21 Bouvy WH, Kuijff HJ, Zwanenburg JJ, Koek HL, Kappelle LJ, Luijten PR, et al.; Utrecht Vascular Cognitive Impairment (VCI) Study group. Abnormalities of Cerebral Deep Medullary Veins on 7 Tesla MRI in Amnesic Mild Cognitive Impairment and Early Alzheimer's Disease: A Pilot Study. *J Alzheimers Dis*. 2017;57(3):705-710.
- 22 Shaaban CE, Aizenstein HJ, Jorgensen DR, MacCloud RL, Meckes NA, Erickson KI, et al.; LIFE Study Group. In Vivo Imaging of Venous Side Cerebral Small-Vessel Disease in Older Adults: An MRI Method at 7T. *AJNR Am J Neuroradiol*. 2017;38(10):1923-1928.
- 23 De Guio F, Vignaud A, Ropele S, Duering M, Duchesnay E, Chabriet H, et al. Loss of venous integrity in cerebral small vessel disease: a 7-T MRI study in cerebral autosomal-dominant arteriopathy with subcortical infarcts and leukoencephalopathy (CADASIL). *Stroke*. 2014;45(7):2124-2126.
- 24 Ling C, Zhang Z, Wu Y, Fang X, Kong Q, Zhang W, et al. Reduced Venous Oxygen Saturation Associates With Increased Dependence of Patients With Cerebral Autosomal Dominant Arteriopathy With Subcortical Infarcts and Leukoencephalopathy: A 7.0-T Magnetic Resonance Imaging Study. *Stroke*. 2019;50(11):3128-3134.
- 25 Bian W, Hess CP, Chang SM, Nelson SJ, Lupo JM. Susceptibility-weighted MR imaging of radiation therapy-induced cerebral microbleeds in patients with glioma: a comparison between 3T and 7T. *Neuroradiology*. 2014;56(2):91-96.
- 26 Sun C, Wu Y, Ling C, Xie Z, Kong Q, Fang X, et al. Deep Gray Matter Iron Deposition and Its Relationship to Clinical Features in Cerebral Autosomal Dominant Arteriopathy With Subcortical Infarcts and Leukoencephalopathy Patients: A 7.0-T Magnetic Resonance Imaging Study. *Stroke*. 2020;51(6):1750-1757.
- 27 Liem MK, Lesnik Oberstein SA, Versluis MJ, Maat-Schieman ML, Haan J, et al. 7 T MRI reveals diffuse iron deposition in putamen and caudate nucleus in CADASIL. *J Neurol Neurosurg Psychiatry*. 2012;83(12):1180-1185.
- 28 Potter GM, Doubal FN, Jackson CA, Chappell FM, Sudlow CL, Dennis MS, et al. Enlarged perivascular spaces and cerebral small vessel disease. *Int J Stroke*. 2015;10(3):376-381.
- 29 Barisano G, Law M, Custer RM, Toga AW, Sepehrband F. Perivascular Space Imaging at Ultrahigh Field MR Imaging. *Magn Reson Imaging Clin N Am*. 2021;29(1):67-75.
- 30 Bouvy WH, Biessels GJ, Kuijff HJ, Kappelle LJ, Luijten PR, Zwanenburg JJ. Visualization of perivascular spaces and perforating arteries with 7 T magnetic resonance imaging. *Invest Radiol*. 2014;49(5):307-313.
- 31 Zong X, Lian C, Jimenez J, Yamashita K, Shen D, Lin W. Morphology of perivascular spaces and enclosed blood vessels in young to middle-aged healthy adults at 7T: Dependences on age, brain region, and breathing gas. *Neuroimage*. 2020;218:116978.
- 32 Bouvy WH, Zwanenburg JJM, Reinink R, Wisse LEM, Luijten PR, Kappelle LJ, et al.; Utrecht Vascular Cognitive Impairment (VCI) Study group. Perivascular spaces on 7 Tesla brain MRI are related to markers of small vessel disease but not to age or cardiovascular risk factors. *J Cereb Blood Flow Metab*. 2016;36(10):1708-1717.
- 33 Hou Y, Park SH, Wang Q, Zhang J, Zong X, Lin W, et al. Enhancement of Perivascular Spaces in 7 T MR Image using Haar Transform of Non-local Cubes and Block-matching Filtering. *Sci Rep*. 2017;7(1):8569.
- 34 Jung E, Chikontwe P, Zong X, Lin W, Shen D, Park SH. Enhancement of Perivascular Spaces Using Densely Connected Deep Convolutional Neural Network. *IEEE Access*. 2019;7:18382-18391.
- 35 van Veluw SJ, Zwanenburg JJ, Engelen-Lee J, Spliet WG, Hendrikse J, Luijten PR, et al. In vivo detection of cerebral cortical microinfarcts with high-resolution 7T MRI. *J Cereb Blood Flow Metab*. 2013;33(3):322-329.
- 36 van Veluw SJ, Zwanenburg JJ, Rozemuller AJ, Luijten PR, Spliet WG, Biessels GJ. The spectrum of MR detectable cortical microinfarcts: a classification study with 7-tesla postmortem MRI and histopathology. *J Cereb Blood Flow Metab*. 2015;35(4):676-683.
- 37 van Veluw SJ, Charidimou A, van der Kouwe AJ, Lauer A, Reijmer YD, Costantino I, et al. Microbleed and microinfarct detection in amyloid angiopathy: a high-resolution MRI-histopathology study. *Brain*. 2016;139(Pt 12):3151-3162.
- 38 van Veluw SJ, Hilal S, Kuijff HJ, Ikram MK, Xin X, Yeow TB, et al. Cortical microinfarcts on 3T MRI: Clinical correlates in memory-clinic patients. *Alzheimers Dement*. 2015;11(12):1500-1509.
- 39 van Veluw SJ, Shih AY, Smith EE, Chen C, Schneider JA, Wardlaw JM, et al. Detection, risk factors, and functional consequences of cerebral microinfarcts. *Lancet Neurol*. 2017;16(9):730-740.
- 40 van Rooden S, Goos JD, van Opstal AM, Versluis MJ, Webb AG, Blauw GJ, et al. Increased number of microinfarcts in Alzheimer disease at 7-T MR imaging. *Radiology*. 2014;270(1):205-211.
- 41 van Veluw SJ, Heringa SM, Kuijff HJ, Koek HL, Luijten PR, Biessels GJ; Utrecht Vascular Cognitive Impairment study group. Cerebral cortical microinfarcts at 7Tesla MRI in patients with early Alzheimer's disease. *J Alzheimers Dis*. 2014;39(1):163-167.

Contact

Assistant Professor Zihao Zhang
State Key Laboratory of Brain and
Cognitive Science
Institute of Biophysics
Chinese Academy of Sciences
15 Datun Road
Beijing 100101
China
zhzhzhang@ibp.ac.cn



Milestones and Applications of High-Resolution 7T MRSI

Gilbert Hangel, Ph.D.^{1,2,3}; Fabian Niess, Ph.D.¹; Eva Niess, Ph.D.¹; Georg Widhalm, M.D.²; Karl Rössler, M.D.^{2,3}; Wolfgang Bogner, Ph.D.^{1,3}; Siegfried Trattnig, M.D.^{1,3}

¹High Field MR Centre, Department of Biomedical Imaging and Image-guided Therapy, Medical University of Vienna, Austria

²Department of Neurosurgery, Medical University of Vienna, Austria

³Christian Doppler Laboratory for MR Imaging Biomarkers, Vienna, Austria

Abstract

In 2019, we introduced a 7T MRSI method that combines free induction decay acquisition with concentric circle readout and short TE/TR that allows fast 3D coverage of the human brain, e.g., neurochemical imaging with 3.4 mm nominal isotropic resolution in 15 minutes.

This article introduces our method¹ and demonstrates the first results of promising applications in pathologies: brain tumors, multiple sclerosis, and epilepsy. We end with an outlook about its application in quantitative exchange label turnover MRSI of deuterium.

Introduction

Combining the spatial resolution of conventional MRI with the ability of magnetic resonance spectroscopy (MRS) to acquire the signal of a range of molecules other than water results in magnetic resonance spectroscopic imaging (MRSI), which can simultaneously measure multiple neurochemical maps in the human brain. MRSI methodology has been available for four decades [1]. However, the lower concentration and thus lower SNR of these neurochemicals, the acquisition schemes necessary to suppress lipid signals from subcutaneous tissue, and the need to acquire longer readouts for processable spectra all limit its clinical application to 1.5T and 3T systems.

With 7T systems, increased SNR and spectral separation of resonances are beneficial, but limitations due to

SAR, B_0 and B_1 -inhomogeneities make acquisition even more challenging [2]. At the High Field MR Centre at the Medical University of Vienna, we have been working since 2010 to overcome the challenges for 7T MRSI. The first step was to avoid what were then the standard localization schemes at lower fields – PRESS and STEAM – and instead go for the direct acquisition of a free induction decay (FID, Fig. 1A) [3, 4]. This allows for TRs down to the range of 200 ms, and significantly reduces SAR and chemical shift displacement errors. Using these short TRs and parallel imaging, we were able to simultaneously increase resolution and decrease scan times for phase-encoded MRSI. For instance, a single-slice scan with a 64×64 matrix and 3.4 mm nominal isotropic resolution took five

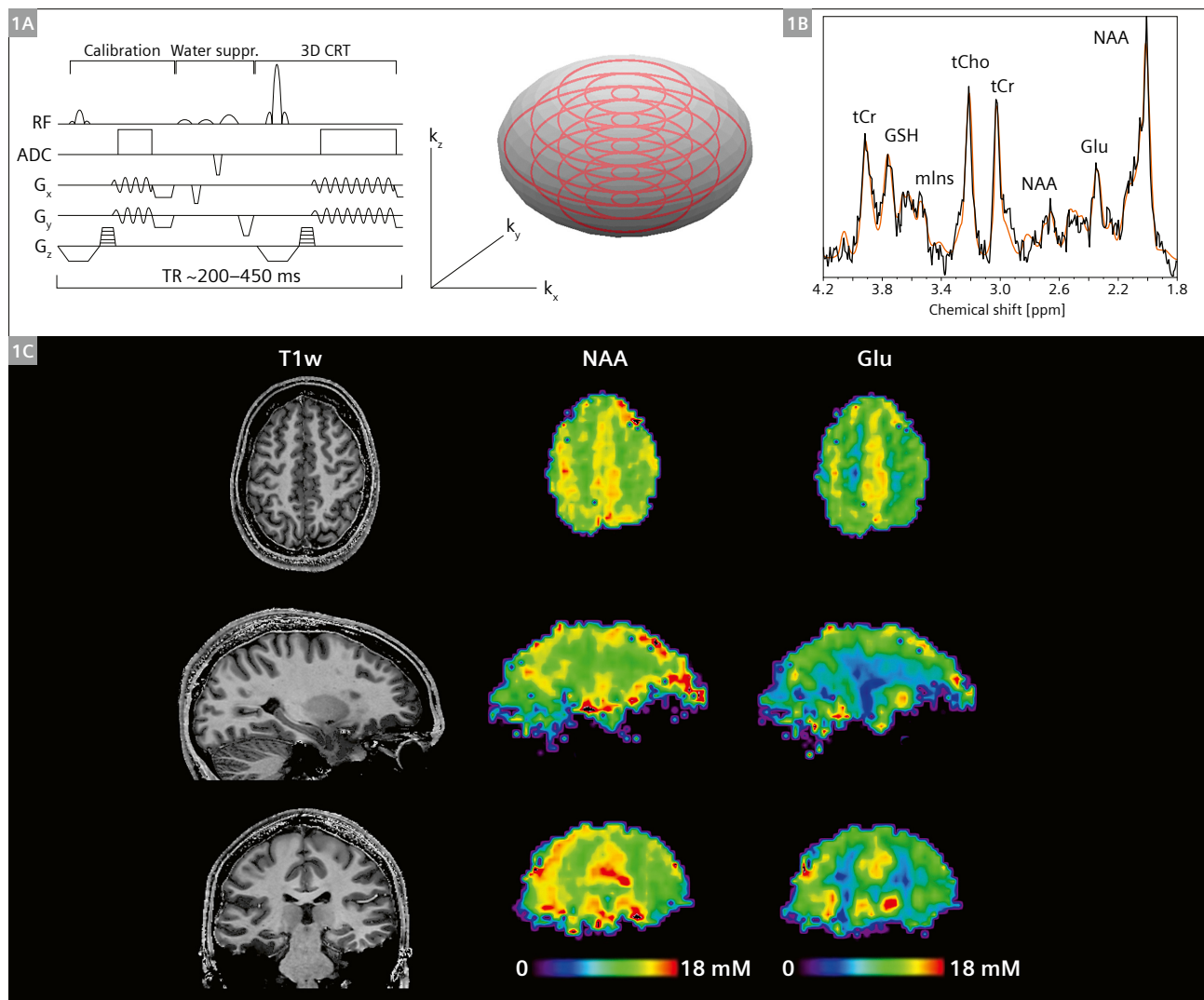
¹Siemens Healthineers Disclaimer: This article describes possible future ideas and concepts. It is not intended to describe specific performance and/or safety characteristics of currently planned or future products. Future realization and availability cannot be guaranteed.

minutes [5, 6]. The improved point-spread function at high resolution, together with lipid signal removal in post-processing reduced the susceptibility to lipid contamination [7], while the fitting of the resulting spectra was conducted using LCModel [8] with basis sets tailored to 7T FID acquisition (Fig. 1B).

The next major advance was the use of spatial-spectral encoding instead of phase encoding in the form of concentric circle trajectories (CRT). Here, during one TR, a circle is repeatedly sampled in k -space using sinusoidal gradient waveforms (Fig. 1A), yielding spectral evolution information of multiple k -space points during one excitation [9]. This process is repeated with different radii until the k -space is filled sufficiently in two or three spatial dimensions and one time dimension. Compared

to common spatial-spectral acquisition strategies at 3T, such as echo-planar or spiral trajectories, CRTs are better suited to the required spectral bandwidths at 7T [2]. Altogether, we were able to accelerate high-resolution MRSI acquisition by a factor of 80 compared to unaccelerated phase-encoded MRSI [9].

The range of reliably quantifiable neurochemicals ultimately depends on SNR and spectral quality, but for our most common application setting of a 15-minute scan of the human cerebrum with 3.4 mm nominal resolution, N-acetylaspartate (NAA), total choline (tCho), total creatine (tCr), glutamate (Glu) and myo-inositol (mIns) can be well quantified in healthy subjects [10]. Using a second water-unsuppressed scan as an internal reference, we are able to also calculate concentration estimates



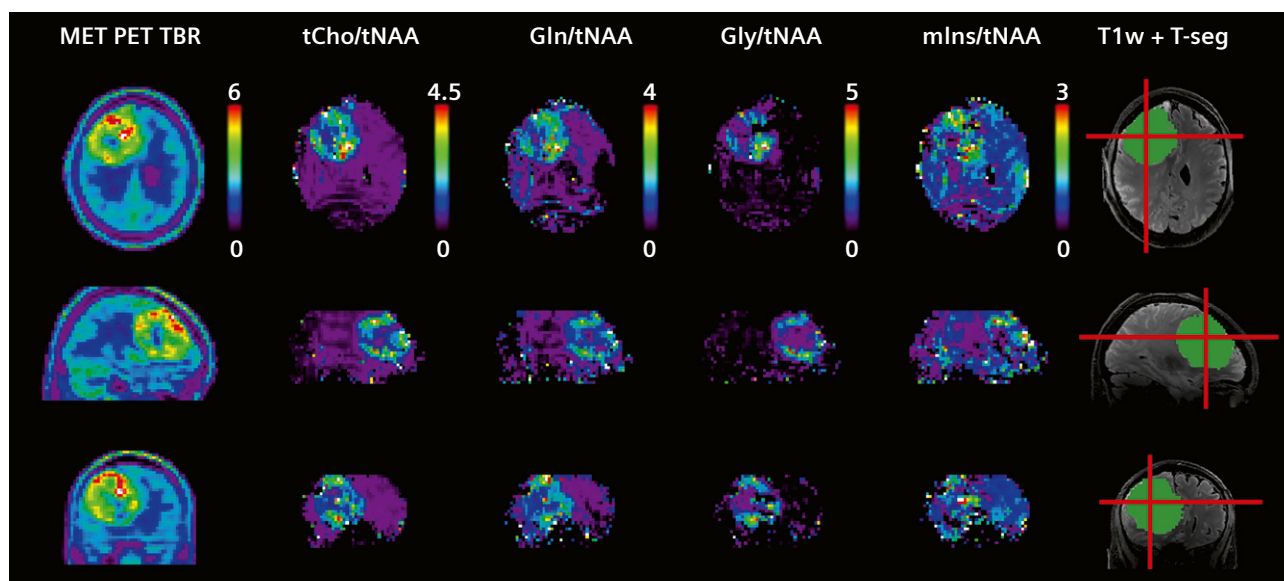
1 (1A) Sequence scheme for 7T CRT-MRSI and k -space trajectories [9]. (1B) Example spectrum showing resonances for tCr, tCho, NAA, mIns, Glu, and glutathione (GSH). (1C) Concentration estimate maps for NAA and Glu show the mappable extent of the brain using our method in a healthy volunteer [10]. 1A and 1B courtesy of Lukas Hingerl.

(Fig. 3C) instead of institutional units, which requires assumptions on metabolite T_1 s and water concentrations within a voxel [10]. Beyond healthy subjects, we have begun to study and validate our method in different pathologies that affect the neurochemical composition of brain tissues.

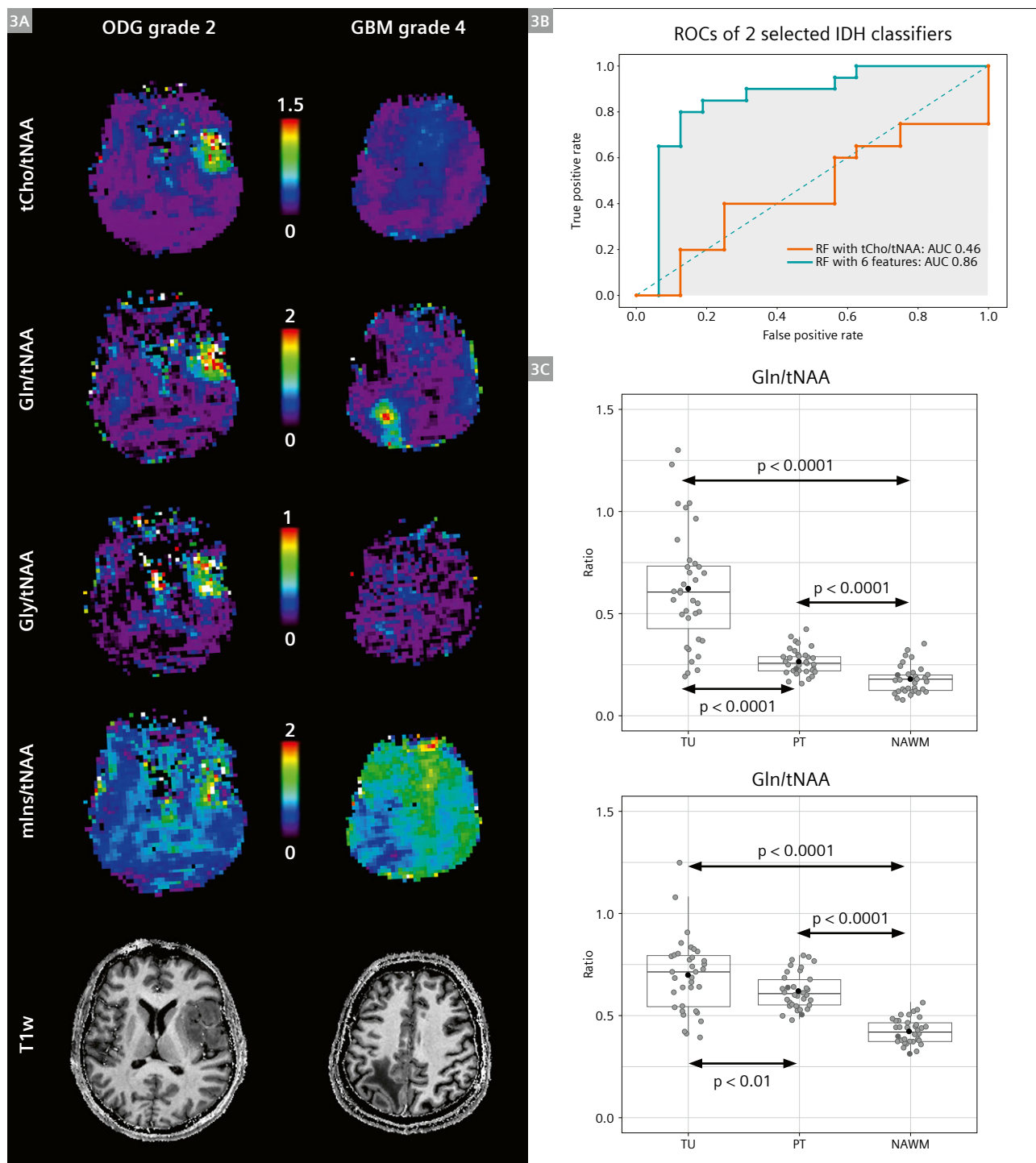
Brain tumors

The umbrella term 'brain tumor' encompasses entities with different cellular origins, such as gliomas, meningiomas, lymphomas, and metastases. Due to these different origins, their molecular and metabolic characteristics vastly differ. One example for this are isocitrate dehydrogenase (IDH) mutations that are now, according to the 2021 WHO Classification of Tumors of the Central Nervous System [11], the main discriminator between oligodendroglioma and astrocytoma with IDH mutation on the one hand, and glioblastoma without IDH mutation (IDH wild type) on the other. In glioma cells, IDH mutations cause the production of 2-hydroxyglutarate (2HG), which is not found in other cells and is detectable by specialized MRS methods. Other compounds of interest in tumor metabolism, edema, and proliferation include glutamine (Gln) [12] and glycine (Gly) [13]. Compared to lower field systems, 7T MRSI is better suited to separate Gln from Glu, and Gly from mins.

While clinical applications of MRSI for brain tumors are currently usually limited to the evaluation of tCho/tNAA in a few voxels that can be placed within the neoplastic volume [14], our MRSI method can use its spatial and spectral resolution to image heterogeneity between tumor microenvironments. This could be used to differentiate between tumor types and compartments (Figs. 2, 3A) and to cover tumor volumes better than MRS, which requires selection boxes. While a thorough analysis of its potential will require larger cohorts, our first studies of gliomas demonstrated promising findings. Imaging Gln and Gly, both amino acids, shows a greater correspondence to amino acid PET than tCho, even if not the same amino acids (Gln/Gly vs. MET/FET) are detected [15]. While our high-resolution FID approach cannot detect 2HG, which would require tailored acquisition techniques [16], and therefore IDH mutation directly, leveraging the number of metabolites and tumor voxels we can acquire, has allowed us to demonstrate that a machine learning-driven classifier using a full metabolic panel can identify IDH mutation better than just tCho/tNAA (Fig. 3B, [17]). We have further explored Glu, which is known to have a role in glioma infiltration and tumor-associated epilepsy [18, 19], and found significantly elevated peritumoral Glu/tNAA compared to a white matter control ROI (Fig. 3C, [38]).



2 In this patient with an astrocytoma (IDH-mutant, grade 4) MRSI-based images of tCho/tNAA, Gln/tNAA, and Gly/tNAA correspond well to MET-PET. All show a spatial heterogeneity within the tumor volume. Adapted from [15] under CC license.



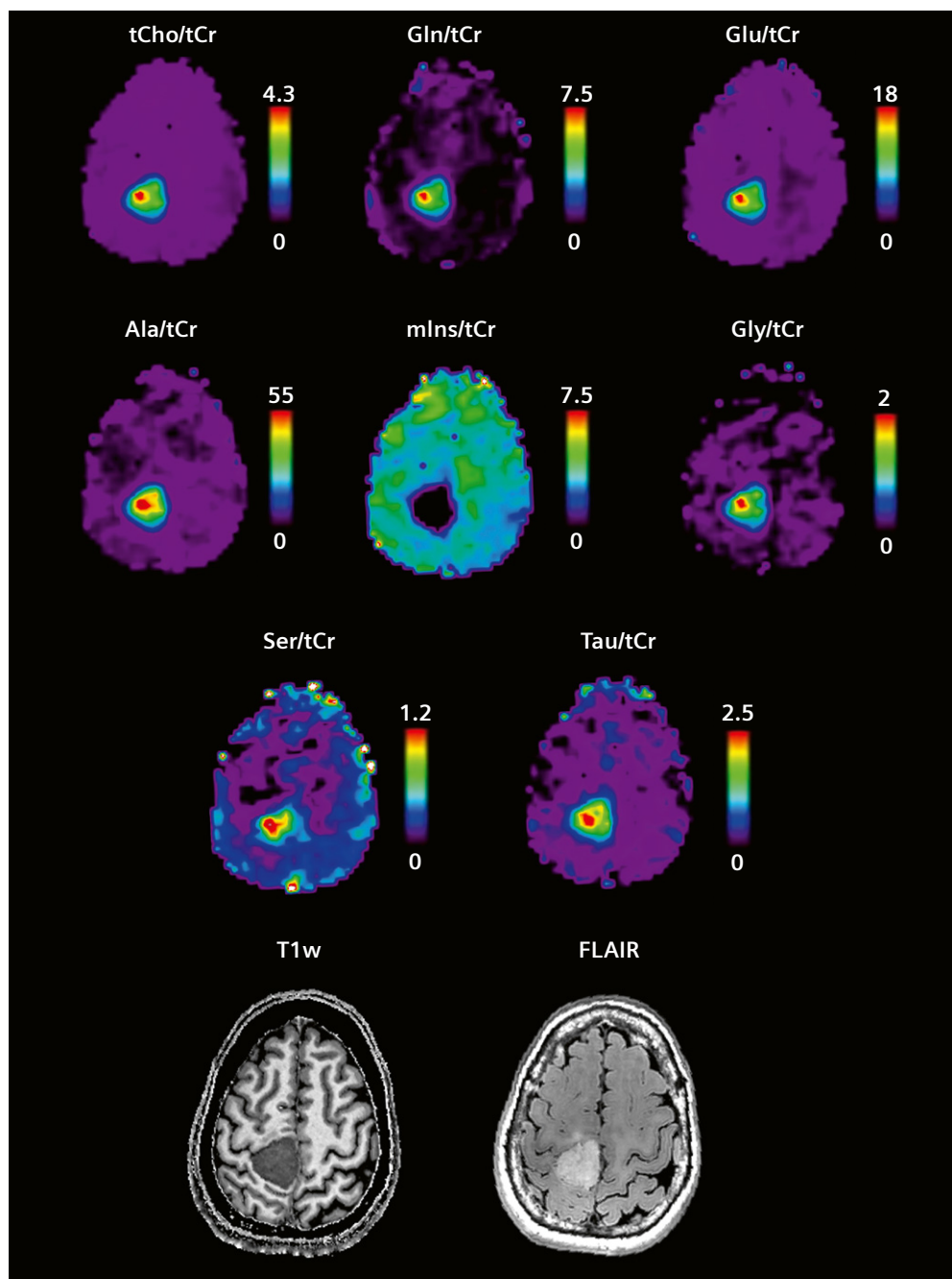
3 (3A) 7T MRSI shows clear metabolic differences between an oligodendroglioma (IDH-mutant, and 1p/19q-codeleted (ODG) grade 2) and the edema/suspected infiltration zone of a glioblastoma (IDH wild type (GBM) grade 4). (3B) ROC curve of a classifier that uses a metabolic panel per voxel to identify IDH mutation on a patient level [17]. (3C) Gln/tNAA and Glu/tNAA ratios (patient-wise ROI medians) show significant differences between tumor volume (TU), a peritumoral region (PT), and normal-appearing white matter (NAWM) [38]. 3B courtesy of Sukrit Shamra and Cornelius Cadrien.

Beyond glioma, our first results of meningioma scans (Fig. 4) show different metabolic profiles, especially alanine (Ala), which fit well with the literature [20] and demonstrate that our method can acquire spectra close to the skull.

In summary, our current data shows promise for clinical use ranging from noninvasive classification of tumors to better presurgical delineation and treatment monitoring.

Multiple sclerosis

Multiple sclerosis was extensively studied in the past using standard MRS methods [21]. The most common findings include decreased NAA, which reflects neuroaxonal damage or dysfunction, and elevated levels of mIns, which are linked to ongoing gliosis and neuroinflammation. With an in-plane resolution of up to $2 \times 2 \text{ mm}^2$ we are now able to detect and visualize these changes in unprecedented detail



4 Metabolic ratio maps derived from 7T MRSI in a patient with an atypical falx meningioma classified as WHO grade 1–2. The increases in alanine (Ala), serine (Ser), and taurine (Tau) fit well with ex vivo NMR data [20].

[22–24] (Fig. 5). This improved resolution has shown larger areas of neurochemical changes and thus a more widespread pathology compared to lesions seen on conventional MRI, or even neurochemical changes not visible on conventional MRI.

In a clinical pilot study, we demonstrated that some neurochemical changes, particularly those associated with neuroinflammation, occur early in the course of the disease, correlate with the EDSS disability score, and may thus be a predictive marker of disease progression [24]. However, the value of MRSI in diagnosis, disease monitoring, and evaluation of treatment efficacy in multiple sclerosis needs to be confirmed in further longitudinal clinical studies.

Epilepsy

For a long time, the application of MRS to epilepsy has been hampered by limited resolution and coverage, which makes VOI placement in MR-negative or unclearly localized epilepsy challenging. At 7T, the acquisition of good-quality spectra is more difficult with B_0 -inhomogeneity in the temporal lobe due to susceptibility artifacts close to the skull base. However, early 7T MRSI studies in epilepsy have shown the same trends of decreased tNAA/tCr and increased tCho/tNAA [25] as seen in lower field MRS studies, and have demonstrated low-resolution mapping of Glu and gamma-aminobutyric acid (GABA) [26].

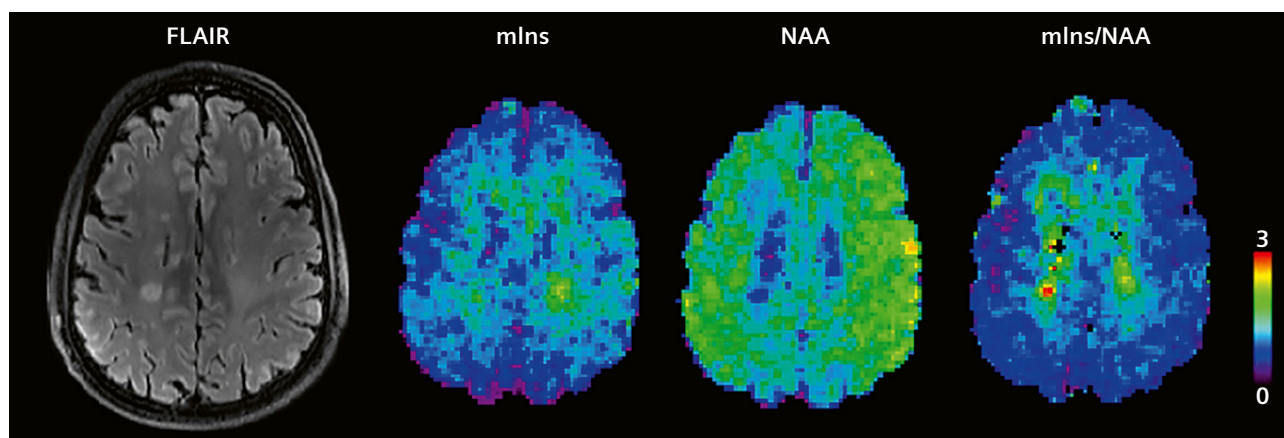
We are currently investigating high-resolution MRSI in epilepsy, and the first promising results were presented at ISMRM 2021 [27]. As seen in Figure 6, MRSI of a patient with a later surgically verified focal cortical dysplasia (FCD) type 2b reveals increased tCho/tNAA, Gln/tNAA, and mIns/tNAA as well as a decrease of Glu/tCr within the lesion and the subsequent extent of surgical resection. In cases without morphologically visible lesions, identifying

metabolic changes that are clearly distinct from artifacts is more challenging. This is further complicated by an incomplete neurochemical understanding of epileptogenicity, such as literature pointing to increased glutamate as an excitatory neurotransmitter [28], while our preliminary data finds increases as well as decreases of glutamate over our cohort. The reasons behind this could be a lack of differentiation between Glu and Gln in most studies, and temporal changes in neurochemicals with epileptogenic activity that are difficult to image with single time point scans. Yet with further improvements in study design and methodology, correlating neurotransmitters with epileptogenicity and localizing MR-negative epileptogenic foci seem to be promising topics for 7T applications in research and clinical settings.

Deuterium-based MRSI

Besides proton MRSI, other nuclei can also be imaged with phosphorous as the most common example. However, in recent years, the possibility of using deuterium, which can replace protons in a variety of molecules, has emerged [29].

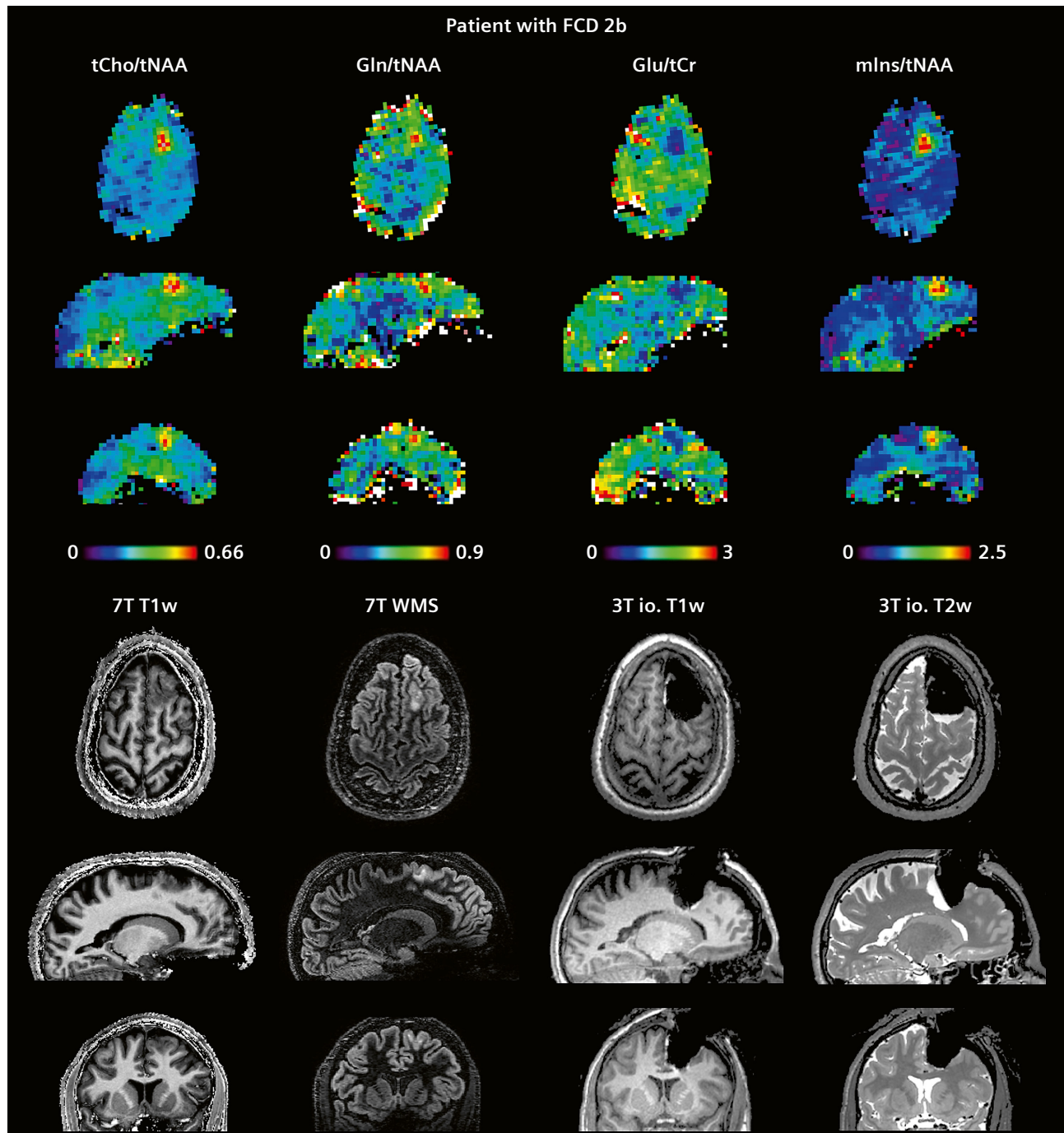
Deuterium metabolic imaging (DMI) [29–31] and quantitative exchange label turnover (QELT) [32–36] are the two emerging MR techniques that use orally or intravenously administered deuterium-labelled glucose as a harmless and non-radioactive tracer, to both, image the glucose uptake, and give quantitative insight in to the synthesis of downstream metabolic products, such as Glu, Gln and lactate. This allows for separating healthy oxidative from pathologic anaerobic metabolic pathways, for example in brain tumors. Our research group has set a strong focus on direct (DMI) and indirect (QELT) deuterium detection using ^2H -MRSI and ^1H -MRSI, respectively.



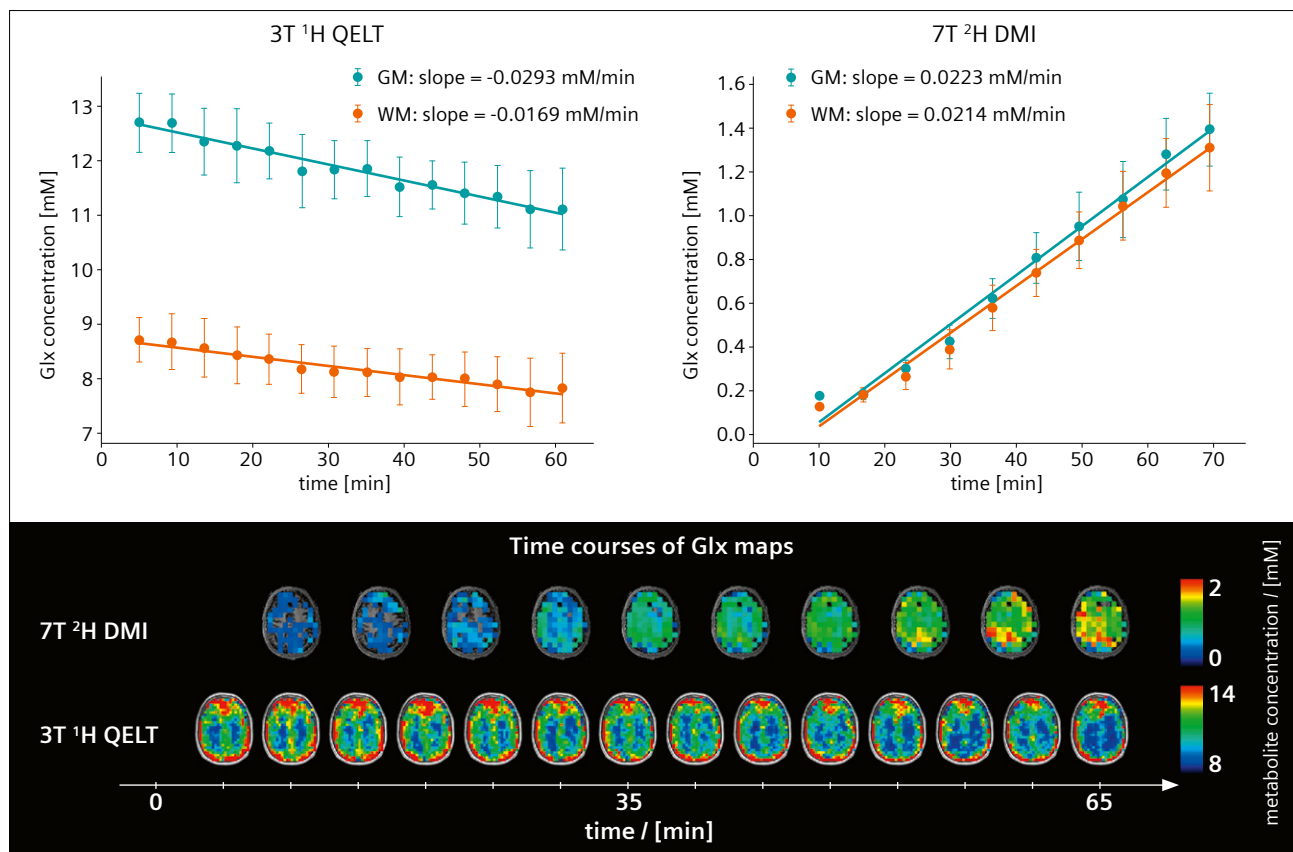
5 Metabolic images derived from 7T MRSI of mIns and NAA in a multiple sclerosis case. Using high-resolution MR spectroscopic imaging at 7T, we can now visualize pathologic changes across different tissues, including relatively small lesions of demyelination and white matter, which appear intact on MRI. The mIns and NAA maps are scaled in arbitrary units.

A successful in vivo application of 7T and 3T QELT has recently been published in *Nature Biomedical Engineering* [32] and *Investigative Radiology* [33]. It presents three-dimensional time-resolved mapping of downstream Glu and Gln synthesis with high resolution in the human brain. At ISMRM 2023 [37], our group will present the repro-

ducibility of the mentioned approaches by comparing indirect deuterium detection in ^1H QELT at clinical 3T [33] with direct detection in ^2H DMI at 7T using quantification of concentration estimates in the same cohort of subjects (Fig. 7).



6 Metabolic ratio maps of an epilepsy patient with an FCD 2b compared to 7T MRI and intraoperative, post resection 3T MRI. tCho/tNAA, Gln/tNAA, and mIns/tNAA are increased within the visible lesion, while Glu/tCr is decreased in and around the lesion. These MRSI-visible neurochemical alterations are all within the later resection zone, with the patient having a class 1 outcome according to ILAE (i.e., completely seizure free).



7 A comparison of 3T QELT with 7T DMI shows how comparable the changes are in deuterated/ non-deuterated Glx over the course of an hour. Compared to DMI, no special hardware is required and application on any clinical MRI system is possible. More details will be presented at ISMRM 2023 [37].

Conclusion

Before our method can become widely available, we will need to develop standardized solutions for B_0 and B_1 -inhomogeneities, as well as the online reconstruction and quantification of MRSI data. Yet with the increased spatial and spectral resolution and coverage we can achieve, we can image metabolic changes in pathologies better than previously possible. We have demonstrated promising applications in brain tumors, multiple sclerosis, and epilepsy, as well as the feasibility of deuterium imaging applications.

In order to precisely define possible clinical benefits, it will also be necessary to move forward to multi-center studies. If you are interested in a C2P agreement for research, do not hesitate to contact us. Keep in mind that this sequence currently requires the implementation of a computing-intensive offline reconstruction pipeline. The compatibility of the reconstruction pipeline might depend on the software level of the system.

References

- Pykett IL, Rosen BR. Nuclear magnetic resonance: in vivo proton chemical shift imaging. Work in progress. Radiology. 1983;149(1):197-201.
- Hangel G, Niess E, Lazen P, Bednarik P, Bogner W, Strasser B. Emerging methods and applications of ultra-high field MR spectroscopic imaging in the human brain. Anal Biochem. 2022;638:114479.
- Henning A, Fuchs A, Murdoch JB, Boesiger P. Slice-selective FID acquisition, localized by outer volume suppression (FIDLOVS) for (1)H-MRSI of the human brain at 7 T with minimal signal loss. NMR Biomed. 2009;22(7):683-696.
- Bogner W, Gruber S, Trattnig S, Chmelik M. High-resolution mapping of human brain metabolites by free induction decay (1)H MRSI at 7 T. NMR Biomed. 2012;25(6):873-882.
- Hangel G, Strasser B, Považan M, Heckova E, Hingerl L, Boubela R, et al. Ultra-high resolution brain metabolite mapping at 7 T by short-TR Hadamard-encoded FID-MRSI. Neuroimage. 2018;168:199-210.
- Strasser B, Považan M, Hangel G, Hingerl L, Chmelik M, Gruber S, et al. (2 + 1)D-CAIPIRINHA accelerated MR spectroscopic imaging of the brain at 7T. Magn Reson Med. 2017;78(2):429-440.
- Bilgic B, Chatnuntawech I, Fan AP, Setsompop K, Cauley SF, Wald LL, et al. Fast image reconstruction with L2-regularization. J Magn Reson Imaging. 2014;40(1):181-191.

- 8 Provencher SW. Automatic quantitation of localized in vivo ¹H spectra with LCMoDel. *NMR Biomed.* 2001;14(4):260-264.
- 9 Hingerl L, Strasser B, Moser P, Hangel G, Motyka S, Heckova E, et al. Clinical High-Resolution 3D-MR Spectroscopic Imaging of the Human Brain at 7 T. *Invest Radiol.* 2020;55(4):239-248.
- 10 Hangel G, Spurny-Dworak B, Lazen P, Cadrien C, Sharma S, Hingerl L, et al. Inter-subject stability and regional concentration estimates of 3D-FID-MRSI in the human brain at 7 T. *NMR Biomed.* 2021;34(12):e4596.
- 11 Louis DN, Perry A, Wesseling P, Brat DJ, Cree IA, Figarella-Branger D, et al. The 2021 WHO Classification of Tumors of the Central Nervous System: a summary. *Neuro Oncol.* 2021;23(8):1231-1251.
- 12 Obara-Michlewska M, Szeliga M. Targeting Glutamine Addiction in Gliomas. *Cancers (Basel).* 2020;12(2):310.
- 13 Kim D, Fiske BP, Birsoy K, Freinkman E, Kami K, Possemato RL, et al. SHMT2 drives glioma cell survival in ischaemia but imposes a dependence on glycine clearance. *Nature.* 2015;520(7547):363-367.
- 14 Mert A, Kiesel B, Wöhrer A, Martínez-Moreno M, Minchev G, Furtner J, et al. Introduction of a standardized multimodality image protocol for navigation-guided surgery of suspected low-grade gliomas. *Neurosurg Focus.* 2015;38(1):E4.
- 15 Hangel G, Lazen P, Sharma S, Hristoska B, Cadrien C, Furtner J, et al. 7T HR FID-MRSI Compared to Amino Acid PET: Glutamine and Glycine as Promising Biomarkers in Brain Tumors. *Cancers (Basel).* 2022;14(9):2163.
- 16 Weng G, Radojewski P, Sherif S, Kiefer C, Schuch P, Wiest R, et al. SLOW: A novel spectral editing method for whole-brain MRSI at ultra high magnetic field. *Magn Reson Med.* 2022;88(1):53-70.
- 17 Sharma S. Glioma Classifications with 7T MR Spectroscopic Imaging. Presented at: ISMRM & ISMRT Annual Meeting & Exhibition, 2023, abstract #4730, June 8, 2:45 p.m., ML/AI for Data Synthesis Session; Toronto, Canada.
- 18 Venkataramani V, Tanev DI, Strahle C, Studier-Fischer A, Fankhauser L, Kessler T, et al. Glutamatergic synaptic input to glioma cells drives brain tumour progression. *Nature.* 2019;573(7775):532-538.
- 19 Lange F, Hörnschemeyer J, Kirschstein T. Glutamatergic Mechanisms in Glioblastoma and Tumor-Associated Epilepsy. *Cells.* 2021;10(5):1226.
- 20 Ijare OB, Hambarde S, Brasil da Costa FH, Lopez S, Sharpe MA, Helekar SA, et al. Glutamine anaplerosis is required for amino acid biosynthesis in human meningiomas. *Neuro Oncol.* 2022;24(4):556-568.
- 21 Swanberg KM, Landheer K, Pitt D, Juchem C. Quantifying the Metabolic Signature of Multiple Sclerosis by in vivo Proton Magnetic Resonance Spectroscopy: Current Challenges and Future Outlook in the Translation From Proton Signal to Diagnostic Biomarker. *Front Neurol.* 2019;10:1173.
- 22 Heckova E, Strasser B, Hangel GJ, Považan M, Dal-Bianco A, Rommer PS, et al. 7 T Magnetic Resonance Spectroscopic Imaging in Multiple Sclerosis: How Does Spatial Resolution Affect the Detectability of Metabolic Changes in Brain Lesions? *Invest Radiol.* 2019;54(4):247-254.
- 23 Lipka A, Niess E, Dal-Bianco A, Hangel GJ, Rommer PS, Strasser B, et al. Lesion-Specific Metabolic Alterations in Relapsing-Remitting Multiple Sclerosis Via 7 T Magnetic Resonance Spectroscopic Imaging. *Invest Radiol.* 2023;58(2):156-165.
- 24 Heckova E, Dal-Bianco A, Strasser B, Hangel GJ, Lipka A, Motyka S, et al. Extensive Brain Pathologic Alterations Detected with 7.0-T MR Spectroscopic Imaging Associated with Disability in Multiple Sclerosis. *Radiology.* 2022;303(1):141-150.
- 25 Pan JW, Duckrow RB, Gerrard J, Ong C, Hirsch LJ, Resor SR Jr, et al. 7T MR spectroscopic imaging in the localization of surgical epilepsy. *Epilepsia.* 2013;54(9):1668-1678.
- 26 van Veenendaal TM, Backes WH, Tse DHY, Scheenen TWJ, Klomp DW, Hofman PAM, et al. High field imaging of large-scale neurotransmitter networks: Proof of concept and initial application to epilepsy. *Neuroimage Clin.* 2018;19:47-55.
- 27 Hangel G, Lazen P, Tomschik M, Wais J, Hečková E, Hingerl L, et al. CRT-FID-MRSI at 7T for the high-resolution metabolic imaging of epilepsy: Preliminary results. Presented at the ISMRM, Virtual Meeting, 2021, vol. 0723.
- 28 Sarlo GL, Holton KF. Brain concentrations of glutamate and GABA in human epilepsy: A review. *Seizure.* 2021;91:213-227.
- 29 De Feyter HM, Behar KL, Corbin ZA, Fulbright RK, Brown PB, McIntyre S, et al. Deuterium metabolic imaging (DMI) for MRI-based 3D mapping of metabolism in vivo. *Sci Adv.* 2018;4(8):eaat7314.
- 30 Kaggie JD, Khan AS, Matys T, Schulte RF, Locke MJ, Grimmer A, et al. Deuterium metabolic imaging and hyperpolarized ¹³C-MRI of the normal human brain at clinical field strength reveals differential cerebral metabolism. *Neuroimage.* 2022;257:119284.
- 31 Serés Roig E, De Feyter HM, Nixon TW, Ruhm L, Nikulin AV, Scheffler K, et al. Deuterium metabolic imaging of the human brain in vivo at 7 T. *Magn Reson Med.* 2023;89(1):29-39.
- 32 Bednarik P, Goranovic D, Svatkova A, Niess F, Hingerl L, Strasser B, et al. Deuterium labeling enables non-invasive 3D proton MR imaging of glucose and neurotransmitter metabolism in the human brain. In review, preprint, Dec. 2021. doi: 10.21203/rs.3.rs-1027370/v1.
- 33 Niess F, Hingerl L, Strasser B, Bednarik P, Goranovic D, Niess E, et al. Noninvasive 3-Dimensional ¹H-Magnetic Resonance Spectroscopic Imaging of Human Brain Glucose and Neurotransmitter Metabolism Using Deuterium Labeling at 3T: Feasibility and Interscanner Reproducibility. *Invest Radiol.* 2023 Feb 3. Epub ahead of print. doi: 10.1097/RLI.0000000000000953.
- 34 Cember ATJ, Wilson NE, Rich LJ, Bagga P, Nanga RPR, Swago S, et al. Integrating ¹H MRS and deuterium labeled glucose for mapping the dynamics of neural metabolism in humans. *Neuroimage.* 2022;251:118977.
- 35 Rich LJ, Bagga P, Wilson NE, Schnall MD, Detre JA, Haris M, et al. ¹H magnetic resonance spectroscopy of 2H-to-¹H exchange quantifies the dynamics of cellular metabolism in vivo. *Nat Biomed Eng.* 2020;4(3):335-342.
- 36 Ruhm L, Avdievich N, Ziegs T, Nagel AM, De Feyter HM, de Graaf RA, et al. Deuterium metabolic imaging in the human brain at 9.4 Tesla with high spatial and temporal resolution. *Neuroimage.* 2021;244:118639.
- 37 Niess F. Reproducibility of non-invasive 3D imaging of glucose downstream metabolism using deuterium labeling: indirect ¹H QELT at 3T vs direct 2H DMI at 7T. Presented at: ISMRM & ISMRT Annual Meeting & Exhibition, 2023, abstract #8006, June 5, 8:15 a.m., X-Nuclei Session; Toronto, Canada.
- 38 Hangel G. An exploration of peritumoral glutamate and glutamine in diffuse gliomas using 7T MRSI. Presented at: ISMRM & ISMRT Annual Meeting & Exhibition, 2023, abstract #0349, June 5, 1:45 p.m., Brain Tumors: Acquisition Session; Toronto, Canada.

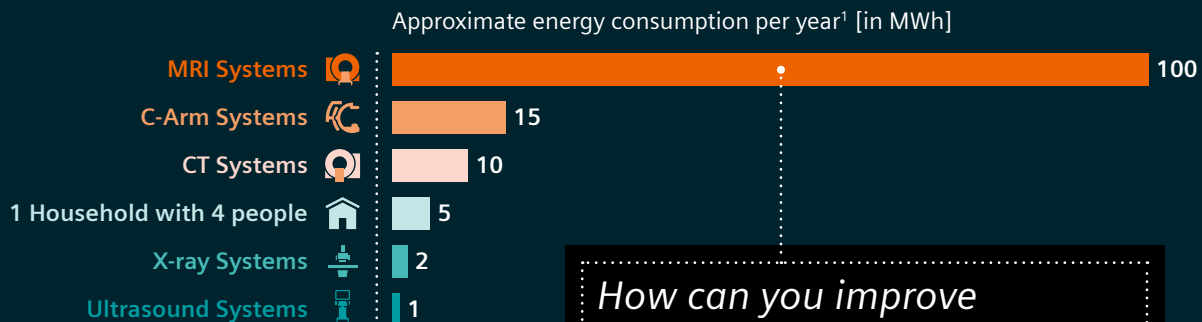


Contact

Gilbert Hangel, Ph.D.
University Assistant
Medical University of Vienna
Währinger Gürtel 18-20
1090 Vienna
Austria
Tel.: +43 14040064710
gilbert.hangel@meduniwien.ac.at

Environmental Sustainability in Magnetic Resonance

MRI is the major contributor in radiology to energy consumption



How can you improve your energy management and save electricity in MRI?



Did you know? We're also working on saving helium!

Zero Helium Boil-off Technology

It was first introduced in 2004 and prevents helium boil-off throughout your scanner's lifetime. It is available for all our MAGNETOM systems.



Up to 37% reduction in helium inventory

A significant reduction in helium inventory is possible with our latest scanner generation.

- Improved magnet & gradient architecture
- Strong reduction of conductive materials
- More efficient cooling

DryCool Technology

Our new class of MRI systems offers you the most compact whole-body MRI with virtually helium-free infrastructure and radically simplified infrastructure requirements:

- Only 0.7 liters liquid helium
- Sealed-for-life magnet design
- No quench pipe
- New benchmark in ramp-up times

Values are computed for a 1.5T MAGNETOM Sola system for illustration purposes.

¹ Data Siemens Healthineers own measurements and assumptions; Actual consumption can vary depending on use pattern, system type, and configuration.

² Assuming the system is turned on during the weekends and overnight.

³ Results are quantified assuming scanning operations as per COCIR standards.

• How to save energy with your MRI system:

Energy consumption for an MRI system in one year, if the scanner is always on²: **100 MWh**



Save ~ 20% energy by turning off your scanner when not in use³ **~ 80 MWh**

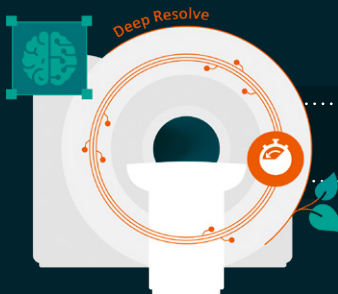


Did you know?

The start-up time for our scanners is only approx. 5.5 minutes and with our System Start-Up Timer you can enable automatic start-up of your scanner. So your system is ready when the workday starts!

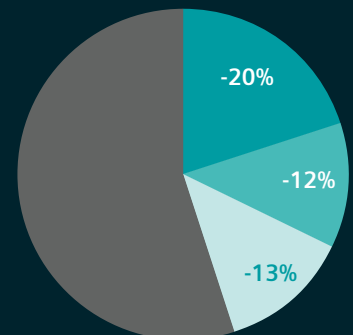


Save ~ 12% energy by using Eco Power mode³ **~ 70 MWh**



Save ~ 13% energy by using Deep Resolve **~ 60 MWh**

Make the most of our innovations and save **~ 40%** energy!



Optimizing EPI Image Quality Beyond Linear Phase Corrections with Dual-Polarity GRAPPA

André Fischer, Ph.D.¹; Wei Liu Ph.D.¹; Kun Zhou Ph.D.²

¹Siemens Healthineers, Erlangen, Germany

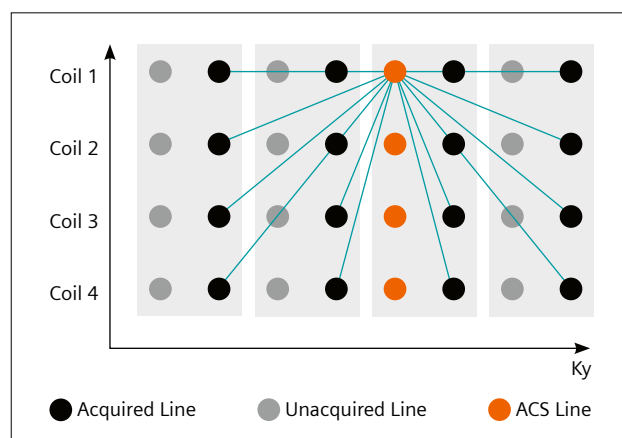
²Siemens Shenzhen Magnetic Resonance Ltd., Shenzhen, China

Echo planar imaging (EPI) [1, 2] is one of the fastest methods to acquire magnetic resonance imaging (MRI) data. Therefore, it has been the method of choice to collect imaging data as fast as possible when the desired signal is quickly decaying. Examples include T2*-weighted imaging, functional MRI (fMRI, [3–6]), and diffusion-weighted imaging (DWI, [7–9]) including diffusion tensor imaging (DTI, [10]). EPI is very sensitive to any magnetic field inhomogeneities. While B_0 inhomogeneities can be largely addressed by shimming, the human body introduces inhomogeneities that are difficult to compensate. Susceptibility-induced inhomogeneities exist at any interface between materials where the magnetic susceptibility quickly changes. Examples include air-tissue interfaces, such as the sinuses in the human skull, that result in significant geometric distortions in these areas. A third mechanism for inhomogeneities are eddy currents that result from the rapid switching of gradient coils. Any material of the MRI scanner and within the patient that has a non-vanishing magnetic susceptibility will introduce eddy currents. When designing an MRI system, great care is taken to minimize eddy currents and implement eddy current compensation mechanisms. However, switching the gradient with opposite amplitude typically results in different eddy currents. Since EPI imaging relies on reading adjacent k -space lines with reverse readout gradient amplitude. Eddy currents on positive readout polarity (RO+) will be slightly different from eddy currents when reading data with negative polarity (RO-). These differences manifest as Nyquist ghosting, which is caused by phase differences between RO+ and RO- readouts. Nyquist ghosting corrections (NGC) typically employ a linear model to compensate these phase differences. However, it is quite obvious that the combination of B_0 inhomogeneities, the presence of the human body, susceptibility changes, and eddy currents can lead to higher order phase differences that are very difficult to model and compensate.

With the introduction of the MAGNETOM Cima.X¹ the most powerful clinical Siemens Healthineers 3T system will be available. The Gemini gradient coil will enable a gradient performance comparable to MAGNETOM Connectom,

which was only designed as a research tool. With MAGNETOM Cima.X, we are planning to make Connectom-like power accessible by the clinical community, enabling to utilize the Human Connectom Project (HCP) protocols and expand even beyond. At the core of the HCP is tractography, which relies on highly diffusion-weighted data acquired in many different diffusion directions. As described above, EPI is at the core of diffusion imaging. Addressing phase errors on MAGNETOM Cima.X to enable the highest quality DWI, DTI, and fMRI was a cornerstone during development, and resulted in the introduction of a new phase correction that is embedded into image reconstruction: dual-polarity GRAPPA (DPG)¹ [12].

DPG is the culmination of several preceding methods that are beyond the scope of this manuscript. However, it is worth mentioning that methods such as ghost elimination via spatial and temporal encoding (GESTE) [13], fast-low angle excitation echo-planar technique (FLEET) [14, 15], and phase labeling for additional coordinate encoding (PLACE) [16] play an instrumental role in designing the latest correction methods. What matters is that DPG is a more powerful technique to address even higher order phase variations in EPI, thereby optimizing in particular high-end diffusion applications in which uncorrected phase variations can have a substantial effect.



1 GRAPPA kernel calibration

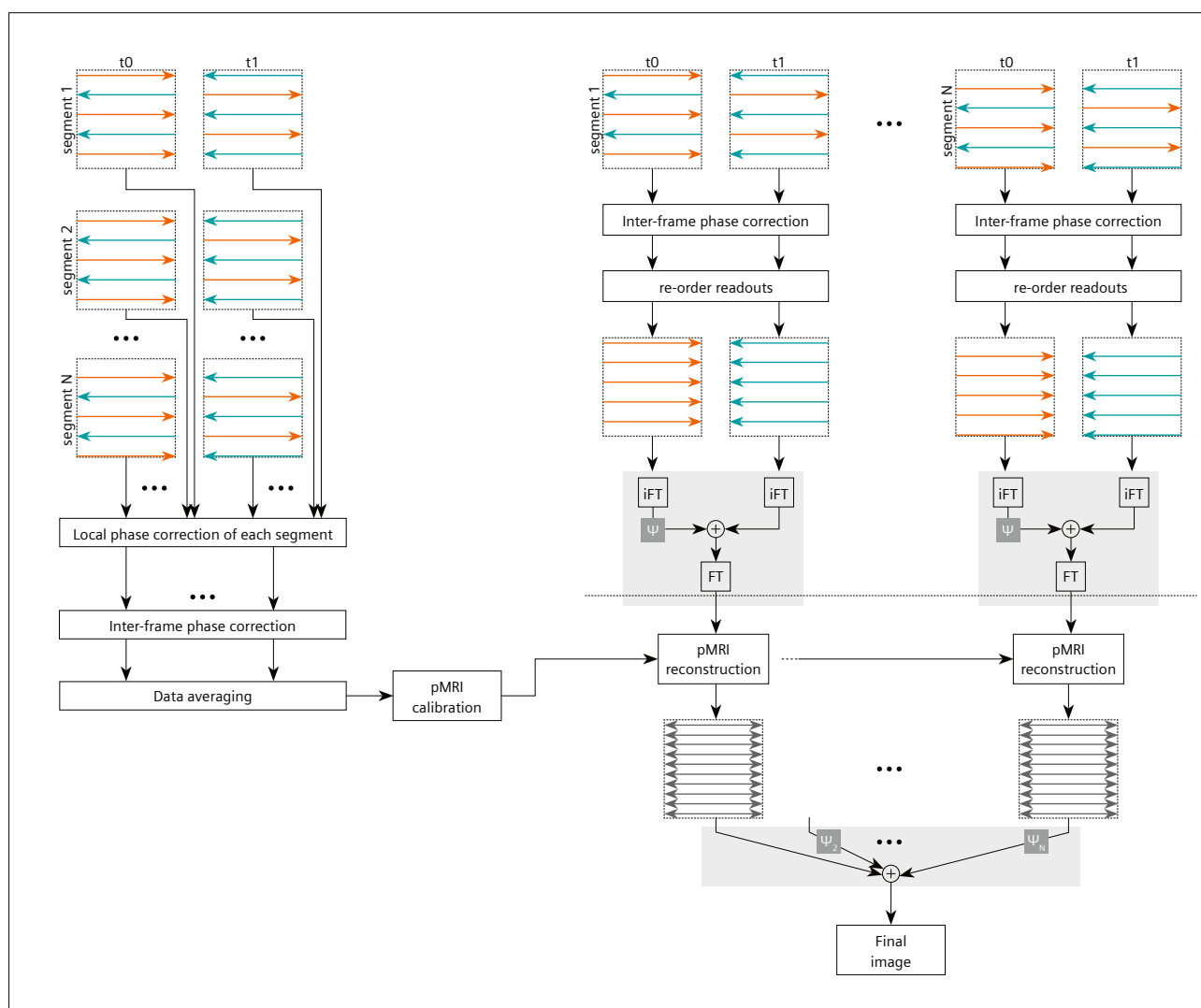
¹Work in progress. The product is still under development and not commercially available. Its future availability cannot be ensured.

As the name implies, DPG is based on GRAPPA [17], the standard parallel imaging reconstruction on MRI scanners from Siemens Healthineers. To understand why DPG is so advantageous, it helps to recapitulate GRAPPA.

When parallel imaging came up around the turn of the millennium, the first method published was SENSE [18], which operates in image space. It relies on explicit knowledge of the coil sensitivities of the receiver array. The final reconstruction is a matrix inversion in image space involving the undersampled images and the coil sensitivity profiles. However, determining these coil sensitivity profiles can be challenging, e.g., in areas with low proton density such as the lungs. Due to the nature of the Fourier transform, all methods that can be employed in image space

should also have a counterpart in k -space, and GRAPPA can be seen as the k -space domain counterpart to SENSE. While the underlying principle is the same as for SENSE, GRAPPA does not require explicitly derived coil sensitivity profiles. Instead, it calibrates a convolution kernel, the GRAPPA kernel, on auto-calibration signal (ACS) lines. These ACS lines are a Nyquist-sampled region in k -space center, solely used for GRAPPA kernel calibration. Subsequently, the kernel is used to synthesize the missing k -space data by convolution with the undersampled k -space data.

The ACS lines used for GRAPPA kernel calibration need to be free of artifacts to result in optimal image quality. This poses a real challenge in EPI due to the phase variations described earlier between k -space lines acquired with



2 Processing for multi-shot EPI calibration data to obtain ghost-free target data for DPG-GRAPPA kernel calibration. Starting on the left side, the FLEET data segments are corrected using LPC, followed by subsequent IFPC. After averaging of these corrected data with PLACE processing, temporary GRAPPA weights are determined for each segment. Moving to the right side, after LPC and IFPC, readouts are reordered such that RO+ and RO- segments emerge. After combination of RO+ and RO- data, the temporary GRAPPA weights determined earlier are applied to reconstruct the missing lines in each segment. Combining these images results in ghost-free target data for DPG calibration.

RO+ and RO- polarity. Consequently, several methods were developed to enable high-quality ACS data to be obtained for GRAPPA kernel calibration. Approaches such as PLACE or GESTE aim to segment and sort the collected data, such that all ACS k -space lines were acquired with either RO+ or RO-, but not a mixed readout polarity.

However, those methods alone can't fully compensate all effects. This is, where DPG comes in: As mentioned, a GRAPPA kernel needs to be calibrated. Calibration here refers to solving the following equation:

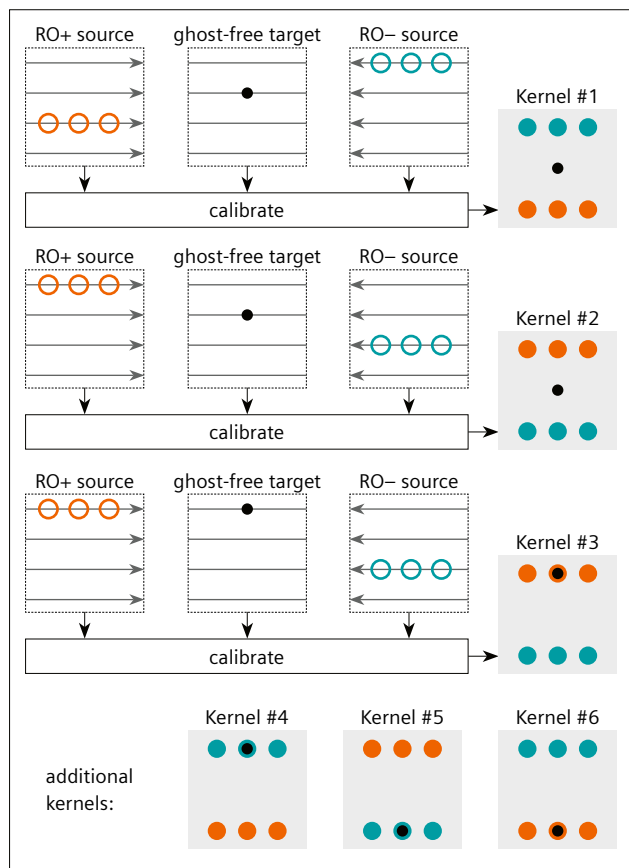
$$T = wS$$

In this linear equation system, S refers to source data points, T refers to the target data points that we want to reconstruct, and w is the weight set that we typically call the GRAPPA kernel. A pictorial description of this procedure can be found in Figure 1. Please note that all depicted source points from all coil elements of the receiver array are fitted to every single target point in every coil element. The coil readout dimension is omitted in Figure 1 for illustration purposes. In DPG, the source data during calibration consist of two different datasets: RO+ and RO-. These data-

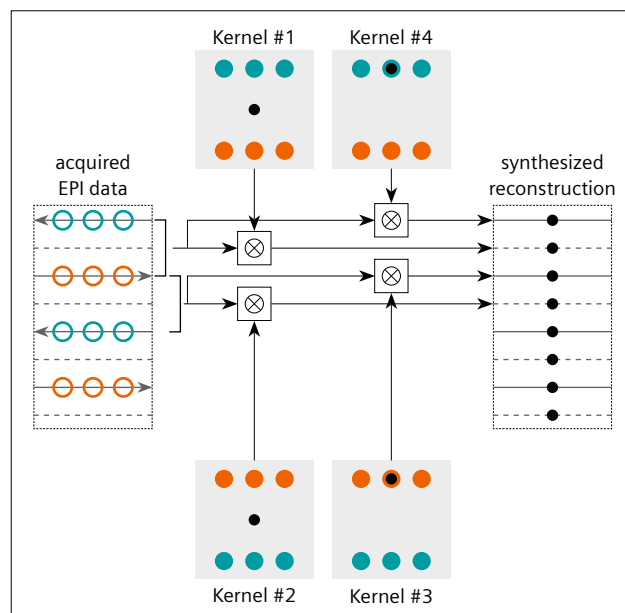
sets have not been ghosting-corrected so far. However, the calibration target data need to be artifact free, i.e., they need to be ghost-corrected and should not show physiological variations. Obtaining these target data requires a combination of FLEET, GESTE, a local phase correction (LPC) [19], and the aforementioned segmentation and sorting of the acquired ACS data. Details on this can be found in the appendix of the DPG paper [12] and in Figure 2. Please note one small difference compared to Figure 10 from [12]: After the LPC step on the left-hand side and before the readout reordering of the segments on the right-hand side, an additional inter-frame phase correction (IFPC) was applied [20]. This IFPC helped to remove linear phase shifts along the phase encoding direction, thereby removing another potential source of ghosting in the calibration data.

Finally, proper GRAPPA weights can be calibrated, the procedure is explained in Figure 3. Source points from RO+ and RO- are compiled and fitted to a target point of the ghost-free target data. As can be seen, many different GRAPPA kernels can be calibrated using such an approach. One substantial difference to standard GRAPPA is shown in kernels #3–#6: Here, a target point sits in the region of the source points. Why would you want to do this? Keep in mind that the RO+ and RO- source point datasets have not yet been ghost-corrected. Consequently, also k -space point locations that lie within the source point region require a reconstruction using DPG to get rid of potential ghosting artifacts in the final reconstructed image.

Once the GRAPPA kernels have been calibrated, the reconstruction procedure is equivalent to standard GRAPPA,



3 Calibration of DPG kernels on exemplary 2×3 pattern with $R = 2$ undersampling

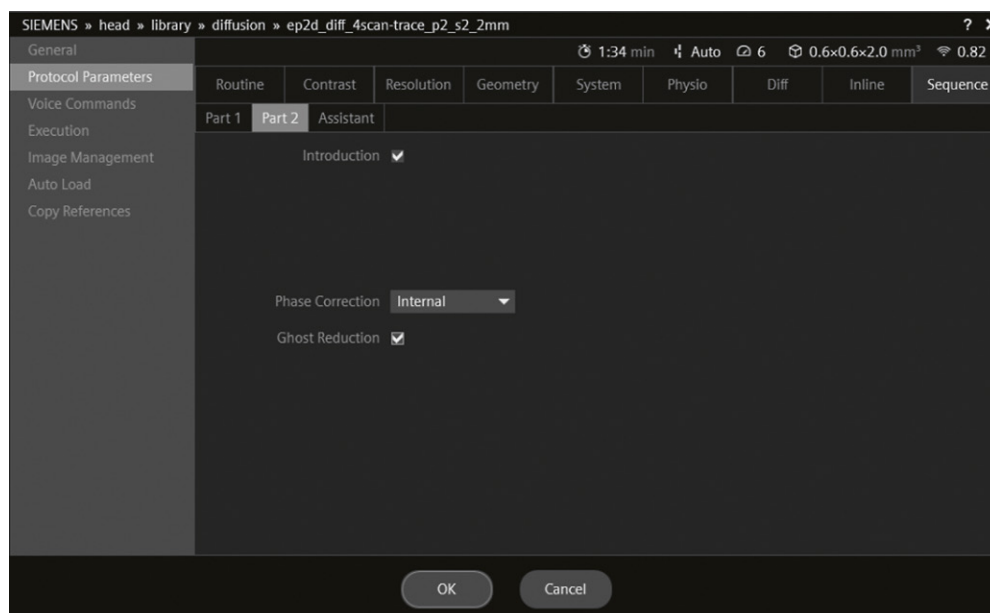


4 Application of calibrated 2×3 DPG kernels

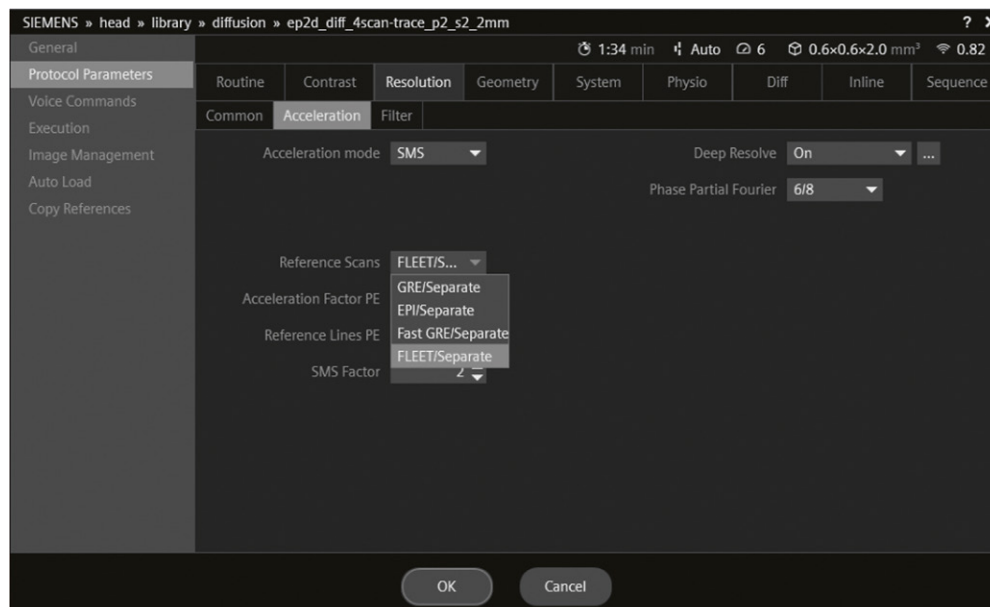
except that several kernels have to be used. Depending on the k -space location, the corresponding kernel has to be applied to the undersampled k -space and ghost-artifact corrected images are the result. This principle is shown in Figure 4 for a $R = 2$ undersampled single-shot EPI example. Neighboring acquired k -space lines have different readout polarity RO+ and RO-, necessitating different kernels to reconstruct missing k -space points and ghost-correct the acquired points.

For the clinical user, DPG will be accessible for EPI imaging via a new checkbox on the Sequence > Part 2 card (see Figure 5). The checkbox name is “Ghost reduction” which precisely describes what DPG is doing. Also, a new reference scan is available: FLEET/Separate can be selected

on the Resolution > Acceleration card under the “Reference Scan” drop down menu (see Figure 6). These options will be available for MAGNETOM Cima.X¹ and Cima.X Fit¹ with software release *syngo* MR XA61. A final remark on FLEET: This new reference scan minimizes the effects of potential motion within one slice due to different motion states of the acquired segments. This motion can occur if the segments that contribute to the k -space of a single slice of reference data are acquired with a large time difference. If motion was present in the reference scan, the GRAPPA weights are suboptimal, resulting in compromised image quality. FLEET can be seen as an additional tool to optimize the quality of the reference scan, but it is not mandatory for use of DPG.



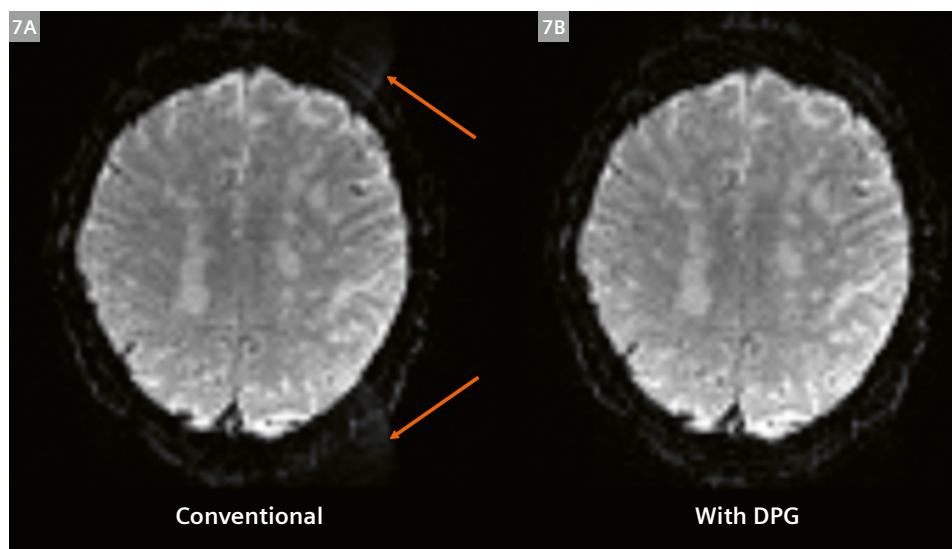
5 Dual-polarity GRAPPA is available when selecting “Ghost Reduction” in the UI and can be found on the Sequence > Part 2 tab



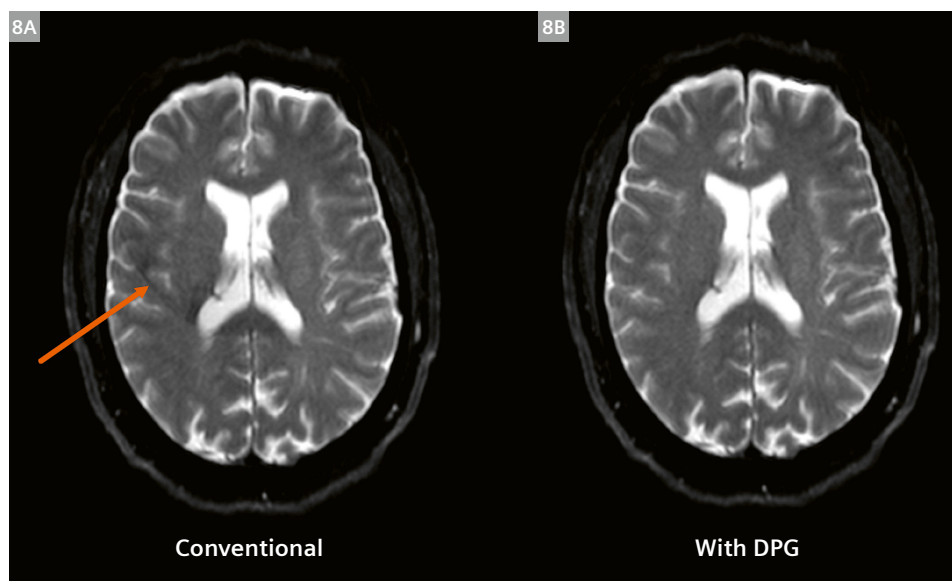
6 The new FLEET reference scan can be selected as usual on the Resolution > Acceleration tab

Figure 7 shows an example of the DPG performance in BOLD imaging for fMRI. If DPG is not used, Nyquist ghosting is visible, here in two locations anterior and posterior of the brain due to the $R = 3$ acceleration. When using DPG in the image reconstruction pipeline, ghosting artifacts are effectively addressed, resulting in optimal image quality in fMRI.

Figure 8 highlights the benefit of DPG in an example of single-shot EPI DWI where b0 images are shown. The subtle ghosting artifact visible in the right hemisphere of the brain can be eliminated by DPG, resulting in artifact-free DWI datasets. Again, DPG does a really good job in eliminating the ghost.



- 7** Effect of Dual-polarity GRAPPA (DPG) in EPI BOLD imaging for fMRI.
(7A) Ghosting is visible in the anterior and posterior of the brain due to $R = 3$ undersampling if ghost reduction is turned off.
(7B) When DPG is turned on, the ghosting is effectively addressed, resulting in clean BOLD images.



- 8** Effect of Dual-polarity GRAPPA (DPG) in EPI diffusion imaging.
(8A) Subtle ghosting is visible on the right side of the brain if ghost reduction is turned off. **(8B)** When DPG is turned on, no ghosting is visible anymore.

Conclusion

EPI imaging is a cornerstone for neuro imaging, including DWI, fMRI, and contrast-enhanced perfusion imaging. Beyond neuro, DWI or perfusion imaging in the prostate and in body imaging is of great clinical relevance. In all the mentioned body regions, susceptibility changes as well as eddy currents are additional sources of phase variations next to the B_0 inhomogeneities of the main magnetic field. Proper phase correction is therefore mandatory for meaningful EPI imaging. DPG is the latest addition to established phase correction methods such as LPC, PLACE and GESTE, and DPG can correct higher order phase variations without explicitly determining or modeling these variations. Therefore, DPG will become a standard ghost reduction tool on all MAGNETOM systems operating on syngo MR XA60/61 or later to enable optimal EPI imaging in all body areas.

References

- Mansfield P. Multi-planar image formation using NMR spin echoes. *J. Phys. C: Solid State Phys.* 1977; 10(3):L55–L58.
- Stehling MK, Turner R, Mansfield P. Echo-planar imaging: magnetic resonance imaging in a fraction of a second. *Science.* 1991;254(5028):43-50.
- Ogawa S, Lee TM, Kay AR, Tank DW. Brain magnetic resonance imaging with contrast dependent on blood oxygenation. *Proc Natl Acad Sci U S A.* 1990;87(24):9868-9872.
- Bandettini PA, Wong EC, Hinks RS, Tikofsky RS, Hyde JS. Time course EPI of human brain function during task activation. *Magn Reson Med.* 1992;25(2):390-397.
- Kwong KK, Belliveau JW, Chesler DA, Goldberg IE, Weisskoff RM, Poncelet BP, et al. Dynamic magnetic resonance imaging of human brain activity during primary sensory stimulation. *Proc Natl Acad Sci U S A.* 1992;89(12):5675-5679.
- Ogawa S, Tank DW, Menon R, Ellermann JM, Kim SG, Merkle H, et al. Intrinsic signal changes accompanying sensory stimulation: functional brain mapping with magnetic resonance imaging. *Proc Natl Acad Sci U S A.* 1992;89(13):5951-5955.
- Stejskal EO, Tanner JE. Spin diffusion measurements: spin echoes in the presence of a Time Dependent Field Gradient. *J Chem Phys.* 1965;42:288-292.
- Le Bihan D, Breton E. Imagerie de diffusion in-vivo par résonance magnétique nucléaire. *Comptes-Rendus de l'Académie des Sciences.* 1985;93 (5):27-34.
- Le Bihan D, Breton E, Syrota A. In-vivo self-diffusion magnetic resonance imaging. *Proc SMRM.* 1985;4:1238-1239.
- Basser PJ, Mattiello J, LeBihan D. Estimation of the effective self-diffusion tensor from the NMR spin echo. *J Magn Reson B.* 1994;103(3):247-254.
- Runge VM, Heverhagen JT. The Clinical Utility of Magnetic Resonance Imaging According to Field Strength, Specifically Addressing the Breadth of Current State-of-the-Art Systems, Which Include 0.55 T, 1.5 T, 3 T, and 7 T. *Invest Radiol.* 2022;57(1):1-12.
- Hoge WS, Polimeni JR. Dual-polarity GRAPPA for simultaneous reconstruction and ghost correction of echo planar imaging data. *Magn Reson Med.* 2016;76(1):32-44.
- Hoge WS, Tan H, Kraft RA. Robust EPI Nyquist ghost elimination via spatial and temporal encoding. *Magn Reson Med.* 2010;64(6):1781-1791.
- Chapman B, Turner R, Ordidge RJ, Doyle M, Cawley M, Coxon R, et al. Real-Time Movie Imaging from a Single Cardiac Cycle by NMR. *Magn Reson Med.* 1987;5:246-254.
- Polimeni JR, Bhat H, Witzel T, Benner T, Feiweier T, Inati SJ, et al. Reducing sensitivity losses due to respiration and motion in accelerated echo planar imaging by reordering the autocalibration data acquisition. *Magn Reson Med.* 2016;75(2):665-679.
- Xiang QS, Ye FQ. Correction for geometric distortion and N/2 ghosting in EPI by phase labeling for additional coordinate encoding (PLACE). *Magn Reson Med.* 2007;57(4):731-741.
- Griswold MA, Jakob PM, Heidemann RM, Nittka M, Jellus V, Wang J, et al. Generalized autocalibrating partially parallel acquisitions (GRAPPA). *Magn Reson Med.* 2002;47(6):1202-1210.
- Pruessmann KP, Weiger M, Scheidegger MB, Boesiger P. SENSE: sensitivity encoding for fast MRI. *Magn Reson Med.* 1999;42(5):952-962.
- T. Feiweier. Magnetic resonance method and apparatus to determine phase correction parameters. US Patent 8,497,681, July 30, 2013.
- Chang YV, Zhou K, Hoge WS, Hoelscher U, Liu W, Polimeni JR. Inter-frame phase alignment for Echo Planar Imaging calibration data acquired with opposite read-out polarities. *Proc ISMRM.* 2019;27:928.



Contact

André Fischer, Ph.D.
Global Segment Manager Neurology
Siemens Healthineers
SHS DI MR M&S CSM
Allee am Roethelheimpark 2
91052 Erlangen, Germany
andre.fischer@siemens-healthineers.com

Retrospective Motion Correction for Brain MRI: A Technical Description of SAMER

Daniel Polak¹, Daniel Nicolas Splitthoff¹, Bryan Clifford², Wei-Ching Lo², Yan Tu Huang³, Nan Xiao³, Heiko Meyer¹, Azadeh Tabari⁴, Komal Awan⁴, Min Lang⁴, John Conklin⁴, Susie Y. Huang^{4,5}, Lawrence L. Wald^{4,5}, Stephen Cauley^{4,5}

¹Siemens Healthcare GmbH, Erlangen, Germany

²Siemens Medical Solutions, Boston, MA, USA

³Siemens Shenzhen Magnetic Resonance Ltd., Shenzhen, China

⁴Department of Radiology, Massachusetts General Hospital, MA, USA

⁵Martinos Center for Biomedical Imaging, Massachusetts General Hospital, MA, USA

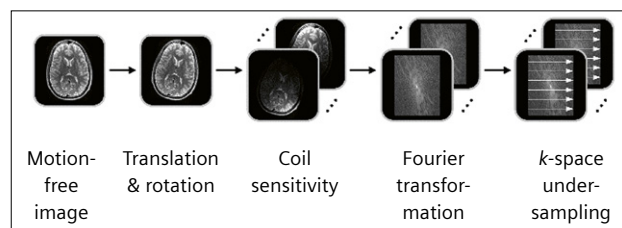
Introduction

Patient motion is a common source of artifacts in brain MRI and accounts for up to 20% of scans being repeated at U.S. hospitals [1]. Motion artifacts often appear as image blurring, ringing, and signal dropouts which may negatively affect image interpretation and diagnosis [2]. 3D volumetric scans with high isotropic spatial resolution are particularly prone to motion due to their long acquisition times. Faster scanning afforded by advanced encoding and reconstruction techniques can reduce the severity of motion [3]. However, even reducing scan times to 1–2 minutes does not solve the problem completely since patient motion typically occurs on the time scale of seconds.

Estimating and correcting for patient motion in clinical brain scans is an active area of research, but no method has found widespread clinical usage. Previously proposed techniques require accurate supplemental tracking data, which is often obtained from external hardware equipment [4, 5] or MRI motion navigators [6, 7]. The position information is used to either update the imaging field of view of the MRI scanner in “real time” (prospective correction) or to inform a motion-aware image reconstruction (retrospective correction). The use of additional tracking data to prospectively or retrospectively correct the image can mitigate motion artifacts, but adoption into clinical protocols is challenging due to the high demands for robustness, reliability, and minimal disruption to the workflow. Specifically, these techniques are expected to yield significant image quality improvement in the presence of moderate to strong patient motion, where the accuracy of the motion parameter measurements is high (measurement error is a small percentage of the motion amplitude). But high image quality must be retained when there is no or limited motion (the amplitude of the motion is below the uncertainty of the tracker’s or navigator’s measurement). Furthermore, the method must not disrupt the clinical

workflow by, for instance, requiring extensive set-up, altering sequence parameters, or delaying image reconstruction. These demanding requirements must be met for all examinations to avoid adversely affecting the large percentage that can be completed with limited or no patient motion.

Data-driven retrospective motion correction provides an opportunity to meet many of these requirements, given that it can be formulated as a “do-no-harm” strategy. These methods extract the motion information and the motion-free image directly from the k -space data of the imaging scan without requiring additional tracking hardware or disruptive sequence modifications [8, 9]. This ensures that the baseline image quality and contrast will be maintained and that the motion-mitigation strategy only adds value to the exam. Radiologists also have the opportunity to directly compare the motion-modeled reconstruction against the original non-corrected images for improved diagnostic utility. Unfortunately, data-driven motion correction is computationally demanding because it often requires the inversion of a large and sophisticated nonlinear physics model that describes the effect of motion on the acquired k -space data. The challenging optimization required for this reconstruction is computationally prohibitive for standard clinical workflows where technologists need to make an intermediate informed decision.



1 Illustration of the SENSE+motion forward model.

The k -space data of a given shot is related to the image volume through image translation and rotation, coil sensitivity shading, Fourier transformation, and k -space undersampling.

¹Work in progress. The product is still under development and not commercially available. Its future availability cannot be ensured.

The recently proposed scout accelerated motion estimation and reduction (SAMER)¹ algorithm [10, 11] will reduce the computational burden of motion estimation by leveraging an ultra-fast scout scan along with the repeated acquisition of a very limited number of additional k -space encoding lines. This approach will facilitate robust and highly efficient retrospective motion correction with clinically acceptable computation times.

SAMER

The SAMER¹ framework is based on SENSE [12] parallel imaging with rigid body motion operators added to describe motion within the forward model. Details of this SENSE+motion model are described in Figure 1. Estimating the motion trajectory and the motion-free image is achieved by minimizing the deviation between the physics model prediction and the acquired k -space data. Directly performing this estimation is a difficult and computationally costly joint optimization problem of both motion unknowns and the image voxels (Fig. 2A). The goal of SAMER is to decouple the motion trajectory and the

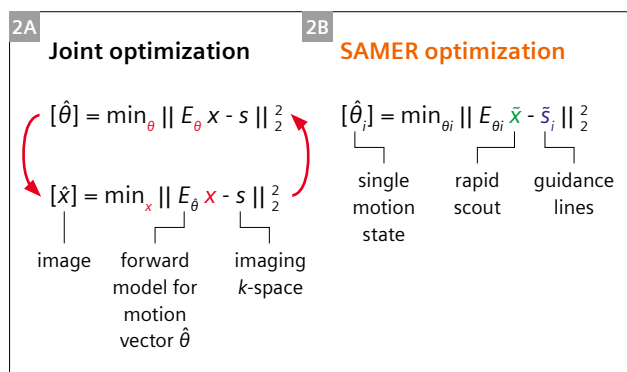
motion-free image estimation. The iterative solution is aided by acquiring additional k -space encoding lines (motion guidance lines) and an ultra-fast scout scan. These serve as a prior and as a guide for the image/motion trajectory optimization problem (Fig. 2B).

The motion guidance lines and the scout are integrated into the standard data acquisition with minimal added acquisition length or timing disruption. In 3D multi-shot sequences such as MPAGE, the data collection is divided into echo trains (shots), each containing about 100–200 phase/partition encoding lines. As illustrated in Figure 3, SAMER adds a small number of additional guidance lines to each echo train. This induces negligible effects on image quality, contrast, and sequence timing. The ultra-fast, low-resolution scout scan with matching contrast to the guidance lines is acquired only once before the imaging sequence (Fig. 3). It is obtained from a single echo train (single-shot) and can be considered motion-free.

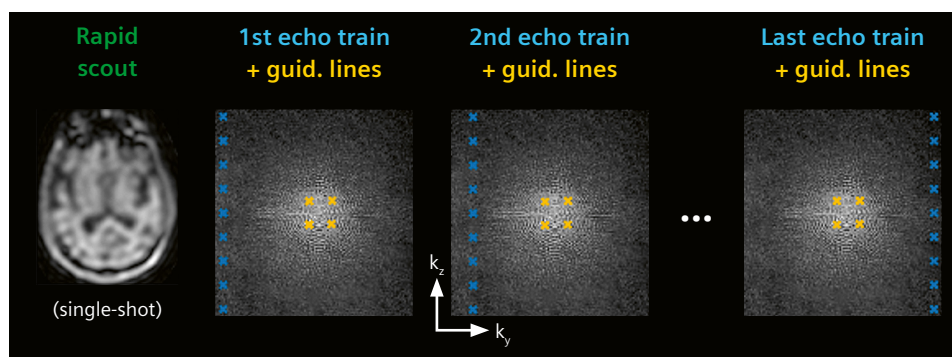
The key computational benefit of SAMER is the ability to estimate the subject's motion for each motion state independently without requiring an intermediate re-estimation of the image volume. This enables very efficient motion estimation (~1 sec/shot) using standard scanner GPU hardware. Moreover, the per-shot motion optimizations can be initiated during the sequence acquisition. This makes efficient use of the scanning time and allows the final motion-aware image reconstruction to start shortly after scan completion.

Applications

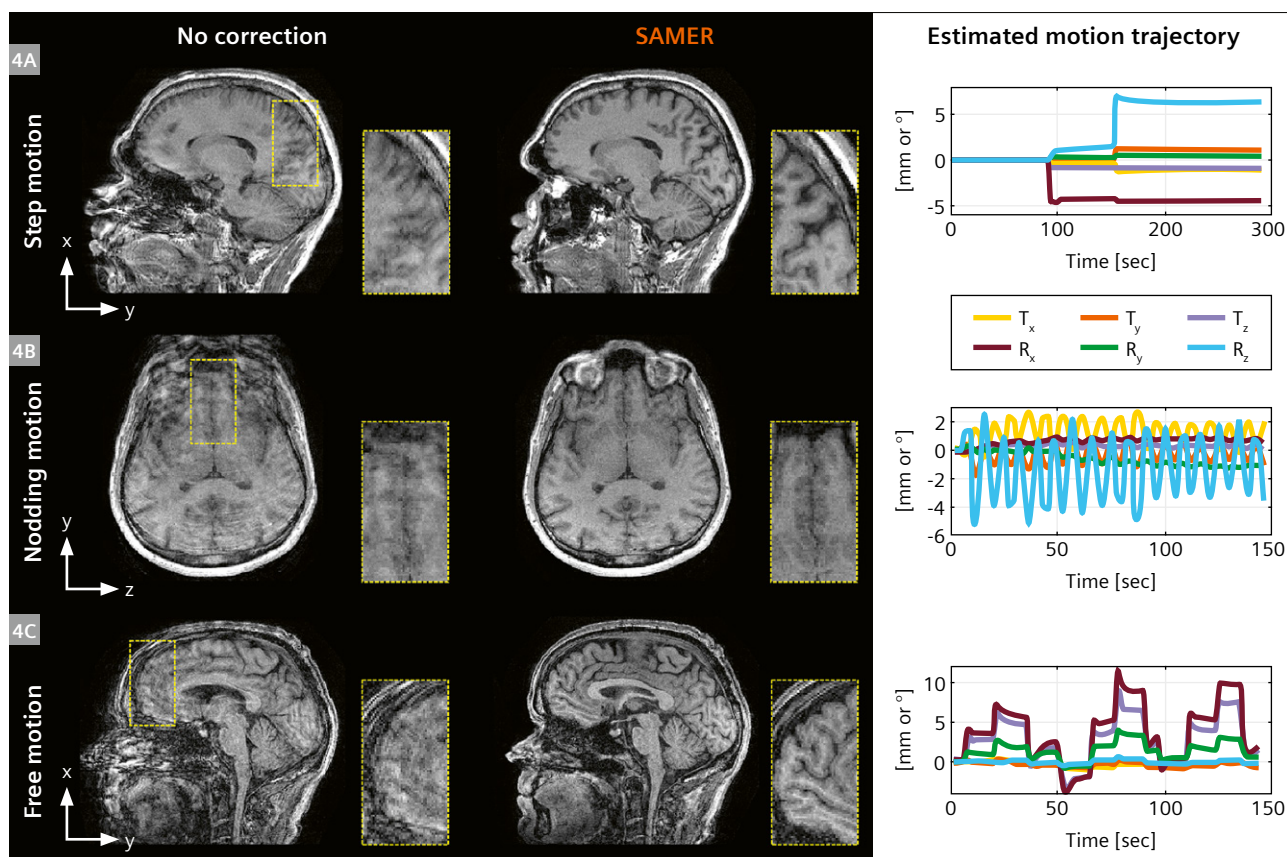
The SAMER framework was implemented into a T1-weighted 3D MPAGE sequence. Scans were performed on two healthy volunteers using a 3T MRI scanner (MAGNETOM Vida; Siemens Healthcare, Erlangen, Germany) and a 20-channel head coil. Volunteers were trained to perform motion patterns that closely resemble clinical scenarios including (i) step motion between three natural positions, (ii) periodic nodding to mimic breathing, and (iii) unsupervised free motion. All reconstructions were performed online using the standard scanner GPU



- 2 Comparison between joint and SAMER¹ motion optimization.** Joint methods alternate between updating the motion parameters θ and the image estimate x . In SAMER, guidance lines \bar{s}_i and the rapid scout \bar{x} facilitate direct (non-joint) motion trajectory estimation. This avoids computationally costly updates of the image volume during the motion optimization and allows each motion state θ_i to be determined independently.



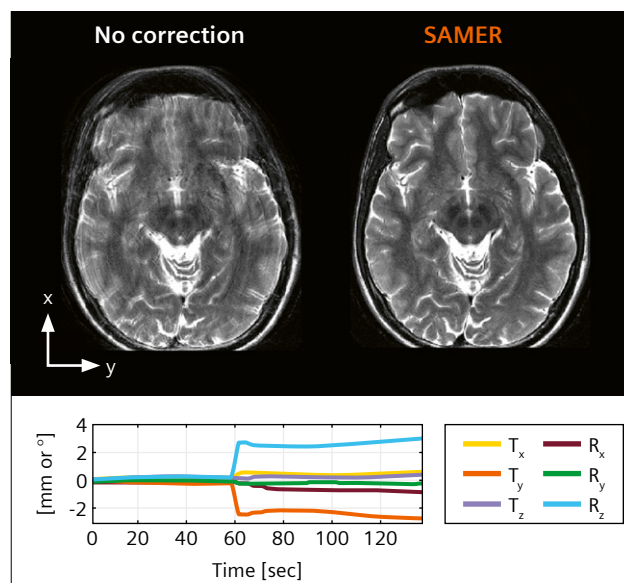
- 3 Illustration of the rapid scout and motion guidance lines in 3D MPAGE.** The low-resolution, single-shot scout is acquired once before the imaging scan. Guidance lines (yellow) are integrated into the standard data acquisition (blue) of each MPAGE echo train.



4 In vivo motion correction of clinically representative motion patterns in 3D MPRAGE. SAMER mitigated most ringing/blurring artifacts and reduced loss of spatial resolution.

hardware. Motion parameters were estimated once per TR with a temporal resolution of 2.5 seconds. The instructed step motion with up to 7° of rotation resulted in image blurring and loss of spatial resolution which was mitigated well by SAMER (Fig. 4A). A similar improvement in image quality was achieved in the scans with instructed nodding and unsupervised free motion, where better depiction of anatomical structures in the frontal cortex can be clearly observed (Fig. 4B, 4C). The efficient inline GPU implementation enabled rapid image-reconstruction times of about 1–2 minutes, which is within standard decision time windows for clinical workflows, i.e., less than a typical MRI scan duration.

Research on SAMER is currently being performed by the Neuroradiology department of the Massachusetts General Hospital (Boston, MA, USA). In a recent study [13], SAMER MPRAGE was explored in inpatient and emergency settings, comparing the level of motion severity with and without correction. It was noted that SAMER reduced the motion severity: 69% of nondiagnostic motion cases were considered diagnostic after correction; on the other hand, no significant adversary effect on the motion grade was reported in cases with minimal or no motion.



5 In vivo motion correction of 2D TSE with instructed step motion. SAMER removed most motion artifacts enabling improved delineation between gray and white matter.

The SAMER framework generalizes to many sequences and imaging scenarios. For example, a first attempt has been made to deploy SAMER into TSE to demonstrate retrospective motion correction with the most commonly used form of 2D imaging (high in-plane resolution, thick-slice protocols). For an initial assessment, T2-weighted TSE data was acquired with instructed step motion, and the SAMER reconstruction was performed offline. Figure 5 shows the improved spatial resolution and reduced ringing artifacts after the motion correction.

In conclusion, the SAMER approach will offer a computationally scalable solution for retrospective motion correction. The ultra-fast scout scan and motion guidance lines can be easily implemented into the standard sequence sampling, ensuring broad applicability across 2D and 3D sequences.

References

- 1 Andre JB, Bresnahan BW, Mossa-Basha M, Hoff MN, Smith CP, Anzai Y, et al. Toward Quantifying the Prevalence, Severity, and Cost Associated With Patient Motion During Clinical MR Examinations. *J Am Coll Radiol*. 2015;12(7):689-695.
- 2 van Heeswijk RB, Bonanno G, Coppo S, Coristine A, Kober T, Stuber M. Motion compensation strategies in magnetic resonance imaging. *Crit Rev Biomed Eng*. 2012;40(2):99-119.
- 3 Zaitsev M, Maclaren J, Herbst M. Motion artifacts in MRI: A complex problem with many partial solutions. *J Magn Reson Imaging*. 2015;42(4):887-901.
- 4 Zaitsev M, Dold C, Sakas G, Hennig J, Speck O. Magnetic resonance imaging of freely moving objects: prospective real-time motion correction using an external optical motion tracking system. *Neuroimage*. 2006;31(3):1038-1050.
- 5 Ooi MB, Aksoy M, Maclaren J, Watkins RD, Bammer R. Prospective motion correction using inductively coupled wireless RF coils. *Magn Reson Med*. 2013;70(3):639-647.
- 6 Tisdall MD, Hess AT, Reuter M, Meintjes EM, Fischl B, van der Kouwe AJ. Volumetric navigators for prospective motion correction and selective reacquisition in neuroanatomical MRI. *Magn Reson Med*. 2012;68(2):389-99.
- 7 Kober T, Marques JP, Gruetter R, Krueger G. Head motion detection using FID navigators. *Magn Reson Med*. 2011;66(1):135-43.
- 8 Cordero-Grande L, Teixeira RP, Hughes EJ, Hutter J, Price AN, Hajnal JV. Sensitivity Encoding for Aligned Multishot Magnetic Resonance Reconstruction. *IEEE Trans Comput Imaging*. 2016;2(3):266-280.
- 9 Haskell MW, Cauley SF, Wald LL. Targeted Motion Estimation and Reduction (TAMER): Data consistency based motion mitigation for mri using a reduced model joint optimization. *IEEE Trans Med Imaging*. 2018;37(5):1253-1265.
- 10 Polak D, Splitthoff DN, Clifford B, Lo WC, Huang SY, Conklin J, et al. Scout accelerated motion estimation and reduction (SAMER). *Magn Reson Med*. 2022;87(1):163-178.
- 11 Polak D, Hossbach J, Splitthoff DN, Clifford B, Lo WC, Tabari A, et al. Motion guidance lines for robust data consistency-based retrospective motion correction in 2D and 3D MRI. *Magn Reson Med*. 2023;89(5):1777-1790.
- 12 Pruessmann KP, Weiger M, Börnert P, Boesiger P. Advances in sensitivity encoding with arbitrary k-space trajectories. *Magn Reson Med*. 2001;46(4):638-651.
- 13 Lang M, Tabari A, Polak D, Ford J, Clifford B, Lo WC, et al. Clinical Evaluation of Scout Accelerated Motion Estimation and Reduction Technique for 3D MR Imaging in the Inpatient and Emergency Department Settings. *AJNR Am J Neuroradiol*. 2023;44(2):125-133.



Contact

Daniel Polak, Ph.D.
Siemens Healthineers
DI MR RCT CLS NEUR
Allee am Roethelheimpark 2
91052 Erlangen
Germany
daniel.polak@siemens.healthineers.com

Diffusion-Weighted Imaging of the Brain with Isotropic Resolution using *syngo* RESOLVE with GRAPPA and SMS

Thomas Illigen; Christian Söldner, Ph.D.

Siemens Healthineers, Erlangen, Germany

Introduction

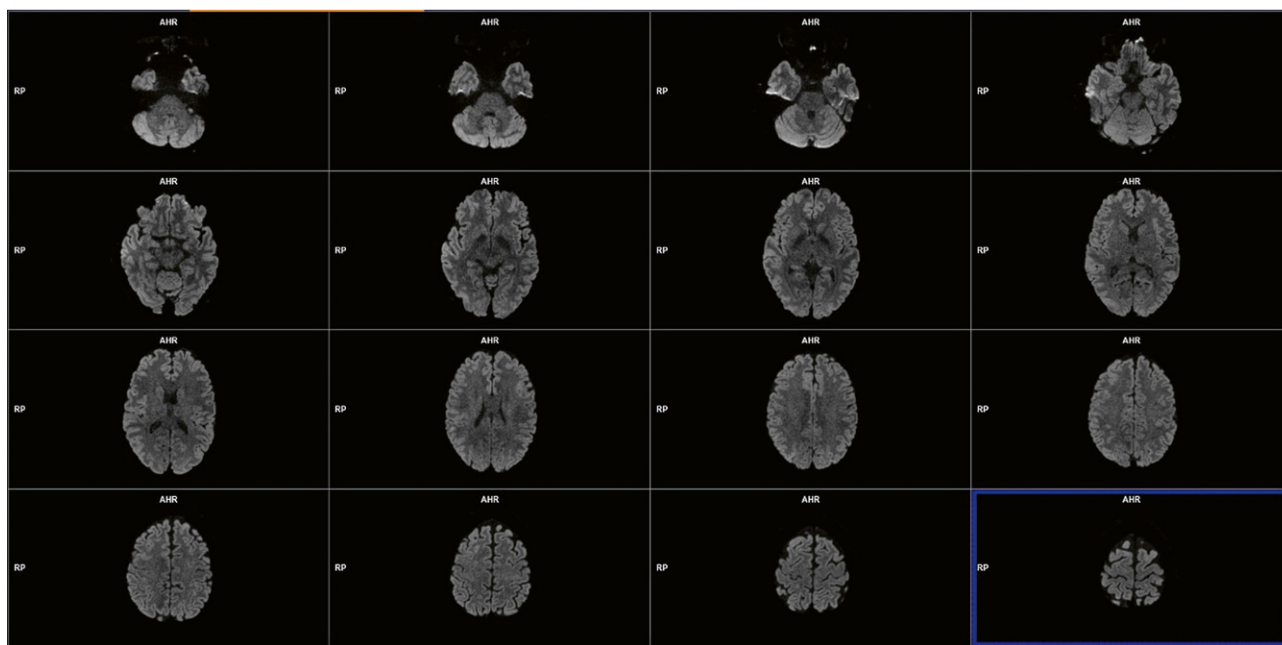
Readout-segmented echo-planar imaging (RESOLVE) produces sharp diffusion-weighted images with high spatial resolution, while GRAPPA (GeneRalized Autocalibrating Partially Parallel Acquisition) and Simultaneous Multi-Slice (SMS)¹ acquisition significantly reduce scan times in clinical MRI.

The clinical benefit of diffusion-weighted imaging (DWI) with isotropic resolution is the volumetric information, e.g., better grading of the progression of an

epidermoid cyst, tumor, or stroke area. High resolution (1.1 mm isotropic) scanning will create severe susceptibility artifacts in single shot EPI. Therefore, RESOLVE is a good alternative, but would require very long scan times on systems with low gradient system configurations. With the 3T MAGNETOM Cima.X², the acquisition time for a RESOLVE sequence with an isotropic resolution of 1.1 mm will be reduced to under 10 minutes, making it applicable for clinical examinations.

¹Simultaneous Multi-Slice (SMS) is part of the Turbo Suite Excelerate package or available as a single chargeable license.

²Work in progress: This product is still under development and not yet commercially available. Its future availability cannot be ensured.



1 RESOLVE with isotropic 1.1 mm resolution; b-value 1000 s/mm²; representative transverse slices show a very homogeneous DWI of the brain.

Material and methods

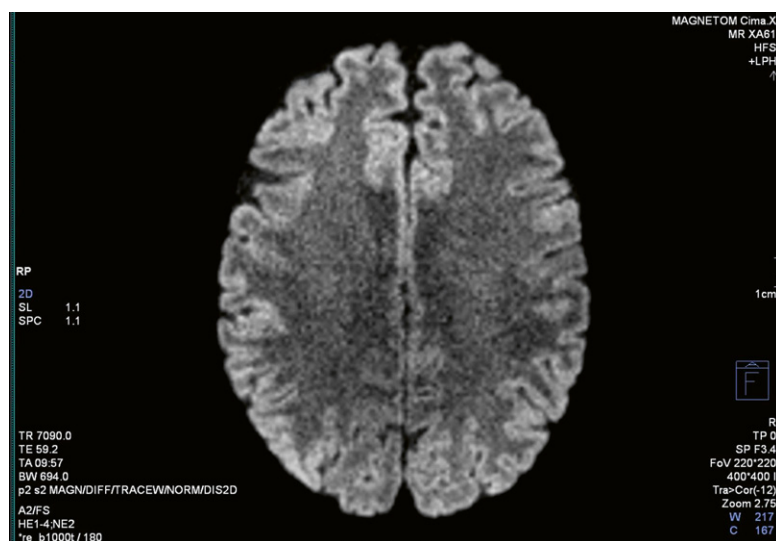
The shown RESOLVE sequence was set up with 7 segments, using GRAPPA (p) and SMS (s), both with an acceleration factor of 2, 100 slices, distance factor (DF) = 0,1 average for b-value 0 s/mm² (b0) and 2 averages for the b-value 1000 s/mm² (b1000), resulting in a scan time of 9:57 min (Fig. 2); acquisition was performed using the BioMatrix Head/Neck 20 coil (BM HN20).

Our preference for the phase-encoding direction is posterior-anterior rather than anterior-posterior, since

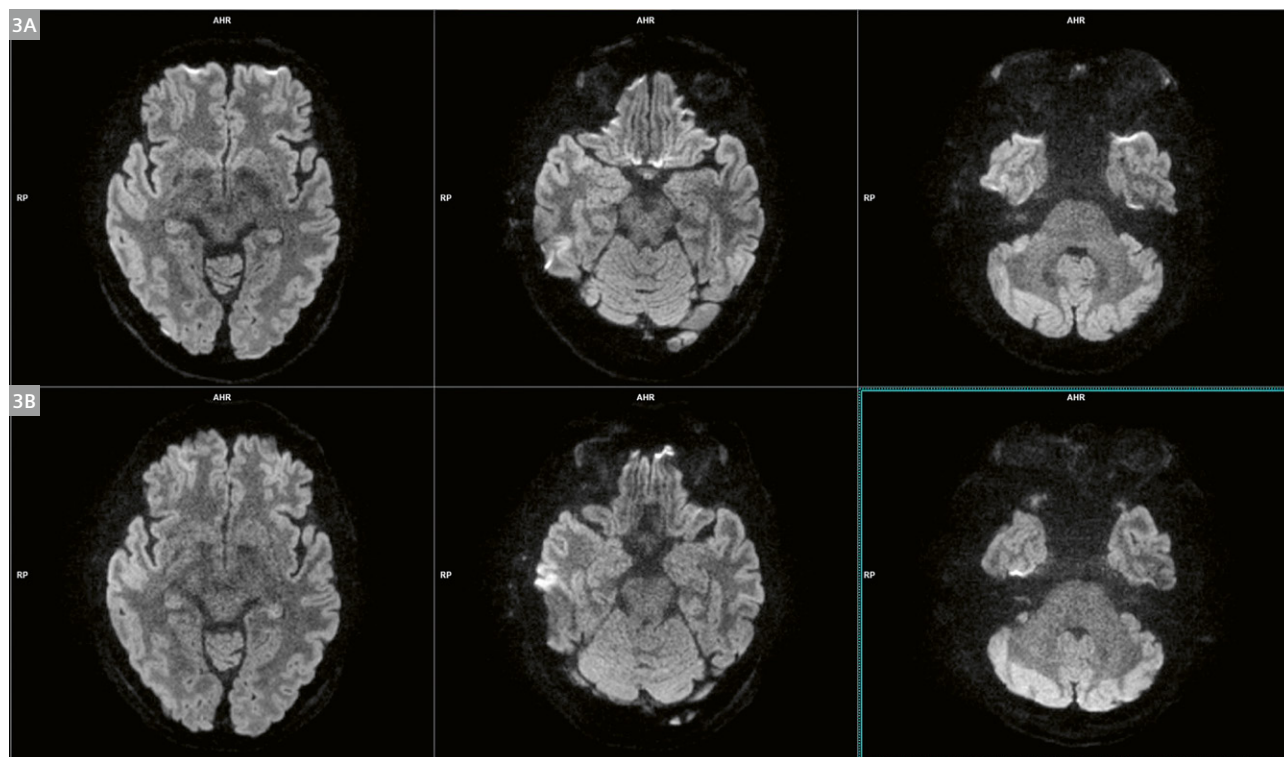
susceptibility artifacts in the mastoid and sella turcica regions are reduced. Also, the frontal lobe area benefits from this change. In any case, the choice of phase-encoding direction has to be considered (Fig. 3).

The expansion of susceptibility artifacts in the slice direction can be reduced by thinner slices, since this reduces the through-plane effect.

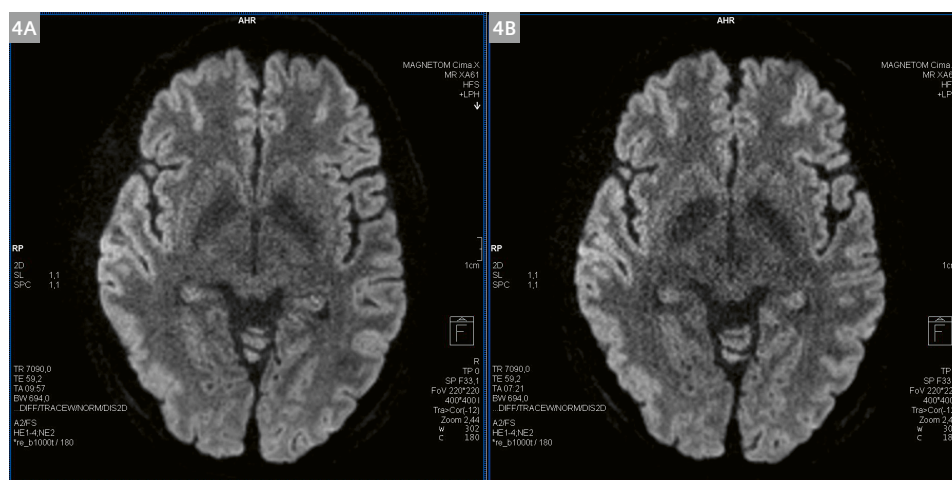
It might be tempting to further shorten the measurement time by using higher acceleration factors, such as p3 and/or s3, or readout partial Fourier, or the acquisition



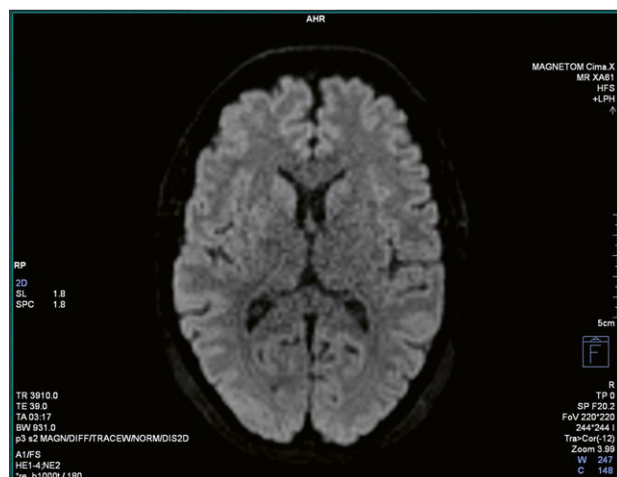
2 RESOLVE with isotropic 1.1 mm resolution; b1000 with TR 7090 ms and TE 59 ms, with an acquisition time of 9:57 minutes.



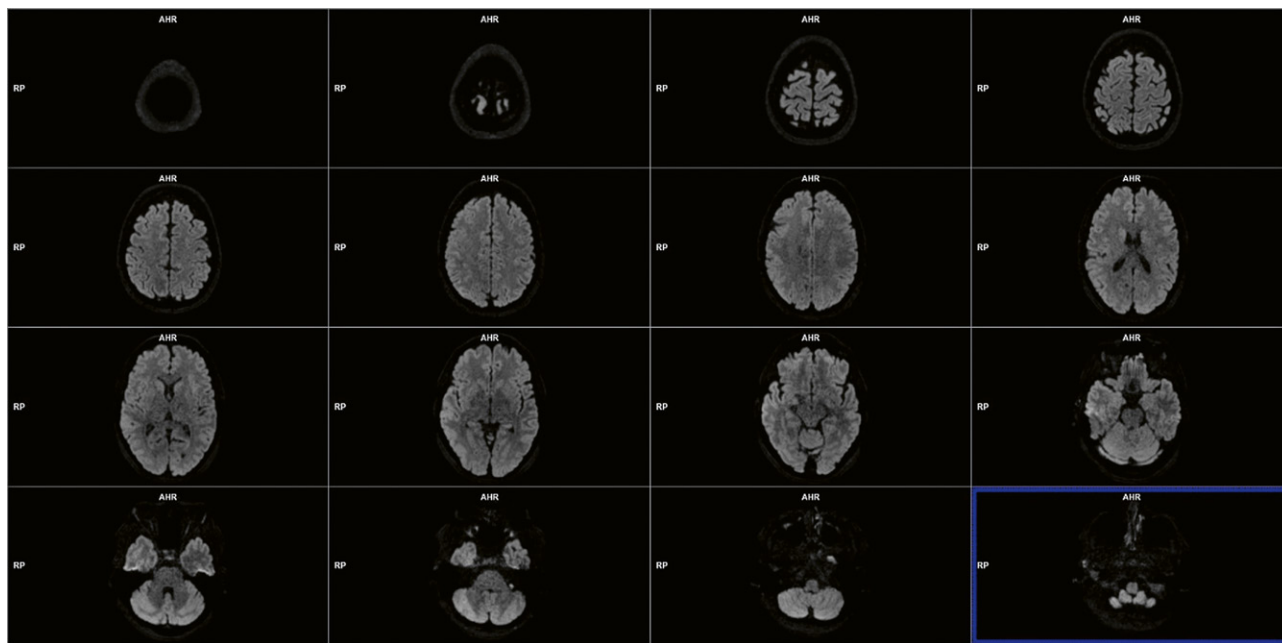
3 RESOLVE with isotropic 1.1 mm resolution, b-value 1000 s/mm², (3A) AP encoded; (3B) PA encoded – the areas most affected by susceptibility artifacts can be compared.



- 4** RESOLVE with isotropic 1.1 mm resolution; b-value 1000 s/mm²; without (4A) and with (4B) readout partial Fourier 6/8, respectively. 5 instead of 7 readout segments; TA: 9:57 minutes vs. 7:21 minutes.



- 5** RESOLVE with an isotropic resolution of 1.8 mm; b1000 image with TR 3910 ms, TE 39 ms, and an acquisition time of 3:17 minutes.



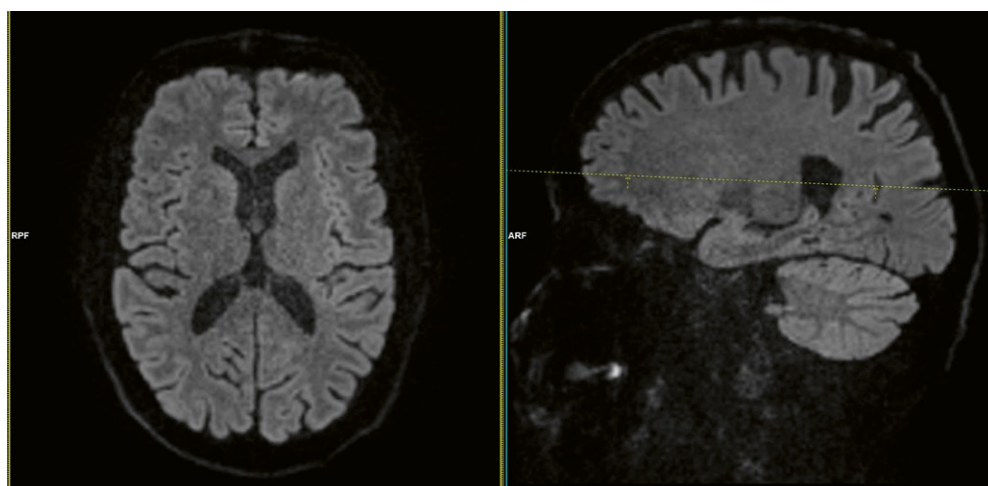
- 6** RESOLVE with an isotropic resolution of 1.8 mm; representative transversal slices of b1000 s/mm².

of fewer segments. All these methods reduce the scan time, indeed – but the resulting images suffer from less SNR (Figure 4 shows a comparison of 7 vs. 5 readout segments, using phase partial Fourier 6/8). Our preferred choice for the high isotropic resolution of 1.1 mm³ is p2s2.

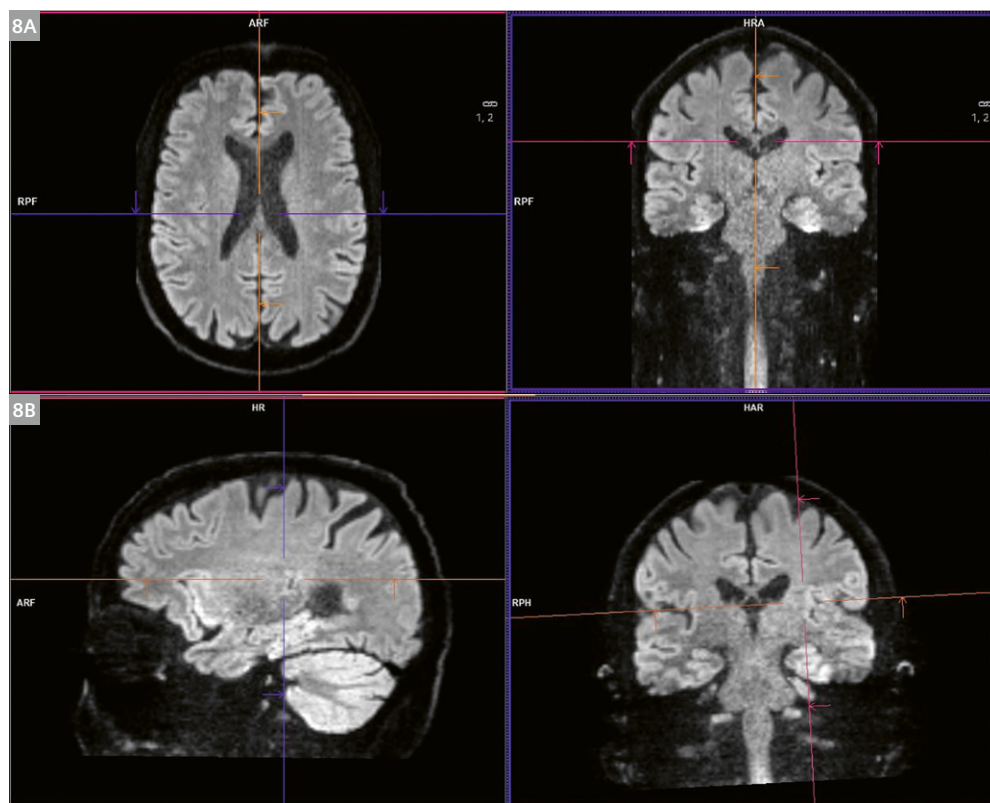
From a practical point of view, and to find the best compromise between resolution and acquisition time, our recommendation for clinical routine examinations would be a protocol with an isotropic resolution between 1.5 and 2 mm. With MAGNETOM Cima.X, the acquisition time for a RESOLVE with an isotropic resolution of 1.8 mm can be reduced to 3:17 minutes with p3s2, b0 and b1000,

with one average each and 80 slices for whole-brain coverage (Figs. 5, 6).

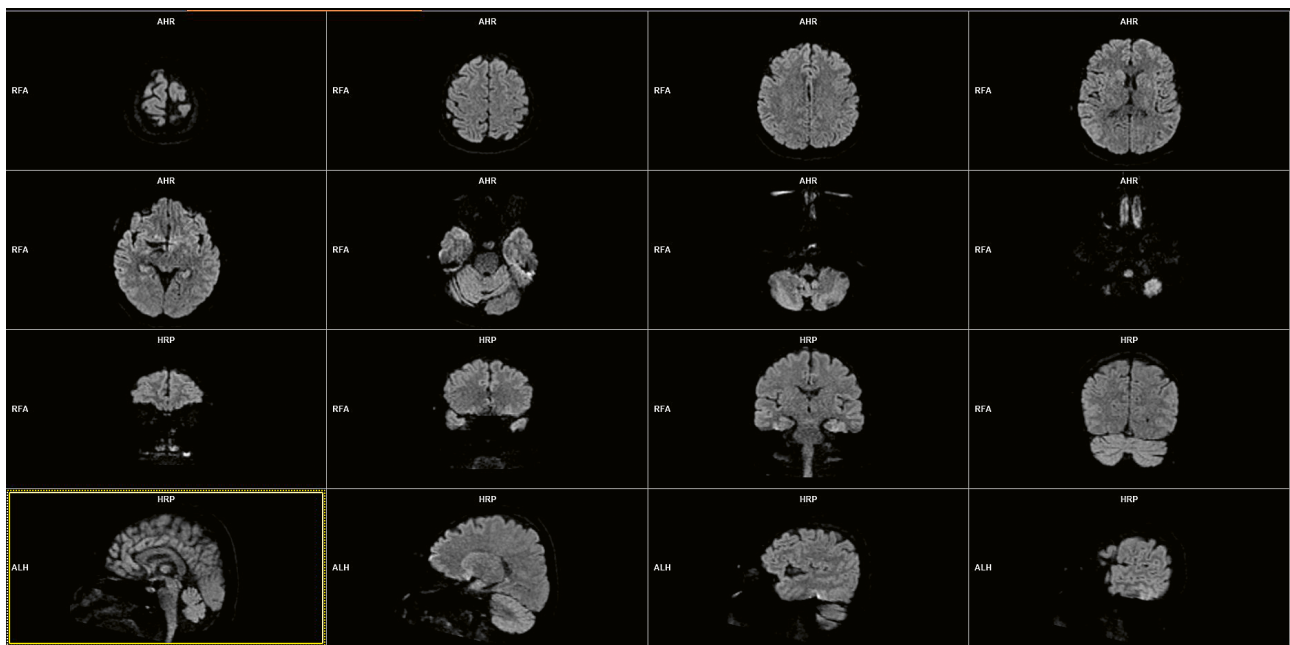
A possible approach might be to acquire the brain sagittally instead of transversally, since sagittal acquisition has the advantage that probably fewer slices are needed for whole-brain coverage. And as far as isotropic resolution is concerned, there should be no significant difference. Due to the weaker susceptibility effects at 1.5T the MRP reconstructions of the 1.5T scans show slightly better image quality than those of the 3T scans. However, the image quality of the acquired slices is very comparable (Figs. 7, 8).



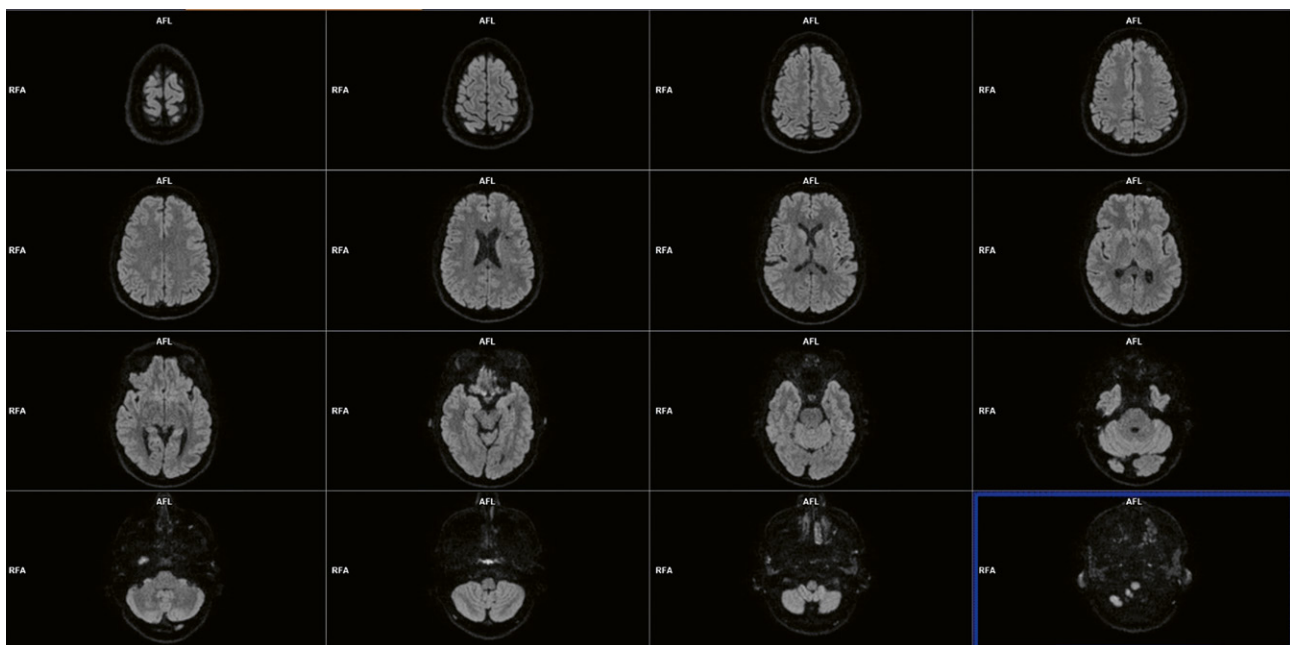
7 RESOLVE with an isotropic resolution of 1.5 mm; b-value 1000 s/mm² from 3T MAGNETOM Vida; representative transversally and sagittally acquired slices.



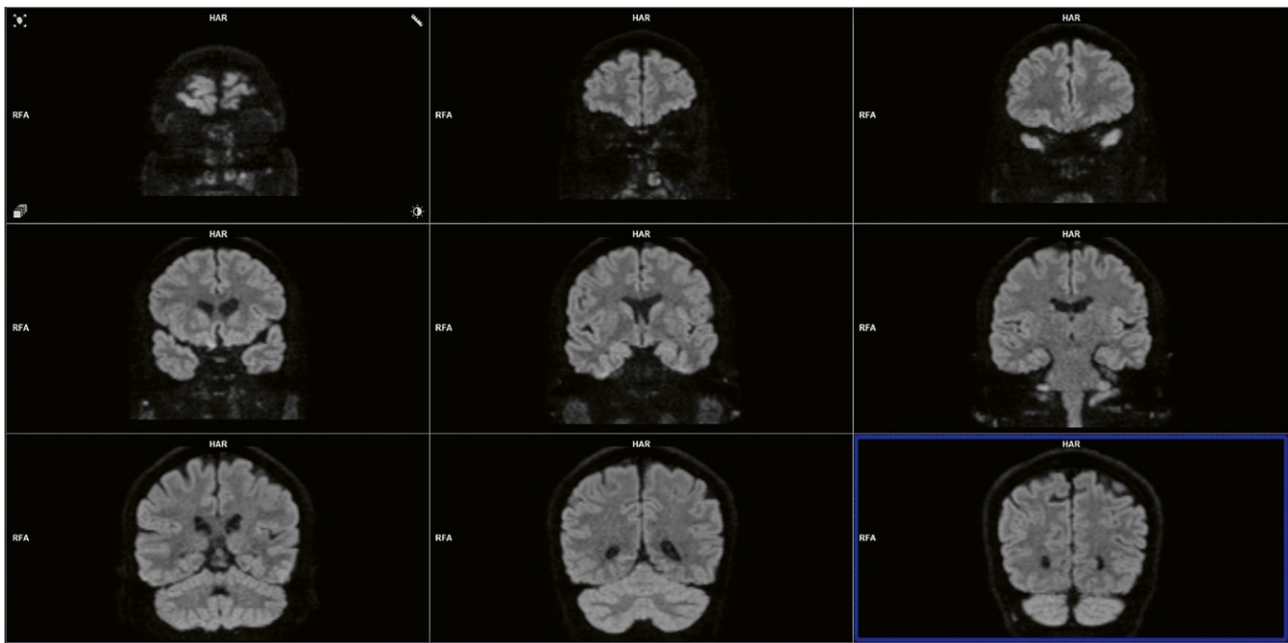
8 (8A) Transversal and coronal multiplanar reconstructions (MPR) from sagittal acquisition show impairing stripes. (8B) Sagittal and coronal MPRs from transversal acquisition do not show stripes.



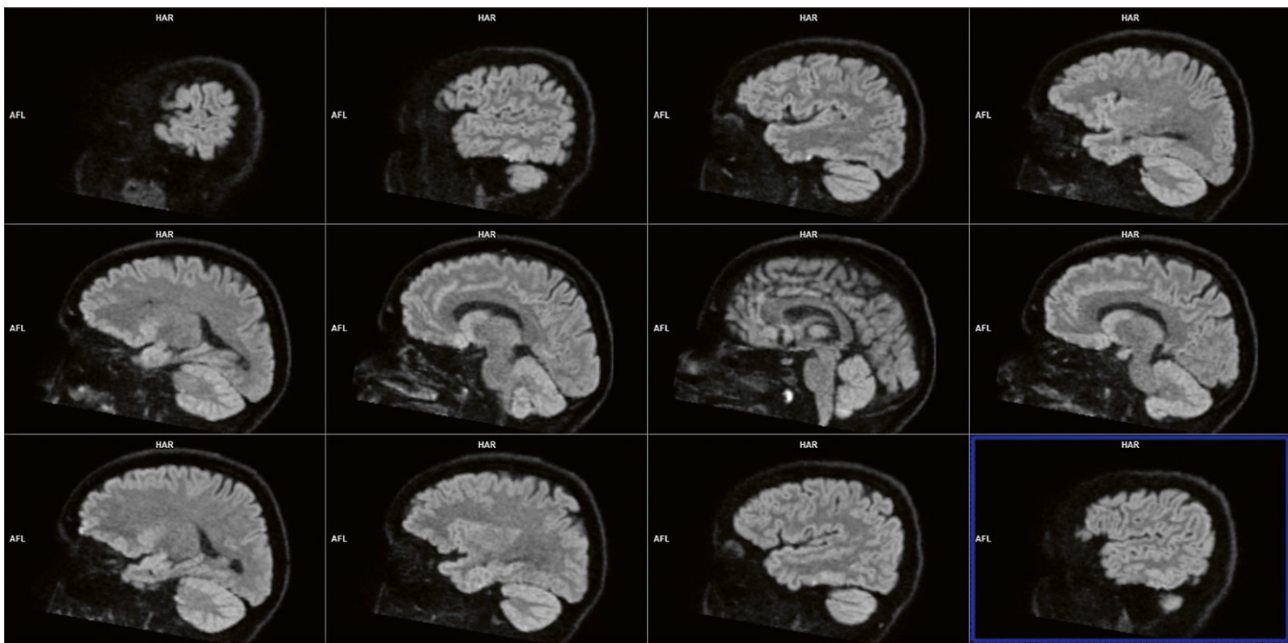
9 1.5T MAGNETOM Altea; RESOLVE with an isotropic resolution of 1.8 mm; b-value 1000 s/mm²; representative transversal slices with coronal and sagittal MPRs.



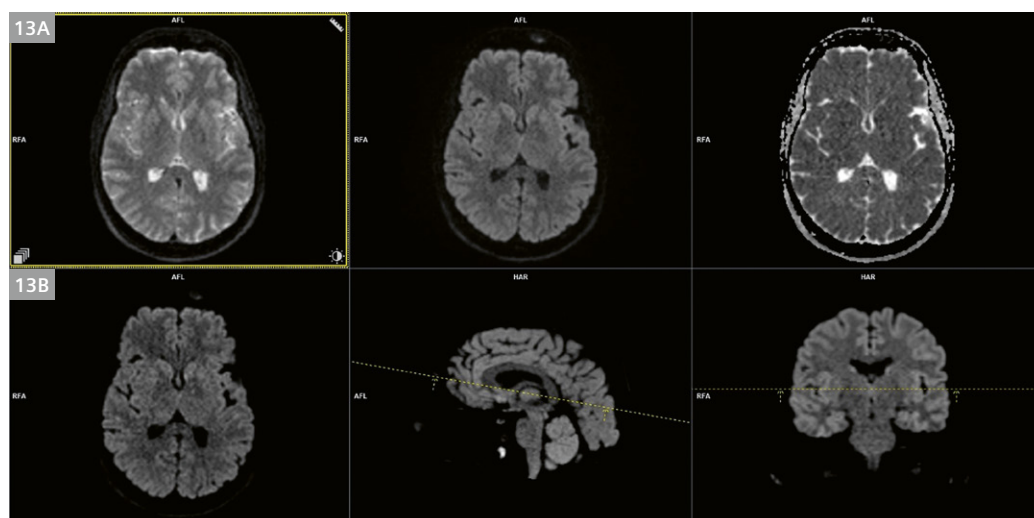
10 1.5T MAGNETOM Sola with XQ gradient system; RESOLVE with an isotropic resolution of 1.8 mm; b-value 1000 s/mm², p2s2, 90 slices, DF = 0, TA: 5:36 minutes; representative transversal slices.



11 1.5T MAGNETOM Sola with XQ gradients; RESOLVE with an isotropic resolution of 1.8 mm; b-value 1000 s/mm²; representative slices from coronal MPR.



12 1.5T MAGNETOM Sola with XQ gradient system; RESOLVE with an isotropic resolution of 1.8 mm; b-value 1000 s/mm²; representative slices from sagittal MPR.



13 1.5T MAGNETOM Sola with XQ gradient system; (13A) shows b0 and b1000 s/mm² and the ADC map; (13B) shows the calculated b1500 s/mm², sagittal and coronal MPRs of b1000 s/mm².

Diffusion-weighted imaging at 3 Tesla is affected to a greater or lesser extent by susceptibility, as seen above. By comparison, a 1.5 Tesla scanner reduces this effect significantly. The image gallery (Figs. 9–13) shows examples of isotropic RESOLVE-scans acquired on the 1.5 Tesla scanners MAGNETOM Altea and MAGNETOM Sola. It is remarkable that almost no susceptibility artifacts occur. We acquired the isotropic RESOLVE sequence typically with b0 and b1000, an ADC map, a calculated b1500 and, in addition, inline generated MPRs (Fig. 13) using the add-ins “MPR Planning” and “MPR Assignment” to obtain consistent results.

Conclusion

A diffusion-weighted measurement with isotropic voxel-sizes at high resolution and convincing image quality – also for the multiplanar reformations (MPR) – in an acceptable acquisition time can be achieved with the RESOLVE sequence using GRAPPA and SMS.

Contact

Thomas Illigen
SHS EMEA CWE DI MR
Karlheinz-Kaske-Str. 2
91052 Erlangen
Germany
thomas.illigen@siemens-healthineers.com



Christian Söldner, Ph.D.
Application Developer
SHS DI MR R&D CCC&CIT AIQ
Allee am Röthelheimpark 2
91052 Erlangen
Germany
christian.soeldner@siemens-healthineers.com



Acknowledgments

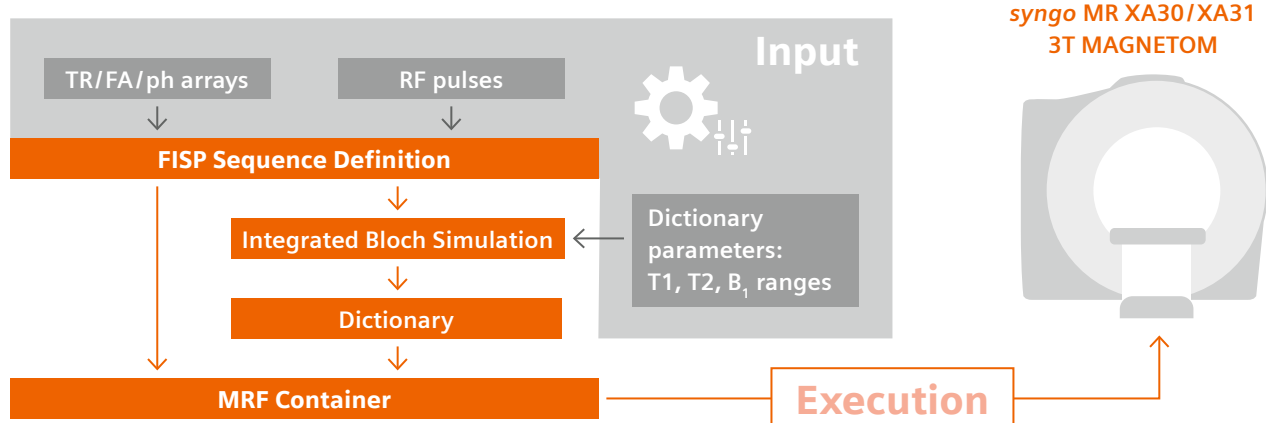
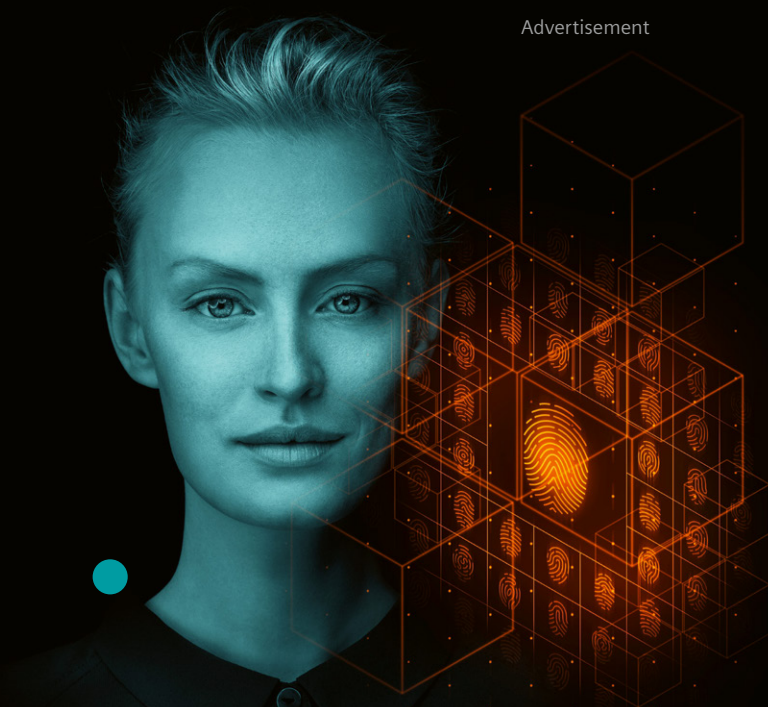
We would like to thank Katrin Schmidt-Kaiser for her generous scanning support and especially Dr. Andreas Bartsch from Radiologie Bamberg for the meaningful discussion.

References

- McNab J A. 3D vs. 2D Diffusion acquisition. Presented at: ISMRM & SMRT Annual Meeting & Exhibition 2014; Milan, Italy.
➤ <https://cds.ismrm.org/protected/14MProceedings/SearchResults.php?Session=Advanced%20Diffusion%20Acquisition>
- Cohen-Adad J. High-Resolution DWI in Brain and Spinal Cord with syngo RESOLVE. MAGNETOM Flash – SMS Supplement to the RSNA Edition. 2012;50(2):16–23.
➤ https://marketing.webassets.siemens-healthineers.com/1800000001345165/aa18a0a08ddb/MRI_52_Cohen-Adad_1800000001345165.pdf
- Filli L, Ghafoor S, Kenkel D, Liu W, Weiland E, Andreisek G, et al. Simultaneous Multi-Slice RESOLVE for Optimized Diffusion-Weighted Imaging of the Breast at 3 Tesla. MAGNETOM Flash. 2016;66(3):126–128.
➤ https://cdn0.scrvt.com/39b415fb07de4d9656c7b516d8e2d907/1800000003527429/894bad0bc7c6/siemens_mri_magnetom-world_hot-topics_simultaneous-multi-slice_sms-resolve_filli_180000003527429.pdf
- Jiang JS, Zhu LN, Wu Q, Sun Y, Liu W, Xu XQ, et al. Feasibility study of using simultaneous multi-slice RESOLVE diffusion weighted imaging to assess parotid gland tumors: comparison with conventional RESOLVE diffusion weighted imaging. BMC Med Imaging. 2020;20(1):93.
- Bartsch A. Case Report: High-Resolution Simultaneous Multi-Slice (SMS) RESOLVE Diffusion Neurography for Evaluation of Peripheral Nerve Entrapment Syndrome and Neuropathy. MAGNETOM Flash. 2016;65(2): 63–67.
➤ https://uploads-ssl.webflow.com/5db282fd014ef87bb8ce927/5db282fd014ef865bf8ceb26_Neurografia%20com%20difusao%20Resolve%20SIEMENS%20REVIEW.pdf

MR Fingerprinting Development Kit

for Tailored Research Applications



The MR Fingerprinting Development Kit¹ takes files describing the input parameters T1, T2, RF- flip angles and pulse phases. This input generates a customized MR Fingerprinting¹ sequence. The input also serves as the basis for a Bloch simulation, which creates a MR Fingerprinting dictionary unique to its input parameters.

In a final step, the new MR Fingerprinting sequence and its unique dictionary are bundled in the so-called MR Fingerprinting container. This container can be transferred and executed on a qualified MAGNETOM 3T scanner from Siemens Healthineers² with a valid MR Fingerprinting license.

The sequence generation, the Bloch simulation, and the creation of the MR Fingerprinting container are performed by running a Windows command line tool³ provided with the MR Fingerprinting Development Kit.

The MR Fingerprinting Development Kit is available for download to all users of MR Fingerprinting at www.magnetomworld.siemens-healthineers.com/hot-topics/mr-fingerprinting/mrf-developer-kit

This unique MRF Development Kit empowers you to tailor the research application to your needs.

¹The product / feature is not for sale in the U.S. Its future availability cannot be guaranteed.

²syngo MR XA30: MAGNETOM Prisma, MAGNETOM Prisma Fit, MAGNETOM Skyra; syngo MR XA31: MAGNETOM Vida

³The user needs to install the MR Fingerprinting Development Kit on a standalone Windows 10 PC.

Installation on the host computer is not possible.

Deep Learning MRI Sequences: The Present and the Future

Saif Afat, M.D.; Haidara Al Mansour, M.D.; Sebastian Gassenmaier, M.D.; Judith Herrmann, M.D.

Department of Diagnostic and Interventional Radiology, Eberhard Karls University Tuebingen, Germany

Introduction

Magnetic resonance imaging (MRI) is an indispensable tool in clinical routine [1]. However, one of the challenges of MRI is the time-consuming nature of acquiring high-quality images. This can increase patient discomfort, limit MRI throughput, and reduce access to this imaging modality [2].

To address this challenge, we have been exploring the use of deep learning in MRI sequences to accelerate the acquisition process while maintaining or even improving the image quality. Deep learning is a type of artificial intelligence that can learn from large datasets and apply that knowledge to new situations [3, 4]. By training deep learning algorithms on large datasets of MR images, researchers have been able to develop novel MRI sequences that can reduce acquisition time while maintaining image quality [2, 4].

The importance of deep learning MRI sequences in the future might be significant. By reducing the acquisition time, clinicians can improve patient comfort and increase the number of patients they can see in a day, thereby improving access to MRI. In addition, deep learning MRI sequences can improve image quality, which can lead to more accurate diagnoses and treatment planning. This could result in better patient outcomes and reduced healthcare costs.

In this context, it is essential to understand the applications and benefits of deep learning MRI sequences in terms of scan time acceleration and image quality improvement.

The jack of all trades: Deep learning (DL)-reconstructed turbo spin-echo (TSE) in several organ systems

1. The role of DL-reconstructed turbo spin-echo sequences (TSE) in imaging of the musculoskeletal system (MSK).

MRI is an essential diagnostic tool for assessing the MSK system. In this context, TSE sequences play a pivotal role and are used to image a variety of joints and the spine.

Looking ahead, accelerating these sequences might play a dominant role in increasing MRI throughput.

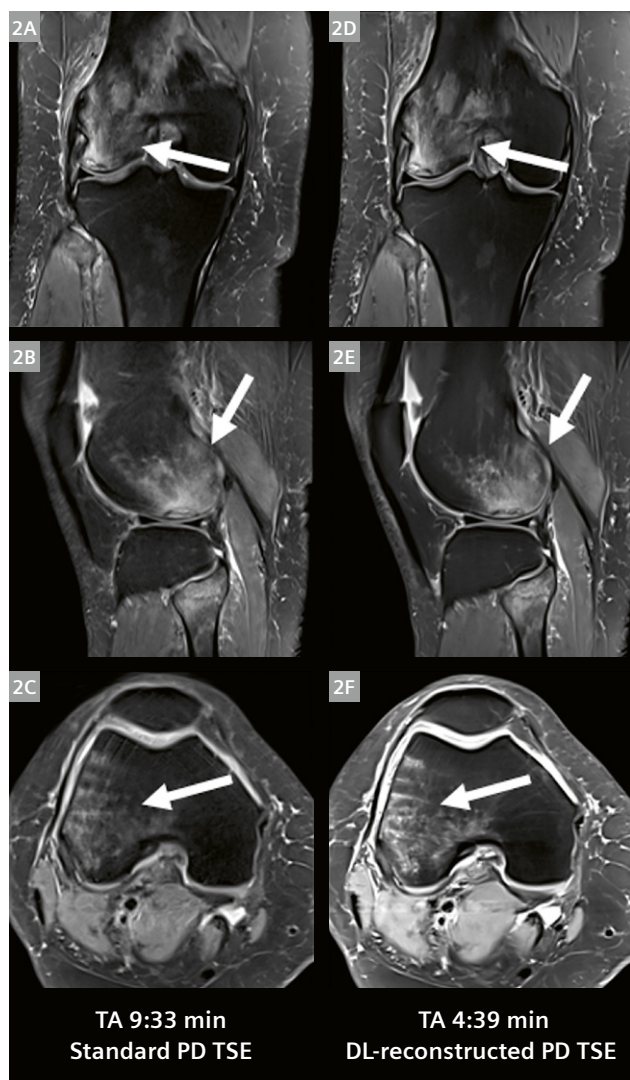
DL reconstruction is a viable way of achieving this. The process can be performed in two steps: Firstly, increasing the acceleration factor to acquire images with TSE



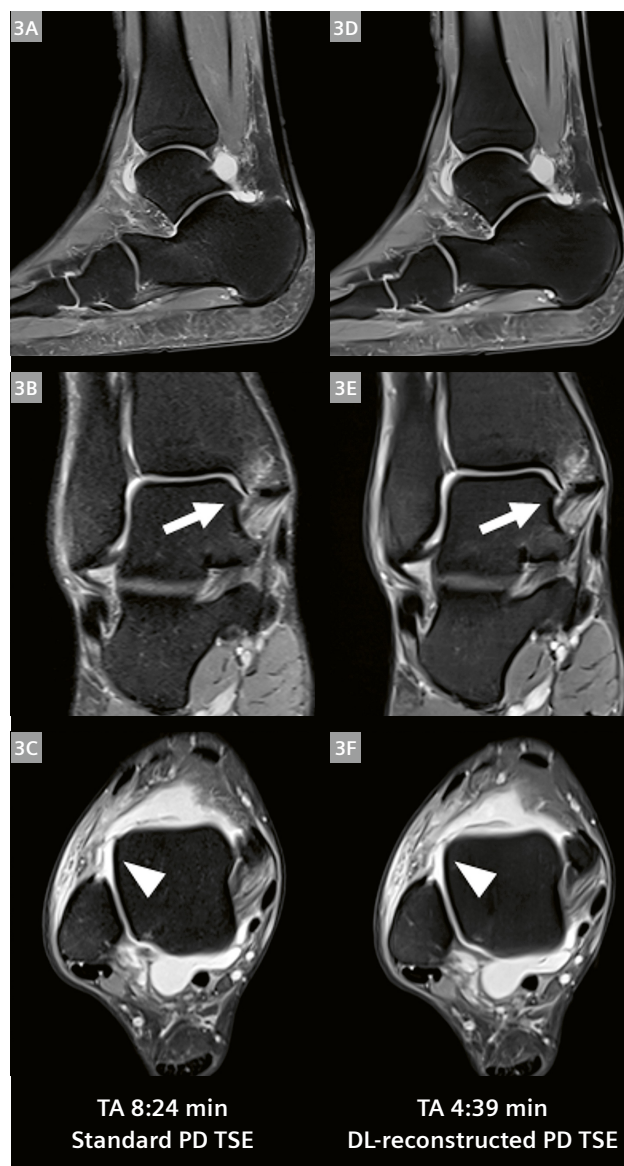
- 1 Sagittal T2-weighted spine MR images of a young patient who presented with lower back pain. (1A) Standard turbo spin-echo (T2 TSE) with an acquisition time (TA) of 2 minutes 20 seconds. (1B) Deep learning reconstructed T2 TSE (T2 TSE DL) with a TA of 35 seconds. Despite a TA reduction of almost 75%, note the similarity between the two images and accurate delineation of minute structures such as the Schmorl's node in T12. Also note the contrast of the two images including the fluid signal of the intervertebral discs.

sequences, which might be suboptimal in terms of contrast, resolution, or signal-to-noise ratio [5]. Secondly, to use the trained DL-reconstruction algorithm to generate desirable images, which are expected to be at least of the same quality as standard clinical imaging [5]. This goal has

been achieved, as shown in many published studies [6–8]. The future aim is to consistently provide better images in less acquisition time. In this section, we provide multiple example cases to illustrate the potential of DL reconstruction in MSK imaging.



2 A 3T knee MRI of a 46-year-old female patient after a fall three weeks prior to imaging, with persistent knee pain on the medial side. Clinical suspicion of an inner meniscus lesion and cartilage damage. Proton density (PD)-weighted TSE is displayed in the coronal (2A, 2D), sagittal (2B, 2E), and axial (2C, 2F) orientation. The subchondral fracture in the lateral femoral condyle, and the adjacent bone marrow edema in both the lateral femoral condyle and the fibular head, can be well delineated in both images.



3 MR images acquired at 1.5T with proton density (PD)-weighted TSE in the sagittal (3A, 3D), coronal (3B, 3E), and axial (3C, 3F) orientation of the right ankle of a 31-year-old female patient after traumatic injury. The posttraumatic bone-marrow edema of the medial malleolus, the edema of the deltoid ligament (arrow), and the rupture of the anterior talofibular ligament (arrowhead) are clearly delineated in both the standard (left) and DL-reconstructed sequences (right). Please note the increased image quality of the TSE DL with less noise. Acquisition time was reduced from 8:24 min for standard PD TSE to 4:39 min for TSE DL.

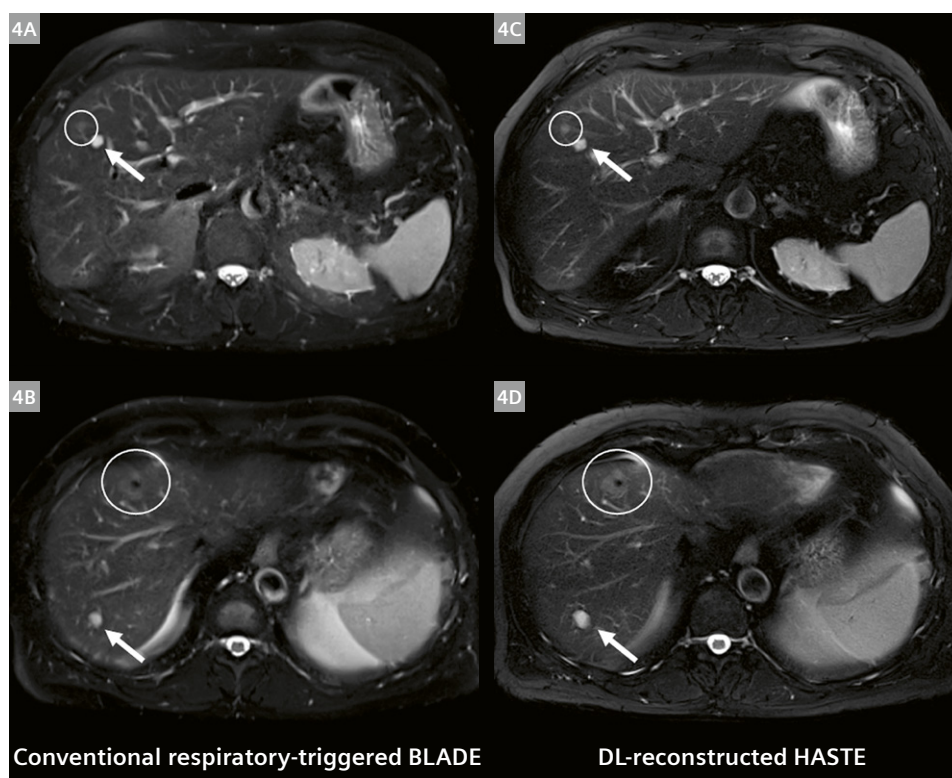
2. The role of DL-reconstructed turbo spin-echo sequences (HASTE) in imaging of the upper abdominal organs.

MRI has become a modality of choice for the diagnosis of several abdominal pathologies [9, 10]. As already mentioned, one big disadvantage of MRI is the long acquisition time, which is usually between 20 and 40 minutes for upper abdominal imaging. Long TAs have downsides such as decreased image quality due to motion artifacts, especially in patients with reduced general condition and shortness of breath.

Clinical implementation of a DL-accelerated T2-weighted (T2w) half-Fourier acquisition single-shot turbo

spin-echo (HASTE) sequence of the upper abdomen could overcome these challenges [11–14]. Image quality in HASTE with DL (HASTE DL) was comparable to that of a T2-weighted sequence (BLADE) with comparable diagnostic performance.

The DL-reconstructed images enabled a significantly reduced TA of only 16 seconds, compared to 4 minutes for BLADE of the upper abdomen. They allowed image acquisition in a single breath-hold. This has the potential to increase patient comfort and increase the number of diagnostic examinations.



4 Liver MRI at 1.5T (MAGNETOM Aera) of a 62-year-old patient with hepatic metastatic uveal melanoma. On the left side are axial images from a conventional respiratory-triggered BLADE sequence. Acquisition time (TA) for the BLADE is 4:00 minutes. On the right are axial images from a single breath-hold HASTE with deep learning reconstruction (HASTE DL) and a TA of 0:16 minutes. Both the BLADE and HASTE DL images show subtle T2w hyperintense metastatic lesions in liver segments VIII and V (circles), and a sharply circumscribed T2w hyperintense lesion compatible with a liver cyst (arrows).

3. The role of DL-reconstructed TSE in mpMRI of the prostate

Multiparametric magnetic resonance imaging (mpMRI) of the prostate is of great importance for accurate detection of clinically significant prostate cancer [15, 16]. Due to the high prevalence of prostate cancer in general, overdiagnosis and overtreatment of clinically insignificant cancers should be avoided. mpMRI can be used for screening purposes and for biopsy planning in cases of MR/ultrasound fusion biopsies [17]. To achieve high diagnostic

image quality, a systematic reporting process has been established, called the Prostate Imaging Reporting and Data System (PI-RADS) [16]. These reporting guidelines also include recommendations regarding the acquisition protocol. However, these recommendations lead to long examination times, which is primarily due to the time-consuming T2-weighted imaging with a recommended slice thickness of 3 mm. These long acquisition times pose a major challenge for daily routine. This is partly because the mostly elderly patient cohort has difficulties remaining

motionless, and partly because the demand for prostate MRI is increasing but MRI scanner availability is limited. Therefore, for further acceleration of scanning, a more aggressive undersampling pathway was investigated using DL-reconstruction methods that allow a drastic reduction in acquisition time without compromising image quality – something that was not possible with conventional methods. By reducing signal averages, a reduction in acquisition time of over 60% could be achieved without loss of image quality [18, 19].

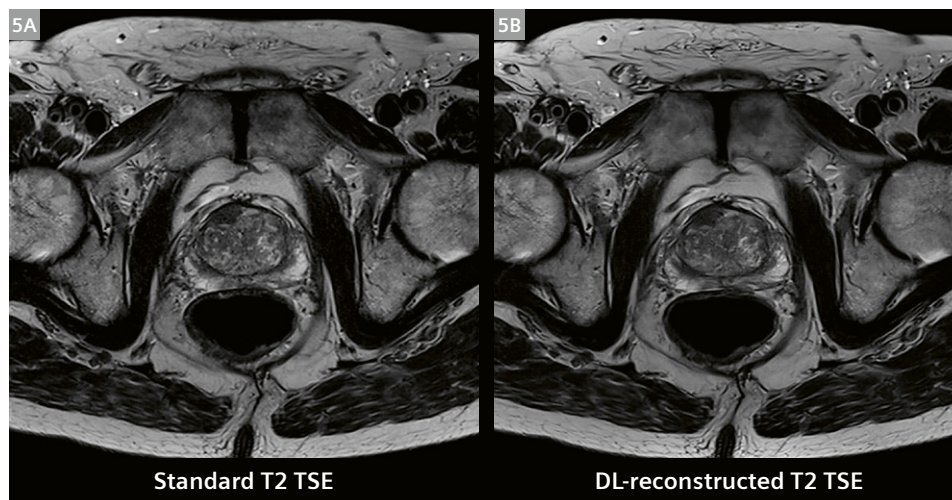
The first studies of DL reconstruction methods demonstrated significant advantages for prostate MRI. However, there is still a lack of data about the possible advantages of thin-slice imaging for cancer detection and the evaluation of capsule infiltration. Therefore, another approach with thin-slice (2 mm) imaging including DL reconstruction and slight reduction of signal averages was investigated and produced promising results [20]. These acquisition changes resulted in similar TA to those in conventional

imaging, but with the advantage of higher morphological resolution and smaller voxel sizes.

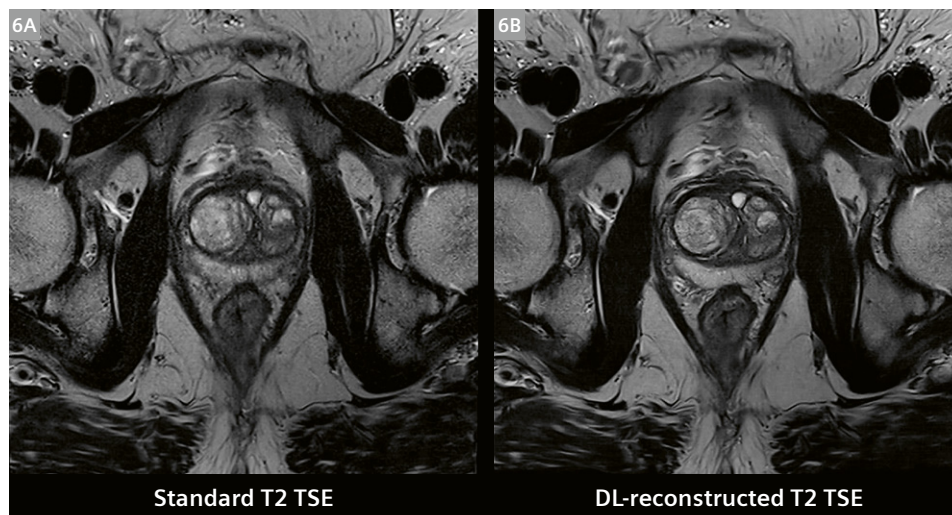
Discussion

Image reconstruction using deep learning has shown promising results in improving MR image quality, reducing acquisition time, and potentially improving diagnostic accuracy [2, 5, 7, 8, 11–13, 18–26]. By using DL algorithms to learn the underlying patterns and structures in MR images, it is possible to reconstruct high-quality images from low-quality input data, resulting in clearer and more accurate images for diagnostic purposes.

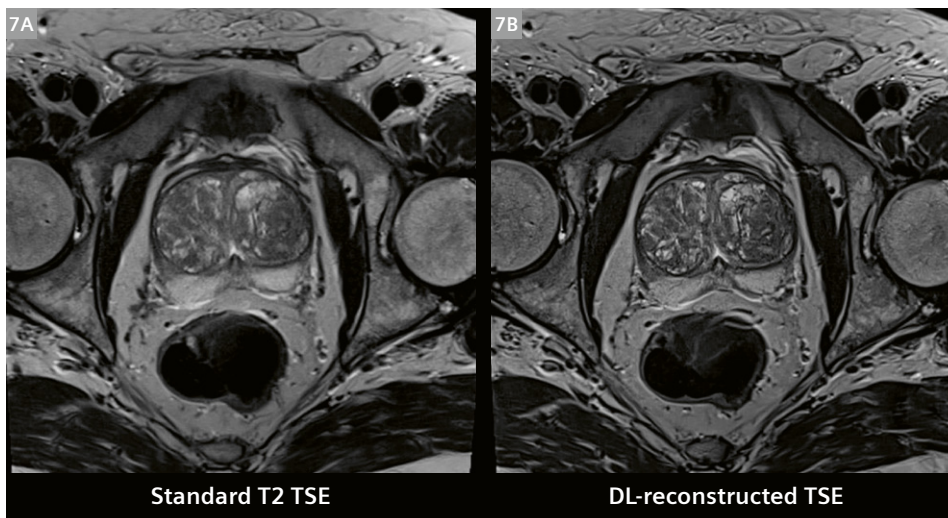
One of the biggest benefits of image reconstruction with DL is its potential to reduce acquisition time. MRI scans can take a long time, which can be uncomfortable for patients and limit the number of scans that can be performed in a given period of time. Using DL algorithms to reconstruct images from a smaller number of data



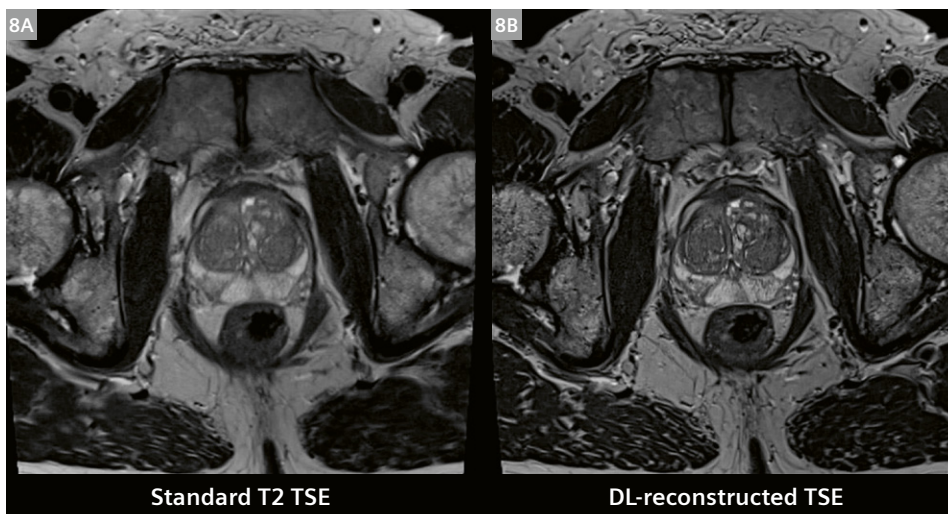
5 (5A) Standard T2-weighted TSE imaging (TA: 4:54 min) and (5B) DL-reconstructed T2-weighted TSE (TA: 1:31 min), both with 3 mm slice thickness. Note the improvement of sharpness and lesion detectability in T2 TSE DL (5B). PI-RADS 5 lesion in the right anterior fibromuscular stromal zone. Biopsy resulted in Gleason 7b.



6 (6A) Standard T2-weighted TSE imaging (TA: 4:53 min) and (6B) DL-reconstructed T2 TSE (1:32 min), both with 3 mm slice thickness. Note the significant improvement of image quality with increased sharpness and fewer motion artifacts.



7 (7A) Standard T2-weighted TSE imaging (3 mm slice thickness; TA: 5:56 min) and (7B) DL-reconstructed T2-weighted TSE imaging (2 mm slice thickness; TA: 6:30 min).



8 (8A) Standard T2-weighted TSE imaging (3 mm slice thickness; TA: 3:52 min) and (8B) DL-reconstructed T2-weighted TSE imaging (2 mm slice thickness; TA: 3:58 min).

points can significantly reduce acquisition time without sacrificing image quality [2].

Apart from pure acceleration, it is also possible to achieve higher morphological resolution within the same time frame as standard imaging [20]. These changes result in image quality in MRI that was previously unimaginable. The higher morphological resolution could help to detect suspicious lesions earlier, which could change treatments and impact interventional procedures. Given the limited data, however, further research on these issues is needed.

There are still some challenges to overcome when using deep learning to reconstruct MR images. One of the biggest is the availability of large, high-quality datasets for training DL models.

In conclusion, using DL for MR image reconstruction holds great promise for improving the accuracy and efficiency of MRI, and could have significant benefits for patient care. However, more research is needed to overcome the challenges and limitations of this approach.

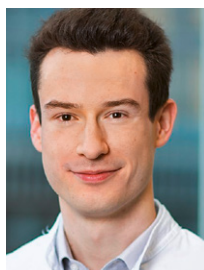
References

- 1 Keogan MT, Edelman RR. Technologic advances in abdominal MR imaging. *Radiology*. 2001;220(2):310–320.
- 2 Gassenmaier S, Küstner T, Nickel D, Herrmann J, Hoffmann R, Almansour H, et al. Deep Learning Applications in Magnetic Resonance Imaging: Has the Future Become Present? *Diagnostics (Basel)*. 2021;11(12):2181.
- 3 Shen D, Wu G, Suk HI. Deep Learning in Medical Image Analysis. *Annu Rev Biomed Eng*. 2017;19:221–248.
- 4 Hyun CM, Kim HP, Lee SM, Lee S, Seo JK. Deep learning for undersampled MRI reconstruction. *Phys Med Biol*. 2018;63(13):135007.
- 5 Herrmann J, Keller G, Gassenmaier S, Nickel D, Koerzdoerfer G, Mostapha M, Almansour H, et al. Feasibility of an accelerated 2D-multi-contrast knee MRI protocol using deep-learning image reconstruction: a prospective intraindividual comparison with a standard MRI protocol. *Eur Radiol*. 2022;32(9):6215–6229.
- 6 Recht MP, Zbontar J, Sodickson DK, Knoll F, Yakubova N, Sriram A, et al. Using Deep Learning to Accelerate Knee MRI at 3 T: Results of an Interchangeability Study. *AJR Am J Roentgenol*. 2020;215(6):1421–1429.

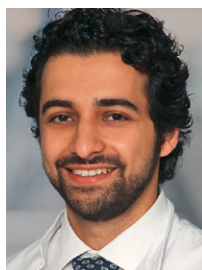
- 7 Almansour H, Herrmann J, Gassenmaier S, Afat S, Jacoby J, Koerzdoerfer G, et al. Deep Learning Reconstruction for Accelerated Spine MRI: Prospective Analysis of Interchangeability. *Radiology*. 2023;306(3):e212922.
- 8 Wessling D, Herrmann J, Afat S, Nickel D, Othman AE, Almansour H, et al. Reduction in Acquisition Time and Improvement in Image Quality in T2-Weighted MR Imaging of Musculoskeletal Tumors of the Extremities Using a Novel Deep Learning-Based Reconstruction Technique in a Turbo Spin Echo (TSE) Sequence. *Tomography*. 2022;8(4):1759–1769.
- 9 Budjan J, Schoenberg SO, Riffel P. Fast Abdominal Magnetic Resonance Imaging. *Rofo*. 2016;188(6):551–588.
- 10 Yang RK, Roth CG, Ward RJ, deJesus JO, Mitchell DG. Optimizing abdominal MR imaging: approaches to common problems. *Radiographics*. 2010;30(1):185–199.
- 11 Herrmann J, Gassenmaier S, Nickel D, Arberet S, Afat S, Lingg A, et al. Diagnostic Confidence and Feasibility of a Deep Learning Accelerated HASTE Sequence of the Abdomen in a Single Breath-Hold. *Invest Radiol*. 2021;56(5):313–319.
- 12 Herrmann J, Nickel D, Mugler JP 3rd, Arberet S, Gassenmaier S, Afat S, et al. Development and Evaluation of Deep Learning-Accelerated Single-Breath-Hold Abdominal HASTE at 3 T Using Variable Refocusing Flip Angles. *Invest Radiol*. 2021;56(10):645–652.
- 13 Herrmann J, Wessling D, Nickel D, Arberet S, Almansour H, Afat C, et al. Comprehensive Clinical Evaluation of a Deep Learning-Accelerated, Single-Breath-Hold Abdominal HASTE at 1.5 T and 3 T. *Acad Radiol*. 2023;30(1):93–102.
- 14 Mulé S, Kharat R, Zerbib P, Massire A, Nickel MD, Ambarki K, et al. Fast T2-weighted liver MRI: Image quality and solid focal lesions conspicuity using a deep learning accelerated single breath-hold HASTE fat-suppressed sequence. *Diagn Interv Imaging*. 2022;103(10):479–485.
- 15 Weinreb JC, Barentsz JO, Choyke PL, Cornud F, Haider MA, Macura KJ, et al. PI-RADS Prostate Imaging – Reporting and Data System: 2015, Version 2. *Eur Urol*. 2016;69(1):16–40.
- 16 Turkbey B, Rosenkrantz AB, Haider MA, Padhani AR, Villeirs G, Macura KJ, et al. Prostate Imaging Reporting and Data System Version 2.1: 2019 Update of Prostate Imaging Reporting and Data System Version 2. *Eur Urol*. 2019;76(3):340–351.
- 17 Giganti F, Rosenkrantz AB, Villeirs G, Panebianco V, Stabile A, Emberton M, et al. The Evolution of MRI of the Prostate: The Past, the Present, and the Future. *AJR Am J Roentgenol*. 2019;213(2):384–396.
- 18 Gassenmaier S, Afat S, Nickel D, Mostapha M, Herrmann J, Othman AE. Deep learning-accelerated T2-weighted imaging of the prostate: Reduction of acquisition time and improvement of image quality. *Eur J Radiol*. 2021;137:109600.
- 19 Gassenmaier S, Afat S, Nickel MD, Mostapha M, Herrmann J, Almansour H, et al. Accelerated T2-Weighted TSE Imaging of the Prostate Using Deep Learning Image Reconstruction: A Prospective Comparison with Standard T2-Weighted TSE Imaging. *Cancers (Basel)*. 2021;13(14):3593.
- 20 Gassenmaier S, Warm V, Nickel D, Weiland E, Herrmann J, Almansour H, Wessling D, Afat S. Thin-Slice Prostate MRI Enabled by Deep Learning Image Reconstruction. *Cancers (Basel)*. 2023;15(3):578.
- 21 Afat S, Wessling D, Afat C, Nickel D, Arberet S, Herrmann J, et al. Analysis of a Deep Learning-Based Superresolution Algorithm Tailored to Partial Fourier Gradient Echo Sequences of the Abdomen at 1.5 T: Reduction of Breath-Hold Time and Improvement of Image Quality. *Invest Radiol*. 2022;57(3):157–162.
- 22 Almansour H, Gassenmaier S, Nickel D, Kannengiesser S, Afat S, Weiss J, et al. Deep Learning-Based Superresolution Reconstruction for Upper Abdominal Magnetic Resonance Imaging: An Analysis of Image Quality, Diagnostic Confidence, and Lesion Conspicuity. *Invest Radiol*. 2021;56(8):509–516.
- 23 Almansour H, Herrmann J, Gassenmaier S, Lingg A, Nickel MD, Kannengiesser S, et al. Combined Deep Learning-based Super-Resolution and Partial Fourier Reconstruction for Gradient Echo Sequences in Abdominal MRI at 3 Tesla: Shortening Breath-Hold Time and Improving Image Sharpness and Lesion Conspicuity. *Acad Radiol*. 2022;S1076–6332(22)00327-0.
- 24 Chaika M, Afat S, Wessling D, Afat C, Nickel D, Kannengiesser S, et al. Deep learning-based super-resolution gradient echo imaging of the pancreas: Improvement of image quality and reduction of acquisition time. *Diagn Interv Imaging*. 2023;104(2):53–59.
- 25 Herrmann J, Koerzdoerfer G, Nickel D, Mostapha M, Nadar M, Gassenmaier S, et al. Feasibility and Implementation of a Deep Learning MR Reconstruction for TSE Sequences in Musculoskeletal Imaging. *Diagnostics (Basel)*. 2021;11(8):1484.
- 26 Wessling D, Herrmann J, Afat S, Nickel D, Almansour H, Keller G, et al. Application of a Deep Learning Algorithm for Combined Super-Resolution and Partial Fourier Reconstruction Including Time Reduction in T1-Weighted Precontrast and Postcontrast Gradient Echo Imaging of Abdominopelvic MR Imaging. *Diagnostics (Basel)*. 2022;12(10):2370.



Judith Herrmann



Sebastian Gassenmaier



Haidara Al Mansour



Saif Afat

Contact

Saif Afat, M.D.
Eberhard Karls University Tuebingen
Department of Diagnostic and
Interventional Radiology
Hoppe-Seyler-Straße 3
72076 Tuebingen
Germany
saif.afat@med.uni-tuebingen.de

Deep Resolve Boost (DRB) and Sharp (DRS) for Diffusion: ADC Phantom Evaluation

Hyun-Soo Lee, Ph.D.¹; Dominik Nickel, Ph.D.²; Gregor Thoermer, Ph.D.²; Thomas Benkert, Ph.D.²

¹MR Research Collaboration, Siemens Healthineers Ltd, Seoul, Republic of Korea

²MR Application Predevelopment, Siemens Healthcare GmbH, Erlangen, Germany

Introduction

Deep Resolve [1] is a reconstruction technique that is based on deep learning (DL) and has the potential to significantly speed up MR scans. Its performance has been demonstrated for various applications. These include turbo spin-echo (TSE) imaging in the spine [2], the prostate [3, 4], and the knee [5], as well as half-Fourier acquisition single-shot turbo spin-echo (HASTE) imaging [6, 7].

Deep Resolve comprises different components that can be used synergistically: Deep Resolve Boost (DRB) [8] is a raw-data-to-image deep learning algorithm that enables shorter scan times by increasing the parallel imaging acceleration (PAT) factor and/or reducing the number of acquired averages. Deep Resolve Sharp (DRS) [9] increases the sharpness of the image by employing a DL-based super-resolution algorithm while preserving the acquired raw data information. In clinical practise, DRB and DRS are typically used in combination to obtain high in-plane resolution at a minimal scan time.

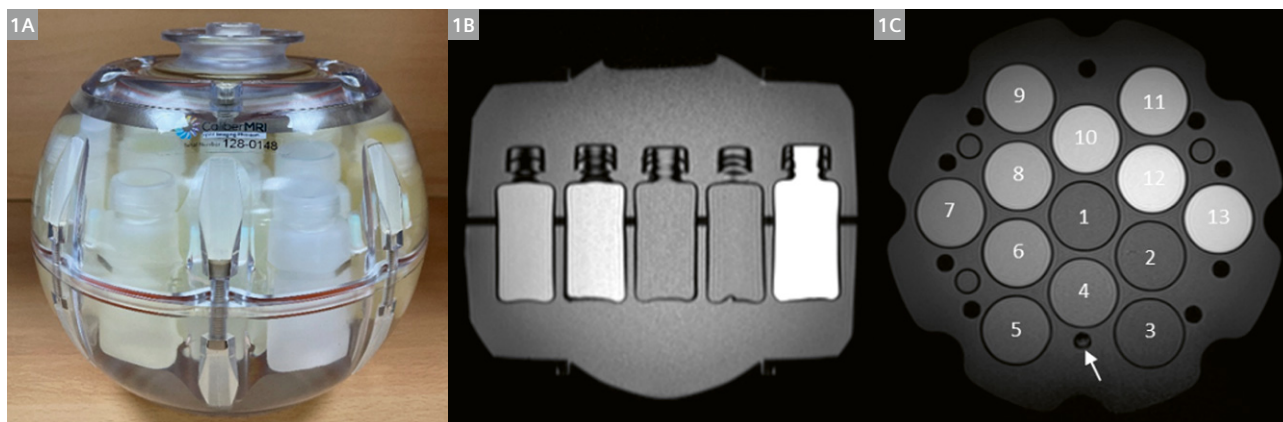
Besides proton density and T1- and T2-weighted imaging, diffusion-weighted imaging (DWI) has shown

high clinical value and is now used in clinical routine as an integral part of the diagnosis of various diseases throughout the body.

Deep Resolve Boost¹ and Sharp¹ can also be applied for diffusion-weighted imaging. Significant scan time decreases were demonstrated across various body regions, including liver DWI [10, 11] and breast DWI [12]. These scan time reductions are typically achieved by lowering the number of averages acquired per b-value and (but not necessarily) by increasing the PAT factor. An apparent diffusion coefficient (ADC) map can be automatically calculated based on the different b-value images (= diffusion weightings) and is increasingly used as a biomarker, for example to assess the probability of malignancy or indicate therapy response. In this context, it is crucial that clinicians can rely on reproducible ADC values when acquisition schemes or parameters are changed.

While different groups have analyzed the potential impact of Deep Resolve Boost and Sharp on ADC measurements in clinical studies [10–12] and found

¹Work in progress. DRB and DRS for Diffusion are still under development and not commercially available yet. Its future availability cannot be ensured.



1 The diffusion phantom contains 13 vials, each with different PVP concentrations (0%–50%) and an MR-readable thermometer (1A). The T1-weighted MPAGE images (1B: axial orientation; 1C: coronal orientation) show the location of the vials within the phantom. The MR-readable thermometer was located in the outer part of the vials (white arrow).

no major deviations, the employed protocols often differed in terms of their settings, such as the PAT factor, the fat saturation scheme, and the number of acquired averages. Additionally, uncontrolled parameters such as patient movement between scans, and variability of ROI placement in human subjects should ideally be excluded for a thorough assessment.

Therefore, the goal of this study was to systematically and objectively assess whether the use of DRB and DRS impacts the ADC for diffusion-weighted imaging, using a dedicated diffusion phantom.

Material and methods

ADC phantom

The diffusion phantom we used (CaliberMRI, Boulder, CO, USA) consists of 13 cylindrical vials with six different concentrations of the polymer polyvinylpyrrolidone (PVP) in aqueous solution. The PVP concentrations were as follows: 0% (vials 1–3), 10% (vials 4–5), 20% (vials 6–7), 30% (vials 8–9), 40% (vials 10–11), and 50% (vials 12–13) (Fig. 1C). Additionally, the phantom contained an MR-readable thermometer, which was used to measure the temperature at the time of acquisition and obtain temperature-corrected reference ADC values (white arrow in Fig. 1C).

Data acquisition

All phantom measurements were performed on a 3T MRI scanner (MAGNETOM Vida; Siemens Healthcare, Erlangen, Germany) using a 64-channel Head/Neck coil array. Three typical DWI protocols with and without DRB+DRS reconstruction were acquired. These protocols covered different imaging scenarios with respect to parameters such as PAT acceleration, Simultaneous Multi-Slice (SMS), and matrix size, and were defined as follows:

- 1) Brain protocol: FOV $240 \times 240 \text{ mm}^2$, matrix size 128×128 , slice thickness 3 mm, PAT2, SMS2
- 2) Liver protocol: FOV $380 \times 304 \text{ mm}^2$, matrix size 140×112 , slice thickness 4 mm, PAT3
- 3) Breast protocol: FOV $380 \times 309 \text{ mm}^2$, matrix size 128×104 , slice thickness 5 mm, PAT2, SMS2

Detailed imaging parameters are summarized in Table 1. To validate the robustness of the ADC maps when using DRB+DRS in accelerated settings, we additionally scanned the above protocols but with a reduced number of averages (Av) and/or a higher PAT acceleration factor.

Before and after the actual DWI imaging experiments, 3D 0.7 mm isotropic T1-weighted MPAGE scans were performed to measure the temperature of the phantom and assess potential temperature changes during the scan.

	Brain	Liver	Breast
Field of view [mm ²]	240 × 240	380 × 304	380 × 309
Slice thickness/gap [mm]	3 / 0	4 / 0.8	5 / 1
Number of slices	50	40	36
Matrix size	128 × 128	140 × 112	128 × 104
In-plane resolution [mm ²]	0.9 × 0.9	1.4 × 1.4	1.5 × 1.5
Repetition time [ms]	5000	2300	3100
Echo time [ms]	64	53	62
PAT acceleration	2	3	2
SMS acceleration	2	–	2
b-values [s/mm ²]	0, 1000	0, 100, 800, 1000	50, 800
Number of averages (Av) per b-value	2/2 Reduced: 1/1	1/1/2/2 Reduced: 1/1/1/1	4/16 Reduced: 2/8
Diffusion mode	4-Scan Trace	3-Scan Trace	3D Diagonal
Receiver bandwidth [Hz/pixel]	2056	2976	2056
Scan time [min:sec]	1:33 Reduced Av: 0:56	4:24 Reduced Av, PAT3: 3:18 Reduced Av, PAT4: 2:51	1:37 Reduced Av: 1:06

Table 1: Acquisition parameters for the brain, liver, and breast protocols.

Furthermore, scans in a healthy volunteer (73-year-old female) were acquired with the identical protocol setup but using appropriate local coil combinations (20-channel head/neck coil; 18-channel breast coil; 18-channel body matrix coil, and 32-channel spine coil) to give an impression of corresponding in vivo image quality.

Quantitative evaluation of phantom ADC values

In the diffusion phantom results, ADC values for the conventional reconstruction and DRB+DRS reconstruction were measured manually in regions of interest (ROIs) that were placed on each vial, covering more than 70% at the central slice. ADC values from individual ROIs and mean ADC/standard deviation were calculated.

Statistical analysis

A paired t-test between protocols with and without DRB+DRS reconstruction was performed. A *p*-value of < 0.05 was considered to be statistically significant.

Results

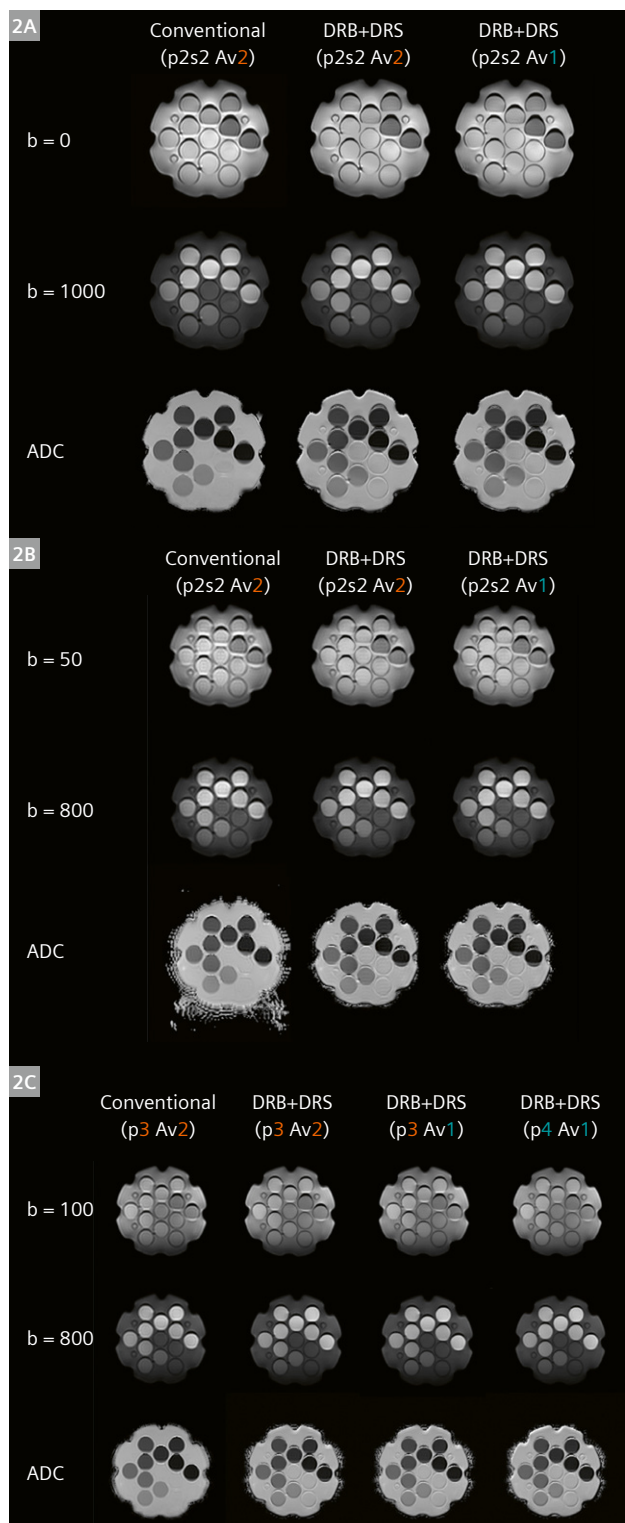
Phantom study

Figure 2 shows representative DWI images and corresponding ADC maps of the diffusion phantom from conventional reconstruction and DRB+DRS reconstruction for three protocol settings. The DWI images and ADC maps with DRB+DRS reconstruction were visually comparable to the conventional reconstruction for all protocols, including the accelerated settings with reduced *Av* or a higher PAT factor (Fig. 2).

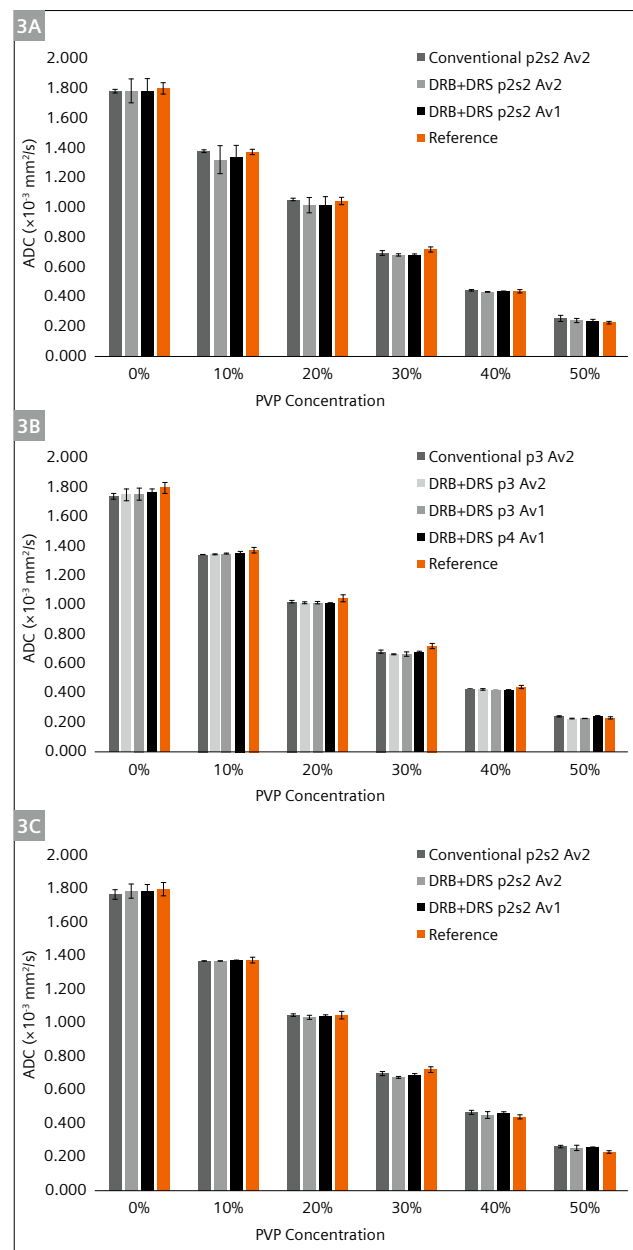
The MPAGE scans confirmed that the phantom temperature stayed constant at 16 °C throughout the phantom scan session. Table 2 and Figure 3 summarize the ADC values for each PVP concentration and mean ADC values, as well as the reference ADC values of 16 °C. There were no significant changes in ADC values across PVP concentrations after DRB+DRS reconstruction for any of the protocol settings employed in the study. Furthermore, the mean ADC values for both conventional and DRB+DRS reconstruction were comparable to those of the reference ADC values within ~3% error.

	Brain protocol			Liver protocol				Breast protocol			Reference
PVP conc. (vial)	Conv. p2s2 Av2	DRB+DRS p2s2 Av2	DRB+DRS p2s2 Av1	Conv. p3 Av2	DRB+DRS p3 Av2	DRB+DRS p3 Av1	DRB+DRS p4 Av1	Conv. p2s2 Av2	DRB+DRS p2s2 Av2	DRB+DRS p2s2 Av1	
0% (1–3)	1.783 ± 0.020	1.786 ± 0.035	1.788 ± 0.034	1.742 ± 0.014	1.752 ± 0.023	1.757 ± 0.021	1.768 ± 0.026	1.768 ± 0.026	1.787 ± 0.032	1.784 ± 0.032	1.799 ± 0.039
10% (4–5)	1.381 ± 0.012	1.325 ± 0.041	1.343 ± 0.040	1.343 ± 0.011	1.346 ± 0.015	1.350 ± 0.015	1.356 ± 0.015	1.370 ± 0.014	1.369 ± 0.016	1.373 ± 0.016	1.376 ± 0.019
20% (6–7)	1.055 ± 0.008	1.019 ± 0.022	1.019 ± 0.020	1.022 ± 0.016	1.016 ± 0.016	1.018 ± 0.015	1.009 ± 0.018	1.047 ± 0.012	1.034 ± 0.034	1.041 ± 0.034	1.047 ± 0.024
30% (8–9)	0.697 ± 0.015	0.685 ± 0.026	0.685 ± 0.024	0.683 ± 0.021	0.665 ± 0.016	0.667 ± 0.016	0.678 ± 0.016	0.699 ± 0.014	0.676 ± 0.034	0.687 ± 0.034	0.722 ± 0.018
40% (10–11)	0.447 ± 0.015	0.436 ± 0.036	0.437 ± 0.030	0.429 ± 0.026	0.425 ± 0.020	0.420 ± 0.020	0.423 ± 0.023	0.467 ± 0.023	0.451 ± 0.027	0.464 ± 0.027	0.440 ± 0.012
50% (12–13)	0.259 ± 0.017	0.244 ± 0.029	0.240 ± 0.028	0.241 ± 0.026	0.229 ± 0.021	0.230 ± 0.021	0.246 ± 0.021	0.263 ± 0.022	0.255 ± 0.023	0.255 ± 0.023	0.231 ± 0.008
Mean ADC (1–13)	1.002 ± 0.557	0.983 ± 0.559	0.986 ± 0.562	0.974 ± 0.547	0.971 ± 0.555	0.972 ± 0.558	0.979 ± 0.557	0.999 ± 0.547	0.995 ± 0.559	0.999 ± 0.556	1.002 ± 0.556
<i>p</i> -value*	–	0.224	0.263	–	0.424	0.673	0.279	–	0.350	0.954	–

Table 2: ADC values for the vials, shown as mean ± standard deviation across all acquired protocol settings. The temperature-corrected reference ADC values are also shown. A graphical representation of this table is given in Figure 3. Abbreviations: p (PAT factor), s (SMS factor), Av (number of acquired averages). The **p*-value was measured from a paired t-test between DRB+DRS and conventional reconstruction.



2 Representative diffusion-weighted images and ADC maps for the brain, liver, and breast protocols using the phantom. **(2A)** DWI ($b = 0, 1000 \text{ s/mm}^2$) and ADC maps of the brain protocols. **(2B)** DWI ($b = 50, 800 \text{ s/mm}^2$) and ADC maps of the breast protocols. **(2C)** DWI ($b = 100, 800 \text{ s/mm}^2$) and ADC maps of the liver protocols.

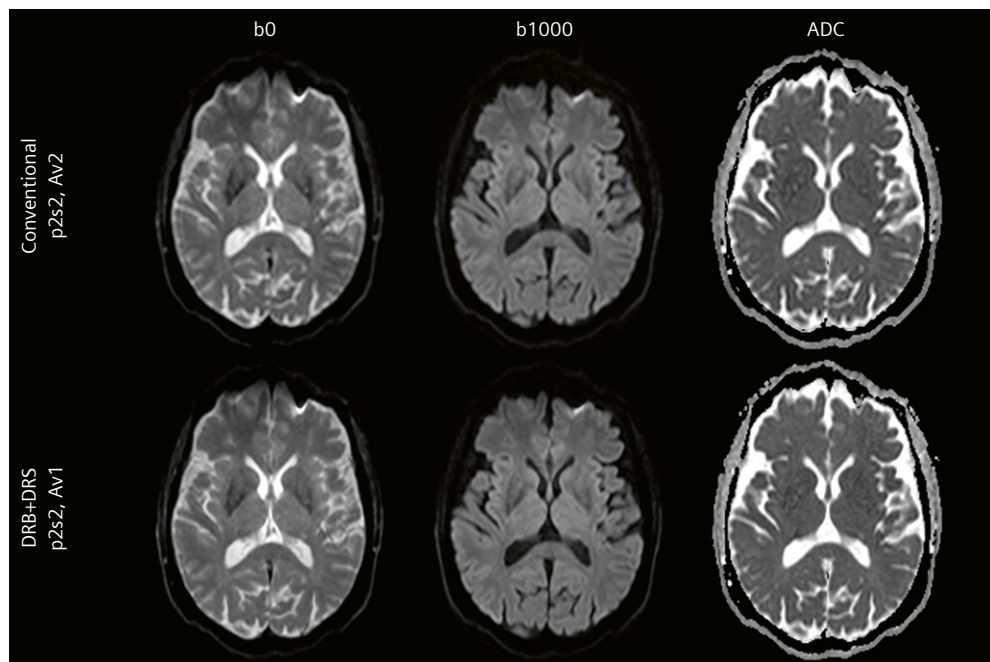


3 Comparison of ADC values measured from the conventional reconstruction and the DRB+DRS reconstruction with various protocols: brain **(3A)**, liver **(3B)**, and breast **(3C)**. Mean ADC values for each concentration are shown with standard deviation as error bars. Reference ADC values of 16°C are displayed as a ground truth. The measured and reference ADC values can be found in Table 2.

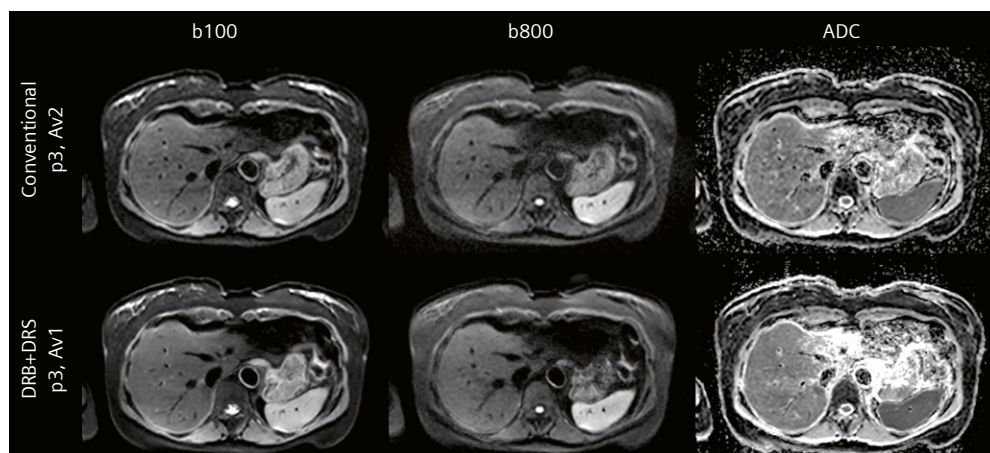
Volunteer study

Representative images of the volunteer scans using the original protocol with conventional reconstruction and the accelerated protocol with DRB+DRS reconstruction are shown in Figure 4 (brain), Figure 5 (liver), and Figure 6

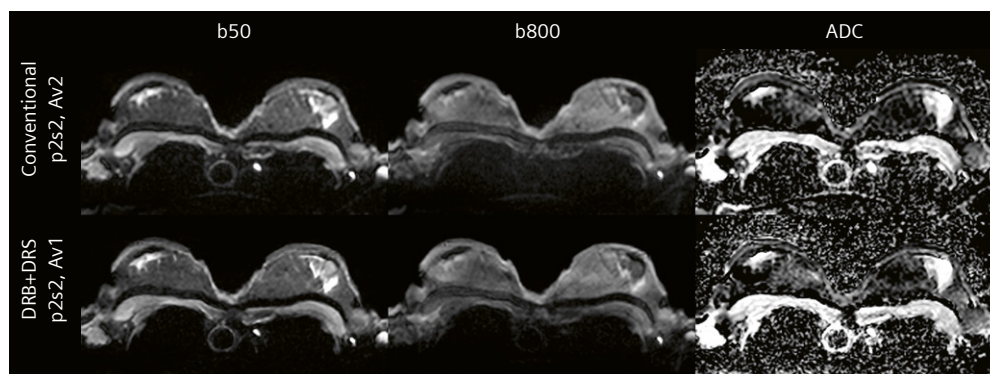
(breast). For all these body regions, DRB+DRS resulted in reduced noise, increased image sharpness, and a shorter acquisition time. The ADC maps do not show significant differences, which is consistent with the phantom results.



4 Representative DWI images (b0 and b1000) and corresponding ADC maps of the brain volunteer scan. Despite a scan time reduction of 40% (1:33 min to 0:56 min), DRB+DRS shows reduced noise and increased sharpness, while no bias is introduced in the ADC map.



5 Results of the liver volunteer scan (b100, b800, and ADC) showing the conventional protocol (conventional reconstruction) and the accelerated protocol (DRB+DRS reconstruction). Analogous to the brain scan, DRB+DRS improves the overall image quality and maintains the appearance of the ADC. Scan time was reduced by 25% (4:24 minutes to 3:18 minutes).



6 b50, b800, and ADC images of the breast volunteer scan showing a similar appearance of both b-value images and the ADC map with DRB+DRS, while the acquisition time is reduced by 32%, from 1:37 min to 1:06 min.

Conclusion

Our study showed that Deep Resolve Boost and Sharp for DWI does not influence ADC values. This holds true for different protocol settings typically applied in clinical contexts, including the use of different PAT factors, SMS, image resolutions, and the number of acquired averages. Therefore, consistent and non-biased ADC values are ensured when using DRB and DRS to accelerate and improve the image quality of DWI scans in different clinical scenarios.

References

- 1 Siemens Healthineers. Deep Resolve [Internet]. Erlangen, Germany: Siemens Healthcare GmbH [Accessed on March 20, 2023]. Available from: <https://www.siemens-healthineers.com/de/magnetic-resonance-imaging/technologies-and-innovations/deep-resolve>
- 2 Almansour H, Herrmann J, Gassenmaier S, Afat S, Jacoby J, Koerzdoerfer G, et al. Deep Learning Reconstruction for Accelerated Spine MRI: Prospective Analysis of Interchangeability. *Radiology*. 2023;306(3):e212922.
- 3 Kim EH, Choi MH, Lee YJ, Han D, Mostapha M, Nickel D. Deep learning-accelerated T2-weighted imaging of the prostate: Impact of further acceleration with lower spatial resolution on image quality. *Eur J Radiol*. 2021;145:110012.
- 4 Gassenmaier S, Afat S, Nickel D, Mostapha M, Herrmann J, Othman AE. Deep learning-accelerated T2-weighted imaging of the prostate: Reduction of acquisition time and improvement of image quality. *Eur J Radiol*. 2021;137:109600.
- 5 Herrmann J, Keller G, Gassenmaier S, Nickel D, Koerzdoerfer G, Mostapha M, et al. Feasibility of an accelerated 2D-multi-contrast knee MRI protocol using deep-learning image reconstruction: a prospective intraindividual comparison with a standard MRI protocol. *Eur Radiol*. 2022;32(9):6215–6229.
- 6 Herrmann J, Wessling D, Nickel D, Arberet S, Almansour H, Afat C, et al. Comprehensive Clinical Evaluation of a Deep Learning-Accelerated, Single-Breath-Hold Abdominal HASTE at 1.5 T and 3 T. *Acad Radiol*. 2023;30(1):93–102.
- 7 Shanbhogue K, Tong A, Smereka P, Nickel D, Arberet S, Anthopolos R, et al. Accelerated single-shot T2-weighted fat-suppressed (FS) MRI of the liver with deep learning-based image reconstruction: qualitative and quantitative comparison of image quality with conventional T2-weighted FS sequence. *Eur Radiol*. 2021;31(11):8447–8457.
- 8 Siemens Healthineers. Deep Resolve Boost [Internet]. Erlangen, Germany: Siemens Healthcare GmbH [Accessed on March 20, 2023]. Available from: <https://www.siemens-healthineers.com/de/magnetic-resonance-imaging/options-and-upgrades/clinical-applications/deep-resolve-boost>
- 9 Siemens Healthineers. Deep Resolve Sharp [Internet]. Erlangen, Germany: Siemens Healthcare GmbH [Accessed on March 20, 2023]. Available from: <https://www.siemens-healthineers.com/de/magnetic-resonance-imaging/options-and-upgrades/clinical-applications/deep-resolve-sharp>
- 10 Bae SH, Hwang J, Hong SS, Lee EJ, Jeong J, Benkert T, et al. Clinical feasibility of accelerated diffusion weighted imaging of the abdomen with deep learning reconstruction: Comparison with conventional diffusion weighted imaging. *Eur J Radiol*. 2022;154:110428.
- 11 Afat S, Herrmann J, Almansour H, Benkert T, Weiland E, Hölldobler T, et al. Acquisition time reduction of diffusion-weighted liver imaging using deep learning image reconstruction. *Diagn Interv Imaging*. 2022;S2211–5684(22)00220-0.
- 12 Lee EJ, Chang YW, Sung JK, Thomas B. Feasibility of deep learning k-space-to-image reconstruction for diffusion weighted imaging in patients with breast cancers: Focus on image quality and reduced scan time. *Eur J Radiol*. 2022;157:110608.



Contact

Hyun-Soo Lee, Ph.D.
MR Research Collaboration
Siemens Healthineers Ltd
SHS APJ KOR DI RC
14, Seocho-daero 74-gil
Seoul Teukbyeolsi 06620
Republic of Korea
hyunsoo.lee@siemens-healthineers.com



Thomas Benkert, Ph.D.
MR Application Predevelopment
Siemens Healthineers
SHS DI MR RCT PRM
Allee am Roethelheimpark 2
91052 Erlangen
Germany
benkert.thomas@siemens-healthineers.com

The Expanding Role of Deep Learning Reconstruction in Prostate MRI

Paulo Gil Agostinho¹, Ana Raquel Clemente¹, Filipe Caseiro Alves¹, Marcel Dominik Nickel³, Livia Sacchetto de Andrade², Marisa Gonçalves², Cristiana Araújo², André Barbosa²

¹Hospital da Luz, Coimbra, Portugal

²Siemens Healthineers, Portugal

³Siemens Healthineers, Erlangen, Germany

Introduction

Prostate cancer is one of the most prevalent oncological pathologies, with the highest incidence observed in Europe [1]. If death rates remain unchanged, the International Agency for Research on Cancer predicts that the burden will rise to 1.7 million new cases and 499,000 deaths by 2030 [1]. The primary diagnosis of this disease is based on prostate-specific-antigen (PSA) screening, and biopsy. Due to the low specificity of PSA screening (36%), false positives are commonly present in the results, as an elevated PSA does not necessarily indicate the presence of cancer [2, 3]. Furthermore, a normal value can neither exclude the presence nor the potential development of a tumor [2, 3].

Because prostate cancer is multifocal in almost 85% of cases [4], ultrasound-guided biopsy may underestimate the extent and grade of the tumor, which may result in an update of the Gleason score after prostatectomy [4]. Additionally, since prostate biopsy is not directed at any specific lesion, it can lead to reduced diagnostic accuracy, particularly in anterior prostate lesions and in lesions located in the apex. Finally, ultrasound biopsy has a negative predictive value (NPV) of 70 to 80%, which means that 20 to 30% of patients with a negative biopsy result may still have prostate cancer [5]. It has been observed that men with continuously high levels of PSA can have negative systematic results in biopsy [6, 7].

This means magnetic resonance imaging (MRI) plays a decisive role in prostate cancer diagnosis. It offers reliable visualization, which is potentially significant for prostate cancer diagnosis, and provides information for staging tumor extent, monitoring treatment response, and guiding focal therapies. MRI has also shown advantages in terms of improving the selection of patients who need to undergo biopsy, and facilitating the targeting of lesions during biopsy.

MRI is therefore an indispensable tool for detecting prostate cancer, especially in men with continuously high levels of PSA despite a negative systematic biopsy [6, 7]. With the huge growth in the volume of exams and the recent recommendations by the Council of the European Union to facilitate a more targeted and less invasive screening by using MRI as a follow-up for PSA screening, there is an urgent need to find a way to provide faster MRI examinations. Also, according to the guidelines on prostate cancer from the European Association of Urology, MRI scanning is strongly recommended before biopsy [8].

The increasing application of deep learning (DL) algorithms, such as convolutional neural networks (CNNs), offers fascinating prospects for the future of both MRI and medicine in general [9]. The use of DL techniques in MRI can help overcome several challenges by reducing acquisition times, increasing spatial and contrast resolution, and thereby improving the overall study quality [10].

The main objective of this study is to determine the role of DL reconstruction algorithms in prostate MRI examinations and their impact on clinical practice and prostate cancer diagnosis.

MRI technique

With conventional reconstruction methods, an acquisition can only be accelerated by accepting compromises between image resolution and signal-to-noise ratio (SNR). In general, acquisition speed, image resolution, and SNR are tightly linked and increasing one of the three automatically has a negative effect on at least one of the other two. The use of receive arrays and parallel imaging has been an important breakthrough in MR image reconstruction and is an essential part of clinical routine in MRI.

Parallel imaging, however, usually comes at the price of higher image noise, especially in regions far from the receiving coil elements. This results in inhomogeneous noise distribution, especially if high acceleration factors are used. In recent years, artificial intelligence (AI) technologies have made their appearance in various research applications and products. In particular, the use of deep neural networks has proven to be helpful when trying to address the limitations of conventional MR image reconstruction, even in routine 2D imaging. DL image reconstruction has the potential to tackle all three limiting factors of MR imaging simultaneously: image resolution, SNR, and acquisition speed [11].

With the introduction of DL reconstruction, convolutional networks were inserted into the image formation process, which now also involves image enhancement steps interleaved with conventional parallel imaging [12].

In DL reconstruction, the image reconstruction comprises a fixed iterative scheme or variational network, alternating between data consistency and a CNN-based regularization. The regularization model architecture is based on a novel hierarchical design of an iterative network that repeatedly decreases and increases the resolution of the feature maps, allowing for a more memory-efficient model than conventional CNNs.

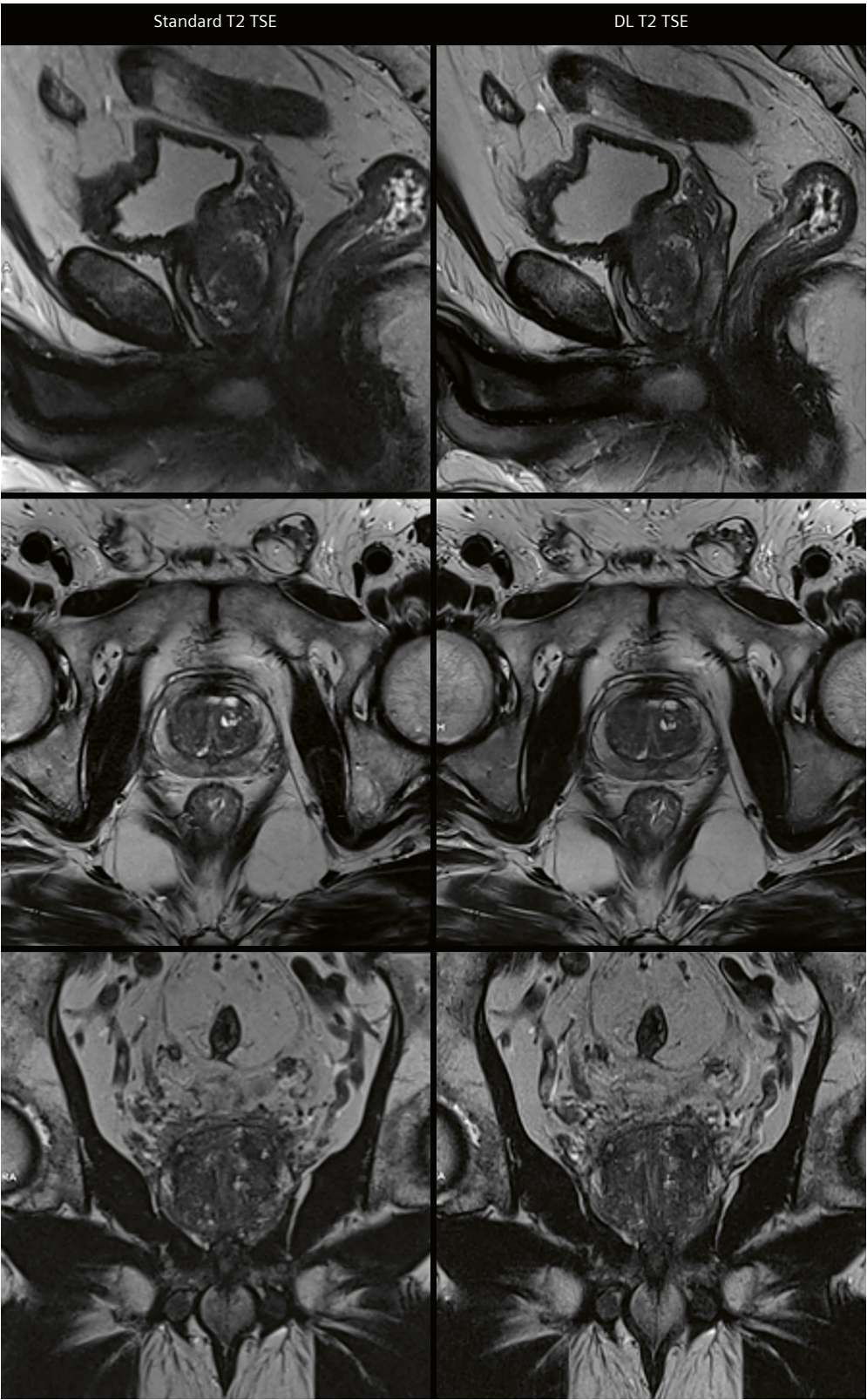
Coil sensitivity maps are estimated from the calibration data in advance as a pre-processing step. For image reconstruction, undersampled *k*-space data, bias field correction maps, and coil sensitivity maps are inserted into the variational network [13].

Materials and methods

A total of 67 patients with an average PSA of 6.3 ng/mL ([0.6;12.71] ng/mL) underwent a multiparametric prostate MRI examination in a clinical 3T scanner (MAGNETOM Vida, Siemens Healthcare, Erlangen, Germany) in supine position with an 18-channel body array and a 32-channel spine array. In addition to diffusion-weighted and dynamic contrast-enhanced sequences, we used two different T2-weighted sequences: One was the standard T2 turbo spin-echo (TSE) sequence and the other was a prototype of a DL-accelerated T2 TSE sequence, which the vendor, Siemens Healthineers, has since productized as Deep Resolve Boost TSE. Both sequences were used to acquire images in the three conventional orientations (transversal, sagittal and coronal). The average total time of acquisition was 10 minutes for the T2 standard sequence and 4:50 minutes for the DL T2 sequence (for detailed parameters, see Table 1).

Sequence	T2 TSE					
	Sagittal		Axial		Coronal	
Orientation Type	Standard	DL	Standard	DL	Standard	DL
Acquisition time (TA) (min:sec)	02:30	01:28	05:05	01:49	02:32	01:30
Field of view (FOV) (mm x mm)	150 x 100	160 x 100	180 x 100	180 x 100	160 x 100	160 x 100
Matrix size (mm)	224 x 320	222 x 320	269 x 384	269 x 384	224 x 320	224 x 320
Repetition time (TR) (msec)	6000	6290	8940	5950	6000	8060
Echo time (TE) (msec)	123	101	116	104	123	101
Slice thickness (mm)	3	3	3	3	3	3
Acceleration factor	2	2	2	3	3	2
Number of averages	2	1	3	1	2	1
Number of slices	28	29	38	35	27	28

Table 1: Acquisition parameters for the standard and DL T2 sequences.



1 Comparison between the standard T2 TSE (left) and DL T2 TSE (right) sequences. The DL sequence reduces the acquisition time by 52% and improves image quality.

Quantitative image analysis

We compared the two sequences in 67 patients in terms of acquisition time (Fig. 1), signal-to-noise ratio (SNR) (Fig. 2A), and contrast-to-noise ratio (CNR) (Fig. 2B) using the formulas

$$SNR = \frac{S_1}{s}$$

$$CNR = \frac{S_1 - S_2}{s}$$

where S_1 and S_2 are the average signal intensity measured in the regions of interest (ROIs), which were placed in the prostate peripheral zone and in the obturator internus muscle, respectively; and s is the standard deviation of the signal intensity of S_2 . The signal intensity of S_2 is the background noise, since the signal intensity of the obturator internus muscle is homogeneous and low.

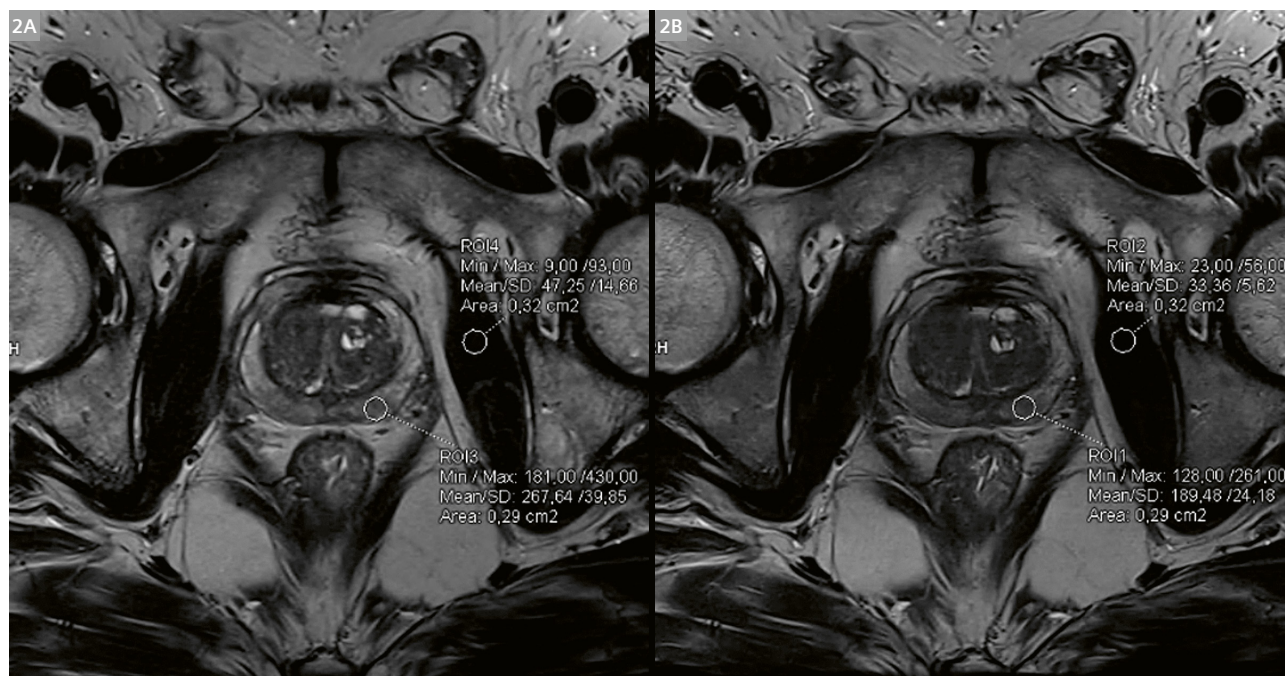
Qualitative image analysis

The image quality of the standard and DL T2 sequences was evaluated by a local radiologist, who compared the images in four anatomical regions of the prostate

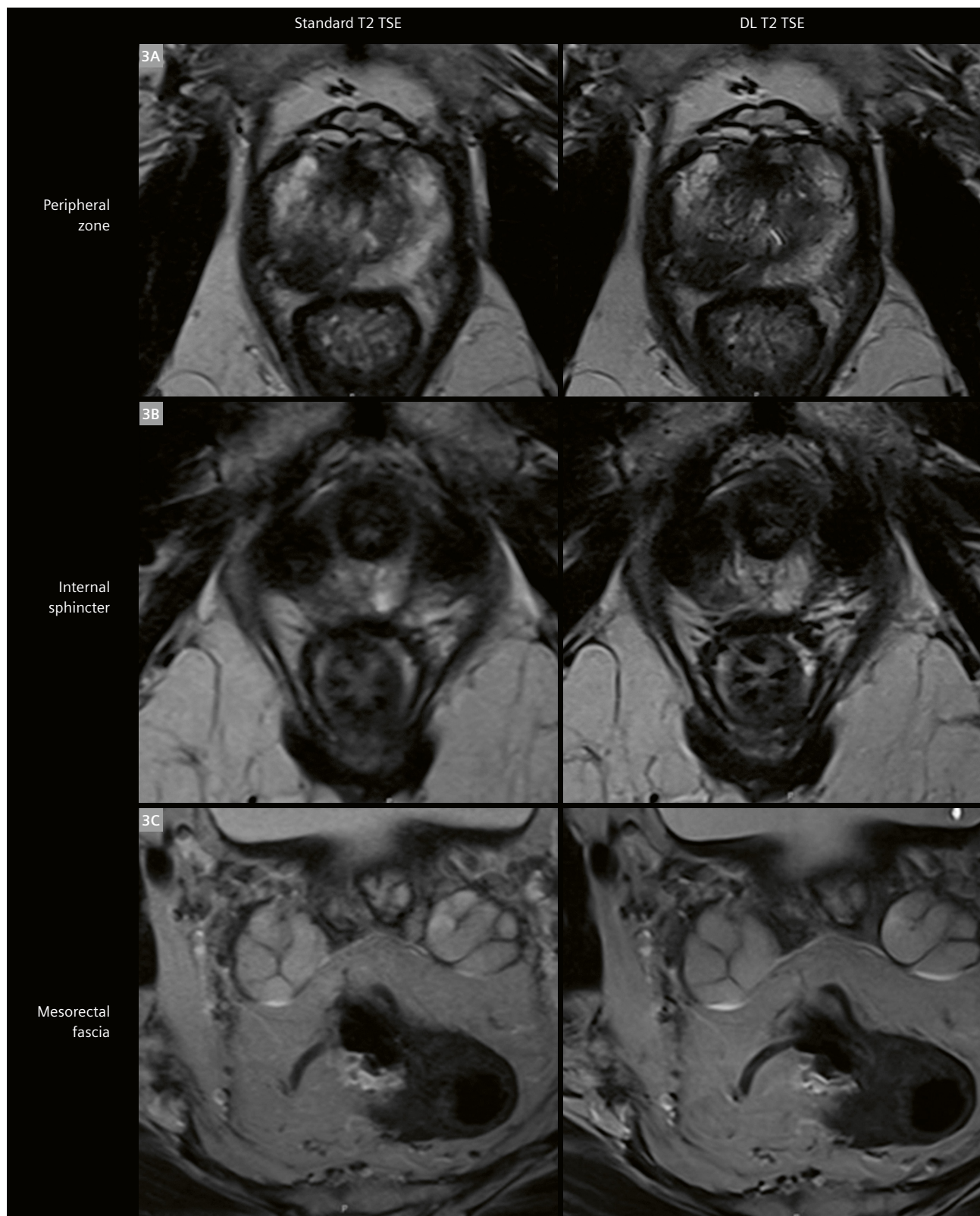
(peripheral zone, internal sphincter, mesorectal fascia, prostatic capsule, and peripheral prostatic lesion) and the presence of lesion. The image quality was rated using a 5-point Likert scale.

Results

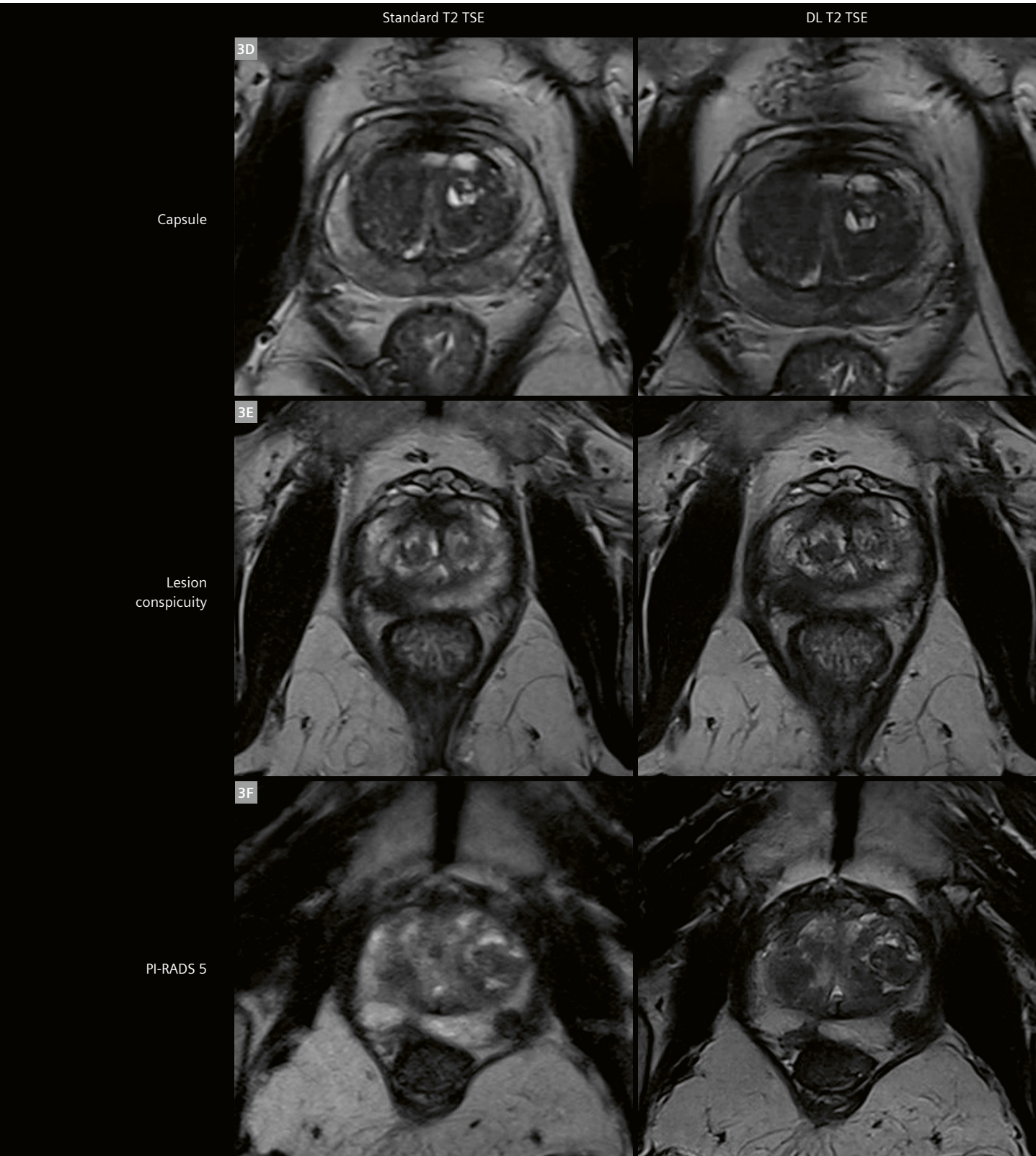
The DL TSE T2 sequence was successfully used in all 67 cases and was compared with the standard T2 TSE sequence in terms of acquisition time, SNR, and CNR. The acquisition time difference between the two sequences (with and without the DL algorithm) was evident, with the DL sequence showing a significant reduction in 97% of the cases. In 40 cases, we observed a 70% reduction; in 25 cases, the time reduction was greater than 65%; in the remaining two cases, we observed a roughly 50% reduction in acquisition time. It is also worth mentioning that the time needed to plan the sequence was also reduced when using the DL sequence, since there was no need to adjust the number of slices in 63% of the cases. By contrast, the number of slices needed to be adjusted in 66% of the cases when using the standard sequence. This is because the DL sequence allows a larger predefined number of slices while maintaining a short scan time, which proved to be adequate for patients with enlarged prostates. In the DL-sequence images, both the SNR and CNR were



2 Evaluation of SNR and CNR using the average signal intensity of ROIs placed in the peripheral prostate and in the obturator internus muscle. (2A) Standard T2: SNR = 19.1, CNR = 15.7; (2B) DL T2: SNR = 33.7, CNR = 27.7



3 Standard T2 TSE versus DL T2 TSE in the peripheral zone (3A), internal sphincter (3B), mesorectal fascia (3C), prostatic capsule (3D), and focal lesion conspicuity (3E), PI-RADS score (3F).



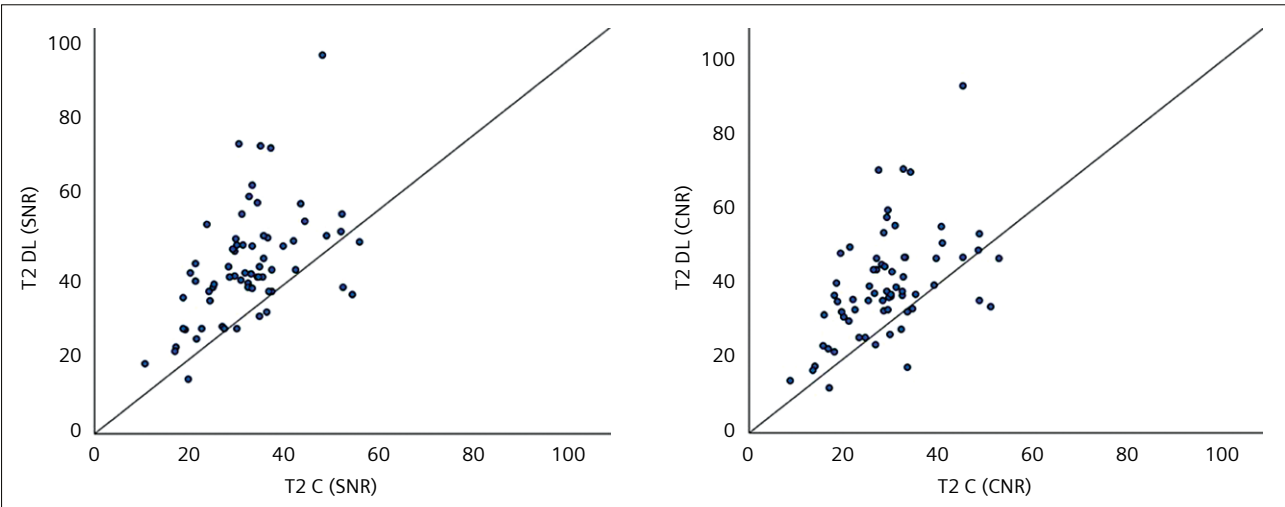
higher in most of the cases, with SNR being higher in 90% of them and CNR in 88%. In very few cases, the DL images presented lower SNR and CNR than the standard images. This can be explained by previously diagnosed prostatitis, a clinical condition known to correlate with low signal in the prostatic peripheral zone.

The quantitative and qualitative results of the comparison between the standard and the DL sequences are summarized in Table 2. The positive difference in median values of SNR and CNR shows a quantitative increase in image quality of the DL sequence, which can be achieved with significantly shorter TA, as shown by the negative median TA difference. Moreover, repeated measurements of SNR, CNR, and TA are moderately and positively correlated (respectively, $r_s = 0.527$, $r_s = 0.510$, and $r_s = 0.418$). In addition, there was a median increase of one Likert point in favor of the DL sequence, related to the identification of each of the five characteristics evaluated for attaining lesion conspicuity, ($p < 0.001$ for each of the five comparisons).

The image quality of the DL sequence was consistently evaluated as being equal to or better than the standard sequence in all anatomical areas. In the peripheral zone, it was considered to have better image quality in 85% of the cases; in the internal sphincter, this was 61%; in the mesorectum, 43%; and in the prostatic capsule, 79%. In the remaining cases, the image quality of the DL sequence was considered to be the same as that provided by the standard sequence.

	Median difference (DL-Std)	p-value
SNR	9.71	< 0.001
CNR	7.14	< 0.001
TA (seconds)	-211	< 0.001
Peripheral prostate	1	< 0.001
Internal sphincter	1	< 0.001
Mesorectal fascia	1	< 0.001
Prostatic capsule	1	< 0.001
Peripheral prostate lesion	1	< 0.001

Table 2: Comparison of results from the standard (Std T2) and deep learning (DL T2) sequences. There is an increase in SNR of 9.71 (IQR (interquartile range): [3.71; 19.01]; $p < 0.001$) and in CNR of 7.14 (IQR: [1.80; 16.89]; $p < 0.001$), a median decrease of 211s (IQR: [186; 236]; $p < 0.001$) in the time of acquisition, corresponding to a reduction of 70.3%, when using the DL sequence. Median difference refers to the image quality evaluation (Likert scale) in the regions evaluated between the DL and standard sequences. All regions present are rated one point higher when using the DL sequence. Statistical analysis: Wilcoxon matched-pairs test. Association between standard T2 and DL T2 was analyzed using Spearman's rank-order correlation. Statistical tests were evaluated at a 5% significance level. Analysis was performed in SPSS Statistics, version 27 (IBM, Armonk, New York, USA).



4 Distribution of SNR and CNR of the DL sequence (T2 DL) against the standard sequence (T2 C). The DL sequence yielded higher SNR and CNR values for most measurements.

Additionally, since 47 cases had lesions in the peripheral zone, the signal intensity in the lesions was compared for the two sequences. Here, the DL sequence showed higher signal intensity in the lesion in 53% of the cases, equal signal intensity in 42%, and lower signal intensity in 4%.

Discussion

Deep learning reconstruction is a very active field of research and is currently being translated into clinical practice. It shows great potential for the future of MR imaging, including denoising and artifact reduction [10]. Most importantly, faster and better MRI will make prostate cancer screening more efficient by enabling a more accurate diagnosis and reaching a broader population.

Deep learning reconstruction of T2 TSE in the prostate enabled an extraordinary reduction in acquisition time, while improving or maintaining SNR and CNR. The overall image quality was also improved in different anatomical regions such as the peripheral zone, internal sphincter, mesorectal fascia, and prostatic capsule. This was in addition to an improvement in the identification of peripheral zone lesions.

References

- 1 International Agency for Research on Cancer. European Urology – International Variation in Prostate Cancer Incidence and Mortality Rates [Internet]. Lyon, France: International Agency for Research on Cancer; 2012 [Accessed on May 3, 2023]. Available from: <https://www.iarc.who.int/news-events/european-urology-international-variation-in-prostate-cancer-incidence-and-mortality-rates/>
- 2 Barentsz JO, Richenberg J, Clements R, Choyke P, Verma S, Villeirs G, et al. ESUR Prostate MR guidelines 2012. *Eur Radiol.* 2012;22(4):746–757.
- 3 Hambrock T, Somford DM, Hoeks C, Bouwense SA, Huisman H, Yakar D, et al. Magnetic resonance imaging guided prostate biopsy in men with repeat negative biopsies and increased prostate specific antigen. *J Urol.* 2010;183(2):520–527.
- 4 Bonekamp D, Jacobs MA, El-Khouli R, Stoianovici D, Macura KJ. Advancements in MR imaging of the prostate: from diagnosis to interventions. *Radiographics* 2011;31(3):677–703.
- 5 Ahmed HU, Kirkham A, Arya M, Illing R, Freeman A, Allen C, et al. Is it time to consider a role for MRI before prostate biopsy? *Nat Rev Clin Oncol.* 2009;6(4):197–206.
- 6 Sonn GA, Chang E, Natarajan S, Margolis DJ, Macairan M, Lieu P, et al. Value of targeted prostate biopsy using magnetic resonance-ultrasound fusion in men with prior negative biopsy and elevated prostate-specific antigen. *Eur Urol.* 2014;65(4):809–815.
- 7 Hoeks CM, Schouten MG, Bomers JG, Hoogendoorn SP, Hulsbergen-van de Kaa CA, Hambrock T, et al. Three-Tesla magnetic resonance-guided prostate biopsy in men with increased prostate-specific antigen and repeated, negative, random, systematic, transrectal ultrasound biopsies: detection of clinically significant prostate cancers. *Eur Urol.* 2012;62(5):902–909.
- 8 European Association of Urology. Prostate Cancer [Internet]. Arnhem, the Netherlands: European Association of Urology; 2023 [Accessed on May 3, 2023]. Available from: <https://uroweb.org/guidelines/prostate-cancer>
- 9 Kim J, Hong J, Park H. Prospects of deep learning for medical imaging. *Precis Futur Med.* 2018;2(2):37–52.
- 10 Suzuki K. Overview of deep learning in medical imaging. *Radiol Phys Technol.* 2017;10(3):257–273.
- 11 Behl N. Deep Resolve – Mobilizing the Power of Networks. *MAGNETOM Flash.* 2021;78(1):29–35. https://marketing.webassets.siemens-healthineers.com/2efe552ddbfa9372/3bcd31c7597b/Behl_DeepResolve_MAGNETOM_Flash_78_ISMRM_2021.pdf
- 12 Mulé S, Massire A, Zerbib P, Nickel D, Luciani A. Fast and Reliable Liver Imaging Using Deep Learning HASTE. *MAGNETOM Flash.* 2021;79(2):28–31. https://marketing.webassets.siemens-healthineers.com/64a9a07fa3ff23f6/2a243add4eb7/MAGNETOM_Flash_79_RSNA_2021.pdf
- 13 Herrmann J, Lingg A, Kündel M, Gassenmaier S, Afat S, Al-Mansour H, et al. Clinical Implementation of Deep Learning Accelerated HASTE and TSE. *MAGNETOM Flash.* 2021;70(2):23–27. https://marketing.webassets.siemens-healthineers.com/be50dfa900db3e9f/b495fd2d0a32/Othman_Herrmann_DL-HASTE_TSE_RSNA-2021.pdf



Contact

Filipe Caseiro Alves, M.D., Ph.D.
Hospital da Luz Coimbra
Praceta Robalo Cordeiro, 1
3020-479 Coimbra
Portugal
luis.caseiro.alves@hospitaldaluz.pt



Paulo Gil Agostinho, M.D.
Hospital da Luz Coimbra
Praceta Robalo Cordeiro, 1
3020-479 Coimbra
Portugal
paulo.gil.agostinho@hospitaldaluz.pt

Expert Insights: Hidden Gems from Application Specialists at Siemens Healthineers

Cristiana Araújo on Append Table Positioning Strategy

Cristiana is curious and loves learning and sharing new knowledge. She is passionate about both healthcare and teaching, so she made it her mission to help improve patient outcomes by teaching healthcare professionals to get the most out of their MRI scanners.

Her journey into medical imaging started in 2004, when she enrolled in a bachelor's of diagnostic radiology at the School of Allied Health Sciences in Porto, Portugal. In 2011, her pursuit for deeper knowledge led her to enroll in an M.Sc. in medical physics at the University of Porto, Portugal. She joined Siemens Healthineers in 2020, embarking on a career in MR as an application specialist. Two years later, she was one of the first application specialists to test the first installation of MAGNETOM FREE.Star. A year after that, she came fifth in the ECR 2023's influencers list, and she has just enrolled in an MR master's program. You might think Cristiana is all about MRI, but she is not one to settle for a single love. In 2020, while working as a radiographer, she boldly took on a new challenge and started an M.Sc. in dentistry, at University Fernando Pessoa in Porto, Portugal.

Outside of work, she loves immersing herself in stories (her personal record is over 200 books in one year). She is also a music lover, adores spending times with friends, and is a devoted mother.

Contact

Cristiana Araújo
SHS EMEA SEU POR S&PSM-DI&AT&US DI&AT
3570, Estrada Nacional 107
4455-491 Porto
Portugal
cristianasantos_machado_araujo@siemens-healthineers.com



My favorite feature ...

... is currently an equipment functionality. I always make sure I explain it to users who have a system that runs on software version syngo MR XA20. It's called Append Table Positioning Strategy.

This amazing new option for Positioning Mode provides the following benefits:

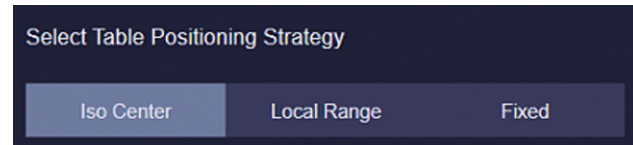
- It greatly reduces the risk of the radiographers selecting the wrong positioning mode. So it prevents non-intentional acquisition outside the center of the bore.
- It provides smoother scanning transition between structures, even using volume coils like a head and neck coil, or a surface coil like the spine coil.

The new Table Positioning Strategy focuses on the whole scan instead of a single protocol, so it's possible to make changes while using the workflow. There are three Positioning Strategy options: ISO, LOC, and FIX.

1. Click the right mouse button in your protocol and select "Append Table Positioning Strategy".

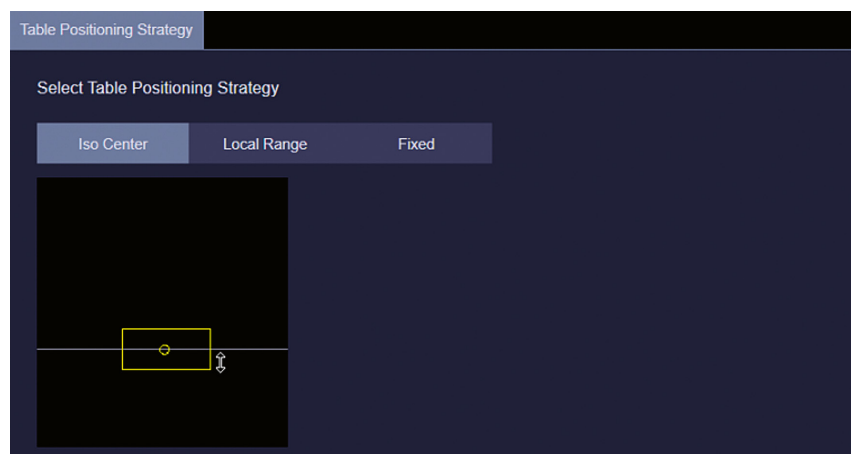
Brain Dot Engine			▶ LOC	⋮	+
1	AAhead_scout	00:19			
2	t1_se_sag	03:07			
3	t2_tse_tra_512	03:37			
4	t2_tse_dark-fluid_tra	04:50			
5	resolve_4scan_trace_tra_p2_150	02:50			
6	t1_se_tra		Append Pause...	Ctrl+Insert	
7	inject contrast agent		Append Table Positioning Strategy		
8	t1_se_tra		Paste	Ctrl+V	
9	t1_se_cor		Clear All	Shift+Del	
			Save as...	Ctrl+S	

2. In the user guidance card of the Table Positioning Strategy, the currently selected positioning strategy is highlighted.



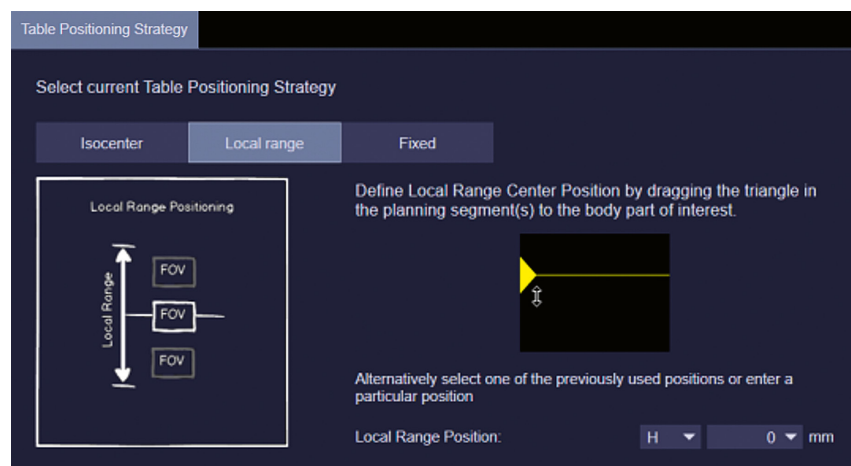
ISO: ISO Center Mode (spine, liver, or pelvis)

The protocol table position is like the scan region center: Whenever a slice group is moved, the table moves to the position of the isocenter for the best image quality.



LOC: Local Range Mode (head, knee, or heart)

The LOC positioning strategy is based on an examination-specific tolerance area and a focus position defining the center of the tolerance area. Slice groups within the tolerance area are measured without repositioning the patient table.



FIX: Fixed Position Mode

The table will not move during the examination. It remains in a fixed position even if the slice/slab group is placed outside the isocenter.

Imaging of the Musculoskeletal System Using 0.55T MRI

Tobias Pogarell; Rafael Heiss, M.D., MHBA

Institute of Radiology, University Hospital Erlangen, Erlangen, Germany

Introduction

When magnetic resonance imaging (MRI) found its way into musculoskeletal imaging in the 1980s, low field strengths in the range of 0.05 to 0.35 Tesla were initially used. Due to the limited image quality, which hampered reliable clinical diagnoses, these devices could not establish themselves permanently in everyday clinical use. Technological developments in MRI systems mean that, nowadays, clinical routine is characterized almost exclusively by high-field systems with field strengths of 1.5T and 3T [1]. In musculoskeletal imaging, these offer the advantage of potentially better image quality than low-field MRI systems due to better contrast, higher resolution, and shorter measurement times. However, some studies have shown that higher field strengths do not automatically lead to an improvement in diagnostic significance, rather it is primarily dependent on the experience of the radiologist reading the image [2]. Nevertheless, the market share of MRI devices < 1.5T has decreased sharply over the last decades, from about 30% in 2000 to about 5% today [3]. However, the increase in field strength in musculoskeletal MRI also has some drawbacks. In addition to the increased acquisition and maintenance costs, high-field MRI systems potentially also require considerable constructional expenditure to maintain the building statics and to shield the magnetic field. In addition, with high-field MRI systems and especially with ultrahigh-field MRI systems at 7T, increased attention must be paid to safety when examining patients with medical implants¹ [4, 5].

Modern low-field MRI systems may increase measurement capacities in the future, due to their lower costs, e.g., for acute traumatological diagnostics. As a consequence of their simpler installation, low-field MRI devices also have the potential to diagnose musculoskeletal disorders on a wider scale, away from specialized centers [1].

At the University Hospital Erlangen, we have been using a modern 0.55T MRI scanner with a superconducting

magnet (MAGNETOM Free.Max; Siemens Shenzhen Magnetic Resonance Ltd., Shenzhen, China) in clinical routine since November 2020. The device enables a wide range of applications for a variety of anatomical locations. Very limited data is available on the diagnostic quality of musculoskeletal imaging performed on such modern low-field devices with state-of-the-art hardware and software. In general, publications on musculoskeletal imaging using low-field MRI systems are several decades old [6]. Therefore, this article aims to provide an overview of the existing studies of conventional low-field MRI devices and of our own experiences with a modern 0.55T whole-body MRI scanner in musculoskeletal imaging.

Low-field MRI

In low-field MRI, essentially two types of devices exist for the diagnosis of musculoskeletal disorders: Permanent magnet systems and superconducting systems. Permanent magnet systems are typically C-shaped, with an open configuration. In addition, portable scanners with permanent magnets are available for dedicated extremity imaging. Advantages of permanent magnets include their durability and low power consumption. Disadvantages are complex correction processes (i.e., shimming) to achieve homogeneity of the magnetic field, and the often very heavy weight of the magnets [3, 7].

Superconducting low-field MRI scanners, on the other hand, are based on the same principle as the corresponding high-field devices. The lower field strength and the material savings in the magnet design reduce acquisition and operating costs² [4]. Regardless of the specific scanner design, low magnetic field strengths generally result in reduced signal-to-noise ratio (SNR) and image quality per image acquisition time [8]. New software-based image reconstruction methods such as iterative image

¹The MRI restrictions (if any) of the metal implant must be considered prior to patient undergoing MRI exam. MR imaging of patients with metallic implants brings specific risks. However, certain implants are approved by the governing regulatory bodies to be MR conditionally safe. For such implants, the previously mentioned warning may not be applicable. Please contact the implant manufacturer for the specific conditional information. The conditions for MR safety are the responsibility of the implant manufacturer, not of Siemens Healthineers.

²The statements by Siemens Healthineers' customers described herein are based on results that were achieved in the customer's unique setting. Since there is no "typical" hospital and many variables exist (e.g., hospital size, case mix, level of IT adoption) there can be no guarantee that other customers will achieve the same results.

reconstruction or reconstruction methods based on artificial intelligence have the potential to increase SNR or reduce measurement time while maintaining image quality [4]. These advances could enable reasonable examination times for diagnostically fully adequate image quality of the musculoskeletal system even at low field strength. Thus, the technical advantages of low field strengths can be exploited for musculoskeletal imaging. Reduced susceptibility artifacts at air–tissue interfaces potentially allow for better imaging of geometrically difficult regions, such as the cervical spine [9]. Lower field strengths also result in fewer susceptibility artifacts near metal implants¹. Another advantage is the longer wavelength of the HF pulse in low-field MRI, which leads to more homogeneous illumination in many cases.

An important disadvantage of MR imaging of the musculoskeletal system at lower field strengths is the smaller difference in the resonance frequencies of fat and water. Conventional low-field scanners have difficulties separating the overlap of these two peaks. As a result, homogeneous spectral fat saturation was often impossible [10]. It was usually necessary to resort to other fat-suppression sequences, such as STIR (short TI inversion recovery) or Dixon, which are often inferior to spectral fat saturation in terms of image quality. This technical limitation seems to have been overcome with the latest generation of low-field MRI scanners. Our initial experience shows very reliable spectral fat suppression of the musculoskeletal system (Fig. 1). This is achieved by optimized

HF pulses in our 0.55T scanner. Table 1 provides a broad overview of the general advantages and disadvantages of low-field MRI in musculoskeletal imaging.



1 MRI at 0.55T of the knee of a 65-year-old patient with persistent knee pain. The coronal proton-density-weighted image with spectral fat saturation shows a complex tear of the medial meniscus with fluid along the medial collateral ligament, a full thickness loss of the cartilage at the medial femur and the medial tibia, and bone marrow edema in the medial tibia. The sequence parameters are provided in Table 2.

Advantages	Disadvantages
Technical considerations	
<ul style="list-style-type: none">• Lower susceptibility at air–tissue interfaces or with medical implants¹ such as orthopedic prostheses• Increased magnetic field homogeneity when imaging geometrically challenging regions such as the cervical spine in adipose patients	<ul style="list-style-type: none">• Low SNR, problematic when encountering small contrast differences in fat-saturated sequences• Low resolution, e.g., in small anatomical structures• Longer acquisition times resulting in potential motion artifacts• Difficulties in spectral fat saturation due to minimal differences in fat and water resonance frequencies
Clinical use	
<ul style="list-style-type: none">• Acute trauma in large joints or the spine, e.g., fractures, contusions, and ligament injuries• Degenerative and inflammatory spinal pathologies• Oncological musculoskeletal diagnostics• Imaging of implants, e.g., diagnosing recurrence of soft-tissue tumors around tumor prostheses	<ul style="list-style-type: none">• Possibly insufficient spatial resolution when examining small peripheral joints such as fingers or wrists• Resolution of small pathologies, e.g., clarification of chronic knee pain (cartilage, meniscus), traumatic injury following shoulder luxations and chronic shoulder pain (Bankart and SLAP lesions)
Socioeconomic aspects	
<ul style="list-style-type: none">• Lower acquisition cost• Lower maintenance cost²• Lower cost per examination²• Possible increase in MRI availability	<ul style="list-style-type: none">• Need to select patients according to the underlying medical issue, no stand-alone installations• Reduced throughput of patients• Potential re-examination using high-field scanners when results are inconclusive

Table 1: Potential advantages and disadvantages of low-field MRI in musculoskeletal imaging

Metal artifacts

A wide variety of materials including metal and metal alloys are used in orthopedic and trauma surgery procedures. Postoperative evaluation often requires reliable imaging of the adjacent soft tissues. The spectrum of conditions to be clarified includes prosthesis infections, prosthesis loosening, and local recurrence after resection of soft-tissue tumors with bridging osteosynthesis. Since metals cause signal cancellation, pronounced artifacts, and a reduction of soft-tissue contrast in their immediate vicinity in MRI, these indications present a particular challenge [11]. However, the susceptibility effects are much less pronounced at low field strengths [3]. This improves the general image quality and especially the periprosthetic and periosteosynthetic image quality. As a result, infections or tumor recurrences adjacent to a prosthesis could become diagnosable in some cases. Lower-field systems therefore have the potential to improve MR imaging of metallic foreign bodies and their vicinity [1].

In a small feasibility study in 2020, Schröder et al. examined eight patients with complications after total knee arthroplasty using a 0.25T scanner (G-scan Brio; Esaote SpA, Genoa, Italy). A radiologist assessed the fixation of the prosthesis and the surrounding structures (bones, tendons, ligaments, and muscles). MRI findings were compared with clinical examination results, computed tomography, and intraoperative revision findings. In most cases, the MRI findings were consistent with the findings of the clinical examination and the intraoperative findings. In all cases, the MRI findings provided comparable results to the diagnosis by computed tomography [12].

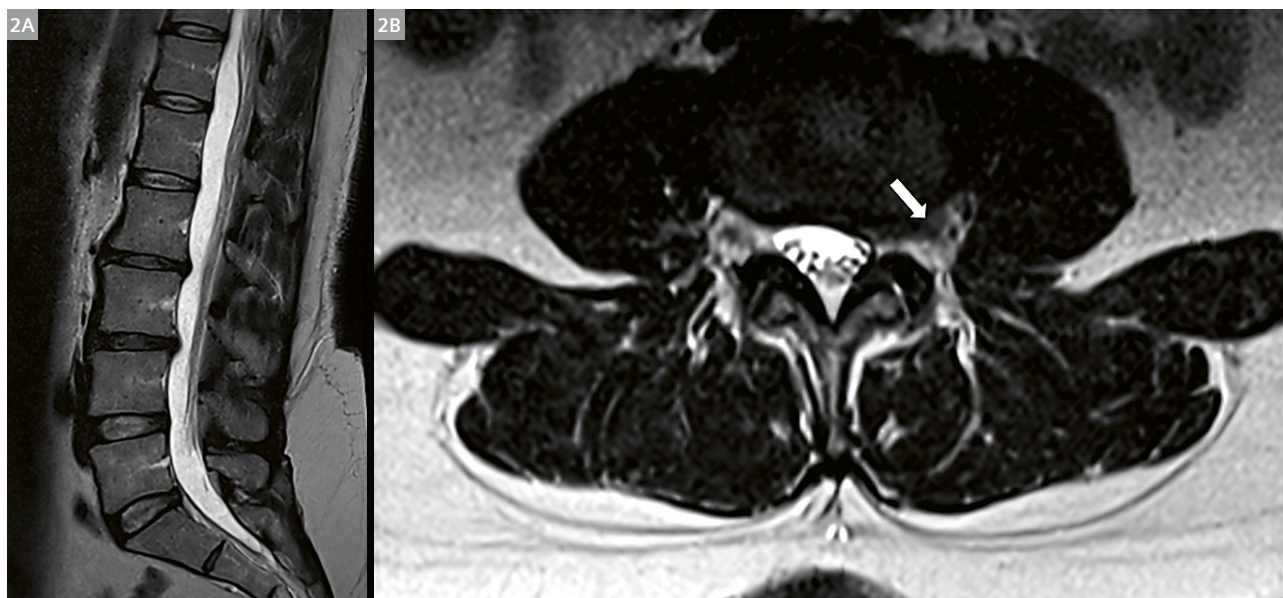
Spine

Thanks to further developments in the design of receiver coils, and to the development of multichannel coils, it is now possible to perform diagnostic examinations of the entire spine at low-field MRI [3]. In 2015, Lee et al. examined 100 patients with neurogenic claudication or sciatica at 0.25T (G-scan; Esaote, Genoa, Italy) and either 1.5T or 3T. There was very good agreement between the low-field and high-field scanners for the diagnosis of degenerative changes of the lumbar intervertebral discs, and good agreement for the diagnosis of nerve root compression. However, the 0.25T examinations were more prone to motion artifacts, most likely due to longer measurement times [13].

In a current statement on lower back pain published by the American College of Radiology, MRI is suggested as the initial imaging modality for persistent lower back pain over a six-week period in patients with cauda equina syndrome, and as first-line imaging in suspected tumor disease or infection [14]. In our experience, these questions, which often require urgent clarification in daily routine, can be answered reliably with state-of-the-art low-field devices (Fig. 2).

Shoulder

The combination of MRI and arthrography is considered the gold standard for evaluating shoulder-joint pathologies such as labral tears and Bankart lesions [15]. In an older study (1999), Loew et al. compared MR arthrography of the shoulder at 0.2T (MAGNETOM Open, Siemens



2 MRI at 0.55T of the lumbar spine of a 44-year-old patient with persistent lower back pain. T2-weighted sagittal (2A) and transversal (2B) images show subligamentous herniations of the intervertebral discs L2–L4. The extraforaminal spinal nerve L4 on the left side is in contact with the herniated disc (arrow). The sequence parameters are provided in Table 2.

Healthcare, Erlangen, Germany) and 1.5T. For this purpose, 38 patients with suspected chronic instability ($n = 12$) or rotator cuff injury ($n = 26$) were examined in a random order at 0.2T and 1.5T by MR arthrography. Surgical correlation was possible in 27 of the 38 patients. There was good agreement between the two scanners in the detection of labral injuries and very good agreement in the detection of complete rotator cuff tears. Again, a disadvantage of low-field imaging was the longer measurement time, resulting in an increased risk of motion artifacts [16].

In a more recent retrospective study (2014), Lee et al. evaluated the diagnostic accuracy of native shoulder images at 0.2T (E-scan Opera; Esaote, Genoa, Italy). For this, MR findings from 79 patients were compared with results obtained arthroscopically within an average of 56 days of MR imaging. Good results were shown for the diagnosis of partial and complete rotator cuff tears. However, this was not the case for superior labrum anterior and posterior (SLAP) injuries [17].

Elbow

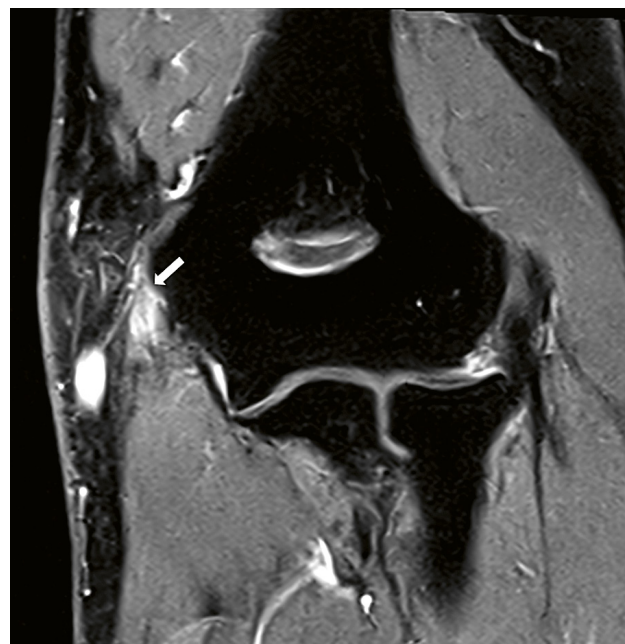
MRI is also generally established for the evaluation of the elbow joint. Many injuries ranging from acute trauma to chronic repetitive overuse, such as from tennis or baseball, involve the ligaments and tendons [18].

In a 2015 study, Okamoto et al. investigated the potential of low-field MRI in the early detection of baseball-associated elbow injuries. Asymptomatic baseball-playing children aged 9 to 12 years ($n = 62$) with a history of elbow pain at the time of the MRI scan were examined with a 0.2T extremity scanner (C-scan; Esaote, Genoa, Italy). Irritation and distension of the ulnar collateral ligament were detected in a large proportion of patients ($n = 26$, 41.9%) [19]. From this, the authors found the use of low-field MRI to be appropriate for early detection of elbow injuries. Furthermore, our experience with a 0.55T MRI scanner shows that, in addition to diagnosing ligamentous

injuries of the elbow, examinations for detecting epicondylopathy or fractures are also possible with good image quality (Fig. 3).

Wrist

A suspected fracture of the scaphoid bone is a diagnostic and therapeutic challenge. The proportion of true fractures among suspected diagnoses is low [20]. However, unrecognized scaphoid fractures and delayed treatment are often associated with complications such as avascular



3 MRI at 0.55T of the elbow of a 57-year-old patient with medial elbow pain. The T1-weighted fat-saturated image shows contrast enhancement at the common flexor tendon group of the elbow (arrow), indicating a medial epicondylitis (also known as golfer's elbow). The sequence parameters are provided in Table 2.

Examination		TE, ms	TR, ms	TA, min	Resolution, mm
Knee	PD TSE FS cor	23	3130	03:36	0.3 × 0.3 × 3.0
Lumbar spine	T2 TSE sag	122	4840	04:07	0.5 × 0.5 × 4.0
	T2 TSE tra	95	3800	05:34	0.6 × 0.6 × 4.0
Elbow	T1 TSE FS cor	16	520	04:20	0.3 × 0.3 × 3.0
Hand	T1 TSE cor DRB SMS	14	500	03:20	0.3 × 0.3 × 2.5
	T2 TSE STIR cor DRB SMS	120	3050	05:11	0.4 × 0.4 × 2.5
Ankle joint	PD TSE tra	24	2800	03:07	0.2 × 0.2 × 3.0
	PD TSE parasagittal	24	2800	04:42	0.4 × 0.4 × 2.0

Table 2: Sequence parameters of the displayed images at 0.55T

TE, echo time; TR, repetition time; TA, acquisition time; TSE, turbo spin echo; tra, transversal; cor, coronal; sag, sagittal; PD, proton density; FS, fat saturated; DRB, Deep Resolve Boost; SMS, Simultaneous Multi-Slice; STIR, short tau inversion recovery

necrosis and the development of pseudarthrosis [15]. Thus, a highly sensitive and widely available tool for reliably diagnosing scaphoid fractures is critical. In contrast to the low sensitivity of conventional radiographs in detecting scaphoid fractures, MRI can differentiate occult fractures from bone bruises, detect ligament injuries, and reveal avascular necrosis [15]. In a study from 2003, Brydie et al. examined 195 patients with suspected scaphoid fractures and unremarkable radiographic findings with a 0.2T extremity scanner (Artoscan; Esaote, Genoa, Italy). Scaphoid fractures were seen in 37 patients (19%), fractures of the distal radius in 28 (14%), and fractures of other wrist bones in 9 (5%). Thus, low-field MRI enabled early definitive diagnoses of wrist fractures or their definite exclusion, and subsequently changed the patient's treatment in 92% of cases [21].

From our experience, this suitability of low-field MRI for diagnosing therapeutically relevant fractures of the carpal bones can also be transferred to modern 0.55T MRI. In contrast to fracture diagnoses, imaging of small anatomical structures such as the intrinsic ligaments of the wrist and the triangulated fibrocartilaginous complex is not suitable in our opinion, due to the reduced SNR. These types of examinations should preferably be performed on scanners with higher field strengths.

Hand

In a study published in 2004, Crues et al. investigated the sensitivity of a portable low-field extremity scanner

(0.2T MagneVu 1000; MagneVu, California, USA) in detecting erosions in the wrist and metacarpophalangeal joints of 132 patients (95% of whom had rheumatoid arthritis) compared to the findings on conventional radiographs. The results showed better sensitivity of MRI, which identified erosions in 125 patients (95%) compared with 78 (58%) on conventional radiography [22].

In addition to the detection of erosions, we have found that low-field MRI also allows the detection of other inflammatory joint changes such as osteitis, synovitis, and tenosynovitis (Fig. 4). However, comparative studies between low-field and high-field scanners are required to further classify the diagnostic quality of low-field images in patients with rheumatologic diseases, especially with regard to the detection of small erosions.

Knee

MRI is widely established for diagnosing both acute and chronic injuries of the knee [15]. Meniscal and cruciate ligament tears are typical examples of indications for MRI of the knee. Some studies have investigated the diagnostic accuracy of low-field versus high-field MRI in meniscal and anterior cruciate ligament (ACL) tears [8]. A study by Vellet et al. (1995), which investigated the diagnostic accuracy of ACL tears at 0.5T (90%; Signa, GE Medical Systems, Milwaukee, USA) and 1.5T (91%), found no significant difference between field strengths [23]. In 2000, Cotten et al. also found no significant differences in sensitivity and specificity between 0.2T (MAGNETOM Open; Siemens



4 MRI at 0.55T of the hand of a 77-year-old patient with rheumatoid arthritis. Coronal T1-weighted (**4A**) and T2-weighted STIR (**4B**) images show erosions at the metacarpophalangeal joint 2 (arrows), and synovitis at the metacarpophalangeal joint 2 and 3, and at the interphalangeal joint 4 (arrowheads). The sequence parameters are provided in Table 2.

Healthcare, Erlangen, Germany) and 1.5T MRI scanners in 90 patients with surgically confirmed meniscal and ACL tears [24]. A review by Puig et al. (2015) also found no difference in diagnostic accuracy for the evaluation of meniscal and ACL tears between low- and high-field devices. However, this was not true for the evaluation of cartilage defects and osteoarthritis, due to insufficient data with few studies and small sample sizes [6]. In our experience, acute traumatic injuries can be well imaged with a modern 0.55T device. Therapeutically urgent findings in the bone, menisci, and ligaments can be reliably diagnosed (Fig. 1). Degenerative changes can also be assessed, especially in advanced stages. However, caution is advised in chronic and recurrent ailments with unremarkable imaging findings, as discrete changes may be missed. These cases should be submitted to high-field MRI primarily or even secondarily.

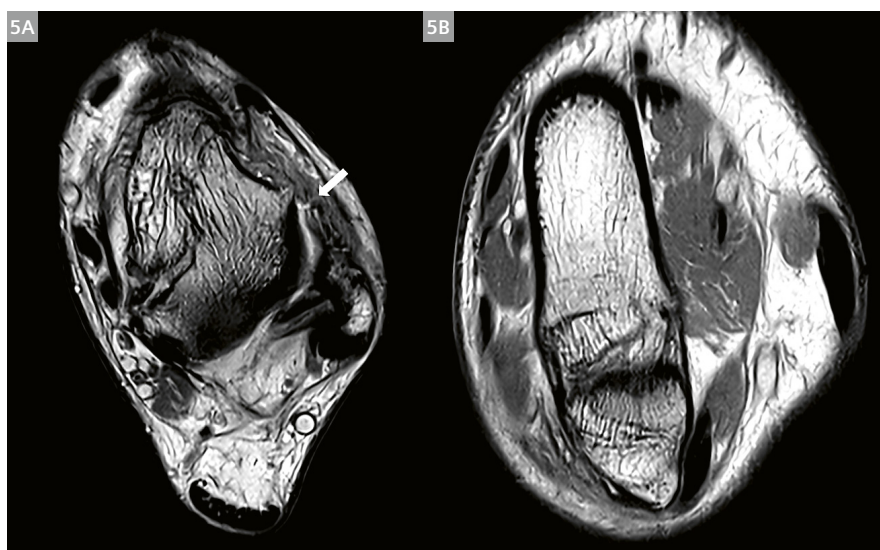
Foot and ankle

MRI is increasingly used in the diagnosis of foot and ankle pathologies [15]. A study published in 1998 found superior image quality of the ankle and foot with a significantly higher SNR in a 1.0T whole-body scanner compared to a 0.2T extremity scanner. Despite the differences in image quality, 96% of lesions detected at 1.0T MRI, such as external ligament injuries and osteochondrosis dissecans, were also diagnosed at 0.2T (Artoscan; Esaote, Genoa, Italy). However, in a post-examination survey that asked the included patients about positioning, measurement time, noise, claustrophobia, confidence in the diagnostic procedure, and willingness to repeat the examination, patient acceptance was clearly in favor of the 1.0T whole-body scanner. Claustrophobia did not play a role in either device. The 0.2T scanner was only superior to the 1.0T scanner in terms of noise perception [25]. In their study from 2000,

Herber et al. recommended performing a low-field MRI of the ankle joint in children and adolescents with unclear ankle pain and unremarkable radiographic findings. Low-field MRI examinations enabled diagnosis of ligamentous ruptures, fractures, and growth plate injuries in the majority of the 55 patients included, resulting in dedicated therapy in 35 cases [26]. From our own experience with a modern 0.55T whole-body MRI, acute ankle injuries such as ligamentous ruptures, fractures, and injuries of the syndesmosis can be diagnosed with high subjective confidence and patient comfort, but this remains to be objectively shown in further scientific studies (Fig. 5).

Conclusion

Developments and technical advancements over the past 40 years have led to a redesign of low-field MRI devices [1]. These modern high-performance, low-field systems have multiple, previously unexplored clinical applications that have the potential to complement existing high-field diagnostics in musculoskeletal imaging. Low-field MRI systems can provide superior image quality of musculoskeletal structures, particularly at critical air–tissue interfaces and especially with metal implants¹. This must be weighed against the reduced image quality with reduced SNR, reduced resolution, and prolonged measurement times when compared to high-field systems. Lower acquisition and operating costs², as well as potentially portable devices that allow sufficient diagnostics despite low field strengths, are factors that could make musculoskeletal imaging more widely available. However due to the unique specifications of low-field MRI, it should only be applied under consideration of the patient's individual medical question or the anatomical structure to be imaged. Accordingly, low-field MRI systems should be regarded as an extension of the existing diagnostic options, and not as



5 MRI at 0.55T of the ankle of a 37-year-old patient after ankle sprain. Transversal proton-density-weighted image (**5A**) shows a rupture of the anterior talofibular ligament (arrow). Parasagittal proton-density-weighted image (**5B**) demonstrates that the anterior and posterior syndesmosis are intact. The sequence parameters are provided in Table 2.

an equivalent or competitive replacement for the established high-field scanners [3]. Due to the limited available data and the age of existing papers, studies comparing modern low-field MRI systems with higher-field systems in terms of diagnostic performance in musculoskeletal imaging are urgently needed.

Acknowledgments

Sincere thanks to Sandy Schmidt from the Department of Radiology, University Hospital Erlangen, Germany, for their technical support and image acquisition. We thank the Imaging Science Institute Erlangen for providing us with measurement time and technical support.

References

- Heiss R, Nagel AM, Laun FB, Uder M, Bickelhaupt S. Low-Field Magnetic Resonance Imaging: A New Generation of Breakthrough Technology in Clinical Imaging. *Invest Radiol.* 2021;56(11):726–733.
- Krampla W, Roesel M, Svoboda K, Nachbagauer A, Gschwantler M, Hruby W. MRI of the knee: how do field strength and radiologist's experience influence diagnostic accuracy and interobserver correlation in assessing chondral and meniscal lesions and the integrity of the anterior cruciate ligament? *Eur Radiol.* 2009;19(6):1519–1528.
- Klein HM. Low-Field Magnetic Resonance Imaging. *Rofo.* 2020;192(6):537–548.
- Runge VM, Heverhagen JT. Advocating the Development of Next-Generation, Advanced-Design Low-Field Magnetic Resonance Systems. *Invest Radiol.* 2020;55(12):747–753.
- Kraff O, Fischer A, Nagel AM, Mönninghoff C, Ladd ME. MRI at 7 Tesla and above: demonstrated and potential capabilities. *J Magn Reson Imaging.* 2015;41(1):13–33.
- Puig S, Kuruvilla YC, Ebner L, Endel G. Magnetic resonance tomography of the knee joint. *Skeletal Radiol.* 2015;44(10):1427–1434.
- Marques JP, Simonis FFJ, Webb AG. Low-field MRI: An MR physics perspective. *J Magn Reson Imaging.* 2019;49(6):1528–1542.
- Tavernier T, Cotten A. High- versus low-field MR imaging. *Radiol Clin North Am.* 2005;43(4):673–681, viii.
- Campbell-Washburn AE, Ramasawmy R, Restivo MC, Bhattacharya I, Basar B, Herzka DA, et al. Opportunities in Interventional and Diagnostic Imaging by Using High-Performance Low-Field-Strength MRI. *Radiology.* 2019;293(2):384–393.
- Del Grande F, Santini F, Herzka DA, Aro MR, Dean CW, Gold GE, et al. Fat-suppression techniques for 3-T MR imaging of the musculoskeletal system. *Radiographics.* 2014;34(1):217–233.
- Harris CA, White LM. White, Metal artifact reduction in musculoskeletal magnetic resonance imaging. *Orthop Clin North Am.* 2006;37(3):349–359, vi.
- Schröder FF, Post CE, van Raak SM, Simonis FFJ, Wagenaar FBM, Huis In't Veld RMHA, et al. The diagnostic potential of low-field MRI in problematic total knee arthroplasties – a feasibility study. *J Exp Orthop.* 2020;7(1):59.
- Lee RK, Griffith JF, Lau YY, Leung JH, Ng AW, Hung EH, et al. Diagnostic capability of low- versus high-field magnetic resonance imaging for lumbar degenerative disease. *Spine (Phila Pa 1976).* 2015;40(6):382–391.
- Hutchins TA, Peckham M, Shah LM, Parsons MS, Agarwal V, Boulter DJ, et al. ACR Appropriateness Criteria® Low Back Pain: 2021 Update. *J Am Coll Radiol.* 2021;18(11s):S361–S379.
- Dean Deyle G. The role of MRI in musculoskeletal practice: a clinical perspective. *J Man Manip Ther.* 2011;19(3):152–161.
- Loew R, Kreitner KF, Runkel M, Zoellner J, Thelen M. MR arthrography of the shoulder: comparison of low-field (0.2T) vs high-field (1.5T) imaging. *Eur Radiol.* 2000;10(6):989–996.
- Lee CS, Davis SM, McGroder C, Kouk S, Sung RM, Stetson WB, et al. Analysis of Low-Field MRI Scanners for Evaluation of Shoulder Pathology Based on Arthroscopy. *Orthop J Sports Med.* 2014;2(7):2325967114540407.
- Steinbach LS, Fritz RC, Tirman PF, Uffman M. Magnetic resonance imaging of the elbow. *Eur J Radiol.* 1997;25(3):223–241.
- Okamoto Y, Maehara K, Kanahori T, Hiyama T, Kawamura T, Minami M. Incidence of elbow injuries in adolescent baseball players: screening by a low field magnetic resonance imaging system specialized for small joints. *Jpn J Radiol.* 2016;34(4):300–306.
- Stirling PHC, Strelzow JA, Doornberg JN, White TO, McQueen MM, Duckworth AD. Diagnosis of Suspected Scaphoid Fractures. *JBJS Rev.* 2021;9(12).
- Brydie A, Raby N. Early MRI in the management of clinical scaphoid fracture. *Br J Radiol.* 2003;76(905):296–300.
- Crues JV, Shellock FG, Dardashti S, James TW, Troum OM. Identification of wrist and metacarpophalangeal joint erosions using a portable magnetic resonance imaging system compared to conventional radiographs. *J Rheumatol.* 2004;31(4):676–685.
- Vellet AD, Lee DH, Munk PL, Hewett L, Eliasziw M, Dunlavy S, et al. Anterior cruciate ligament tear: prospective evaluation of diagnostic accuracy of middle- and high-field-strength MR imaging at 1.5 and 0.5 T. *Radiology.* 1995;197(3):826–830.
- Cotten A, Delfaut E, Demondion X, Lapègue F, Boukhelifa M, Boutry N, et al. MR imaging of the knee at 0.2 and 1.5 T: correlation with surgery. *AJR Am J Roentgenol.* 2000;174(4):1093–1097.
- Verhoek G, Zanetti M, Duewell S, Zollinger H, Hodler J. MRI of the foot and ankle: diagnostic performance and patient acceptance of a dedicated low field MR scanner. *J Magn Reson Imaging.* 1998;8(3):711–716.
- Herber S, Kreitner KF, Kalden P, Löw R, Berger S, Thelen M. [Low-field MRI of the ankle joint: initial experience in children and adolescents using an open 0.2 T MR-system]. *Rofo.* 2000;172(3):267–273.

Contact

Rafael Heiss, M.D., MHBA
Associate Professor for Radiology
Institute of Radiology
Universitätsklinikum Erlangen
Maximiliansplatz 1
91054 Erlangen
Germany
Tel: +49(0)9131-8535525
Rafael.Heiss@uk-erlangen.de



Tobias Pogarell
Institute of Radiology
Universitätsklinikum Erlangen
Maximiliansplatz 1
91054 Erlangen
Germany
Tel: +49(0)9131-8535525
Tobias.Pogarell@uk-erlangen.de



Exploring the Potential of Low-Field Musculoskeletal MRI at 0.55T: Preliminary Results in Patients with Large Metal Implants

Hanns-Christian Breit, M.D.¹; Jan Vosshenrich, M.D.¹; Martin Clauss, M.D.^{2,3}; Markus M. Obmann, M.D.¹; Michael Bach, Ph.D.¹; Dorothee Harder, M.D.¹; Ricardo Donners, M.D.¹

¹Department of Radiology, University Hospital Basel, University of Basel, Switzerland

²Center for Musculoskeletal Infections, University Hospital Basel, University of Basel, Switzerland

³Department for Orthopedics and Trauma Surgery, University Hospital Basel, University of Basel, Switzerland

Introduction

Low-field MRI scanners are currently experiencing a renaissance, thanks to technical innovations in gradient construction, coil design, and AI-based reconstruction methods [1]. Advantages over the 1.5T and 3T scanners used predominantly in clinical routine include lower acquisition and maintenance costs, and higher patient comfort [2, 3]. Potential advantages of low-field MR imaging include clinical scenarios where imaging using scanners with higher field strengths encounters technical limitations. This is especially the case when imaging patients with metal implants¹ where susceptibility artifacts are expected to be substantially less severe at 0.55T [4, 5]. This may be of particular interest in clinical routine, given an aging global population with an associated higher prevalence of metal implants, e.g., following joint replacement surgery [6]. This patient population has been shown to benefit from MR imaging [7].

The aim of this report is to provide a perspective on the possibilities and potential advantages of using a new-generation 0.55T low-field MRI system in imaging patients with large metal implants.

Materials and methods

Patient population

Three patients underwent complementary MR imaging at 0.55T in addition to their regular clinical imaging work-up.

MRI scanners

Low-field MR imaging was performed using a 0.55T MAGNETOM Free.Max scanner (Siemens Shenzhen Magnetic Resonance Ltd., Shenzhen, China, gradient amplitude 26 mT/m, slew rate 45 T/m/s, 80 cm bore). A six-channel flex coil was used for the examination of the knee and the upper limb.

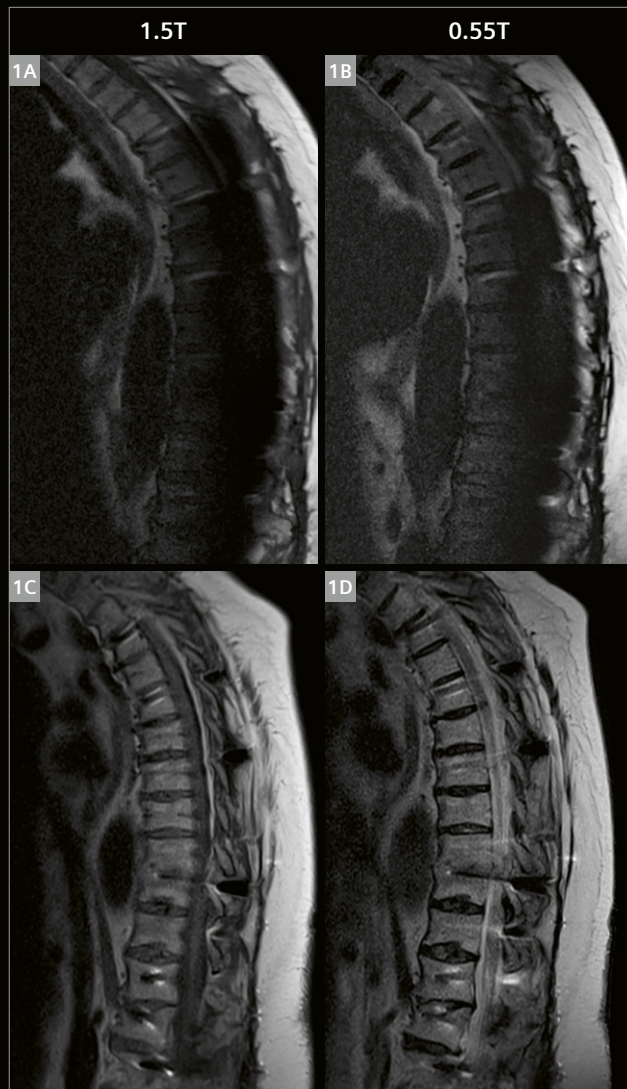
The 1.5T examinations were performed using a MAGNETOM Avanto Fit system (Siemens Healthcare, Erlangen, Germany, gradient amplitude 45 mT/m, slew rate 200 T/m/s, 60 cm bore). The 3T examinations were performed on a MAGNETOM Skyra system (Siemens Healthcare, Erlangen, Germany, gradient amplitude 45 mT/m, slew rate 200 T/m/s, 70 cm bore).

¹The MRI restrictions (if any) of the metal implant must be considered prior to patient undergoing MRI exam. MR imaging of patients with metallic implants brings specific risks. However, certain implants are approved by the governing regulatory bodies to be MR conditionally safe. For such implants, the previously mentioned warning may not be applicable. Please contact the implant manufacturer for the specific conditional information. The conditions for MR safety are the responsibility of the implant manufacturer, not of Siemens Healthineers.

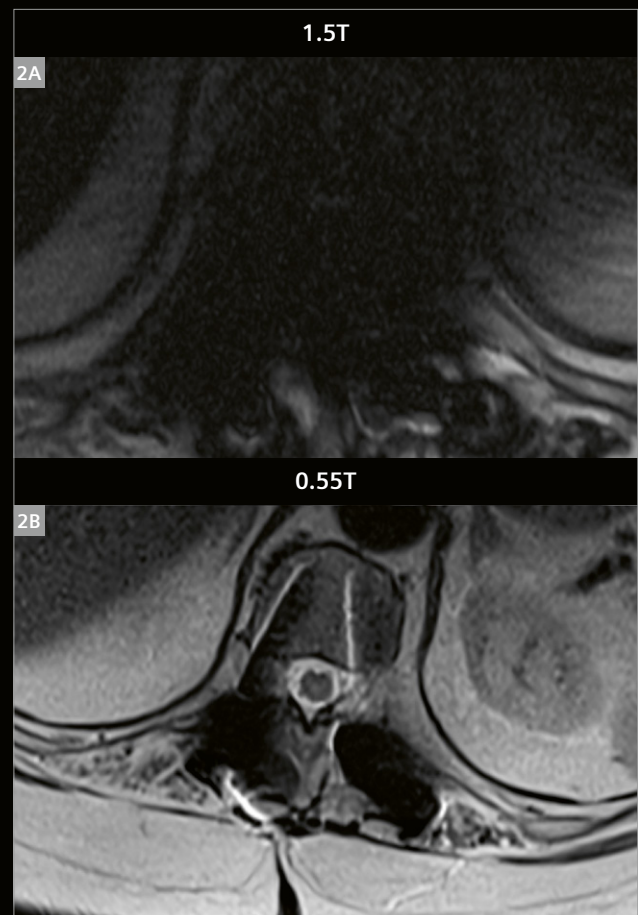
Case 1

A 59-year-old patient with several prior surgical procedures of the thoracic spine, including multi-level decompression and spinal fusion, presented with back pain refractory to medication. MR imaging of the thoracic spine was requested for the assessment of the spinal canal prior to epidural catheter placement. Routine imaging was performed at 1.5T, followed by a supplemental MR examination at 0.55T.

Due to severe susceptibility artifacts, the spinal canal was not assessable at 1.5T, neither on sagittal or axial T2-weighted sequences, nor on the T1-weighted sequence in the sagittal plane. At 0.55T, visibility and assessability of the spinal canal was substantially improved. Artifact superimposition was only minor, allowing for conclusive evaluation. Contraindications for epidural pain catheter placement could therefore be ruled out at 0.55T. Representative slices from 1.5T and 0.55T imaging are shown in Figures 1 and 2.



1 Preoperative imaging in a 59-year-old patient with multiple prior surgical procedures of the spine, prior to epidural pain catheter placement. Due to susceptibility artifact superimposition, the spinal canal was not assessable at 1.5T, neither in T2-weighted (1A) nor T1-weighted (1C) sequences. Artifact severity was substantially lower at 0.55T, allowing for assessment with high diagnostic confidence (1B, 1D).



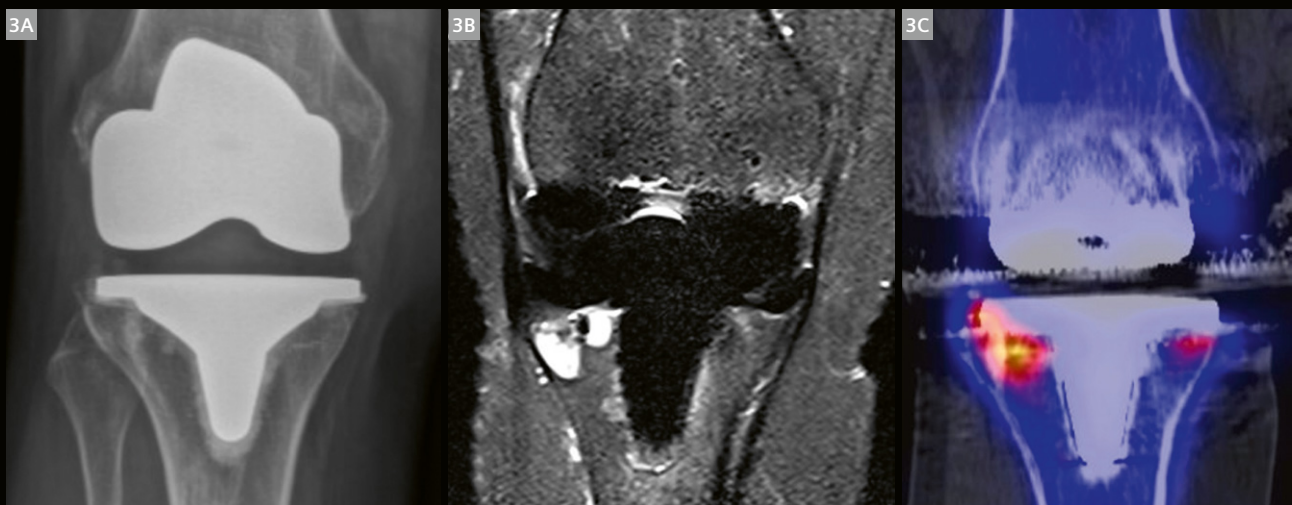
2 Similar to the sagittal images shown in Figure 1, the evaluation of the spinal canal was also only possible using the axial T2-weighted images acquired at 0.55T (2B); while 1.5T did not allow for assessment due to artifact superimposition (2A).

Case 2

A 59-year-old female patient presented with persistent knee pain five years after total knee arthroplasty. Given unremarkable radiographic examinations without signs of loosening, SPECT/CT and supplemental MR imaging at 0.55T were performed.

Radiography did not show signs of implant loosening or other postoperative complications (Fig. 3A). In contrast, MR imaging at 0.55T clearly depicted edema-equivalent signal changes adjacent to the tibial implant component in the lateral tibial plateau, and to a lesser extent also in the medial tibial plateau, indicative of implant loosening.

Findings were consistent with the results from SPECT/CT imaging, which showed increased tracer uptake in the aforementioned locations. This was interpreted as implant loosening by a board-certified nuclear medicine physician (Figs. 3B, C).



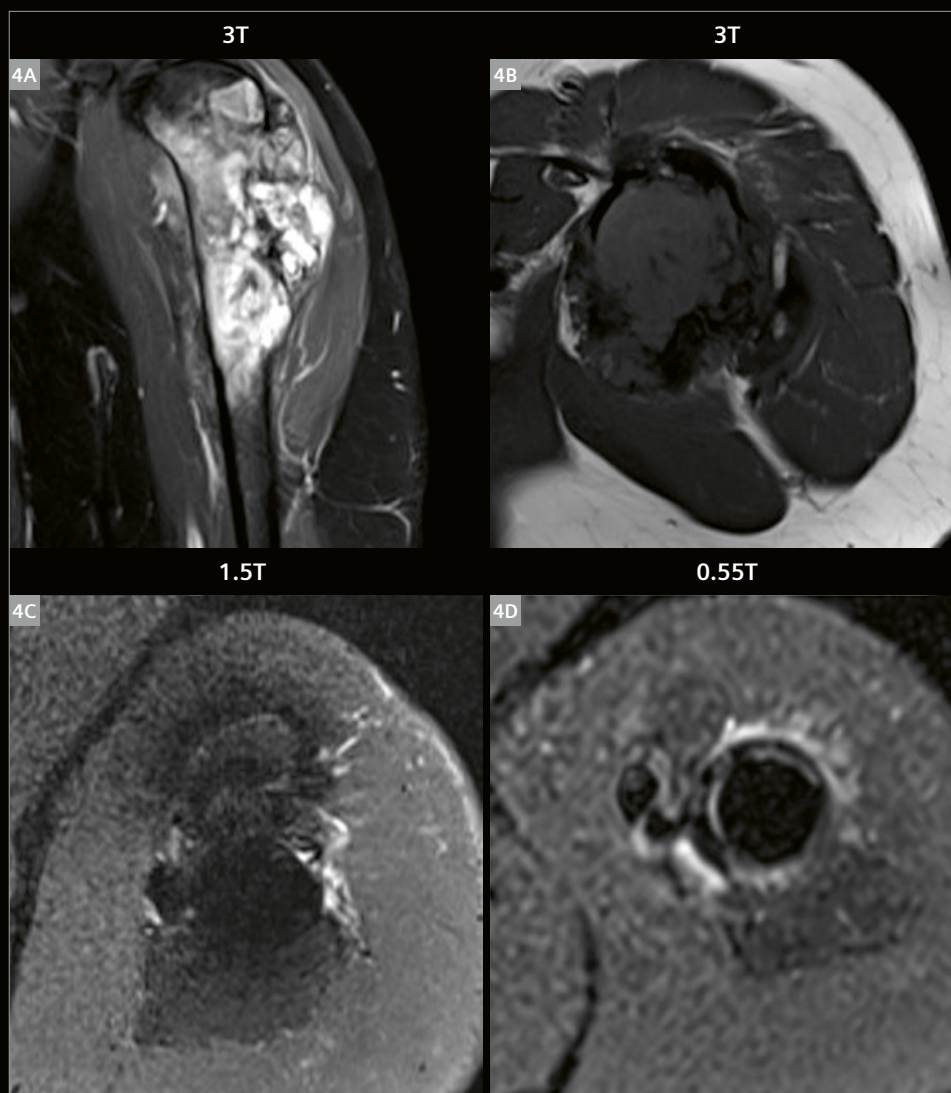
3 A 59-year-old female patient with persistent knee pain five years after total knee replacement. In contrast to conventional radiography (3A), both 0.55T MR imaging (3B) and SPECT/CT imaging (3C) demonstrated implant loosening of the tibial implant component. The 0.55T MRI also allowed for assessment of ligamentous structures around the knee.

Case 3

A 39-year-old patient presented for routine follow-up imaging after resection of an osteosarcoma of the proximal left humerus and placement of a tumor prosthesis two years ago. Preoperative imaging was first performed at 3T. Follow-up imaging after surgery was performed at 1.5T and 0.55T.

The patient underwent regular postoperative follow-up imaging at 1.5T and supplemental imaging at 0.55T following osteosarcoma resection and tumor prosthesis implantation in the proximal left humerus. Preoperative imaging was performed at 3T (Figs. 4A, B). Comparing the

follow-up MRI examinations, especially the soft tissues immediately adjacent to the tumor prosthesis shaft can be delineated clearly better at 0.55T (Fig. 3D) than at 1.5T (Fig. 3C) in the axial T2-weighted fat-suppressed sequences. In the scenario of patients undergoing follow-up imaging after bone tumor resection, potential local tumor recurrence close to the stem can be diagnosed or ruled out with greater confidence at low-field MRI, thanks to better delineation of adjacent structures due to fewer susceptibility artifacts.



4 A 39-year-old patient who was diagnosed with osteosarcoma of the proximal humerus at 3T (4A, 4B). Following tumor resection and tumor prosthesis implantation, follow-up imaging to assess for local tumor recurrence with axial T2-weighted fat-suppressed sequences is improved at 0.55T (4D) compared to 1.5T (4C), with better delineation of the soft tissue structures immediately adjacent to the shaft.

Discussion

In order to achieve the best image quality, the acquisition protocol for handling metal implant imaging must be carefully optimized, regardless of the field strength. In the cases reported here, we employed our optimized clinical protocols for all field strengths used for the image acquisitions. Certain protocol features could contribute to more robust acquisition despite of the metal, while others can correct the resulting artifacts. Metal artifact correction methods, however, are often SAR intensive and result in longer acquisition times. By imaging at 0.55T one can also reduce the concern associated with increased SAR, while often being able to get good clinical results by employing a high-bandwidth protocol.

This brief case series emphasizes the potential of low-field MR imaging at 0.55T in patients with large metal implants. This is in accordance with recently published literature that outlines, for example, the advantages of low-field MR imaging over imaging at higher field strengths in patients with total hip arthroplasty [8]. Our initial experiences as demonstrated in this case series also suggest diagnostic benefits of 0.55T MR imaging in patient groups with other types of large metal implants, such as extensive thoracic or thoracolumbar spondylodesis. Reducing metal-implant-related susceptibility artifacts allows for improved assessment of structures and soft tissues immediately adjacent to the implants, which is of particular importance for detecting local recurrence following tumor resections. Additionally, low-field MR imaging may be helpful in the detection of implant loosening and could complement SPECT/CT imaging by providing details on soft-tissue structures around the knee prior to revising total knee replacements.

In conclusion, it appears to be worth conducting dedicated studies to assess potential applications and opportunities in metal implant imaging – especially in cases of large metal implants – to establish a role for 0.55T low-field MR imaging in clinical routine.

References

- 1 Runge VM, Heverhagen JT. Advocating the Development of Next-Generation, Advanced-Design Low-Field Magnetic Resonance Systems. *Invest Radiol.* 2020;55(12):747–753.
- 2 Vosschenrich J, Breit HC, Bach M, Merkle EM. Ökonomische Aspekte der Niederfeld-Magnetresonanztomographie : Anschaffung, Installation und Unterhaltskosten von 0,55 T-Geräten [Economic aspects of low-field magnetic resonance imaging: Acquisition, installation, and maintenance costs of 0.55 T systems]. *Radiologe.* 2022;62(5):400–404. German. Epub Mar 29
- 3 Rusche T, Vosschenrich J, Winkel DJ, Donners R, Segeroth M, Bach M, et al. More Space, Less Noise—New-generation Low-Field Magnetic Resonance Imaging Systems Can Improve Patient Comfort: A Prospective 0.55 T–1.5 T-Scanner Comparison. *J Clin Med.* 2022;11(22):6705.
- 4 Farahani K, Sinha U, Sinha S, Chiu LC, Lufkin RB. Effect of field strength on susceptibility artifacts in magnetic resonance imaging. *Comput Med Imaging Graph.* 1990;14(6):409–413.
- 5 Bernstein MA, Huston III J, Ward HA. Imaging artifacts at 3.0T. *J Magn Reson Imaging.* 2006;24(4):735–746.
- 6 Abdelaal MS, Restrepo C, Sharkey PF. Global Perspectives on Arthroplasty of Hip and Knee Joints. *Orthop Clin North Am.* 2020;51(2):169–176.
- 7 Jungmann PM, Agten CA, Pfirrmann CW, Sutter R. Advances in MRI around metal. *J Magn Reson Imaging.* 2017;46(4):972–991.
- 8 Khodarahmi I, Brinkmann IM, Lin DJ, Bruno M, Johnson PM, Knoll F, et al. New-generation low-field magnetic resonance imaging of hip arthroplasty implants using slice encoding for metal artifact correction: first in vitro experience at 0.55 T and comparison with 1.5 T. *Invest Radiol.* 2022;57(8):517–526.



Contact

Hanns-Christian Breit, M.D.
University Hospital Basel
Department of Radiology
Spitalstrasse 21
4031 Basel
Switzerland
Tel.: +41 61 328 56 33
hanns-christian.breit@usb.ch

Fetal Low Field MRI – the First 150 Cases

Jana Hutter, Ph.D.^{1,2}; Jordina Aviles Verdera^{1,2}; Raphaël Tomi-Tricot, Ph.D.³; Kelly Payette, Ph.D.^{1,2}; Alena Uus, Ph.D.^{1,2}; Sara Neves Silva^{1,2}; Sebastien Ourselin, FEng²; Shaihan Malik, Ph.D.^{1,2}; Mary Rutherford, M.D.^{1,2}; Joseph Hajnal, Ph.D.^{1,2}

¹Centre for the Developing Brain, School of Biomedical Engineering, King's College London, UK

²Biomedical Engineering Department, School of Biomedical Engineering, King's College London, UK

³MR Research Collaborations, Siemens Healthcare Limited, Camberley, UK

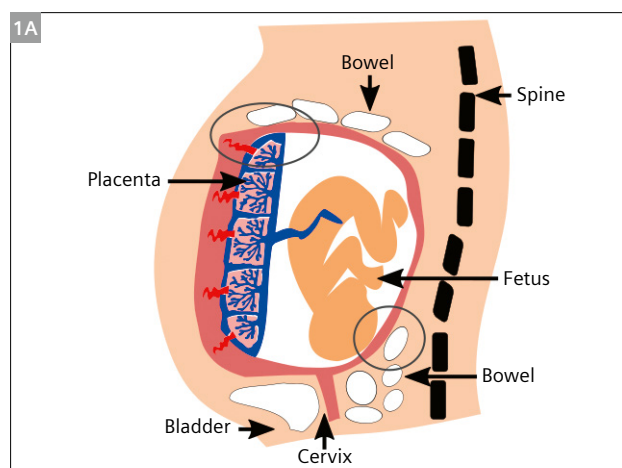
Introduction

Fetal¹ magnetic resonance imaging (fetal MRI) has continuously increased its prominence in both research and clinical applications. The wide range of available contrasts, the high resolution, the ability to image the entire fetus up until late gestation, and operator-independence make it an essential research tool and an ideal complementary modality to ultrasound for clinical care. Fetal MRI is mainly used to image suspected clinical abnormalities found through ultrasound that require further clarification, such as neurological, spine, thorax, and abdominopelvic malformations or masses. It can also be used for detailed evaluations in cases of abnormal placentation, for antenatal surgical planning of spinal lesion closure in fetuses with spina bifida, and for laser ablations in monozygotic twin pregnancies or fetuses with congenital heart disease.

While anatomical imaging using turbo spin-echo (HASTE) sequences originally dominated, functional contrasts are increasingly being employed for a variety of indications in both research and clinical settings. They are either adapted from other parts of radiology or developed specifically for fetal indications, and include diffusion-weighted MRI [1, 2], T2* relaxometry [3], T1 relaxometry [4], and perfusion MRI [5]. As these complex functional techniques are being developed, they further increase the range of indications and hence applicability of fetal MRI.

While the current trend in MRI is to image at higher field strengths, some of the significant challenges encountered in fetal MRI may be addressed by operating at a lower field strength.

Advanced imaging techniques may be hampered by geometric distortion artifacts arising at air–tissue interfaces. This is made worse by the need to run highly efficient EPI-based read-outs for diffusion MRI, functional MRI, and multi-echo gradient echo sequences for T2* relaxometry, which leads to an increasing need for specialist image-based shim techniques [6]. This increases examination time and the need for specialized fetal MRI technologists. Further challenges include B₁ inhomogeneity-related artifacts



1B Localizer

Clinical protocol

Anatomical MRI (T2-weighted HASTE)	11 min whole uterus
Diffusion MRI (Diffusion-weighted spin echo single shot EPI)	3 min whole uterus
Dynamic single-slice scan (cine)	1 min 1 slice
T2* Relaxometry (Multi-echo gradient echo single-shot (EPI))	* 4 min whole uterus

Research protocol

T1 Relaxometry (Multi-echo gradient echo single-shot EPI)	* 3 min whole uterus
Combined T2*-Diffusion MRI (Multi-echo gradient echo single shot EPI)	* 8 min whole uterus
HARDI-Diffusion MRI (Diffusion-weighted spin echo single-shot EPI)	* 4 min placenta

No image-based shimming/calibration

1 (1A) Schematic representation of the area of interest. The black circles signify areas of significant distortion due to air–tissue interfaces. (1B) Protocol overview for the clinical 20-minute exam and the research additions. The asterisks indicate custom-made sequences.

¹Siemens Healthineers disclaimer: MR scanning has not been established as safe for imaging fetuses and infants less than two years of age. The responsible physician must evaluate the benefits of the MR examination compared to those of other imaging procedures

enhanced by the presence of amniotic fluid, and specific-absorption-rate (SAR) limitations [7] resulting in inefficiencies in the sequences. Both B_0 and B_1 inhomogeneities increase with higher field strengths. Therefore, lower field strengths reduce both the impact of the aforementioned artifacts and the need for specialist correction tools.

$T2^*$ is quickly becoming a widely used functional modality, especially to assess the placenta in major pregnancy complications such as pre-eclampsia and fetal growth restriction. The increase in $T2^*$ at lower field strengths provides a clinically beneficial $T2^*$ dynamic range that is ideal for these assessments. Similarly, shorter $T1$ times at low field can potentially increase acquisition speed for $T1$ relaxometry, facilitating its application in fetal MRI.

While comfort and space are paramount for any patient undergoing an MRI scan, pregnant women in the later weeks of pregnancy present a population where space and comfort is both particularly important and challenging to achieve in a standard-sized MRI bore. In addition, the number of obese pregnant women is rising – with 24% of all pregnant women in the UK and U.S. considered obese as of 2020 [8]. This presents a currently underserved population that could benefit from fetal MRI, as these women often do not receive adequate prenatal imaging due in part to the detrimental effect of increased abdominal fat on ultrasound imaging. Lower-field strength MRI typically allows a homogeneous field even with a wider bore. Increasing the bore size to 80 cm and reducing the required length of the magnet may enable MRI to complement ultrasound in the routine clinical screening of the obese pregnant patient.

Finally, a field strength-independent challenge concerns unpredictable and uncontrollable fetal motion, especially in early-to-mid gestation when fetuses have enough space for large displacements. This can be particularly problematic for fetal functional MRI modalities, which rely on the acquisition of the same slice location multiple times in a time-series format, to then be combined for spatiotemporal analysis. Both post-processing base techniques such as slice-to-volume registration (SVR) [9, 10] and prospective motion-correction techniques based on localization and tracking may be employed at low field strengths.

Main benefits:

- 20-minute efficient and robust clinical imaging workflow at low field
- Improved patient comfort due to wide bore
- Increased magnetic field homogeneity and reduced imaging artifacts
- First evidence proving the efficacy of low-field clinical fetal MRI

Materials and methods

Patient preparation and comfort

Pregnant patients are consented for research by either a research midwife or obstetrician and then prepared for the scan. The weight of the pregnant uterus on the vena cava in supine position can in rare cases lead to vasovagal episodes. To mitigate this and allow early detection, tight blood pressure controls are performed in multiple positions. A first blood pressure reading is taken while the patient is sitting on the scanner table, after which they lie on their left side for a second blood pressure reading, and then slowly the patient is eased onto their back in head first supine position to limit the compression of the vena cava. Padding for the lower back, the head, and the legs is provided as requested. Throughout the scan, blood pressure readings are performed automatically at 10-minute intervals, the maternal heart rate and saturation are continuously monitored, and frequent verbal interaction is maintained.

Clinical protocol

The protocol was crafted to allow assessment of the fetal brain and body, the placenta, and the cervix (see Figure 1A for an overview). It consists of a clinical session (Fig. 1B), which lasts about 20 minutes, and a research session of up to 40 minutes. Both are designed specifically with the advantages and challenges of 0.55T in mind and are therefore modified from our standard fetal imaging at 1.5T and 3T in the following way:

The resolution for the anatomical HASTE scans was reduced, using a slice thickness of 4.5 mm instead of 2.5 mm (in-plane resolution $1.4 \times 1.4 \text{ mm}^2$) and 9 stacks (3 uterus stacks, 3 fetal brain stacks, and 3 fetal body stacks) instead of 6 to allow robust SVR.

A multi-echo gradient echo EPI sequence was modified to include multiple echoes, allowing for motion-robust $T2^*$ mapping of the entire uterus with 20 dynamics. $T2^*$ shortens with advanced gestational age and with most major pathologies. Compared to higher field strengths, the increased $T2^*$ at low field allows longer read-outs and the conservation of signal over longer echo times at later gestation and in cases with placental disease. A diffusion MRI scan, allowing both apparent diffusion coefficient (ADC) and intravoxel incoherent motion (IVIM) calculations as typically used for fetal imaging, was acquired covering the entire uterus. Finally, a dynamic (CINE) single-slice HASTE scan was acquired ($TR = 4$ seconds) to visualize cardiac activity and limb and head motion.

Research protocol

The gradient echo sequence was modified with a global adiabatic inversion pulse and slice-shuffling to reap the benefits of the reduced $T1$ at this field strength for an efficient quantitative fetal $T1$ acquisition. A previously

proposed multi-echo diffusion MRI scan [11] was used to sample a large parameter space, combined synergistically with the longer T2* and allowing sampling for a longer time.

Importantly, none of these elements included image-based shimming or any other advanced shimming of the kind required on higher-field scanners, thus saving scanning time.

Analysis and quantities obtained

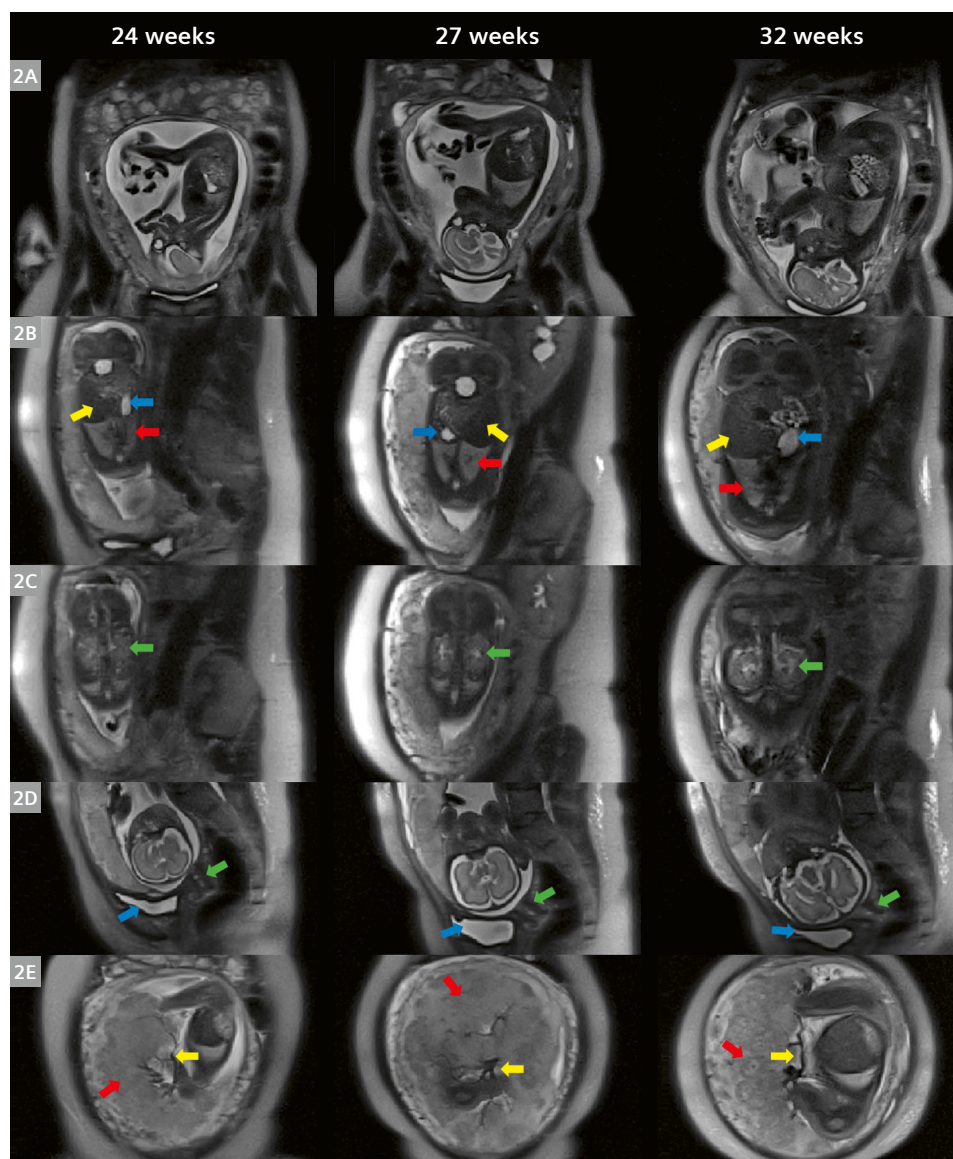
An anatomical brain report is obtained from the HASTE stacks and includes bi-parietal diameter, transcerebellar diameter, ventricular sizes, presence of orbits, ears, and more. The cervical length and the lung are segmented individually to obtain respective quantitative values. The stacks are also reconstructed to 3D volumes using

SVR resulting in automatic segmentations and volumes for 16 brain regions. Mono-exponential fitting is performed on the T2* and T1 data to obtain quantitative maps for the brain and placenta. Finally, the dynamic T2* scans are processed using SVR and AI-based localization and segmentation to obtain organ-specific T2* maps and values for 10 organs of interest.

Results

Comfort and success of the examination

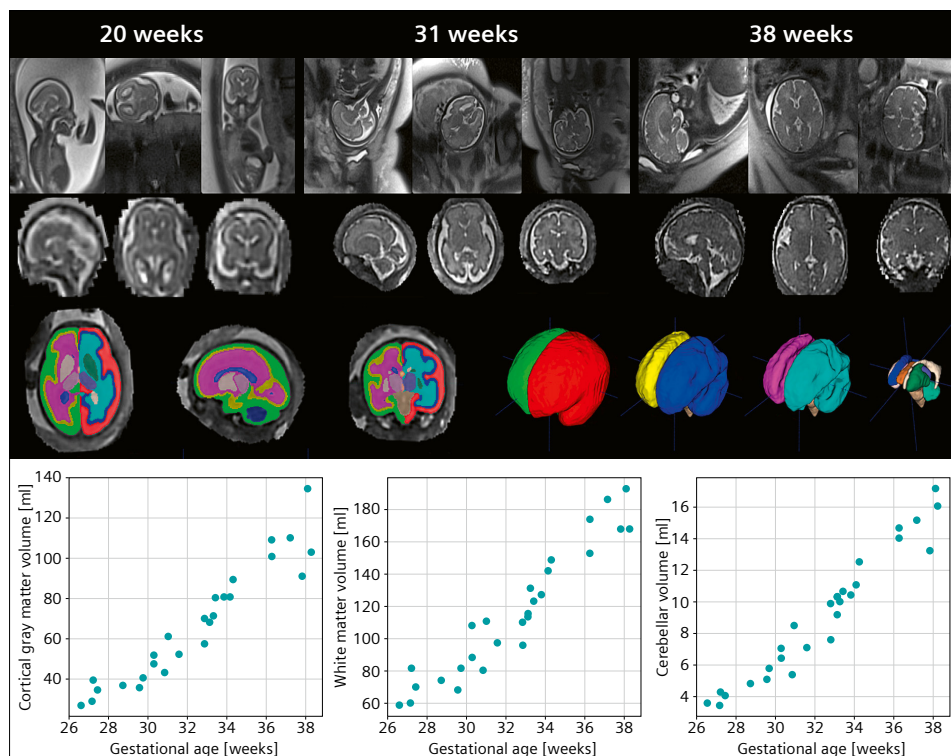
In the first nine months, a total of 150 fetal scans from 16+0 to 40+2 weeks of gestational age were performed on the 0.55T scanner, including 25 patients referred for clinical indications. This cohort includes patients with either significant claustrophobia or a BMI that does not



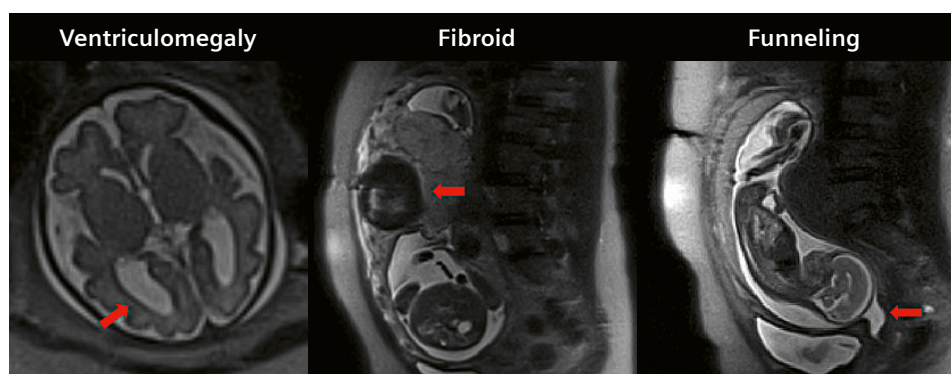
2 Fetal case scanned longitudinally at three time points during pregnancy (24, 27, and 32 weeks) illustrating (2A) a coronal whole uterus view; (2B) the fetal lung (red), stomach (blue), and liver (yellow); (2C) the kidney (green); (2D) the cervix (green arrow) and bladder (blue arrow); and (2E) a coronal whole uterus view through the placenta showing chorionic vessels connecting the placenta to the umbilical cord (yellow arrows) and the increasing heterogeneity with age within placental lobules (red arrow).

allow comfortable examination on any other available scanner (max BMI = 49.9 kg/m²). The pathologies studied included neurological abnormalities (ventriculomegaly, midline cysts, mega cisterna magna, scalp tumor), fetal body abnormalities (cystic kidney), and big obstetrical syndromes associated with the placenta (pre-eclampsia, fetal growth restriction). They also included findings such as funnels in the cervix, endometrial cysts, and fibroids. Patient feedback from a small cohort of pregnant women who had both a low-field and a high-field MRI scan during the same pregnancy revealed an increase in comfort (from 2.9 to 4.3 on a scale of 1 “not comfortable” to 5 “very comfortable”). This was also reflected in the large number of research patients choosing to come back for up to four scans.

Anatomical data obtained as illustrated in a longitudinal case (the same fetus was scanned at 24, 27, and 32 weeks) shown in Figure 2 clearly depicts all fetal structures (lungs, liver, stomach, and kidney are marked with arrows), the placental vasculature (yellow arrow), heterogeneity (red arrow), and the cervix (green arrow). Figure 3 shows more detailed views of the brain in radiological planes and after SVR at three time points. The results from automatic regional segmentation on these SVR results are shown for 60 healthy control cases in the bottom row, illustrating the ability of the data to accurately assess growth. Finally, Figure 4 shows zoomed images of the described pathologies, illustrating the ability of the low-field data to robustly visualize and quantify these.



3 Detailed views of the HASTE data from the brain, acquired in radiological planes (top row) and after SVR (second row) at 20, 31, and 38 weeks. Results from the automatic subregion brain segmentation (third row) and volumetric brain assessment over gestational age (bottom row) from left to right: cortical gray matter volume, white matter volume, and cerebellar volume.



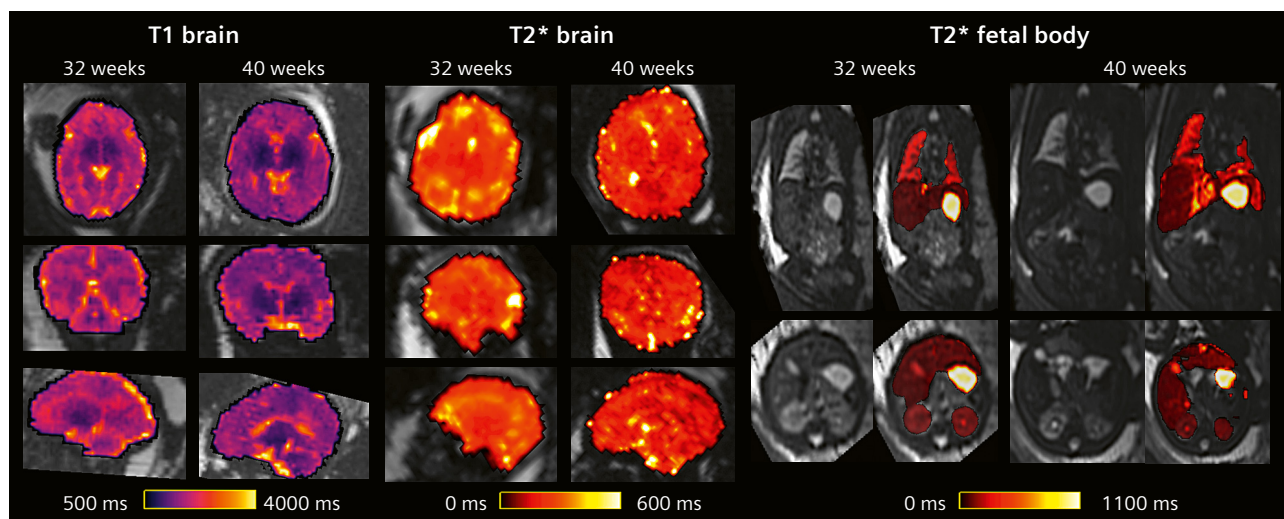
4 Fetal HASTE images of selected pathologies, including ventriculomegaly, an enlarged cisterna magna, a low signal-intensity fibroid, and funneling of the cervix.

Functional data and case study: BMI of 49.9 kg/m²

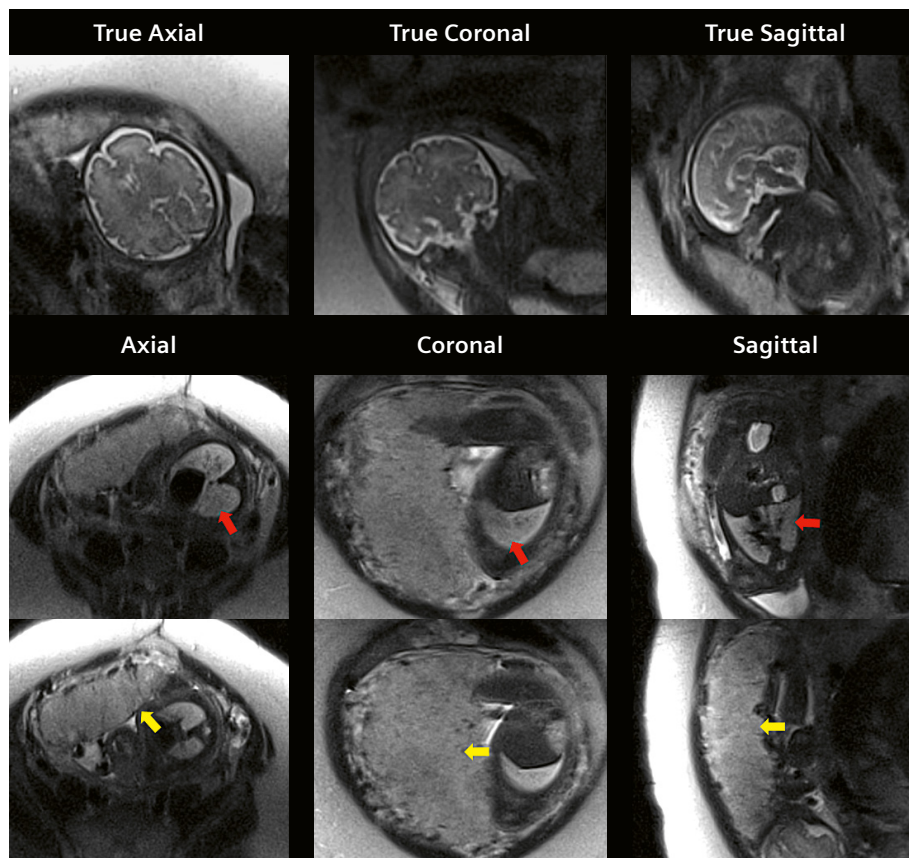
A total of 128 full sets of functional data were acquired, including T1 and T2* relaxometry and diffusion MRI. Imaging from a longitudinal case (same fetus scanned at 32 and 40 weeks) for T1 and for T2* (Fig. 5) depicts good delineation of major and fine brain structures. Finally, the T2* obtained for each fetal organ shows the ability of the

proposed protocol at 0.55T to acquire quantitative information even for small fetal structures throughout gestation.

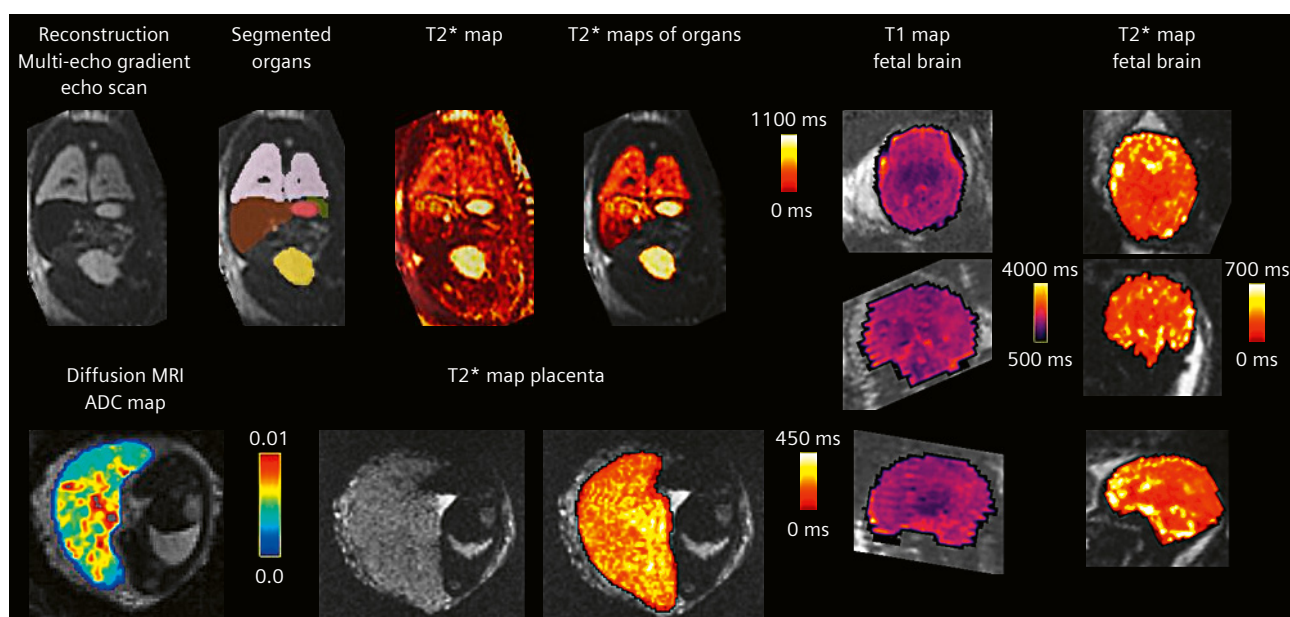
Results in a selected case with BMI = 49.9 kg/m² (Figure 6 for the anatomical and Figure 7 for the functional data) demonstrate the ability to obtain detailed results even in such challenging cases.



5 Longitudinal T1 (left) and T2* (middle) brain maps, and fetal organ T2* maps (right) for a subject scanned at 32 and 40 weeks' gestational age.



6 Case study of fetal MRI at BMI 49.9 kg/m²: Part I: Anatomical results for a participant with BMI = 49.9 kg/m² showing the ability to depict the brain structures (top row), the lungs (middle row, red arrows) and the placenta (bottom row, yellow arrows).



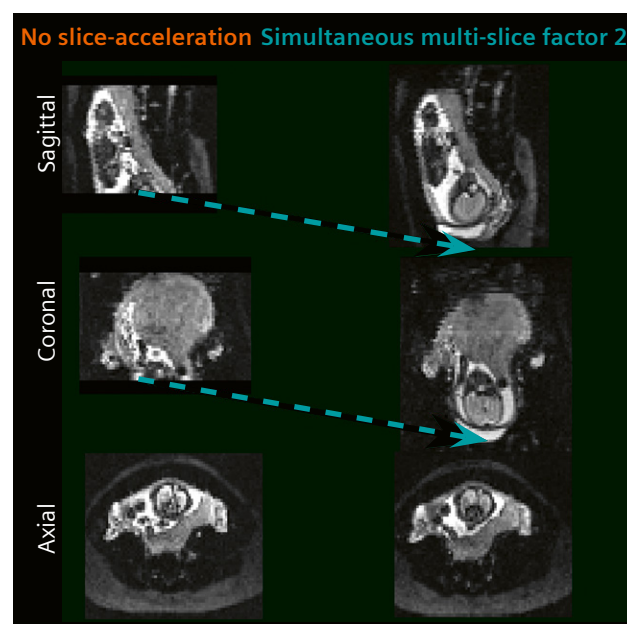
7 Case study of fetal MRI at BMI 49.9 kg/m²: Part II: Functional results from the same case for a participant with BMI = 49.9 kg/m² showing the individual organ T2* maps, the T1 and T2* maps of the brain, and the placental ADC and T2* map.

Discussion and conclusion

Fetal MRI at 0.55T is feasible, offers essential benefits, and is thus a promising direction for future antenatal imaging. The proposed short protocol allows anatomical and functional assessment of the fetus within 20 minutes. This is facilitated by foregoing any need for image-based shimming or other special correction tools, and carefully drafted to make use of the longer T2* and shorter T1 at low field. The research sequences allow further insights into desired regions of interest such as placental and lung microstructure and function. The wider bore size and shorter length increases comfort and thus increases access to fetal MRI until late gestation and in patients with higher BMIs. The fact that the scanner is a commercially available system makes it easy to integrate state-of-the-art techniques such as simultaneous multi-slice imaging, illustrated at 0.55T in Figure 8. Next steps will include adding fetal cardiac sequences; scanning further clinical cohorts such as patients with invasive placentation, preeclampsia, and congenital heart disease; and assessing the fetal placental unit prior to labor to assist in birth management. Other routinely used sequences for fetal MRI such as TrueFISP and T1-weighted contrasts will be added in the future.

An important future step is to further increase the availability of fetal MRI by allowing operation in hospitals and imaging centers without fetal MRI specialists. To come closer to this goal, a first step was the development of a prospective motion-correction technique that can detect fetal head translational displacements using deep learning and then feeds this information back to the scanner to continuously update the acquisition geometry in real time.

This prospective motion correction shows great potential for applications that would highly benefit from precise correction of motion artifacts and immediate enhancement of the image quality during the scan. This can also be developed to be used to assess the tissue microstructure of the fetal brain through the quantification of the fetal brain's blood-oxygen-level-dependent (BOLD) response to maternal oxygenation and diffusion MRI.



8 Simultaneous multi-slice imaging for T2* imaging at 0.55T illustrating the extension of the field of view by a factor of nearly two in the same scan time.

References

- 1 Bonel HM, Stolz B, Diedrichsen L, Frei K, Saar B, Tutschek B, et al. Diffusion-weighted MR imaging of the placenta in fetuses with placental insufficiency. *Radiology*. 2010;257(3):810–819.
- 2 Slator PJ, Hutter J, Palombo M, Jackson LH, Ho A, Panagiotaki E, et al. Combined diffusion-relaxometry MRI to identify dysfunction in the human placenta. *Magn Reson Med*. 2019;82(1):95–106.
- 3 Sørensen A, Hutter J, Seed M, Grant PE, Gowland P. T2*-weighted placental MRI: basic research tool or emerging clinical test for placental dysfunction? *Ultrasound Obstet Gynecol*. 2020;55(3):293–302.
- 4 Gowland PA, Freeman A, Issa B, Boulby P, Duncan KR, Moore RJ, et al. In vivo relaxation time measurements in the human placenta using echo planar imaging at 0.5 T. *Magn Reson Imaging*. 1998;16(3):241–247.
- 5 Zun Z, Limperopoulos C. Placental perfusion imaging using velocity-selective arterial spin labeling. *Magn Reson Med*. 2018;80(3):1036–1047.
- 6 Gaspar AS, Nunes RG, Ferrazzi G, Hughes EJ, Hutter J, Malik SJ, et al. Optimizing maternal fat suppression with constrained image-based shimming in fetal MR. *Magn Reson Med*. 2019;81(1):477–485.
- 7 Abaci Turk E, Yetisir F, Adalsteinsson E, Gagoski B, Guerin B, Grant PE, et al. Individual variation in simulated fetal SAR assessed in multiple body models. *Magn Reson Med*. 2020;83(4):1418–1428.
- 8 Creanga AA, Catalano PM, Bateman BT. Obesity in Pregnancy. *N Engl J Med*. 2022;387(3):248–259.
- 9 Uus A, Zhang T, Jackson LH, Roberts TA, Rutherford MA, Hajnal JV, et al. Deformable Slice-to-Volume Registration for Motion Correction of Fetal Body and Placenta MRI. *IEEE Trans Med Imaging*. 2020;39(9):2750–2759.
- 10 Kuklisova-Murgasova M, Quaghebeur G, Rutherford MA, Hajnal JV, Schnabel JA. Reconstruction of fetal brain MRI with intensity matching and complete outlier removal. *Med Image Anal*. 2012;16(8):1550–1564.
- 11 Hutter J, Slator PJ, Christiaens D, Teixeira RPAG, Roberts T, Jackson L, et al. Integrated and efficient diffusion-relaxometry using ZEBRA. *Sci Rep*. 2018;8(1):15138.

Contact

Jana Hutter, Ph.D.
 Centre for the Developing Brain
 School of Biomedical Engineering
 King's College London
 Westminster Bridge Road
 London, SE1 7EH
 United Kingdom
jana.hutter@kcl.ac.uk



Cardiac MRI on the MAGNETOM Free.Max: The Ohio State Experience

Orlando P. Simonetti¹, Juliet Varghese¹, Ning Jin², Daniel Giese³, Yingmin Liu¹, Chong Chen¹, Rizwan Ahmad¹, Yuchi Han¹

¹The Ohio State University, Columbus, OH, USA

²Siemens Healthineers, Malvern, PA, USA

³Siemens Healthineers, Erlangen, Germany

Background

As the cardiovascular magnetic resonance (CMR) program at The Ohio State University has expanded, we added both a higher (3T, MAGNETOM Vida) and a lower (0.55T, MAGNETOM Free.Max) field system to our existing 1.5T MAGNETOM Sola. Having access to scanners with three different field strengths has enabled us to investigate the pros and cons of each across different CMR applications, with the aim to match the right field strength for the right patient and pathology. The first step in this process was to develop and implement cardiac imaging techniques for the MAGNETOM Free.Max, which was delivered without CMR product pulse sequences. We have worked closely with our colleagues at Siemens Healthineers to put together a comprehensive package of CMR techniques¹, which currently are still in the preliminary stage of development.

While signal-to-noise ratio (SNR) is directly proportional to the main magnetic field (B_0), lower B_0 offers a number of potential advantages for CMR [1, 2]. The higher field homogeneity and lower specific absorption rate (SAR) at lower-field benefits techniques that are dependent on balanced steady-state free precession (bSSFP), potentially increasing safety and reducing artifacts in patients with implanted devices². Lower B_0 means lower Lorentz forces, reducing audible noise and potentially improving the patient experience. Reduced B_0 also offers greater flexibility in magnet design. The Free.Max platform has a unique, 80 cm diameter bore and an optional 705 lb / 320 kg patient table limit, which eliminates barriers to MRI for those with severe obesity. One of our primary motivations to pursue the development of CMR techniques on the MAGNETOM Free.Max is to increase the accessibility to CMR for obese patients, as well as those with severe

claustrophobia who may benefit from the larger bore and quieter scans.

The United States Centers for Disease Control and Prevention (CDC) reports that the prevalence of obesity (body mass index (BMI) > 30 kg/m²) now exceeds 40% and is projected to affect 50% of the U.S. population by 2025 [3]. The obesity epidemic is not unique to the USA, with a prevalence now exceeding 20% in most Western European countries. Obesity increases the risk of cardiovascular disease (CVD) [4] and these risks are even greater in those with severe obesity, i.e., BMI > 40 kg/m², which now accounts for more than 9% of the adult USA population. This significant population segment faces serious healthcare challenges, especially in terms of access to non-invasive cardiovascular imaging. Most cardiac imaging equipment is not designed to accommodate the weight and girth of severely obese patients; furthermore, radiation-based modalities such as CT and SPECT require excessive radiation for adequate image quality, while attenuation of ultrasound by adipose tissue limits the utility of echocardiography [5, 6]. If not for the bore diameter (60 cm – 70 cm) and table weight limits (typically < 450 lbs / 200 kg) of standard magnetic resonance imaging (MRI) systems, MRI could provide a safe, comprehensive assessment of CVD in even the most severely obese patients. The 80 cm bore and optional 705 lb / 320 kg table weight limit of MAGNETOM Free.Max offer this possibility.

Several years ago, our group recognized the potential for low-field cardiovascular MRI [1], and demonstrated the feasibility of CMR at 0.35T in comparison with standard field strengths [7]. Our work, together with preliminary results published by others using a prototype scanner

¹Work in progress: the application is currently under development and is not for sale in the U.S. and in other countries. Its future availability cannot be ensured.

²The MRI restrictions (if any) of the metal implant must be considered prior to patient undergoing MRI exam. MR imaging of patients with metallic implants brings specific risks. However, certain implants are approved by the governing regulatory bodies to be MR conditionally safe. For such implants, the previously mentioned warning may not be applicable. Please contact the implant manufacturer for the specific conditional information. The conditions for MR safety are the responsibility of the implant manufacturer, not of Siemens Healthineers.

ramped-down to 0.55T [2, 8], supported the concept that high quality CMR could be feasible at reduced field strength. We hypothesized that the ultra-wide bore MAGNETOM Free.Max system could deliver the proven benefits of CMR to the severely obese patient population, i.e., patients who face significantly limited diagnostic image quality and radiation dosing challenges from other imaging modalities, and set a goal of developing a comprehensive suite of CMR techniques for the MAGNETOM Free.Max. To achieve this goal, however, requires overcoming two primary technical challenges;

- 1) the deficit in SNR as compared to higher field systems, and
- 2) the reduced gradient performance (26 mT/m max. amplitude and 45 mT/m/ms max. slew rate) of MAGNETOM Free.Max, resulting in longer echo times (TE) and repetition times (TR).

Taken together, these performance differences can lead to significantly longer scan times, and compromised spatial and temporal resolution. These factors are especially critical in CMR where scan time is often limited to a short breath-hold to avoid respiratory motion, and sufficient temporal resolution is required to avoid cardiac motion artifact, or to accurately resolve cardiac motion and flow. The initial steps we have taken to address these limitations include the implementation of dedicated pulse sequences, optimization of scan parameters, judicious use of advanced reconstruction strategies, and machine learning driven denoising. Preliminary results are shown in the following sections where we review the various component techniques that comprise the comprehensive cardiac package, and present example results we have obtained to date in animal models, healthy volunteers, and patients with cardiovascular disease, including those with severe obesity.

Our cardiac package

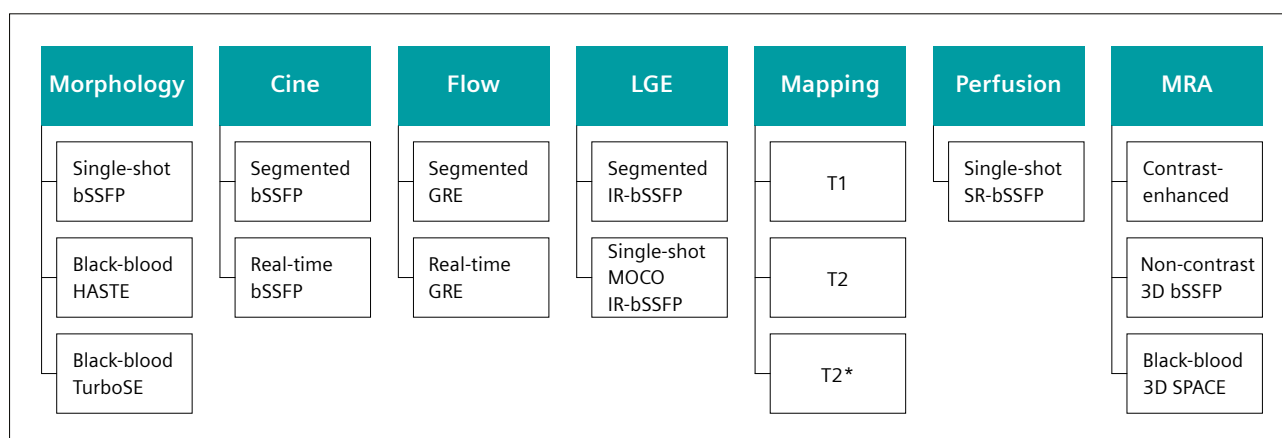
Overview

As the MAGNETOM Free.Max does not include dedicated sequences released for cardiac imaging, all of the following sequences and reconstruction techniques are research packages¹ that were enabled and/or developed by our group in collaboration with Siemens Healthineers. Furthermore, the MAGNETOM Free.Max does not have an integrated ECG triggering system; yet, it is capable of accepting an external triggering signal, and this can be provided by a variety of third-party patient monitoring systems.

At this early stage of the project, we have developed working techniques covering all of the clinical CMR applications shown in Figure 1. Our ultimate goal is to run protocols that obviate the need for patient breath-hold, and can be completed within 30 minutes; however, at this stage of development, some methods still rely on conventional segmented *k*-space, breath-hold acquisition. As we continue to innovate and combine advanced compressed sensing (CS) and deep learning-based reconstruction techniques paired with custom data acquisition strategies, we fully expect to achieve our goal of a rapid, comprehensive free-breathing CMR suite.

Morphology

Dark-blood turbo spin echo (TSE) based techniques are useful to distinguish morphological features and to characterize masses and tumors. The limited SNR and gradient speed available on MAGNETOM Free.Max impact the performance of some CMR techniques more than others. Given that TSE images tend to have relatively high SNR and the sequence is not reliant on fast gradients, the translation from higher field and faster gradient systems was

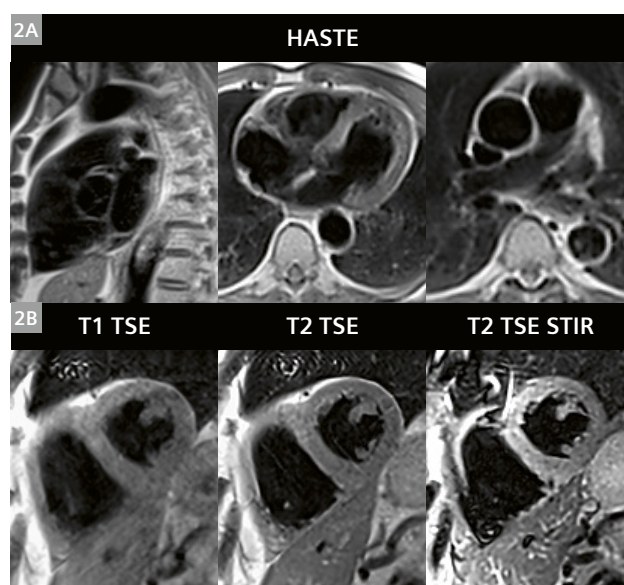


¹ Shown are the primary components of the comprehensive cardiac imaging package¹. All of the basic components are in place, although many of these techniques rely on breath-hold, segmented *k*-space acquisitions. Optimization of techniques and scan parameters is ongoing in our effort to maximize SNR, contrast, and image quality. We also continue working to develop strategies to support free-breathing image acquisition across all categories.

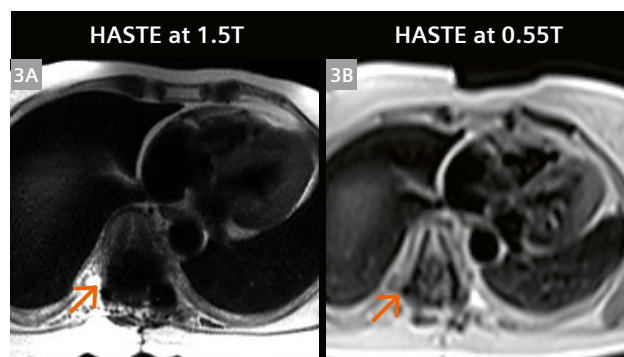
straightforward, and the technique performed well at low field with little modification. Example images in a healthy volunteer are shown in Figure 2, demonstrating the commonly used variants of black-blood T1 and T2-weighted TSE, and STIR. These are standard acquisitions with each 2D slice acquired in a short breath-hold of 10 to 12 heartbeats, and employed the Deep Resolve AI-based image denoising technique provided by Siemens Healthineers. Exemplary scan parameters used at 0.55T and 1.5T are listed in Table 1. Example images (Fig. 3) at both 1.5T and 0.55T in a patient with Harrington rods in their spine illustrate the reduced artifact surrounding metal implants² that can be expected at lower B₀ field strength.

Cine

Cine imaging is at the core of every CMR exam, providing information on cardiovascular morphology and function. Measurements can be made on the cine images to quantify global and regional cardiac function. Cine typically relies on balanced steady-state free precession, (bSSFP) and therefore has inherently high SNR relative to other techniques. Thus, the reduced SNR at low field is not a significant obstacle; however, bSSFP cine does require short TR for high temporal resolution, thus presenting a challenge on this scanner where gradient performance is limited. We have addressed this challenge through the utilization of CS reconstruction methods [9]. Table 2 lists the imaging parameters achieved at 0.55T, in comparison to a 1.5T scanner with faster gradients. With highly accelerated CS-based sequences, we have been able to achieve high-quality cine results with segmented breath-hold techniques, as well as real-time, free-breathing imaging. Segmented *k*-space, breath-hold cine images acquired in the same patient at 1.5T and at 0.55T are shown in Figure 4. This patient has an artificial aortic valve with metallic components². The size of the signal void around the valve is less in the 0.55T images, as might be expected due to the reduced susceptibility gradients surrounding the metal. The degree of metal artifact is highly dependent on the specific material used to construct the implant².



2 Dark-blood images acquired in a volunteer. Single-shot HASTE images in different cardiac views are shown in the top row (2A). The bottom row shows T1 TSE, T2 TSE and T2 TSE STIR images in a mid-short axis view (2B). Each TSE image was acquired in a 12-heartbeat breath-hold.



3 Single-shot axial images acquired in a patient with Harrington rods post spinal fusion². HASTE images acquired on a 1.5T MAGNETOM Avanto system (3A) from a prior exam demonstrate significant susceptibility artifact (orange arrows) compared to localized artifact on the corresponding HASTE image at 0.55T (3B).

	Scanner	Flip angle (deg)	TE (ms)	Echo spacing (ms)	RBW Hz/pixel	Turbo factor	Temporal resolution (ms)	Slice thickness (mm)	Pixel size (mm)	Acceleration	Scan time
T2 TSE	1.5T MAGNETOM Sola	180	60	3.54	849	17	60	5	1.3 × 1.3	G 2	10 HB
	0.55T MAGNETOM Free.Max	180	43	5.36	401	14	75	6	2.0 × 2.0	G 2	12 HB
HASTE	1.5T MAGNETOM Sola	120	35	3.94	501	104	409	6	1.3 × 1.3	none	1 HB
	0.55T MAGNETOM Free.Max	160	16	4.1	1502	72	295	10	3.6 × 3.6	G 2	1 HB

Table 1: Acquisition parameters for breath-hold segmented turbo spin echo (TSE) (top rows) and single-shot HASTE (bottom rows) shown for 1.5T MAGNETOM Sola and 0.55T MAGNETOM Free.Max.

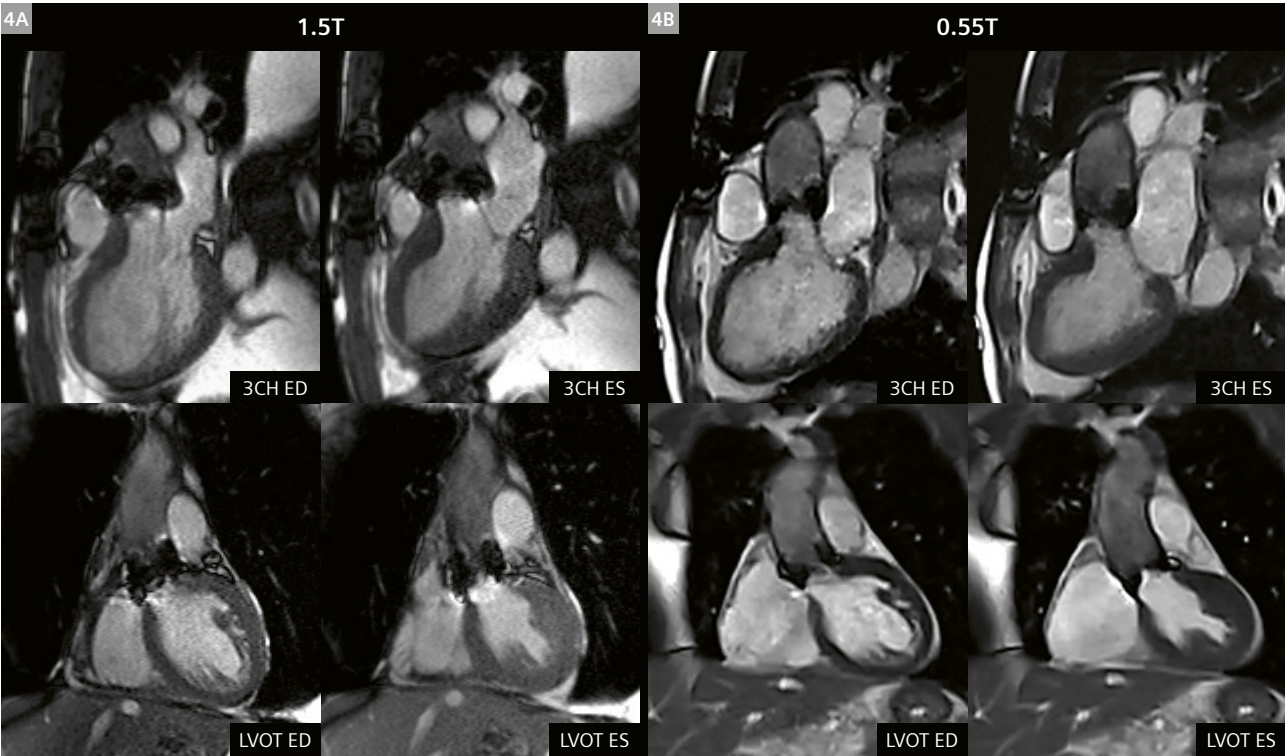
It is also dependent on TE and TR, and therefore will be affected by gradient performance as well as field strength. Figure 5 shows a comparison of breath-held segmented *k*-space cine images and real-time cine images, all acquired at 0.55T using the scan parameters listed in Table 2. Despite the high acceleration rates used to overcome slower gradient performance, SNR and overall image quality are maintained with CS reconstruction.

Flow quantification

Phase contrast (PC) imaging is the standard MRI method used to measure blood flow. While low-field offers advantages of reduced susceptibility and greater field homogeneity, the inherently low SNR of the spoiled gradient echo (GRE) sequences used for PC MRI can be challenging at low-field, and higher acceleration is needed to overcome slower gradients. We have successfully implemented segmented *k*-space, breath-hold flow quantification on the MAGNETOM Free.Max [10] and sample results

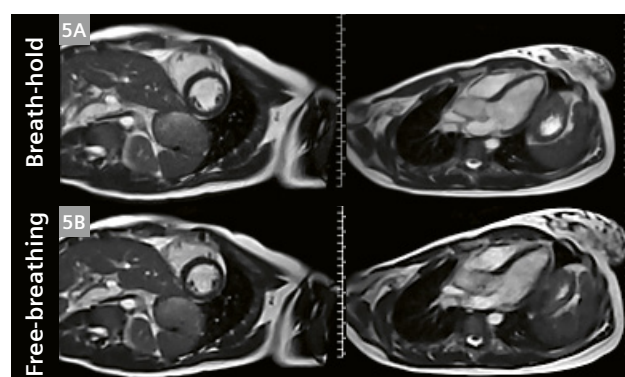
	Scanner	Flip angle (deg)	TE (ms)	TR (ms)	RBW Hz/pixel	Seg-ments	Temporal resolution (ms)	Slice thickness (mm)	Pixel size (mm)	Acceler-ation	Scan time
BH-Cine	1.5T MAGNETOM Sola	75	1.16	2.71	930	12	32.5	6	1.8 × 1.8	CS 4.3	3 HB
	0.55T MAGNETOM Free.Max	110	1.95	4.65	930	6	27.9	8	1.8 × 1.8	CS 4.3	6 HB
RT-Cine	1.5T MAGNETOM Sola	75	1.04	2.43	1184	18	43.7	8	2.0 × 2.0	CS 7.4	1 HB
	0.55T MAGNETOM Free.Max	110	1.84	4.55	1002	10	45.5	8	2.0 × 2.0	CS 9.7	1 HB

Table 2: Acquisition parameters for breath-hold segmented *k*-space cine (top rows) and real-time free-breathing cine (bottom rows) shown for 1.5T MAGNETOM Sola with faster gradients than the 0.55T MAGNETOM Free.Max. Higher acceleration rates are used for real-time cine on the MAGNETOM Free.Max to overcome the slower gradients.



4 End-diastole (ED) and End-systole (ES) cine frames acquired in a three-chamber view (3CH) and left ventricular outflow tract (LVOT) are shown. The 1.5T (MAGNETOM Avanto) (**4A**) images shown were acquired in the same patient in a prior exam using a GRAPPA-based breath-held segmented SSFP method. Images at 0.55T (**4B**) were acquired using a compressed sensing-based breath-held segmented SSFP method. Note that the patient has an artificial valve², and the metal artifacts in proximity to the valve are reduced at 0.55T.

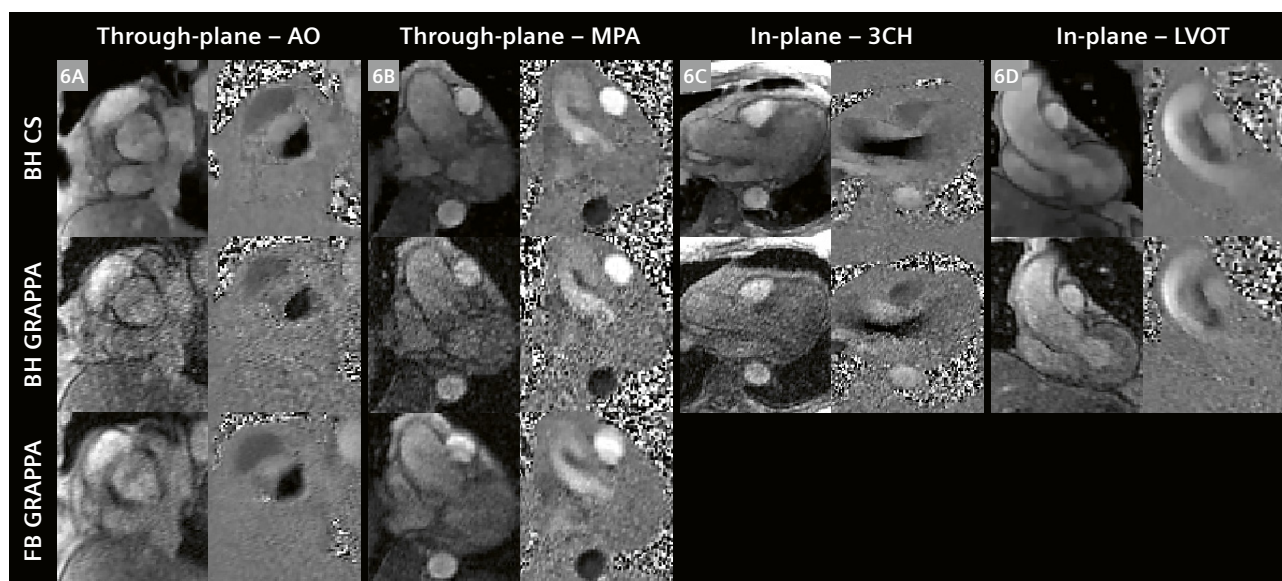
in comparison with GRAPPA parallel imaging are shown in Figure 6. In preliminary testing, CS-based reconstruction provides the high acceleration rates needed while maintaining spatial and temporal resolution and SNR. Real-time flow imaging requires significantly higher acceleration rates and is still under development, but free-breathing acquisition can be achieved through the use of signal averaging to suppress respiratory motion artifact, as also shown in Figure 6. Exemplary PC-MRI scan parameters are listed in Table 3. Although initial results demonstrate the feasibility of flow quantification on the MAGNETOM Free.Max, several sources of errors related to low-field and/or lower gradient performance (e.g., Maxwell-Terms and Flow Displacement Artifacts) are still under investigation.



5 Breath-held segmented *k*-space cine frames (**5A**) and real-time free-breathing cine frames (**5B**) acquired in a healthy volunteer. Despite use of a high under-sampling rate of near 10× in real-time cine, CS reconstruction provides sufficient image quality at 0.55T.

	Scanner	Flip angle (deg)	TE (ms)	TR (ms)	RBW Hz/pixel	Seg-ments	Temporal resolution (ms)	Slice thickness (mm)	Pixel size (mm)	Acceler-ation	Scan time
BH Flow	1.5T MAGNETOM Sola	15	2.26	4.23	501	5	42.3	6	2.0 × 2.0	G 2	10 HB
	0.55T MAGNETOM Free.Max	12	4.49	7.64	427	3	45.8	6	1.8 × 1.8	CS 3	13 HB
FB Flow	1.5T MAGNETOM Sola (RT)	12	2.51	4.41	560	6	52.9	10	2.8 × 2.8	CS 16	1 HB
	0.55T MAGNETOM Free.Max (avg)	12	3.67	6.55	427	3	39.3	8	1.9 × 1.9	G 2	58 HB

Table 3: Acquisition parameters for breath-hold segmented *k*-space flow quantification sequence (top rows) and free-breathing acquisition (bottom rows) shown for 1.5T MAGNETOM Sola and 0.55T MAGNETOM Free.Max. Free-breathing (FB) acquisition is currently achieved by signal averaging to suppress respiratory motion on MAGNETOM Free.Max, while real-time (RT) flow data acquisition is possible at 1.5T using compressed sensing. Real-time flow requires significantly higher acceleration, which is challenging in face of the reduced SNR at 0.55T.



6 Through-plane (**6A** aortic root and **6B** main pulmonary artery) and In-plane (**6C** 3-chamber view and **6D** left ventricular outflow tract) 2D phase contrast flow images acquired in a patient with a bicuspid aortic valve, aortic dilatation and aortic regurgitation. The top row shows magnitude and phase images acquired with a breath-held compressed sensing-based 2D PC MR sequence, while the middle row shows images from a breath-held GRAPPA sequence. Images in the bottom row were acquired free-breathing using a GRAPPA sequence with four averages to boost SNR. AO = aorta, MPA = main pulmonary artery, 3CH = cardiac 3-chamber view, LVOT = left ventricular outflow tract view.

Late Gadolinium Enhancement (LGE)

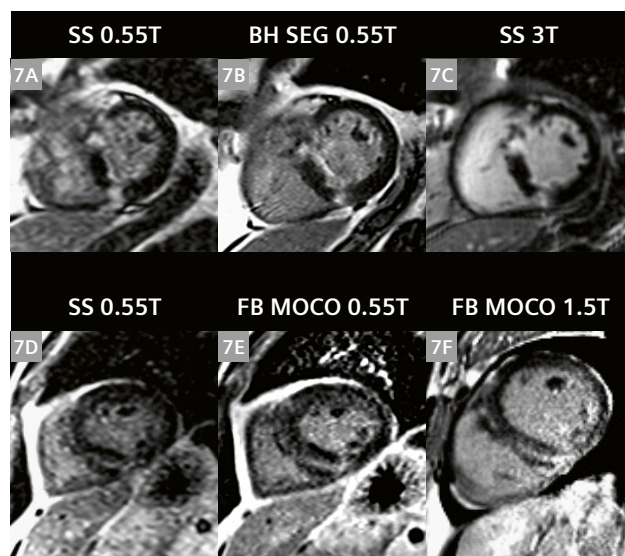
LGE provides unique information on myocardial tissue changes, including scar, fibrosis, and edema. We are currently optimizing both breath-hold segmented LGE and single-shot free-breathing LGE with motion correction and averaging, all based on bSSFP readout which provides high SNR. Exemplary scan parameters are listed in Table 4, along with 1.5T parameters for reference. Example images from two patients with non-ischemic cardiomyopathies showing segmented breath-hold, single-shot, and free-breathing, motion corrected LGE at 0.55T, along with comparative images acquired at 1.5T and 3T, are shown in Figure 7. Additional improvements in acquisition speed and image quality are anticipated as we incorporate compressed sensing into LGE image acquisition and reconstruction.

Gadolinium contrast agent T1 relaxivity is generally a function of field strength, and as shown by Campbell-Washburn et al., relaxivity at 0.55T may be slightly higher or lower than at 1.5T, depending on the particular agent [2]. All of the contrast-enhanced images shown here used gadobutrol, which may have a slightly lower (worse) relaxivity at 0.55T than at 1.5T. Additionally, because the native T1 times are shorter, the differential contrast enhancement at lower field may be less. Thus far, in our preliminary studies, we have observed the use of gadolinium-based contrast agent to be effective for the visualization of myocardial scar, perfusion defects, and blood pool in MRA, but careful studies are required to evaluate the diagnostic efficacy.

Myocardial relaxation parameter mapping

Myocardial longitudinal (T1) and transverse (T2) relaxation times are elevated with fibrosis, edema, and inflammation. Quantitative myocardial parameter mapping methods are being used clinically at higher field to evaluate these

pathological changes in myocardium that can accompany a variety of diseases. We implemented parameter mapping schemes for T1 and T2 taking into consideration the shorter T1 relaxation times and longer T2 relaxation times at 0.55T in comparison to higher field. The T1-mapping scheme was based on that typically used for post-contrast T1 mapping at 1.5T (4(1)3(1)2), with the addition of a fourth inversion pulse and two more images at the shorter



7 Top row (7A–7C) shows LGE images acquired in a patient with hypertrophic cardiomyopathy with fibrosis of the left ventricle. (7A) Single-shot inversion recovery prepared bSSFP image at 0.55T, (7B) breath-held segmented LGE image at 0.55T, and (7C) single-shot IR-prepared bSSFP LGE acquired on a 3T MAGNETOM Vida system for comparison. Bottom row (7D–7F) shows LGE images acquired in a different patient with non-ischemic septal mid-wall fibrosis. Single-shot (7D) and free-breathing motion-corrected averaged (7E) LGE images were acquired on MAGNETOM Free.Max, while the corresponding MOCO LGE image, shown in (7F), was acquired on a 1.5T MAGNETOM Sola system.

	Scanner	Flip angle (deg)	TE (ms)	TR (ms)	RBW Hz/pixel	Seg-ments	Temporal resolution (ms)	Slice thickness (mm)	Pixel size (mm)	Acceleration	Scan time
BH LGE	1.5T MAGNETOM Sola (GRE)	20	1.55	4.06	465	31	142	8	1.4 × 1.4	none	8 HB
	0.55T MAGNETOM Free.Max (bSSFP)	80	2.48	6.66	200	21	140	10	1.6 × 1.6	none	12 HB
MOCO LGE	1.5T MAGNETOM Sola (bSSFP)	50	1.18	2.79	1085	86	240	8	1.4 × 1.4	G 2	16 HB
	0.55T MAGNETOM Free.Max (bSSFP)	50	1.84	4.69	698	63	295	8	1.5 × 1.5	G 2	24 HB

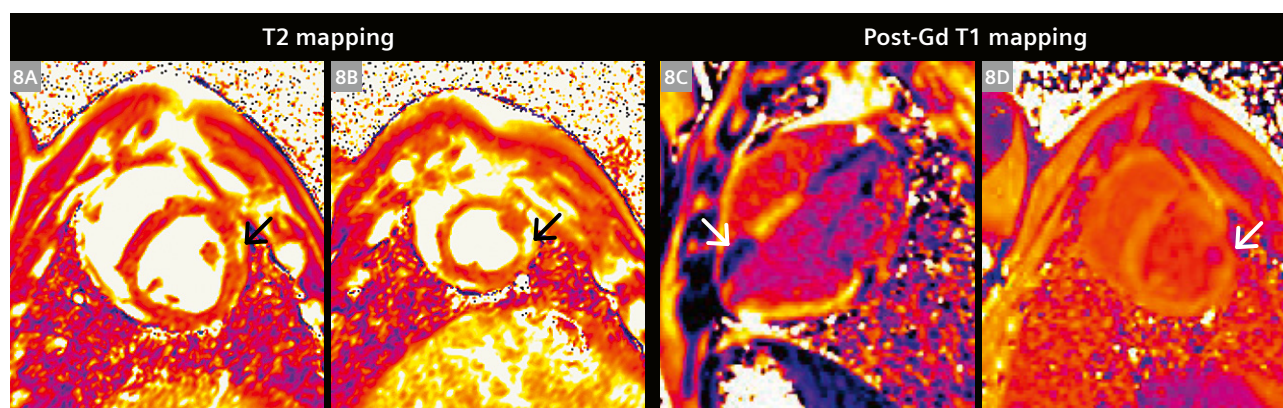
Table 4: Acquisition parameters for breath-hold segmented *k*-space LGE (top rows) and free-breathing LGE based on single-shot acquisition with motion correction (MOCO) and averaging (bottom rows) shown for 1.5T MAGNETOM Sola and 0.55T MAGNETOM Free.Max. Additional averages were used at 0.55T in the MOCO LGE scan to boost SNR. Note also that the standard segmented breath-hold approach at 1.5T and 3T typically utilizes a GRE readout, while bSSFP is employed at 0.55T to boost SNR. The higher B_0 homogeneity allows broader utilization of bSSFP without risk of dark band artifacts that could confound the interpretation of LGE, first pass perfusion, and other techniques where changes in myocardial signal intensity are of interest.

inversion times (4(1)3(1)2(1)2). The T2 mapping scheme was modified to acquire 6 source images at 3 different T2 preparation times (0, 25, and 60 ms). Scan parameters are listed in Table 5, along with typical parameters used at 1.5T for comparison. Results shown in Figure 8 acquired in a porcine infarct model at 0.55T utilized an increased number of source images to boost SNR through the pixel-wise parameter fitting process. We are continuing to work

on applying the same CS strategies that have been instrumental in boosting SNR and acceleration rates in cine and flow, and expect that this will improve SNR and sharpness in the resulting parameter maps, while reducing the scan duration. Prospective respiratory motion compensation techniques based on the Pilot Tone technology [11] are under development and will be used to further improve free-breathing methods.

	Scanner	Flip angle (deg)	TE (ms)	TR (ms)	RBW Hz/pixel	Segments	Temporal resolution (ms)	Slice thickness (mm)	Pixel size (mm)	Acceleration	Scan time
T1 mapping	1.5T MAGNETOM Sola	35	1.01	2.42	1085	60	145	8	2.0 × 2.0	G 2	11 HB
	0.55T MAGNETOM Free.Max	50	1.77	4.3	539	60	258	10	2.4 × 2.4	G 2	14 HB
T2 mapping	1.5T MAGNETOM Sola	70	1.04	2.43	1184	55	133	8	2.1 × 2.1	G 2	7 HB
	0.55T MAGNETOM Free.Max	70	1.69	4.18	558	60	250	10	2.4 × 2.4	G 2	16 HB

Table 5: Acquisition parameters for myocardial T1 mapping (top rows) and T2 mapping (bottom rows) listed for both 1.5T MAGNETOM Sola and 0.55T MAGNETOM Free.Max. Additional source images are acquired at 0.55T to boost SNR, leading to slightly longer scan times. Longer TR due to slower gradients also degrades temporal resolution, and this can cause some motion artifact at higher heart rates. Approaches to increase acceleration rate to improve temporal resolution are being developed using Compressed Sensing.



8 Myocardial T2 (8A, 8B) and post-Gd T1 (8C, 8D) maps acquired in a porcine model of acute myocardial infarction. These images, acquired five days post 90-minute occlusion-reperfusion of the left circumflex coronary artery, illustrate the feasibility of parameter mapping at 0.55T. Antero-lateral infarct is visible as regionally elevated T2 (black arrows in panels 8A and 8B), and shortened post-contrast T1 (white arrows in panels 8C and 8D).

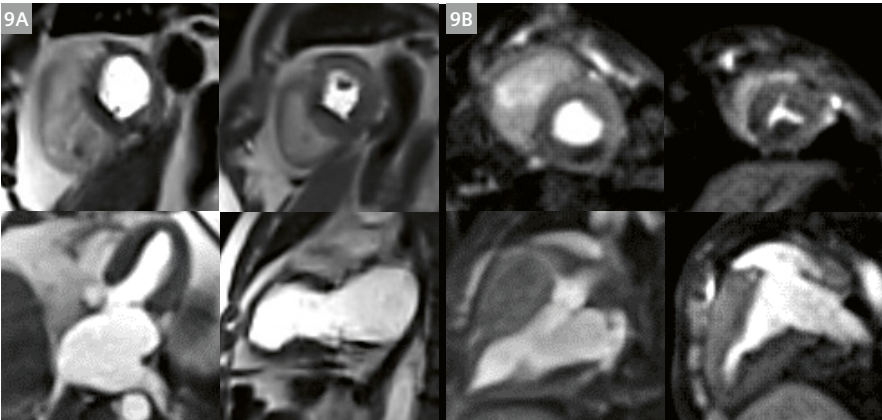
	Scanner	Flip angle (deg)	TE (ms)	TR (ms)	RBW Hz/pixel	Segments	Temporal resolution (ms)	Slice thickness (mm)	Pixel size (mm)	Acceleration	Scan time
First-pass Perfusion SR-bSSFP	1.5T MAGNETOM Sola (bSSFP)	50	1.04	2.5	1085	37	92.5	8	1.9 × 1.9	G 3	50 HB
	0.55T MAGNETOM Free.Max (bSSFP)	90	1.81	4.04	868	25	101	8	3.0 × 3.0	CS 4	50 HB

Table 6: Acquisition parameters for myocardial first-pass perfusion imaging for 1.5T MAGNETOM Sola (top row) and 0.55T MAGNETOM Free.Max (bottom row). Saturation-recovery (SR) bSSFP is used on both scanners. Compressed Sensing is used on MAGNETOM Free.Max to push the acceleration rate to 4× to overcome the longer TR, and to maintain SNR. Even with higher acceleration there is some compromise in spatial and temporal resolution when compared to 1.5T. Further investigation is required to determine the impact of these parameter differences.

First-pass perfusion

Gadolinium-enhanced first-pass perfusion imaging, combined with vasodilator stress, is the most critical component of the CMR evaluation of patients with known or suspected ischemic heart disease. With the requirements

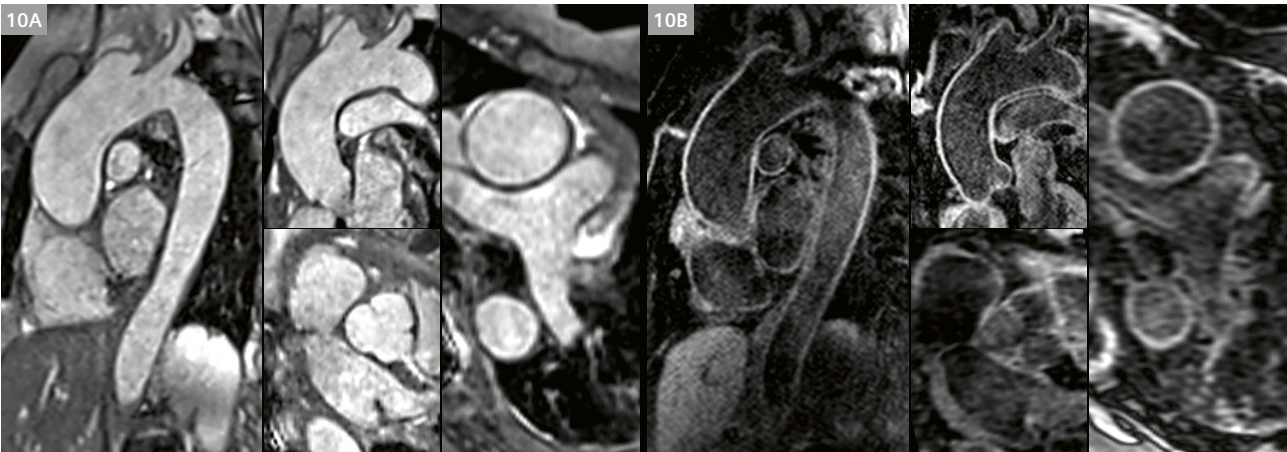
of delivering multi-slice coverage within a single heartbeat, and high T1-contrast images with little motion artifact, first-pass perfusion imaging pushes the speed and SNR limits of CMR even at higher field. Whether or not these requirements can be met at lower field with reduced



9 Rest perfusion images indicate perfusion defect in a patient with hypertrophic cardiomyopathy (9A) and in a porcine model with left circumflex artery infarct (9B).

	Scanner	Flip angle (deg)	TE (ms)	TR (ms)	RBW Hz/pixel	Segments or turbo factor	Temporal resolution (ms)	Slice thickness (mm)	Pixel size (mm)	Acceleration	Scan time
non-contrast MRA navigator bSSFP	1.5T MAGNETOM Sola	90	1.45	3.38	592	35	118	1.3	1.6 × 1.6	G 2	78 HB
	0.55T MAGNETOM Free.Max	110	1.89	4.61	501	35	161	1.5	1.6 × 1.6	G 2	142 HB
non-contrast MRA navigator SPACE	1.5T MAGNETOM Sola	variable	23	1RR	744	35	130	1.3	1.3 × 1.3	G 2	205 HB
	0.55T MAGNETOM Free.Max	variable	23	1RR	630	25	214	1.3	1.6 × 1.6	G 2	289 HB
Gd ce-MRA ECG gated GRE	1.5T MAGNETOM Sola	30	1.25	2.97	591	100	297	1.4	1.4 × 1.4	CS 9	10 HB
	0.55T MAGNETOM Free.Max	30	1.71	3.68	781	80	294	1.5	1.6 × 1.6	CS 7	13 HB

Table 7: Acquisition parameters for 3D MR angiography (MRA) sequences used on the 1.5T MAGNETOM Sola and 0.55T MAGNETOM Free.Max. Three different techniques are listed: 3D navigator respiratory gated bSSFP (top rows), 3D navigator gated dark-blood SPACE (middle rows), and 3D contrast enhanced ECG-gated MRA. Some compromises are made in spatial resolution on the MAGNETOM Free.Max to offset reduced SNR and gradient speed.



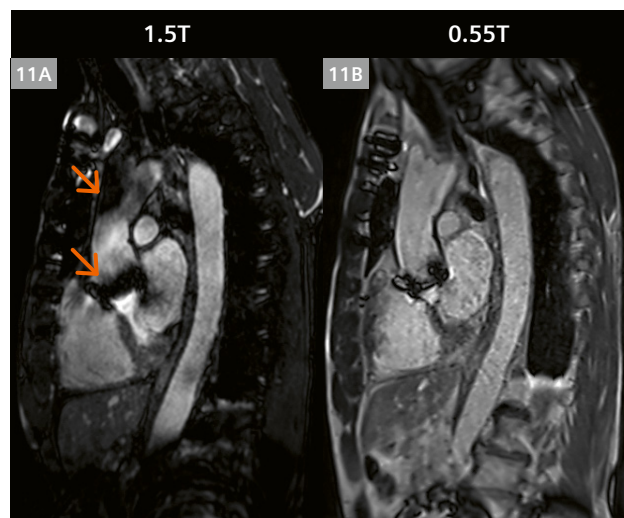
10 2D reformatted images from non-contrast 3D MRAs acquired in a patient with Harrington spinal rods² being evaluated for aortic dilatation. Images in (10A) show reconstructions from a bright-blood ECG-triggered, navigator gated bSSFP MRA, while (10B) shows reconstructions from a dark-blood 3D SPACE sequence used to highlight vessel wall anatomy.

gradient performance is an important question. We have experimented with a bSSFP perfusion sequence (parameters listed in Table 6) that applies the same CS-based approach to data sampling and reconstruction [9] that has been successfully utilized to accelerate real-time cine imaging without sacrificing SNR. While this method has yet to be tested with vasodilator stress, initial results acquired at rest in a porcine model of myocardial infarction, and in volunteers and patients, are promising (Fig. 9).

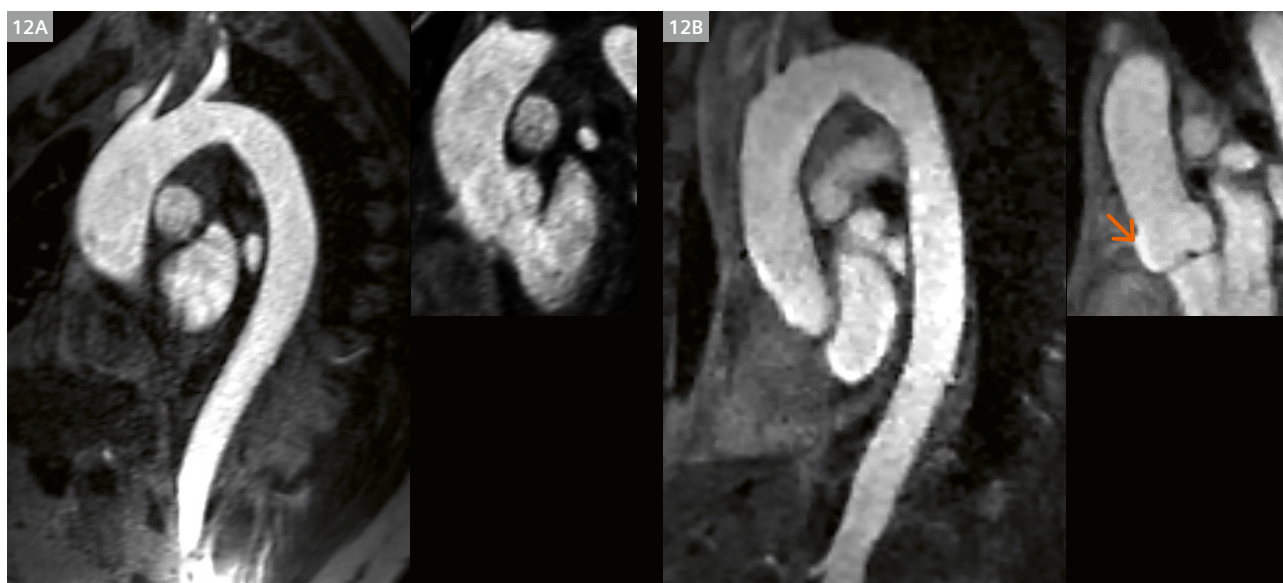
MR Angiography

Thoracic MR angiograms of the aorta, pulmonary arteries, and pulmonary veins form an important component of the comprehensive cardiovascular imaging exam in many of our patients. While the standard method is contrast-enhanced MR angiography (ce-MRA), non-contrast MRA using a 3D bSSFP sequence with navigator respiratory gating is now being utilized more frequently at our institution. We also frequently employ a 3D dark blood SPACE sequence to visualize vessel wall morphology; SPACE is also less sensitive to metal artifact around implants². Parameters for all three methods are listed in Table 7 for 0.55T and 1.5T. We have implemented and investigated all three of these MRA techniques in volunteers and patients. Contrast-enhanced MRA has been tested both with and without ECG gating, while the non-contrast technique is always ECG-triggered. ECG-gated ce-MRA places high demands on acceleration and we have employed a CS-based technique to maintain high spatial resolution and a reasonable breath-hold duration of 18 heartbeats or less.

Navigator-gated non-contrast MRA data were acquired during free-breathing with scan times of 6 minutes or less, depending on heart rate and the extent of anatomical coverage. 3D SPACE acquisition times are longer as signal averaging is used at both 1.5T and 0.55T. Examples of non-contrast and contrast-enhanced MRA acquired at 0.55T are shown in Figures 10, 11, and 12.



11 2D reformatted images from ECG triggered, navigator gated non-contrast enhanced 3D bSSFP MRA scans acquired in the same patient at 1.5T (**11A**) and at 0.55T (**11B**). This patient has an artificial aortic valve² and sternal wires. The extent of signal dephasing artifacts (orange arrows) seen at 1.5T are reduced at 0.55T. Cine images from this patient are shown in Figure 4.

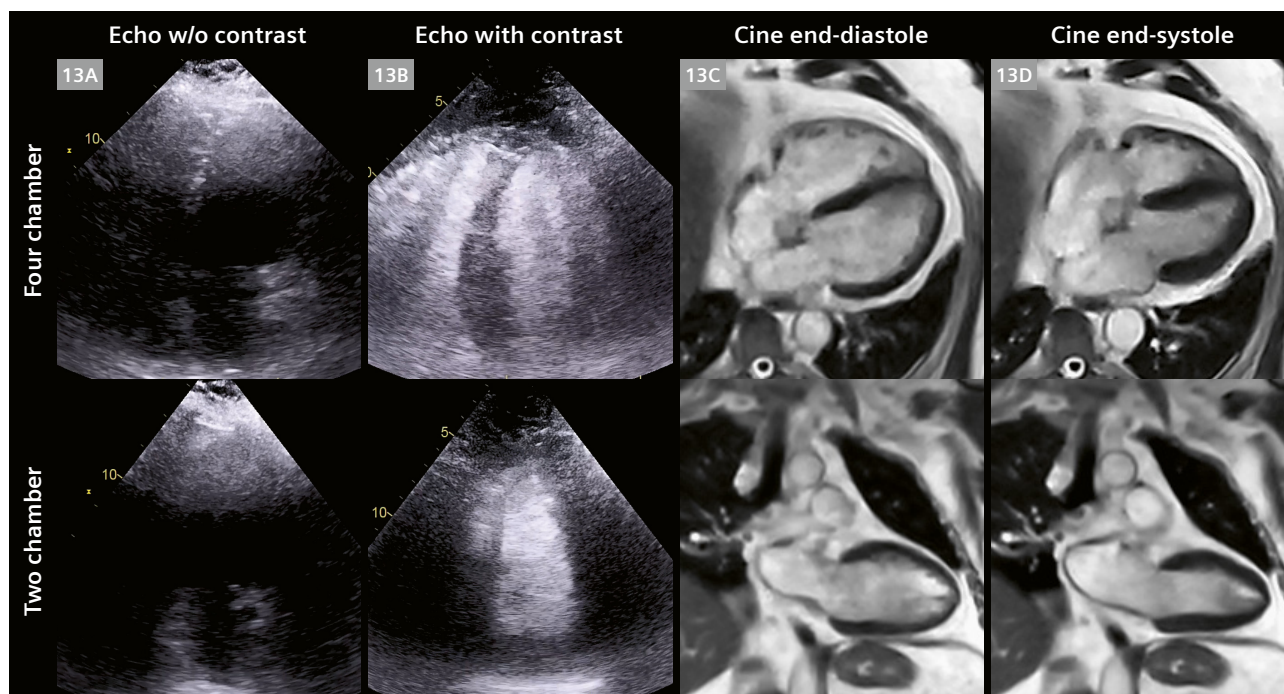


12 2D reformatted images from 3D contrast-enhanced (ce-)MRA scans in two different subjects. On the left (**12A**) a non-gated contrast-enhanced 3D MRA acquired in an obese patient shows a dilated thoracic aorta. The patient was unable to proceed with a cardiac MR exam in a standard 70 cm bore MR system but successfully completed an evaluation on the MAGNETOM Free.Max; additional images from this patient are shown in Figure 13. On the right (**12B**) is an ECG-gated ce-MRA scan from a healthy volunteer. Note the clear delineation of the aortic root and valve leaflets in the gated MRA (orange arrow), as compared to the non-gated MRA.

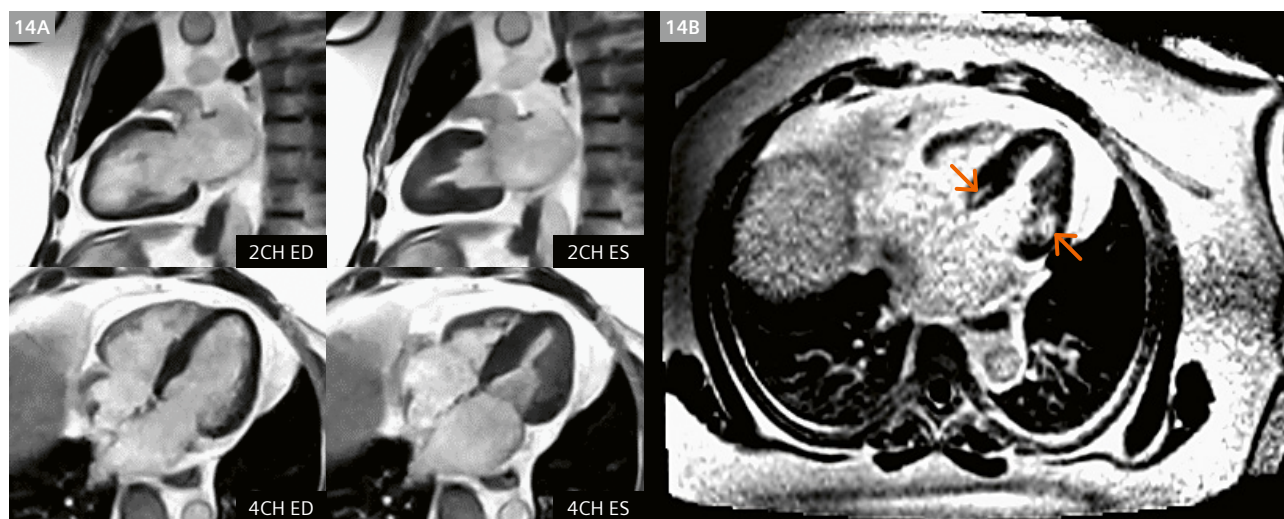
Putting it all together

After compiling the sequences required to cover all of the basic cardiac imaging applications, we have recently begun to identify and scan severely obese patients who were referred for clinical CMR, but whose body habitus made it

impossible, or too uncomfortable, to be scanned on systems with a standard 70 cm bore diameter. In Figure 13, images acquired on the MAGNETOM Free.Max are shown from a patient weighing 350 lbs / 159 kg with BMI > 48 being evaluated for possible cardiomyopathy and dilated



13 4-chamber view (top row) and 2-chamber view (bottom row) echocardiographic (13A without contrast, and 13B with contrast) and CMR images (13C end-diastole, and 13D end-systole) acquired in an obese patient with BMI > 48 kg/m². Echo image quality is degraded by large body habitus, and this patient could not fit into a 70 cm magnet bore. The MAGNETOM Free.Max provides access to MRI for severely obese patients for whom no other good options exist for cardiac imaging. MRA for this patient is shown in Figure 12.



14 Example images from a patient weighing 410 lbs / 186 kg with BMI 57 kg/m². This patient being evaluated for cardiomyopathy, was unable to complete the exam on a 70 cm bore system. Compressed Sensing-based breath-held segmented bSSFP cine images acquired on the MAGNETOM Free.Max are shown in panel (14A) on the left. End-diastolic and end-systolic cardiac phases are shown. In panel (14B) on the right is shown an LGE image acquired during free-breathing using the technique of single-shot motion corrected (MOCO) imaging with averaging. Basal regions of enhancement (orange arrows) indicate areas of fibrosis.

aorta. While the weight of this patient can be accommodated by most scanners, their body habitus prevented them from fitting into a 70 cm bore. They were comfortably scanned on the MAGNETOM Free.Max, and the bSSFP cine images are shown here in comparison to echocardiography images acquired with and without echo contrast. The echo image quality is poor, and MAGNETOM Free.Max offers the potential for high-quality cardiac imaging for these severely obese patients in whom other modalities including echo and CT may be limited. The contrast-enhanced MR angiogram acquired in this patient is shown in Figure 12. MAGNETOM Free.Max images from another patient with a BMI of 57 (weight 410 lbs / 186 kg) diagnosed with heart failure with preserved ejection fraction (HFpEF) being evaluated for cardiomyopathy are shown in Figure 14. This patient was able to initially enter the bore of a 70 cm scanner, but was too uncomfortable to complete the exam. The patient reported being comfortable in the MAGNETOM Free.Max. The exam, including cine and LGE imaging was successfully completed, revealing normal biventricular function, but scarring evident at the base of the left ventricle.

Summary

While this project to develop and optimize cardiac imaging techniques for the 0.55T MAGNETOM Free.Max is still in relatively early stages, the images and results obtained thus far show great promise for the breadth of techniques and image quality that this system will be able to deliver in the future. We will continue to explore the cardiac imaging potential for this ultra-wide bore 0.55T system and anticipate that in the near future it will provide a solution to accurately diagnose and guide clinical cardiovascular care of patients with severe obesity, as well as those with severe claustrophobia.

Acknowledgements

The entire OSU CMR team, and Siemens Healthineers collaborators. Funding support from National Heart Lung and Blood Institute (R01HL161618) and The Robert F. Wolfe and Edgar T. Wolfe Foundation. Columbus, Ohio, USA.

References

- 1 Simonetti OP, Ahmad R. Low-Field Cardiac Magnetic Resonance Imaging: A Compelling Case for Cardiac Magnetic Resonance's Future. *Circ Cardiovasc Imaging*. 2017;10(6):e005446.
- 2 Campbell-Washburn AE, Ramasawmy R, Restivo MC, Bhattacharya I, Basar B, Herzka DA, et al. Opportunities in Interventional and Diagnostic Imaging by Using High-Performance Low-Field-Strength MRI. *Radiology*. 2019;293(2):384-393.
- 3 Hales CM, Carroll MD, Fryar CD, Ogden CL. Prevalence of Obesity and Severe Obesity Among Adults: United States, 2017-2018. *NCHS Data Brief*. 2020;(360):1-8.
- 4 Virani SS, Alonso A, Aparicio HJ, Benjamin EJ, Bittencourt MS, Callaway CW, et al. Heart Disease and Stroke Statistics-2021 Update: A Report From the American Heart Association. *Circulation*. 2021;143(8):e254-e743.
- 5 Fursevich DM, Limarzi GM, O'Dell MC, Hernandez MA, Sensakovic WF. Bariatric CT Imaging: Challenges and Solutions. *RadioGraphics*. 2016;36(4):1076-1086.
- 6 Finkelhor RS, Moallem M, Bahler RC. Characteristics and impact of obesity on the outpatient echocardiography laboratory. *Am J Cardiol*. 2006;97(7):1082-1084.
- 7 Varghese J, Craft J, Crabtree CD, Liu Y, Jin N, Chow K, Ahmad R, Simonetti OP. Assessment of cardiac function, blood flow and myocardial tissue relaxation parameters at 0.35 T. *NMR Biomed*. 2020;33(7):e4317.
- 8 Bandettini WP, Shanbhag SM, Mancini C, McGuirt DR, Kellman P, Xue H, et al. A comparison of cine CMR imaging at 0.55 T and 1.5 T. *J Cardiovasc Magn Reson*. 2020;22(1):37.
- 9 Chen C, Liu Y, Schniter P, Jin N, Craft J, Simonetti O, et al. Sparsity adaptive reconstruction for highly accelerated cardiac MRI. *Magn Reson Med*. 2019;81(6):3875-3887.
- 10 Jin N, Liu Y, Chen C, Giese D, Ahmad R, Simonetti O. Highly accelerated 2D phase contrast imaging on a low-field 0.55T MRI system. *ISMRM Workshop on Low Field MRI*, March 2022.
- 11 Speier P, Fenchel M, Rehner R. PT-Nav: a novel respiratory navigation method for continuous acquisitions based on modulation of a pilot tone in the MR-receiver. *ESMRMB 2015, 32nd Annual Scientific Meeting, Edinburgh, UK, 1-3 October: Abstracts, Thursday, Magnetic Resonance Materials in Physics, Biology and Medicine*. 2015; 28:1-135.



Contact

Orlando P. Simonetti, PhD, MScMR, FISMRM, FAHA
John W. Wolfe Professor of Cardiovascular Research
Professor of Internal Medicine and Radiology
The Ohio State University
Biomedical Research Tower
460 W. 12th Ave.
Columbus, OH 43210
USA
Tel.: +1 614-293-0739
Orlando.Simonetti@osumc.edu

How to Deal with Arrhythmia in Cardiac MRI

Tilman Emrich, M.D.¹; Bart Schraa, MSc.²; Anna Wing Fai Lam, MRT(MR)(R)⁴; Christian P. Houbois, M.D.^{3,4}

¹Department of Radiology and Radiological Science, Medical University of South Carolina, Charleston, USA

²Siemens Healthineers, Oakville, Ontario, Canada

³Department of Medical Imaging, University of Toronto, Toronto, Ontario, Canada

⁴Department of Medical Imaging, Sunnybrook Health Sciences Centre, Toronto, Ontario, Canada

Introduction

Cardiac magnetic resonance imaging (CMR) in patients with arrhythmia is challenging. This article discusses indications, imaging techniques, and issues with CMR in arrhythmia. Furthermore, it provides solutions for improving image quality and suggests a workflow for dealing with arrhythmia during the examination process.

Arrhythmias are common and affect electrical conduction throughout the heart. They can range from benign to life-threatening and be caused by various factors. The management of arrhythmias requires accurate diagnosis and characterization of the underlying mechanism, which is often challenging. Multiparametric myocardial tissue characterization with CMR provides insights into the underlying causes of various cardiomyopathies. In recent years, CMR has become an established imaging modality in clinical routine to assess structural heart disease. However, it is challenging to perform a high-quality CMR examination in patients with arrhythmia. This is because the condition often causes image artifacts, which make qualitative and quantitative analyses difficult.

Arrhythmias may result in skipped or ectopic heartbeats, causing issues with data acquisition and image reconstruction. This results in degraded image quality and therefore inferior diagnostic accuracy. To solve this issue, different image acquisition approaches are available to improve image quality. However, in some scenarios, they may increase scan time. An often-used approach is arrhythmia detection/rejection [1]. This software-based solution can be applied to balanced steady-state free precession sequences (bSSFP, or TrueFISP) when using retro gating to cover the complete cardiac cycle, but it increases scan time. Real-time cine imaging is a different approach where all data needed is acquired in a single heart-beat, but one that comes at the cost of image quality [2]. In recent years, new techniques such as compressed sensing have become available [3]. Compressed sensing accelerates the

acquisition and reduces scan time in the case of segmented imaging or increases resolution in case of single-shot real-time imaging. An alternative is prospective triggering [1] and reducing the acquisition window to more or less only covering the systole. All these approaches may overcome issues with arrhythmia in CMR and make the scan more efficient with substantially better image quality.

Indications: Why is CMR important in arrhythmia patients?

Patients suffering from arrhythmia may have various underlying causes of cardiomyopathies. In non-ischemic cardiomyopathies (NICM), left ventricular ejection fraction (LVEF) is the primary marker to decide whether patients need a cardiac resynchronization therapy pacemaker (CRT-P) or a cardiac resynchronization therapy defibrillator (CRT-D), also known as implantable cardioverter defibrillator (ICD). Depending on the type of heart failure, these devices are either for primary prevention of cardiac arrest or to improve cardiac function. Typically, this is considered an indication if the LVEF is < 35%. However, some patients with NICM may be eligible for pacemaker/ICD placement, even when the LVEF is > 35%.

The first-line imaging modality for cardiac assessment is echocardiography. However, it lacks myocardial fibrosis analysis. CMR can help to identify the underlying causes of NICM and can further risk-stratify patients with multiparametric tissue characterization, mainly based on late gadolinium enhancement (LGE) [4]. CMR with LGE may help identify arrhythmogenic substrates. In patients with ventricular arrhythmias, CMR can identify structural heart disease in up to 25% of cases (e.g., myocarditis, arrhythmogenic right ventricular cardiomyopathy, dilated cardiomyopathy), even when patients have a normal echocardiography [5].

With regards to interventional procedures such as myocardial ablation, a pre-procedural CMR is essential to assess for areas of fibrosis, which are potential arrhythmogenic correlates. There is also a strong association between areas of LGE and ECG findings [6]. CMR also demonstrates efficacy in arrhythmia recurrence after ablation. This suggests CMR can be used to determine the optimal ablation approach, and therefore decrease the overall time required for the ablation procedure.

Usually, LGE imaging is performed with 2D inversion recovery T1-weighted sequences. However, a fast and high-resolution isotropic approach is needed to identify small areas of fibrosis. A suitable technique is 3D LGE imaging, which allows for more detailed LGE information. Data is available using a 3D LGE compressed sensing (CS) research application¹ with higher image quality and spatial resolution than 2D inversion recovery T1-weighted sequences. Recent publications have shown promising results with 3D LGE in combination with compressed sensing or other acceleration techniques [7–9] but these are not widely available yet.

Issues and problems with arrhythmia

CMR is the reference standard for assessing cardiac function and volumes [10]. However, in patients with arrhythmias, quantitative analysis can be hampered. This may have different causes, such as ectopic beats, atrial fibrillation, or issues with breath-holding. As a result of suboptimal image acquisition, image quality is degraded. Most commonly, images are blurred, which substantially decreases the delineation of the heart's epi- and endocardial contours [11]. This contributes to inaccurate cardiac volumes and function determination, and lower accuracy.

¹Work in progress. The product is still under development and not commercially available. Its future availability cannot be ensured.

Techniques behind arrhythmia imaging and how to improve image quality

There are several strategies for arrhythmia imaging, depending on the severity of the irregular heartbeats.

1. Cine imaging strategies

a) Standard retrospective gating

Usually, regular segmented TrueFISP cine images are acquired during a breath-hold over several heart-beats for one to three slices in a retrospective fashion. Retrospective image acquisition of a defined RR interval is performed after triggering the ECG R-peak to the next heartbeat. All image data is collected and, during the reconstruction process, assigned to a specific cardiac phase. Retrospective gating assumes a periodicity of the temporal motion of the heart. Hence, this method may be prone to arrhythmic heartbeats as the final image is based on data from several heartbeats, which will lack a constant periodicity in cases of arrhythmia. Therefore, arrhythmic heartbeats may result in image artifacts and degrade image quality.

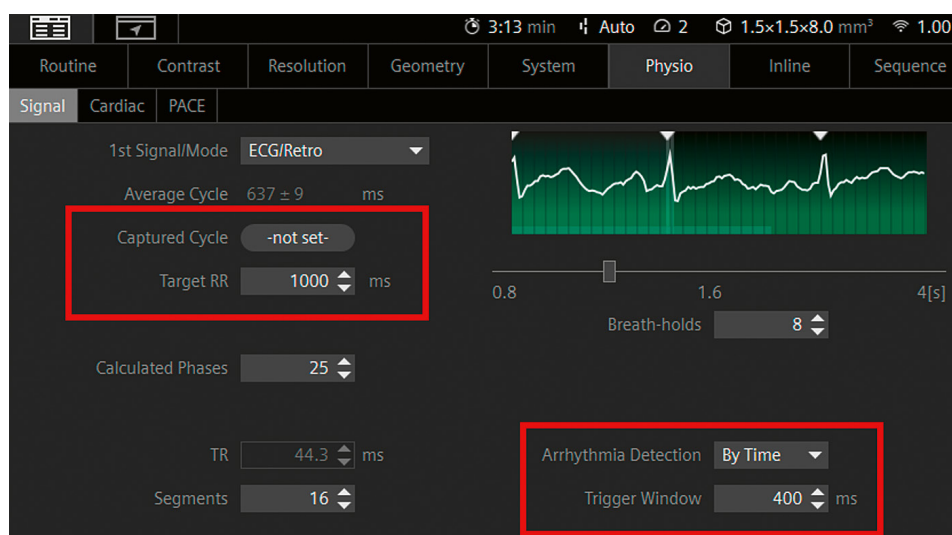
One way of dealing with relatively mild arrhythmia is to use arrhythmia detection/rejection. This method allows the rejection of irregular RR intervals and relies on cardiac frequency as the basis of a regular heart rate. Variations in the RR interval over a certain threshold are rejected and not used for image reconstruction. In addition, another heartbeat after the arrhythmic one will not be used (Fig. 1).

While this imaging technique might improve image quality in mild arrhythmias, it may be inefficient for specific patient populations as it increases scan time due to the rejection of specific cardiac cycles. It may be prone to errors in specific, "constant" arrhythmias, such as long-short-long RR intervals.

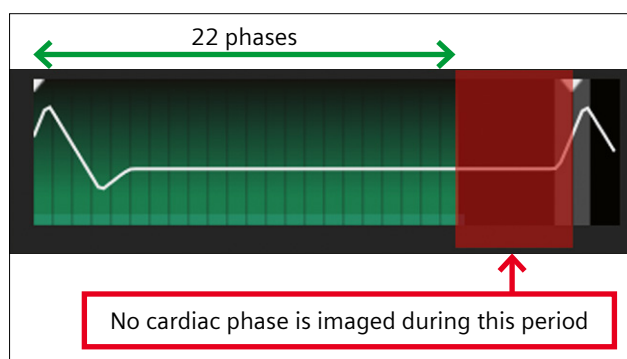
To use arrhythmia detection, switch it on ("By Time") in the Physio/Signal card (Fig. 2). Next, set the target RR



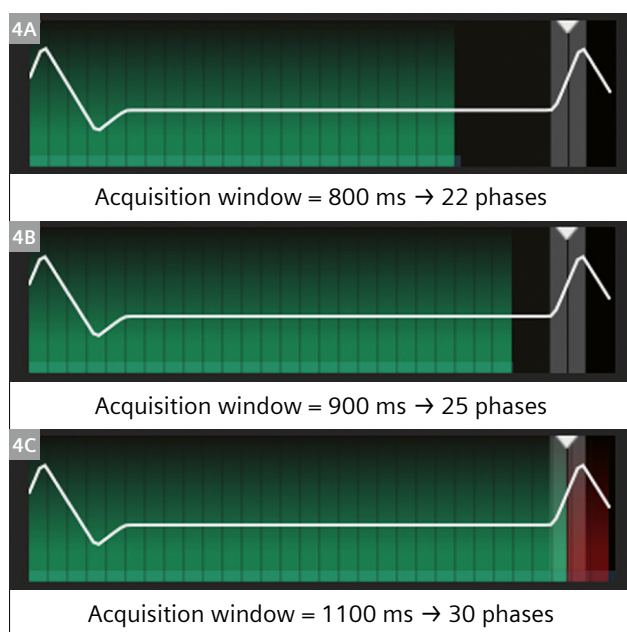
1 Arrhythmia detection: rejecting heartbeats.



- 2 Regular retrospective gated TrueFISP cine sequence with arrhythmia detection turned on.



- 3 Influence of acquisition window on coverage of the cardiac cycle.



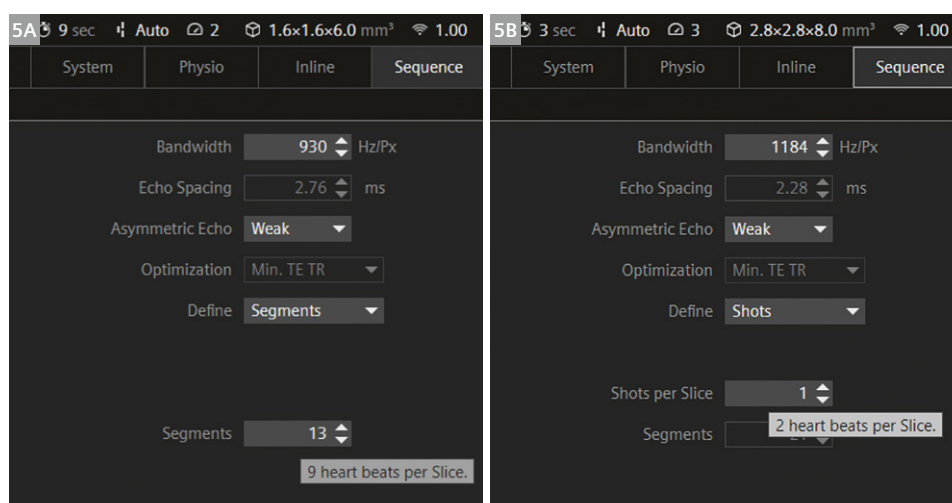
- 4 Influence of acquisition window on coverage of the cardiac cycle and number of phases: RR interval = 1000 ms, TR = 35.9 ms.

to the value that would be the “normal” RR interval (Fig. 2, left red box). This setting will allow the heartbeats with an RR interval of target RR $\pm \frac{1}{2}$ trigger window, which in this case is 800–1200 ms. The larger the trigger window, the more heartbeats are accepted, which may lead to blurrier images. A smaller window may lead to more heartbeats being rejected, but better image quality. However, that can come at the cost of longer scan times since more heartbeats need to be re-acquired, potentially leading to breath-holding times that exceed the patient’s capabilities.

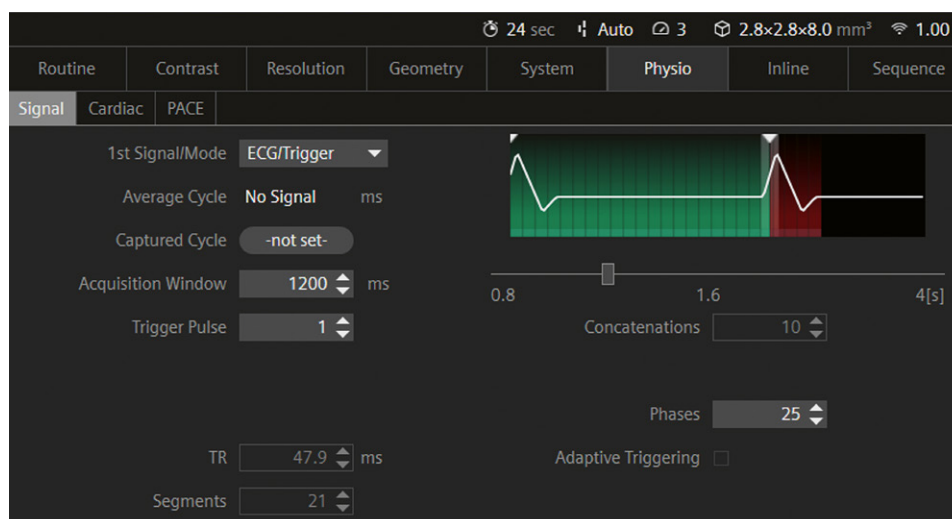
b) Prospective ECG gating

Another option for more severe arrhythmias is prospective ECG triggering. Data acquisition starts after estimating the number of cardiac phases within an RR interval. The data acquisition is triggered by each R-wave and stopped after the data of the estimated number of phases has been acquired. This means that part of the cardiac cycle is not captured in the images mainly end-diastole (Fig. 3).

The acquisition window can be set automatically by pressing the Captured Cycle button. However, it can also be set manually, and this might be the better choice when the RR interval changes from beat to beat. In both cases, watch the coverage of the cardiac cycle with the set acquisition window before applying the protocol to ensure the correct value has been set. The influence of the number of phases on capturing the cardiac cycle can be seen in Figure 4. When the number of phases is too low, a relatively long cardiac cycle phase is not imaged (Fig. 4A). The best scenario would be to stay as close as possible to the RR interval to ensure that as much of the cardiac cycle is visualized as possible (Fig. 4B). If the number of cardiac phases is chosen too high, more than the RR-to-RR interval is imaged. This would result in missing the R-wave for triggering, leading to degraded image quality and double the scan time (Fig. 4C).



- 5** Segmented cine vs. real-time cine; (5A) segmented cine 1 + 8 heartbeats, (5B) real-time cine, 1 + 1 heartbeats.



- 6** Acquisition window in triggered real-time cine imaging.

In case of more severe arrhythmias, this technique may be used by setting the acquisition window to the shortest RR interval. However, this strategy will result in time intervals with no data collection. Therefore, it will underestimate quantitative parameters of the cardiac cycle outside of rather basic parameters such as ejection fraction. Some cardiac analysis software packages may not be able to handle stacks with a varying number of phases for ventricular analysis. They require a constant number of phases throughout the whole short-axis stack.

c) Real-time imaging

In the worst-case arrhythmic scenarios such as atrial fibrillation, bigeminy, or premature ventricular contractions, both strategies mentioned above may fail to produce reliable CMR images. Hence, developments over recent decades have introduced real-time imaging, which may be extremely helpful in severe arrhythmia. Real-time imaging is based on fast imaging sequences, which allow imaging with high (sub-second) temporal resolution [1]. Each

cardiac phase is taken as a single shot instead of regular cine imaging, where data is collected over several heartbeats (typically 6 to 10) for each phase.

The first option is to use the R-wave to trigger data collection and then collect data over at least one heartbeat (Fig. 5). Each protocol has one dummy heartbeat to achieve a steady state before data collection. While the segmented cine collects the data over eight heartbeats, the real-time cine collects all cardiac phases in just one heartbeat.

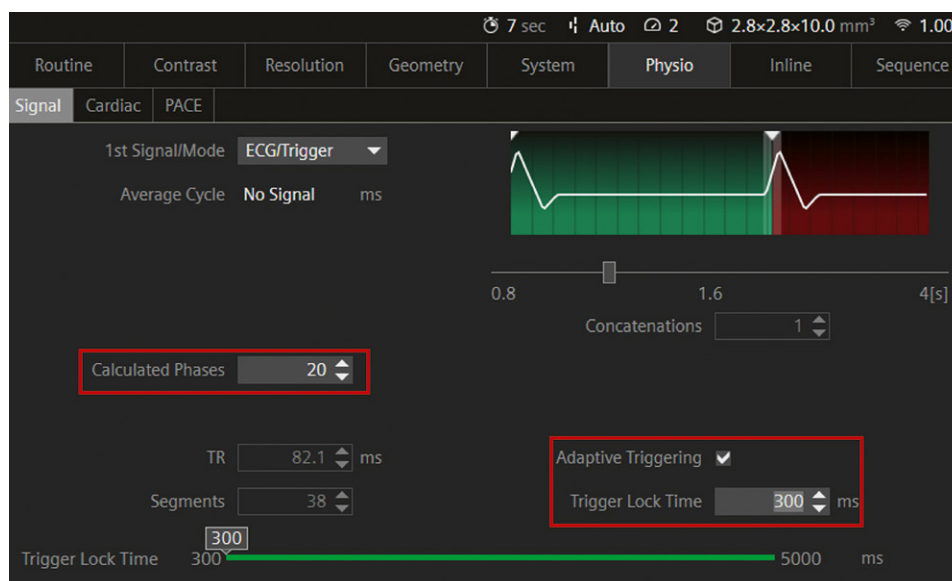
When using the real-time cine, the acquisition window should be set longer than the longest expected RR interval to ensure that the complete cardiac cycle is visualized. For example, when the RR interval is 1000 ms, the acquisition window should be set to 1200 ms, as shown in Figure 6. The data collected here can still be used for ventricular analysis, provided that the number of cardiac phases is the same over the complete short-axis images, but would require (manually) setting the diastolic and systolic phases in the postprocessing software.

The second option for real-time cine imaging is to use prospective adaptive triggering. Adaptive triggering will make sure that the same number of images are calculated for each slice, regardless of the number of phases that could be collected, and ensures that there are no issues with post-processing the images for ventricular analysis (Fig. 7).

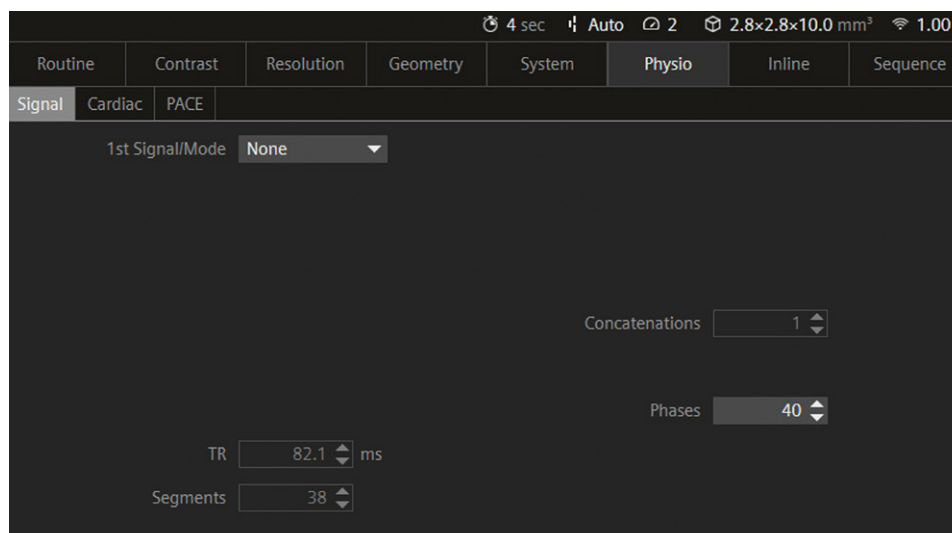
The number of calculated phases can be set in the same way as for retrospective cine imaging. The trigger lock time defines the minimum acquisition window, which can exclude (very) short RR intervals within the acquisition of the short-axis stack. The advantage of using adaptive triggering is that the whole cardiac cycle is covered and that the same number of images are acquired for each slice, and each slice contains all phases between two RR intervals, like retrospective cine imaging.

The second option is to use no trigger at all for real-time images. The only thing to consider here is to ensure that at least one full cardiac cycle is covered. Since no R-wave is used as a trigger, there is also no acquisition window to set. Therefore, we need to make sure that we collect enough phases to cover a full RR cycle. This scan length is determined by defining the number of phases, for example, 3284 ms (40×82.1 ms) (Fig. 8).

This technique is relatively robust to motion and allows the acquisition of images without gating: During free breathing, all image data from a full cardiac cycle will be acquired. However, the high temporal resolution limits the image quality and spatial resolution of conventional real-time images. Therefore, combining real-time imaging with other strategies, such as efficient sampling



7 Real-time imaging with adaptive prospective triggering.



8 Number of phases in non-triggered real-time cine imaging.

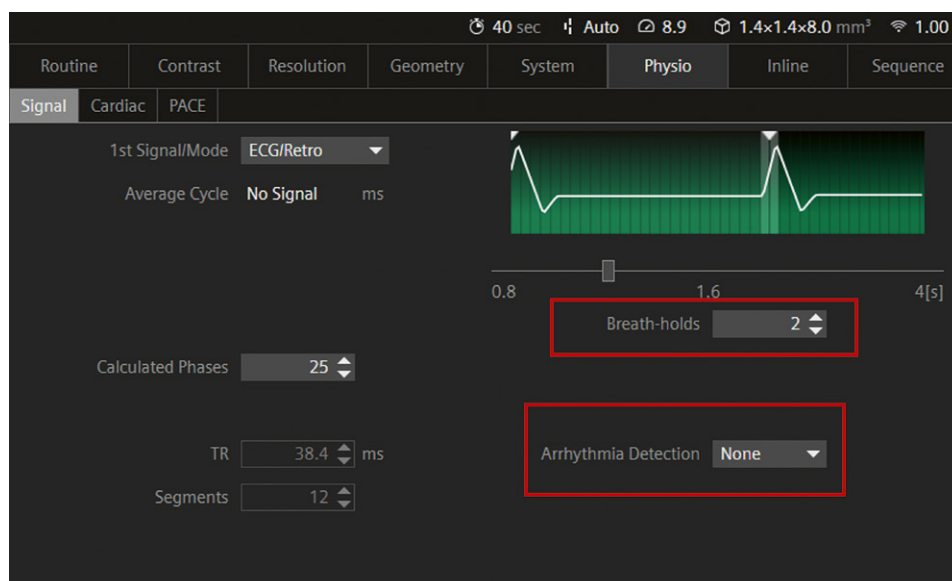
trajectories and reconstruction techniques, has shown benefits when acquiring 2D and 3D cardiac imaging with high spatiotemporal resolution [1]. One of these strategies is the combination of real-time imaging with CS. Compressed sensing is a way of accelerating MRI acquisition by acquiring fewer data through random under-sampling of the k -space. Random under-sampling of k -space will lead to noise-like artifacts in the image, which are reduced by exploiting the inherent data sparsity (compressibility of imaging data) and nonlinear iterative reconstructions. This combination enables the acquisition of cardiac images during free breathing at a similar temporal and spatial resolution with comparable image quality to conventional segmented TrueFISP cine sequences, but with the acquisition time of the real-time sequence. In other words, data is

collected within two heartbeats, and the entire short-axis stack can be acquired in just two breath-holds (Fig. 9).

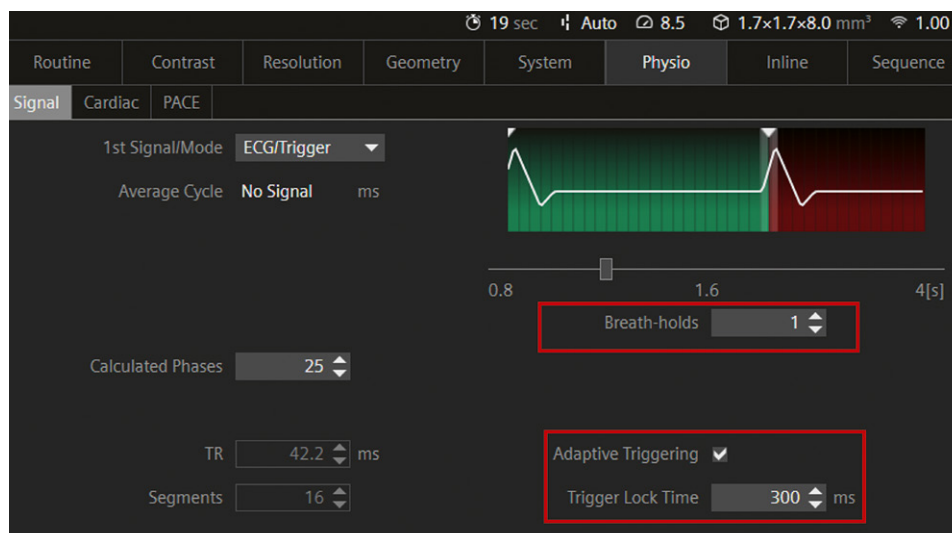
Real-time cine imaging can also be combined with CS, which only needs one heartbeat per slice for data collection and produces images much closer to segmented cine imaging. When used with adaptive triggering, the complete cardiac cycle is visualized in just one breath-hold (Fig. 10).

There is growing evidence that the techniques described above can acquire reliable basic quantitative parameters, such as ventricular volumes and ejection fraction, with high correlation and good agreement to conventional sequences, even in patients with arrhythmias [12–16]. However, under-sampling of the cardiac cycle (e.g., by prospective gating or dedicated k -space sampling)

- 9** Retrospectively gated CS cine sequence without using arrhythmia detection. This is a protocol with 10 slices to cover a complete short-axis stack.



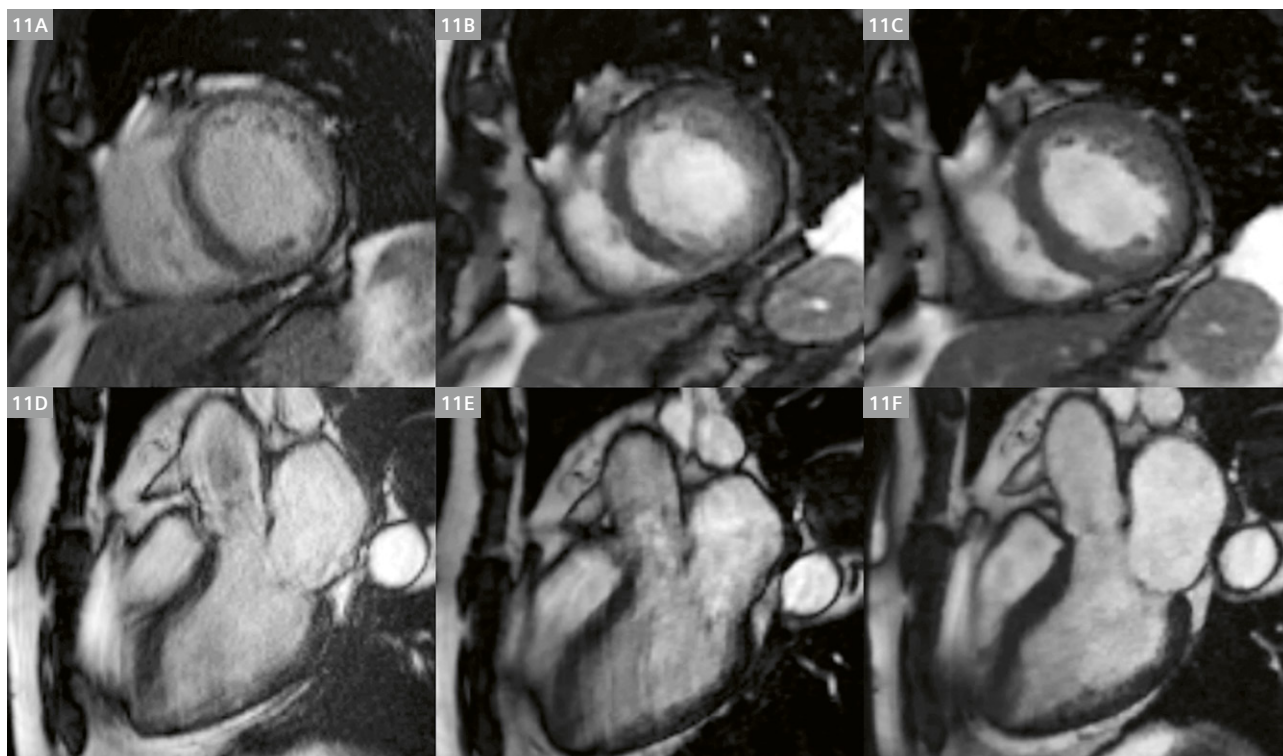
- 10** CS real-time cine imaging with adaptive triggering. This is a protocol with 10 slices to cover a complete short-axis stack.



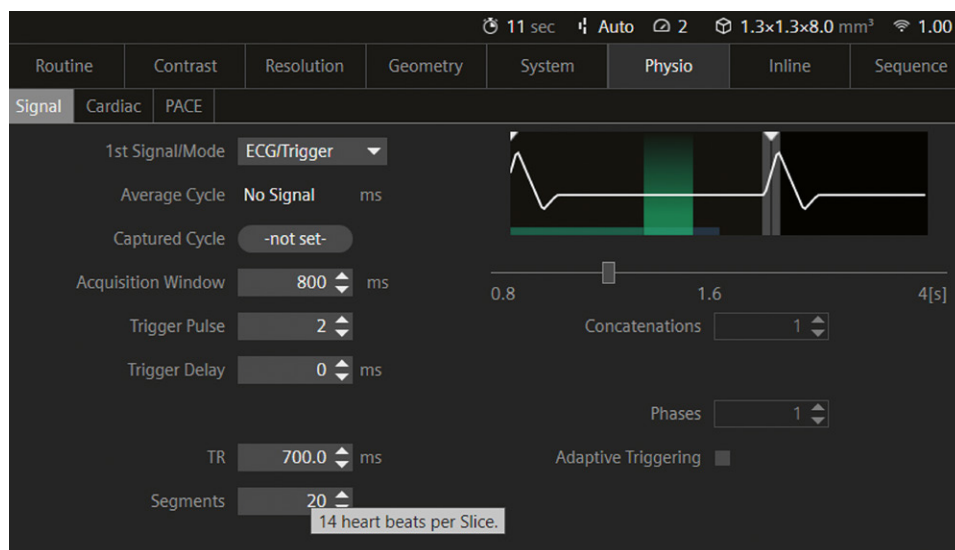
may affect more advanced quantitative imaging parameters of cardiac function, such as strain imaging [17]. It should be used cautiously for performing serial investigations of patients with different imaging strategies. Furthermore, the described techniques improve image quality in patients with arrhythmias (Fig. 11).

2. Late gadolinium enhancement (LGE) imaging

Similar to TrueFISP cine imaging, several options exist to reduce artifacts due to arrhythmias in LGE images. The standard technique for LGE imaging uses a segmented TurboFLASH (tfl) sequence, which acquires data over several heartbeats (Fig. 12).



11 Image quality improvement in a patient with arrhythmia, using CS and adaptive triggering. Panels **11A** and **11D** show standard retrospectively gated cine TrueFISP images without arrhythmia detection. Panels **11B** and **11E** show retrospectively gated images with CS but no arrhythmia detection. Panels **11C** and **11F** show prospectively gated images with CS and arrhythmia detection. The last two panels demonstrate significant image-quality improvement compared with the standard cine TrueFISP images. Panels 11A–11C: SAX views; panels 11D–11F: 3-chamber views.



12 Standard TurboFLASH LGE imaging (14 heartbeats).

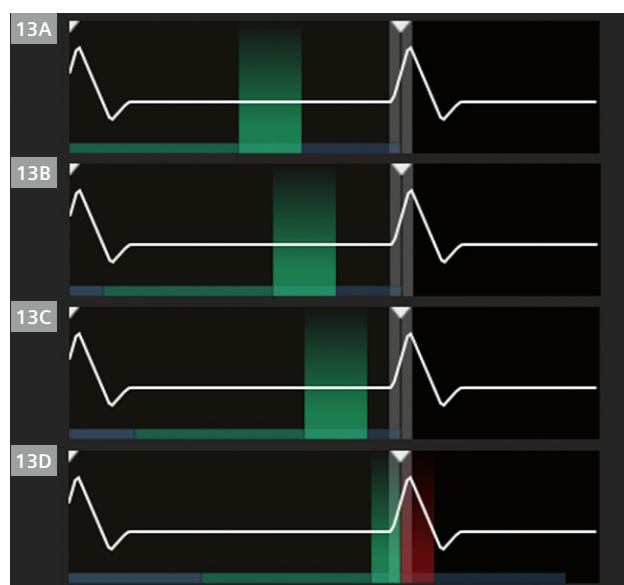
For patients with arrhythmia, several heartbeats within this period could be either shorter or longer than the anticipated RR interval. The protocol can automatically capture the cycle and automatically set the TR and acquisition window. However, depending on the variation in the heart rate, it might be better to set the acquisition window, TR, and trigger delay manually instead. The sequence timing should be set so that data is acquired during the diastolic phase. Generally, TR is kept constant, and trigger delay (TD) is used to move the data acquisition time to the part of the cardiac cycle with the least cardiac movement during the diastolic phase. Figure 13 shows the influence of TD on the data acquisition time graphically, as seen in the user interface. Situations such as those in Figure 13D should be avoided because the data acquisition occurs (partly) during the systolic phase. Besides motion artifacts, this also causes the next R-wave to be missed, leading to a (much) longer breath-hold time for the patient.

The first option for improving image quality is to use a single shot rather than a segmented sequence. These protocols can typically be found in the heart/tissue characterization/trufi ir with "overview" in the protocol name (Fig. 14).

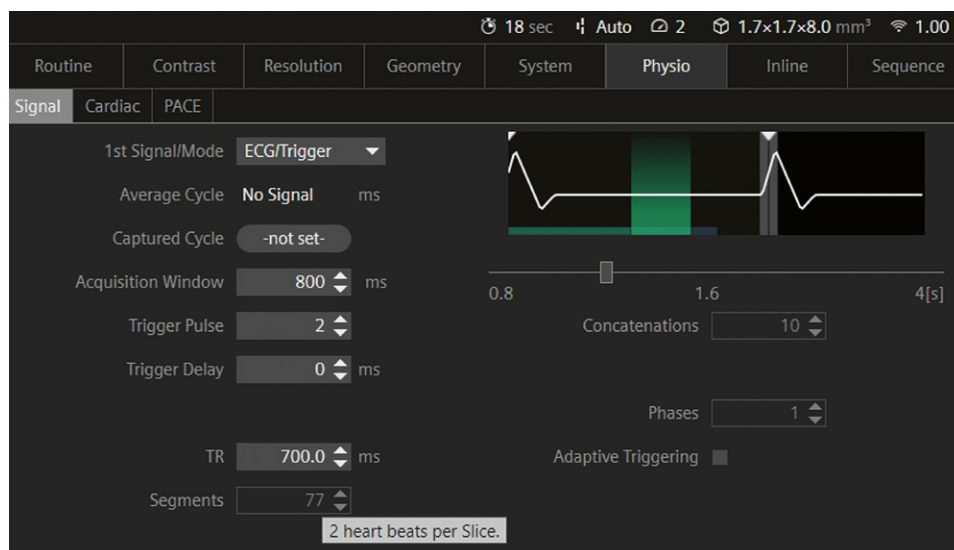
The data acquisition in single-shot phase-sensitive inversion recovery (PSIR) sequences requires only two heartbeats. Therefore, there is less chance of issues with varying RR intervals due to arrhythmias, and it can be easily repeated. To use only one heartbeat, the reconstruction on the Contrast/Common card can be switched to Magnitude only. In that case, only one heartbeat is needed.

The second option for improving image quality in arrhythmia patients is to use HeartFreeze. HeartFreeze is a free-breathing single-shot acquisition with multiple averages and motion correction (Fig. 15).

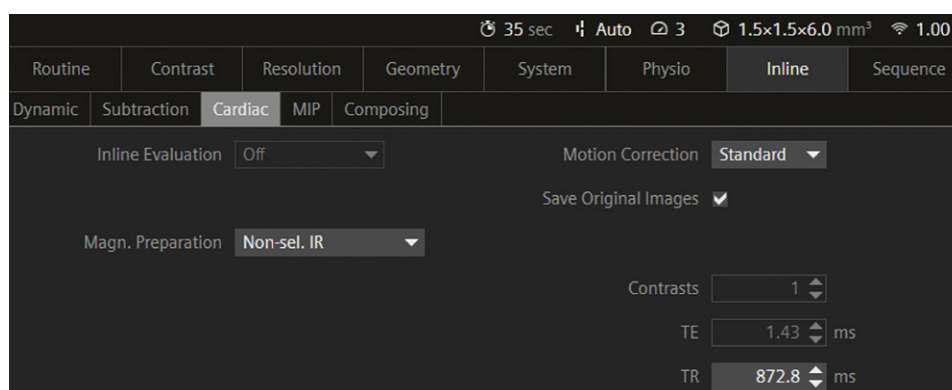
The number of averages is typically 8, and 75% of the most similar averages (after motion correction) are used to generate the image with multiple averages. The main advantages of this technique are that it reduces the chance of motion artifacts because it is a single-shot technique, and it has motion correction, which reduces the shot-to-shot variation (due to arrhythmias). Moreover, because it is a free-breathing technique, there is less chance of acquisitions where the patient cannot (or can no longer) hold their breath due to the long cardiac exam with many breath-holds. These types of images are acquired at the end of the exam.



13 Influence of trigger delay on time of data acquisition: (13A) TD = 0 ms, (13B) TD = 100 ms, (13C) TD = 200 ms, (13D) TD = 400 ms



14 Example of a single-shot LGE protocol.



15 HeartFreeze: Motion correction in the Inline/ Cardiac parameter card.

Conclusion

Cardiac MRI is an integral part of the diagnostic algorithm for patients with arrhythmia. Challenges in image acquisition may be overcome with dedicated techniques added to usual TrueFISP cine sequences, such as arrhythmia detection/rejection, or real-time cine imaging with or without CS and adaptive triggering. Assessment for fibrosis with LGE sequences can also be optimized in arrhythmia. All these approaches may result in more efficient scan times and improve image quality, which leads to more accurate cardiac assessments and better patient care.

References

- Ismail TF, Strugnell W, Coletti C, Božić-Iven M, Weingartner S, Hammernik K, et al. Cardiac MR: From Theory to Practice. *Front Cardiovasc Med*. 2022;9:826283.
- Uribe S, Muthurangu V, Boubertakh R, Schaeffter T, Razavi R, Hill DL, et al. Whole-heart cine MRI using real-time respiratory self-gating. *Magn Reson Med*. 2007;57(3):606–613.
- Lustig M, Donoho D, Pauly JM. Sparse MRI: The application of compressed sensing for rapid MR imaging. *Magn Reson Med*. 2007;58(6):1182–1195.
- Becker MAJ, Cornel JH, van de Ven PM, van Rossum AC, Allaart CP, Germans T. The Prognostic Value of Late Gadolinium-Enhanced Cardiac Magnetic Resonance Imaging in Nonischemic Dilated Cardiomyopathy: A Review and Meta-Analysis. *JACC Cardiovasc Imaging*. 2018;11(9):1274–1284.
- Andreini D, Dello Russo A, Pontone G, Mushtaq S, Conte E, Perchinunno M, et al. CMR for Identifying the Substrate of Ventricular Arrhythmia in Patients With Normal Echocardiography. *JACC Cardiovasc Imaging*. 2020;13(2, Pt 1):410–421.
- Park J, Desjardins B, Liang JJ, Zghaib T, Xie S, Lucena-Padros I, et al. Association of scar distribution with epicardial electrograms and surface ventricular tachycardia QRS duration in nonischemic cardiomyopathy. *J Cardiovasc Electrophysiol*. 2020;31(8):2032–2040.
- Fenski M, Grandy TH, Viezzer D, Kertusha S, Schmidt M, Forman C, et al. Isotropic 3D compressed sensing (CS) based sequence is comparable to 2D-LGE in left ventricular scar quantification in different disease entities. *Int J Cardiovasc Imaging*. 2022. doi: 10.1007/s10554-022-02571-6. Epub ahead of print.
- Zeilinger MG, Kunze KP, Munoz C, Neji R, Schmidt M, Croisille P, et al. Non-rigid motion-corrected free-breathing 3D myocardial Dixon LGE imaging in a clinical setting. *Eur Radiol*. 2022;32(7):4340–4351.
- Peters AA, Wagner B, Spano G, Haupt F, Ebner L, Kunze KP, et al. Myocardial scar detection in free-breathing Dixon-based fat- and water-separated 3D inversion recovery late-gadolinium enhancement whole heart MRI. *Int J Cardiovasc Imaging*. 2023;39(1):135–144.
- Leiner T, Bogaert J, Friedrich MG, Mohiaddin R, Muthurangu V, Myerson S, et al. SCMR Position Paper (2020) on clinical indications for cardiovascular magnetic resonance. *J Cardiovasc Magn Reson*. 2020;22(1):76.
- van der Graaf AW, Bhagirath P, Ghoerbiën S, Gotte MJ. Cardiac magnetic resonance imaging: artefacts for clinicians. *Neth Heart J*. 2014;22(12):542–549.
- Yin G, Cui C, An J, Zhao K, Yang K, Li S, et al. Assessment of Left Ventricular Systolic Function by Cardiovascular Magnetic Resonance Compressed Sensing Real-Time Cine Imaging Combined With Area-Length Method in Normal Sinus Rhythm and Atrial Fibrillation. *Front Cardiovasc Med*. 2022;9:896816.
- Zou Q, Xu HY, Fu C, Zhou XY, Xu R, Yang MX, et al. Utility of single-shot compressed sensing cardiac magnetic resonance cine imaging for assessment of biventricular function in free-breathing and arrhythmic pediatric patients. *Int J Cardiol*. 2021;338:258–264.
- Lin L, Li Y, Wang J, Cao L, Liu Y, Pang J, et al. Free-breathing cardiac cine MRI with compressed sensing real-time imaging and retrospective motion correction: clinical feasibility and validation. *Eur Radiol*. 2023;33(4):2289–2300.
- Longere B, Pagniez J, Coisne A, Farah H, Schmidt M, Forman C, et al. Right Ventricular Volume and Function Assessment in Congenital Heart Disease Using CMR Compressed-Sensing Real-Time Cine Imaging. *J Clin Med*. 2021;10(9):1930.
- Altmann S, Halfmann MC, Abidoye I, Yacoub B, Schmidt M, Wenzel P, et al. Compressed sensing acceleration of cardiac cine imaging allows reliable and reproducible assessment of volumetric and functional parameters of the left and right atrium. *Eur Radiol*. 2021;31(10):7219–7230.
- Kido T, Hirai K, Ogawa R, Tanabe Y, Nakamura M, Kawaguchi N, et al. Comparison between conventional and compressed sensing cine cardiovascular magnetic resonance for feature tracking global circumferential strain assessment. *J Cardiovasc Magn Reson*. 2021;23(1):10.

Contact

Christian P. Houbois, M.D.
Department of Medical Imaging
University of Toronto
Sunnybrook Health Sciences Centre
2075 Bayview Avenue
Toronto, Ontario, M4N 3M5
Canada
Tel.: +1 416-480-6100 Ext. 85389
Christian.Houbois@sunnybrook.ca



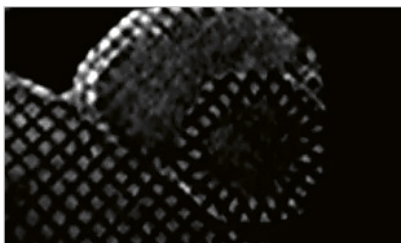
Try them on your system

Many applications are available as a trial license free of charge for a period of 90 days.



PSIR HeartFreeze

Late Gadolinium Enhancement (LGE) imaging in free-breathing.



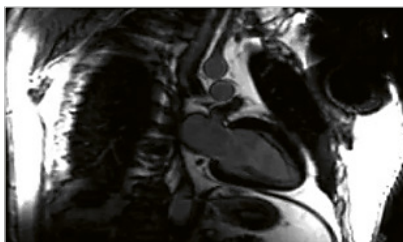
Advanced Cardiac

Special sequences and protocols for advanced cardiac imaging.



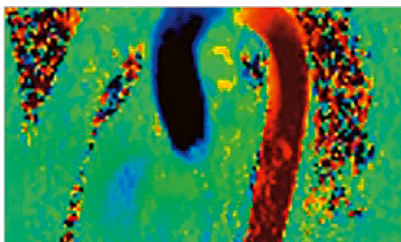
MyoMaps

The next step in quantitative cardiac assessment.



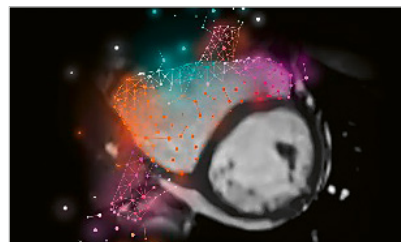
High Bandwidth Inversion Recovery

Cardiac inversion recovery for patients prone to susceptibility artefacts.



Flow Quantification

Special sequences (only AWP) for quantitative flow determination studies, measuring blood/CSF flow non-invasively.



Compressed Sensing Cardiac Cine

Beyond speed.
Beyond breathholds.

Additional technical prerequisites may apply. Upon receiving your request, your local Siemens Healthineers representative will clarify whether your system meets the requirements.

For further details, product overviews, image galleries and general requirements please visit us at:



www.siemens-healthineers.com/magnetic-resonance-imaging/options-and-upgrades

Skip the Electrodes, But Not A Beat: The Engineering Behind the Beat Sensor

Peter Speier, Ph.D. (manuscript) and Mario Bacher (box texts)

Siemens Healthineers, Erlangen, Germany

Introduction

Early in the development of cardiac MR, even long before bSSFP/TrueFISP made it clinically useful [1], the ECG was established as the standard trigger source [2] despite its well-known drawbacks of complex patient preparation and MR-related artifacts caused by the magnetohydrodynamic (MHD) effect and the gradient pulses of the MR measurement [3, 4]. Its main advantage is the early and well defined trigger time point based on the R-wave that precedes the ventricular contraction.

The only other clinically adopted cardiac trigger method is the finger-tip pulse sensor peripheral plethysmogram (PPG) [5], but its late and patient-state-dependent trigger position in the cardiac cycle reduces both its versatility and stability. Therefore, PPG is used only as a back-up.

Over the years, the reliability and ease of use of the ECG have been improved dramatically by the introduction of the vector ECG [6], wireless connections, and standardized handling procedures [3, 4]. Still, over the last 12 years, quite a few alternative methods of cardiac triggering have been proposed [7–12], indicating that there is still a need for more reliable and easier-to-use cardiac trigger methods. Some of these methods are based on optical or mechanical measurements. However, the MRI scanner is already a very sophisticated electromagnetic signal generation and sensing device. Therefore, trigger methods like the BioMatrix Beat Sensor (Glossary), which are based on electromagnetic effects are a good match as they can re-use already existing facilities of the MRI machine.

BioMatrix Beat Sensor – the Pilot Tone

The development of the BioMatrix Beat Sensor started with a power pitch presentation that I attended at the ISMRM 2014 in Milan, Italy. It was about respiratory noise navigation and was given by Anna Andreychenko [13]. It is well known that respiration modulates the electric load of the MR receiver coils. If the receivers are matched to maintain constant signal under load variations, this results in a modulation of the thermal noise power. Andreychenko demonstrated that respiratory navigation can be derived from measurements of the noise power. I was intrigued by this method and tried it out upon my return from the

conference. I quickly realized that the number of noise data points required to characterize respiration is quite high and difficult to achieve during fast measurements like bSSFP. Luckily, I remembered a presentation that Lars Hanson had given at the IDEA developer conference in Freiburg, Germany, back in 2007 [14]. There, he described a system for “burning” electroencephalography (EEG) information into MR images by modulating the information onto a weak RF carrier close to Larmor frequency. The modulation is extracted by the MR receiver together with the MR data, and the EEG data appears as a stripe artifact in the image, or, if the carrier frequency is placed just outside of the frequency band of the image, i.e., in the oversampling region, the MR data remains uncontaminated by the additional signal. I postulated that any body-motion would modulate a constant coherent RF signal and that the achievable SNR per unit time would be higher than for noise navigation. I discussed the idea with a few experts in the factory in Erlangen who agreed that it should be feasible to use the signal for respiratory navigation. Markus Vester suggested the term “Pilot Tone” (PT) for the new motion-sensing method. In communication engineering, a Pilot Tone refers to a reference signal that is transmitted together with the payload signal to characterize the transmission path.

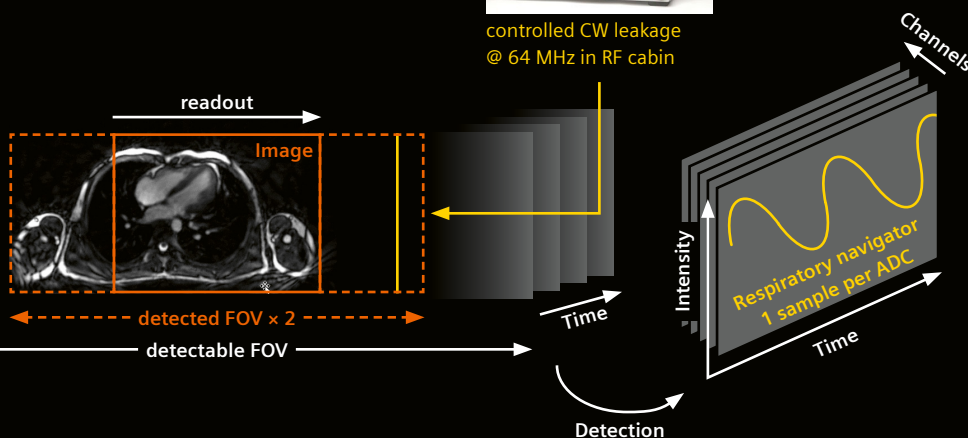
We presented our case and received approval from MR management for an initial cross-departmental investigation. We started the first volunteer tests with an off-the-shelf signal generator in the control room connected through the wave-guide hole to an untuned pickup loop taped to the funnel of a 1.5T MAGNETOM Espree. For the setup, see Figure 1A. The first experiment featured a series of breath-holds alternating between inspiration and expiration. We looked at the data in the command line tool *measdataviewer* directly on the scanner and could immediately see a strong and clean modulation with respiratory position. Over the year, we continued experiments and built an inline-processing module in our image reconstruction environment ICE that would generate live respiratory information and clean up the MR data. I presented the initial results at the ESMRMB 2015 in Edinburgh, UK [15].

1A Pilot Tone Userland implementation

- Generate ultra-low-power "leakage" CW signal with fixed frequency just outside MR signal band
- Detect with MR receiver, calc. navigator in recon

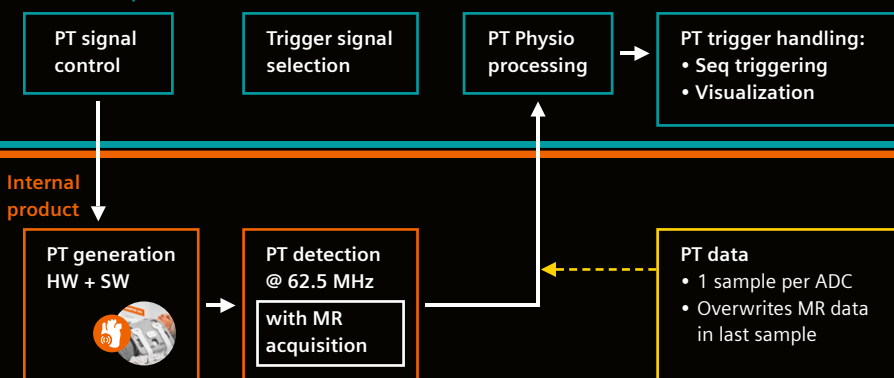


controlled CW leakage
@ 64 MHz in RF cabin



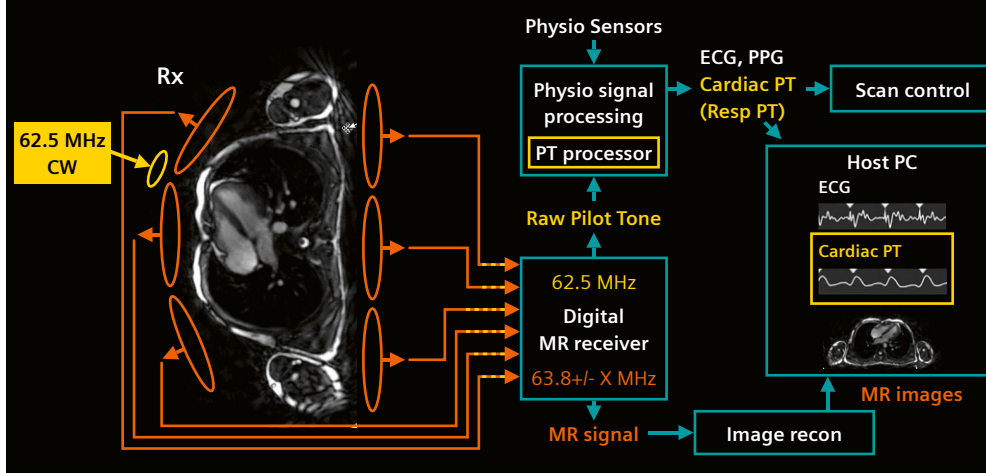
1B Beat Sensor – Demonstrator WIP ready*

Userland (Seq+ICE)



*Active during WIP acquisition only

1C System integrated Pilot Tone



- Three integration levels of the Pilot Tone subsystem:
 - (1A) Vendor-independent "userland" implementation;
 - (1B) Integrated PT generation and detection for increased signal stability for experimental use by collaboration partners;
 - (1C) Fully integrated PT subsystem to continuously provide physiological information.

Since this abstract is difficult to obtain, it is reprinted with kind permission of ESMRMB in the Appendix.

In summer 2015, we started a collaboration with Fernando Boada's group at CAI2R at NYU. They set up their own version of the experiment on their Biograph mMR and published their first results at the ISMRM 2016 in Singapore [16]. They have continued to develop respiratory PT applications for MR-PET [41, 17] and they even offer their own version of a battery-powered PT generator¹. Other sites also built their own PT setups for respiratory work and investigated its application to free-breathing MR Fingerprinting (MRF) [18] and prospective slice tracking in free-breathing cardiac MRI [19, 20].

This "userland"² approach to PT applications is vendor agnostic, but has three main drawbacks which introduce complications that can reduce their stability:

¹<https://cai2r.net/resources/3t-pilot-tone>

²The term "userland" is used here in analogy to the usage in the Linux community to denote functionality programmed only using the vendor-provided programming toolset, for MRI typically limited to sequence and image reconstruction.

1. The PT data is acquired only when the sequence plays out an ADC. So, if the measurement is not continuous (e.g., a cine), but contains recovery periods or other pauses (e.g., TSE), no PT data is available in the pauses unless the sequence is modified to fill the gaps with ADCs. However, additional ADCs increase the raw data size significantly. Also, there is no PT data in pauses between measurements.
2. The frequency of the PT must be adapted to the frequency band used by the current protocol: It must fall into the oversampling region that is outside the reconstructed frequency band but inside the oversampled band. The width of the frequency band depends on the protocol (the receiver bandwidth). In addition, the band shifts with in-plane slice shifts in readout direction. The frequency selection becomes easier to fulfill if the oversampling factor (standard is factor 2) is increased, but this also increases the raw data size by the same factor and might not be possible for protocols that utilize high receiver bandwidth.

Box 1: A history of electromagnetic monitoring and MR

In 1958, YE Moskalenko, who worked on electroplethysmography in the context of the Russian space program, demonstrated that a radar transmission setup operating at 1 GHz (much higher than the operating frequency of a clinical MRI scanner) could be used to observe respiration and cardiac activity [33].

The first report on an electromagnetic navigation (EMN) signal at low frequency observed in humans was published ten years later by Tarjan and McFee [34]. Their goal was a contactless measurement of blood volume. They adapted a method known in geophysics as an "induction measurement": They projected a magnetic field with a frequency of only 100 kHz into the chest of a volunteer and observed the resulting field with a set of two coaxially aligned receive coils while suppressing direct coil-to-coil coupling. A change in body conductivity would result in a modulation of the received field. They observed a modulation of a few percent due to respiration and a smaller modulation due to cardiac motion of about one percent. They also noted that the signal seems to represent cardiac volume change.

While it has been known in NMR and MRI that an electrically conductive sample loads the coil, and that for optimal efficiency and SNR, the coil must be tuned and matched to the sample, the effect was not exploited for physiologic monitoring until 1988, when Buikman et al. proposed to measure the modulation of the reflection of an RF pulse in the body coil to record respiratory and cardiac information [35].

However, the idea was not picked up widely until quite recently, when new developments enabled robust separation of the different modulation sources: the availability of near-infinite computing power, the availability of massively parallel receive systems on virtually all clinical MRI scanners, and the availability of highly parallel transmit systems on high-field MRI scanners. Where highly parallel transmit systems are available, the reflection of all their elements can be monitored during RF pulses [36]. When measuring the coupling between all elements, high-quality rich data is obtained that allows separation of multiple motion contributions [37], but only while transmitting RF pulses.

The noise navigator [13] and the Pilot Tone [15] require multi-channel capability on the receive side only. Therefore, they can be implemented on all modern MRI systems and while the MR receiver operates, navigation data can be obtained.

The most recent development in EMN for MRI is the "Beat Pilot Tone" [38]: The method removes the requirement that the PT frequency be near the Larmor frequency by generating the signal close to the Larmor frequency only in the MR receive chain as an intermodulation product of two electromagnetic signals with higher frequencies, where these two frequencies are separated by approximately the Larmor frequency. This approach allows low-cost integration of EMN at radar frequencies into the MR scanner by using the MR receive system as a continuous wave (CW) radar detector.

3. The PT appears as a peak in the Fourier-transformed ADC. The peak position is a function of the PT frequency and the scanner's detection frequency; thus, it depends on the slice geometry, i.e., on the off-center shift in readout direction. This correction is deterministic and can be calculated exactly from protocol parameters and raw data headers. However, the eddy current compensation contains a B_0 correction, which is realized by varying the receive frequency. The correction thus generates additional, small transient shifts in the PT peak position when gradients are applied. These will become noticeable when the eddy current steady state changes markedly, e.g., when toggling between slice orientations. To avoid this problem, the PT peak position must be redetermined with every substantial change in the gradients, e.g., when switching slice orientations or when playing out large phase encoding jumps. In addition, the PT frequency from a generator that is not synchronized to the MR scanner will drift with time, and the detection frequency must be adapted if the drift is too large.

To eliminate these problems, we integrated the Pilot Tone generation into the MAGNETOM architecture as a prototype. The solution was to generate the PT at a fixed frequency and detect it directly after digitization before the "userland" signal with all corrections is derived. This made it necessary to implement the PT detection in firmware. To save field-programmable-gate-array (FPGA) resources we picked as frequency Nyquist/2 in the digitized frequency band, where the detection algorithm would not require multiplications but only additions. This led to the currently used PT frequency 62.5MHz @ 1.5T. To avoid drifts of the PT signal in frequency and phase, and thus enable complex valued processing, the PT signal is generated by the scanner itself using a "spare" frequency generator.

In parallel, we continued to explore the possibilities of the new method in a master's thesis in the cardiac predevelopment team, together with the local university [21]. Our department head, Lars Lauer, challenged us to extend the scope of the thesis beyond respiratory navigation and aim for cardiac triggering. At that time, we had no indication that this would be feasible, as we had never seen a cardiac signal with our remote generator set-up. If we had studied the scientific literature better (Box 1), we might have been more hopeful, but this only happened in the following master's thesis [22]. Halfway into Lea Schröder's thesis, Jan Bollenbeck built a battery-powered PT generator that could withstand the RF pulses of the MR experiment. The aim was to place the generator closer to the patient's chest to reduce sensitivity to non-respiratory motion, e.g., head or foot movement. We first attached the generator to the scanner's inner bore cover over the chest and didn't see anything new. However, when we placed it directly on the chest of the volunteer, we could see the cardiac signature directly in the raw data. These results were presented at ISMRM 2016 in Singapore [23] (Fig. 2). Internally, they also raised a lot of interest because of the potential for developing the new method into an alternative to ECG.

These initial results were seen promising enough to start the product integration. The first goal was to enable collaboration sites to start their own PT experiments with an integrated, stable, and easy-to-use system that featured local PT generation. I was able to convince Peter Gall, the product manager of the new system platform that was in the planning stage at that time, to include the necessary hardware (HW) and software (SW) in the system project.

Early in 2016, we started a second master's thesis on PT, this time with the Graz University of Technology in Austria, to further develop the cardiac application of the PT [22]. Using a second generation of the battery-powered PT generator, Mario Bacher ran a volunteer cohort study and developed signal processing SW for retrospective and

A novel method for contact-free cardiac synchronization using the PT navigator

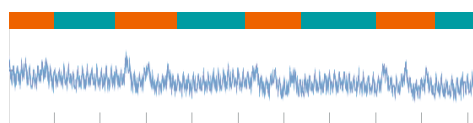
Local PT navigator



Battery-driven autonomous RF source placed on chest

... „sees“ respiratory motion + something else

PT navigator example for instructed breathing:
Interleave 3 deep breaths and breath hold



Question: Is this cardiac motion?

Task: Separate signal contributions

- 2 The key slide from [23] demonstrates that cardiac motion can be detected using a locally generated Pilot Tone.

Box 2: PT physics: The transformer model

The PT signal, like all electromagnetic applications, is a result of the Maxwell equations ;-). To understand real-world scenarios, especially complex ones like humans, numerical simulations are required. However, insight into the basic principles can be obtained with idealized, simple models: the main mechanism of the PT modulation by cardiac motion can be understood by comparing the setup to an electric transformer. The pre-condition is that the PT-generating loop is much smaller than the electromagnetic wavelength and thus mainly generates a magnetic field and only a negligibly small electric field. Thus, the PT is a purely magnetic signal which exists only as a near field; contrary to radar, which is a self-propagating electromagnetic wave, used in its far field.

A transformer consists of two coils: The primary driving coil (yellow, left side) produces an oscillating magnetic field. The resulting flux through the second coil (yellow, right side) induces a voltage. The flux between the coils is maximized by connecting the two coils with a magnetic, but non-conductive medium. Luckily for us MRI people, the human body is only weakly magnetic and it conducts electricity quite well. Therefore, the body can be seen as a magnetically transparent but lossy transformer core. The primary magnetic field (blue) will generate eddy currents in the tissues (orange), depending on the local conductivity. These eddy currents in turn generate secondary magnetic fields (orange). The secondary field opposes the primary field at the point of origin. In this example we observe the superposition of both fields in the receive coil on the right where both field lines point in different directions. Thus, depending on the geometry

the secondary field can cause decreasing or increasing amplitude and/or phase shifts.

The body consists of tissues that have different electrical conductivity and change their position during motion. When conductive tissues move, the eddy current distribution changes and the net secondary field with it. The resulting modulation of the received fields is observed as the Pilot Tone signal. Even though the heart is relatively small, its motion is clearly observable because during cardiac contraction, highly conductive heart muscle and blood are replaced by weakly conductive fat and lung tissue.

As mentioned earlier, the Pilot Tone frequency needs to be chosen fairly close to the Larmor frequency: 62.5 MHz for 1.5T systems. Again, we were lucky: These frequencies hit a sweet spot where on the one hand wavelengths are long enough (2.4 m to 4.8 m in a vacuum, a few decimeters in tissues) so that the signal penetrates the body quite freely and can therefore be described by this simple model, and where, on the other hand the frequency is high enough that the induced eddy currents and consequently the secondary magnetic fields are strong enough to be easily detected.

All these factors together enable reliable detection of cardiac, respiratory, and even head motion at standard clinical field strengths. However, as Anand et al. [38] have shown, exciting opportunities also await at very high frequencies! When venturing into the GHz range, the transformer model is no longer applicable, as we are entering the domain of radar. Here, higher order interactions start to dominate the signal and limit its penetration into the body, which is expected to optimize the detection of rigid motion.

How does it work?

Transformer model

Assumption¹: $B \gg E$

A transformer consists of

- Primary **driving coil** $\rightarrow \vec{B}$
- Secondary **receiving coil**
- A (highly) magnetic but non-conductive medium

If medium is conductive \rightarrow eddy currents i_e

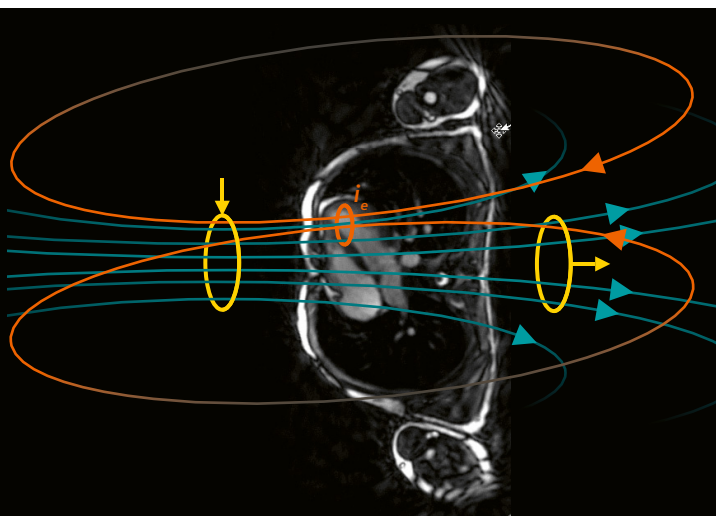
\rightarrow Opposing \vec{B}_e

Conductivity σ : Blood > Muscle > Lung > Fat

Motion changes EC distribution

\rightarrow received signal changes in amplitude **and** phase

¹Ensured by small generator loop



finally also for prospective cardiac triggering (Box 3). He obtained his first prospectively triggered cardiac cine still with a battery-powered generator and a pure “userland” implementation. He went on to work on a PhD thesis on the topic at Lausanne University Hospital (CHUV) in Switzerland. In his work, he also unearthed the early history of electromagnetic navigation and its use in MRI (Box 1), and the physics of signal generation (Box 2).

For the first version of the integrated PT-generation and detection system, (Fig. 1B) the PT was generated inside the new BioMatrix 12 coil. The PT was still detected only during ADCs and evaluated in ICE, but it was already much more stable. In this context, the term “Beat Sensor” was introduced to describe the cardiac application of the Pilot Tone (Glossary). This system was subsequently used at the Royal Brompton Hospital (RBH) in London, UK, to acquire the first cardiac PT patient data [24], and at CHUV and Ohio State University (OSU), Columbus, OH, USA, to develop and evaluate respiratory and retrospective cardiac applications (see e.g., Falcão [25] and Chen [26]).

Developing a robust and complete cardiac PT application takes time, and we went through several releases that gradually moved us closer to the current product. First, we implemented a general PT framework (see Fig. 1C) with the following main features:

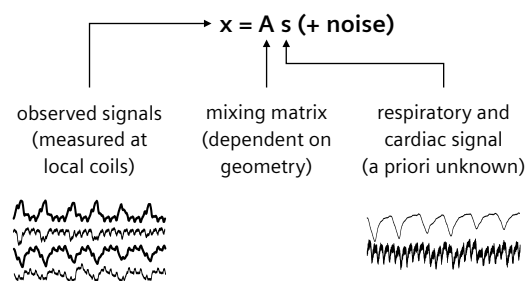
- An acquisition-independent and continuously acquired PT data stream, with samples being flagged as invalid during RF pulses
- Pairing each PT sample with information about the preceding RF pulse to enable spike subtraction
- A PT-processing framework that can be exchanged and reconfigured for individual measurements to enable rapid prototyping and work-in-progress packages.

The first point amounts to quite a substantial paradigm shift: Before, the MR receiver had to be configured and active only during measurements. Now, the receiver had to be always configured and active to receive PT data during and between measurements. To achieve this, a dedicated team spent much of the development time

Box 3: Signal processing basics

A key advantage of the PT method is the use of all connected coil elements for receiving the PT signal. Each receive coil “sees” a different combination of cardiac, respiratory and other motion, depending on its location. Since we are interested in observing cardiac and respiratory motion by themselves, these components must be separated first.

This can be accomplished by a class of algorithms known as “Blind Source Separation”. The problem statement is simple: Given a multitude N of sensors measuring signals x which are a combination A of $M < N$ independent signals, separate the underlying signals s .



In other words: the equation needs to be solved for A , the so-called mixing matrix. Initially we used FastICA (Independent Component Analysis, [39]), in which the non-Gaussianity is optimized as a proxy for statistical independence [22]. While this algorithm worked well for Cine sequences, which are not affected by RF inter-

ference, a new PCA-based algorithm was developed in collaboration with the Shenzhen team, based on [27], in which the RF contamination of the PT signals is minimized by mixing vectors that are orthogonal to the main principal components of the eigenspace of interference signals.

To enable robust cardiac triggering, the cardiac motion signal needs to be de-noised in real-time. Classical digital filters, however, would introduce an unacceptably large time delay for the cardiac application (e.g., > 600 ms for an 80 dB stopband FIR lowpass at 6 Hz).

In [12, 22], we proposed to use a Kalman filter to denoise the signal. A Kalman filter, named after Rudolf E. Kalman, is an algorithm that uses a series of measurements, including noise and other inaccuracies, and attempts to fit these measurements in a least-squares sense to a predefined signal model. In our case, the signal is modeled using a constant velocity motion model similar to Spincemille et al. [40], in which the signal evolution is modeled as the 1D motion of a particle with constant velocity. This approach has two additional advantages: First, it does not only provide a de-noised signal, but also an estimation of the signals first derivative, i.e., velocity, which is subsequently used for trigger detection (see Box 4). And second, it can interpolate over short gaps in the data that occur while sending RF pulses.

on writing and debugging the HW–SW interconnectivity. The flexible processing framework drastically sped up the subsequent development by enabling us to test new code on previous stable baselines and SW versions. To minimize porting efforts, we kept interfaces constant and minimized dependencies on other modules.

In 2021, we released the first clinical application: Beat Sensor triggering for Cines only. The limitation to Cine was necessary because we had not yet implemented a general RF-artifact compensation, and for Cine a simple signal average is sufficient. Most of the development time was spent on optimizing signal processing and workflow. For about one year we had regular volunteer shifts to test stability and usability of the latest developments. A lot of time was spent on the special coil handling required for Beat Sensor-triggered measurements: The PT signal is acquired using the coil elements currently selected for imaging, and signal-processing training is valid for one

coil select only. Therefore, Beat Sensor-triggered protocols must automatically select the coils used in training.

While the team in Erlangen, Germany, had been working towards productization of the cardiac application of PT, the Siemens Healthineers development team in Shenzhen, China, had been developing the respiratory application of PT. After an initial ramp-up phase, the team in Shenzhen independently developed and released a first product for respiratory triggering on MAGNETOM Amira – A BioMatrix System. After this release, the two groups intensified their collaboration: Yan Tu Huang in Shenzhen integrated his respiratory processing into the PT framework, and several algorithms were exchanged between the sites and applications. The cardiac application benefited most by rebasing on the robust method for RF-artifact suppression [27] that Shenzhen had developed for the respiratory application. We jointly extended this algorithm for the cardiac application. Based on this algorithm we were able to stabilize

Box 4: PT signal characteristics and trigger time point

The cardiac component of the Pilot Tone closely follows the cardiac volume curve without a delay: At the time of the R-wave, in end-diastole, when the heart is fully expanded, it assumes its maximum value. During end-systole, when the heart is fully contracted, it assumes its minimum value, and during the static mid-diastolic period it plateaus at an intermediate value. The Beat Sensor signal, shown on the right, is the inverted time derivative of this cardiac component. It has the advantage that it features a rather narrow positive peak at the beginning of the cardiac cycle and provides additional suppression of respiratory contamination.

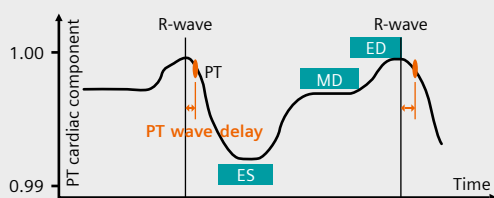
The Beat Sensor triggers when the systolic contraction starts (specifically, when the derivative reaches 40% of its maximum value). This trigger point was chosen for its stability and occurs approximately 100 ms after the R-wave. This wave delay is learned during the

Beat Sensor training phase using only the waveform of the cardiac component as the distance between trigger point and the preceding maximum. Low-pass filters in the signal processing add roughly 100 ms to this, resulting in a total delay of about 200 ms. If a finger pulse sensor (PPG) is present as well, its delay with respect to the R-wave is also determined.

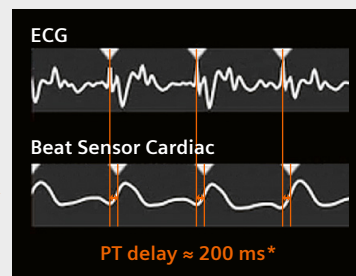
One crucial functionality for cardiac exams is “Capture Cycle”: based on the current heart rate, an algorithm places the acquisition in the end-diastolic cardiac phase where motion is minimal. For the ECG, that triggers on the R-wave, this placing is achieved by maximizing the trigger delay. For Beat Sensor and PPG triggering, the algorithm has been modified to account for the trigger delays learned during Beat Sensor training. Thus, after the training “Capture RR” can be used for all three trigger sources.

PT Cardiac trigger time and display

- Trigger (I) in acceleration phase @ early mid-systole
- Calibration: take distance from trigger to previous signal maximum



- Delay is considered for ED planning
- if PPG is present, PPG delay is determined as well



$$\begin{aligned} \text{*PT delay} &= \text{PT wave delay} + \text{filter delay} \\ &\approx 100 \text{ ms} \quad \approx 100 \text{ ms} \end{aligned}$$

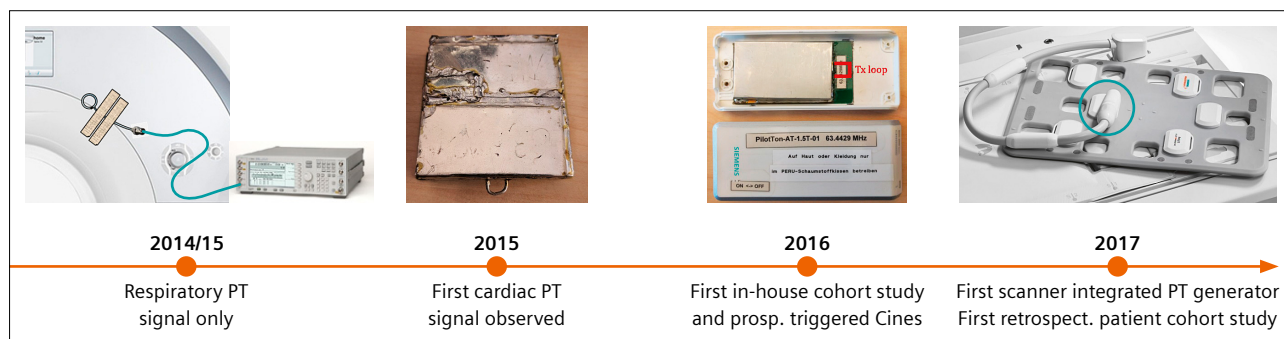
cardiac triggering for all cardiac protocols. The signal characteristics of the current implementation are described in Box 4.

To collect customer feedback early, we developed a work-in-progress package (WIP) of Beat Sensor triggering for the whole cardiac exam. The WIP was initially installed at four different sites (Jan Yperman Hospital, Ieper, Belgium; Royal Brompton Hospital, London, UK; Ohio State University, Columbus, OH, USA; and Northwestern University (NWU), Evanston, IL, USA). While the feedback on clinical performance was positive [28–30], the calibration workflow proved to be too complex and error-prone. Thus, we reworked and hardened the calibration workflow just before the development deadline and could release Beat Sensor triggering for the whole cardiac exam for the current SW version *syngo* MR XA51A for the 1.5T BioMatrix Systems MAGNETOM Sola, MAGNETOM Altea, and MAGNETOM Sola Fit. The next SW version for 3T systems will bring this functionality to MAGNETOM Vida and MAGNETOM Lumina.

The development of PT-based methods is ongoing.

The clinical use of the first complete release of the Beat Sensor will certainly reveal limitations, but it will also show distinct advantages when compared with the ECG. We are committed to removing limitations and turning the advantages into clinically useful features. So please try out the Beat Sensor in your clinical routine and let us know about your experiences.

Looking beyond cardiac to general motion management, the use of Pilot Tone is still in its infancy and we have only scratched the surface of many aspects and applications. Two examples are two-dimensional characterization of respiration [31] and characterization of head motion [32]. The scanner-integrated PT with its continuous data stream and its flexible processing framework is a powerful tool to enable these upcoming investigations and developments.



3 Four generations of Pilot Tone generators: From initial respiratory experiments to a scanner-integrated solution.

Acknowledgment

A big Thank you to all contributors. Especially:

- **Generator hardware:** Jan Bollenbeck
- **Physio-SW:** Michael Schwertfeger
- **PT processing:** Mario Bacher, Yan Tu Huang
- **Sequences, exam prototypes and data analysis:** Carmel Hayes, Randall Kroeker
- **Volunteer data:** Manuela Rick
- **Early patient data:** Peter Gatehouse (RBH)



Appendix: Reprint of Ref. 15

PT-Nav: a novel respiratory navigation method for continuous acquisitions based on modulation of a pilot tone in the MR-receiver

P. Speier¹, M. Fenchel¹, R. Rehner²

¹MR PI, Siemens Healthcare, Erlangen, Germany

²MR R&D, Siemens Healthcare, Erlangen, Germany

Purpose/Introduction

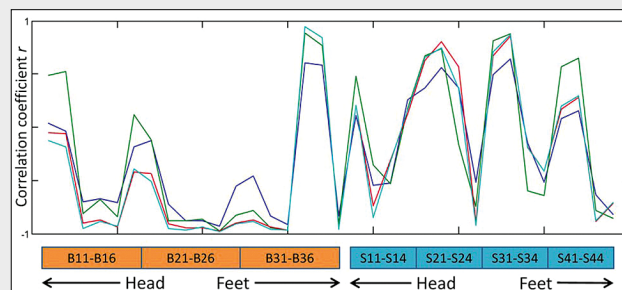
High-resolution 3D abdominal or cardiac MR imaging requires synchronization to respiratory motion. The motion can be tracked by dedicated respiratory sensors, MR navigators, selfgating algorithms, or, as recently proposed, by analyzing the received noise [1] or measuring load changes of the transmit coil [2]. These methods increase setup complexity, require interruption of steady state, special k-space trajectories and high SNR per scan, long averaging times, or additional scanner-integrated hardware. We hypothesize that a coherent signal from an independent source, received in parallel with the MR signal, can be used as a high-quality navigator that does not suffer from the drawbacks of the previous methods.

Subjects and methods

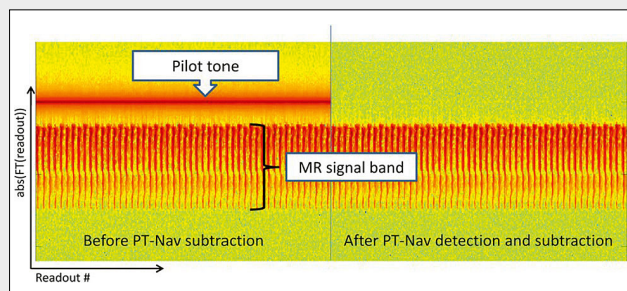
Continuous series of sagittal bSSFP or GRE images (500...1000 images, 3...5 images/s, $(1.5...2 \text{ mm})^2 \times 10 \text{ mm}$) of the right liver dome were acquired with anterior and posterior multi-channel receive coils. Meanwhile, a continuous-wave (CW) RF signal, generated by a commercial signal generator, was transmitted as a pilot tone into the magnet bore by a non-resonant pickup coil, placed on the table or outer magnet cover, with a frequency outside of the frequency band of the MR signal and the FOV, but inside the received frequency band, and an amplitude

adjusted to be detectable in the linear operating regime of the receiver.

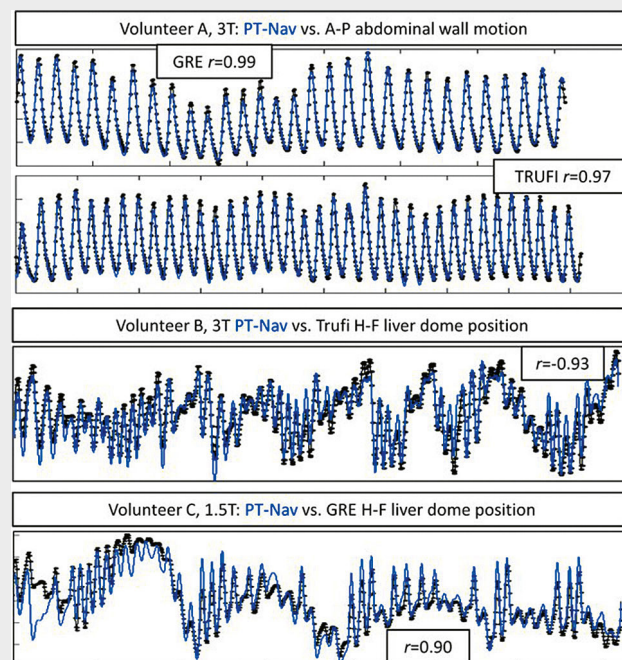
Image reconstruction was modified in-house for pilot tone detection: During a learning phase, the pilot tone frequency f in the received data was determined. Then, for each k-space line and channel, the pilot tone was fit to the model $A \times \exp(i2\pi ft)$, the complex amplitude A logged as PT-navigator, and the model subtracted from the data (Fig. 1). Offline processing was performed in MATLAB (Math-Works). The positions of the liver dome (HF direction) or abdominal wall (AP direction) were tracked in the images, and their correlations to low-pass (1 Hz-Hann-window)-filtered PT-navigators were calculated for all channels.



2 Exemplary correlation coefficients of anterior (orange) and posterior (blue) coil elements for 4 measurements of volunteer B



1 Exemplary Fourier-transformed raw data (one channel), demonstrating successful detection and elimination of a pilot tone placed next to the MR-signal band



3 Exemplary correlations between best PT-Nav channel and image-based navigators (curves shown after mean subtraction and amplitude normalization)

Results

Measurements of 5 volunteers were performed on three systems (MAGNETOM Espree, Aera, and Skyra, Siemens Healthcare). Correlation factors varied in sign and amplitude between channels (Fig. 2). For all volunteers, receive channels with high correlation coefficients $r \geq 0.9$ were found while volunteers laid still, allowing precise characterization of even quite irregular respiratory patterns (Fig. 3). Correlations could be slightly improved by combining channels.

Glossary

Electromagnetic navigation (EMN)

Characterizing motion by its influence on low-frequency electro-magnetic fields inside the body, used here with a focus on scanner-integrated methods

Pilot Tone (PT)

MR-integrated EMN, the only hardware part is the field generator

BioMatrix Beat Sensor

- 1. Cardiac application of Pilot Tone
- 2. Hardware integrated Pilot Tone generator (BioMatrix 12, BioMatrix 18 coils)

BioMatrix Respiratory Sensor

- 1. Respiratory Sensor hardware in BioMatrix Spine coils on 1.5T MAGNETOM Sola, and MAGNETOM Altea, as well as on 3T MAGNETOM Vida, and MAGNETOM Lumina (this is EMN, but not PT based)
- 2. Respiratory PT application on 1.5T MAGNETOM Amira - A BioMatrix System (uses a PT generator in the BioMatrix 13 coil)

Discussion/Conclusion

Our early results suggest that the proposed PT-Nav method can provide, with minimal hardware requirements, respiratory information for continuous sequences that is comparable to that of “gold-standard” MR navigators.

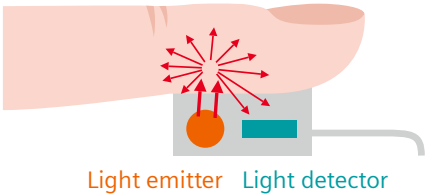
References

- 1 A. Andreychenko, ISMRM 2014, #92.
- 2 I. Graesslin, ISMRM 2010, #3045.

Why is “Beat Sensor” an appropriate term for the Pilot Tone generator?

Like the finger pulse sensor, the Beat Sensor is an active sensing method: It emits a signal into the body and receives the motion-induced modulation of this signal. The Beat Sensor hardware, that is built into the BioMatrix 12 and BioMatrix 18 coils, fulfils the function of a signal generator but does not receive the signal. It can be likened to the light emitter in the finger pulse sensor. The role of the light receiver is implemented by modifying the SW of the already existing MR receive system.

HW	Pulse Sensor	Beat Sensor
Generator	Light emitter	PT generator: dedicated hardware in BioMatrix 12 and BioMatrix 18 coils
Receiver	Light detector	PT receiver (reuse MR receive system)



References

- Carr JC, Simonetti O, Bundy J, Li D, Pereles S, Finn JP. Cine MR angiography of the heart with segmented true fast imaging with steady-state precession. *Radiology*. 2001;219(3):828-834.
- Lanzer P, Botvinick EH, Schiller NB, Crooks LE, Arakawa M, Kaufman L, et al. Cardiac imaging using gated magnetic resonance. *Radiology*. 1984;150(1):121-7.
- Niendorf T, Winter L, Frauenrath T. Electrocardiogram in an MRI Environment: Clinical Needs, Practical Considerations, Safety Implications, Technical Solutions and Future Directions. In: Millis RM (Editor). *Advances in Electrocardiograms*. IntechOpen. 2012. doi:10.5772/24340.
- MRI Questions: EKG Detection [Internet]. Elster LLC; 2021 [cited November 29, 2022]. Available from: <https://mriquestions.com/ekg-problems.html>
- Denslow S, Buckles DS. Pulse oximetry-gated acquisition of cardiac MR images in patients with congenital cardiac abnormalities. *AJR Am J Roentgenol*. 1993;160(4):831-3.
- Chia JM, Fischer SE, Wickline SA, Lorenz CH. Performance of QRS detection for cardiac magnetic resonance imaging with a novel vectorcardiographic triggering method. *J Magn Reson Imaging*. 2000;12(5):678-88.
- Frauenrath T, Hezel F, Renz W, d'Orth Tde G, Dieringer M, von Knobelsdorff-Brenkenhoff F, Prothmann M, Schulz Menger J, Niendorf T. Acoustic cardiac triggering: a practical solution for synchronization and gating of cardiovascular magnetic resonance at 7 Tesla. *J Cardiovasc Magn Reson*. 2010 Nov 16;12(1):67. doi: 10.1186/1532-429X-12-67. PMID: 21080933; PMCID: PMC2998500.
- Nedoma J, Fajkus M, Martinek R, Nazeran H. Vital Sign Monitoring and Cardiac Triggering at 1.5 Tesla: A Practical Solution by an MR-Balistocardiography Fiber-Optic Sensor. *Sensors (Basel)*. 2019;19(3):470.
- Spicher N, Kukuk M, Maderwald S, Ladd ME. Initial evaluation of prospective cardiac triggering using photoplethysmography signals recorded with a video camera compared to pulse oximetry and electrocardiography at 7T MRI. *Biomed Eng Online*. 2016;15(1):126.
- Kosch O, Thiel F, Seifert F, Sachs J, Hein MA. Motion detection In-Vivo by multi-channel ultrawideband radar. *IEEE International Conference on Ultra-Wideband*. 2012:392-396. doi: 10.1109/ICUWB.2012.6340451.
- Kording F, Schoennagel B, Lund G, Ueberle F, Jung C, Adam G, et al. Doppler ultrasound compared with electrocardiogram and pulse oximetry cardiac triggering: A pilot study. *Magn Reson Med*. 2015;74(5):1257-65.
- Bacher M, Speier P, Bollenbeck J, Fenchel M, Stuber M. ISMRM 2018 Paris, Abstract #2960, Pilot Tone Navigation Enables Contactless Prospective Cardiac Triggering: Initial Volunteer Results for Prospective Cine.
- Andreychenko A, Crijns S, Raaijmakers A, Stemkens B, Luijten P, Legendijk J, et al. ISMRM 2014 Milan, Abstract #0092, Noise variance of an RF receive array reflects respiratory motion: a novel respiratory motion predictor.
- Hanson LG, Lund TE, Hanson CG. Encoding of electrophysiology and other signals in MR images. *J Magn Reson Imaging* 2007, 25(5), 1059-1066.
- Speier P, Fenchel M, Rehner R. PT-Nav: a novel respiratory navigation method for continuous acquisitions based on modulation of a pilot tone in the MR-receiver. *ESMRMB 2015, 32nd Annual Scientific Meeting, Edinburgh, UK, 1-3 October: Abstracts*, Thursday, Magnetic Resonance Materials in Physics, Biology and Medicine. 2015; 28:1-135.
- Koesters T, Brown R, Zhao T, Fenchel M, Speier P, Feng L, et al. ISMRM 2016 Singapore, Abstract #4250, Motion Correcting Complete MR-PET Exams Via Pilot Tone Navigators.
- Solomon E, Rigie DS, Vahle T, Paška J, Bollenbeck J, Sodickson DK, et al. Free-breathing radial imaging using a pilot-tone radiofrequency transmitter for detection of respiratory motion. *Magn Reson Med*. 2021;85(5):2672-2685.
- Huang SS, Boyacioglu R, Bolding R, MacAskill C, Chen Y, Griswold MA. Free-Breathing Abdominal Magnetic Resonance Fingerprinting Using a Pilot Tone Navigator. *J Magn Reson Imaging*. 2021;54(4):1138-1151.
- Ludwig J, Speier P, Seifert F, Schaeffter T, Kolbitsch C. Pilot tone-based motion correction for prospective respiratory compensated cardiac cine MRI. *Magn Reson Med*. 2021;85(5):2403-2416.
- Ludwig J, Kerkering KM, Speier P, Schaeffter T, Kolbitsch C. Pilot tone-based prospective correction of respiratory motion for free-breathing myocardial T1 mapping. *MAGMA*. 2022 Aug 3. doi: 10.1007/s10334-022-01032-4. Online ahead of print. PMID: 35921020.
- Schröder, L. Information content of a novel MR navigator relating to physiological activities. Advisors: Haderlein T, Maier A, Wetzl J, Speier P. Siemens Healthcare GmbH. Started June 2015. [Not accessible online].
- Bacher M. Cardiac Triggering Based on Locally Generated Pilot-Tones in a Commercial MRI Scanner: A Feasibility Study [master's thesis. Graz: Graz University of Technology; 2017. 103 p.] <https://digi.ub.tugraz.at>, linked via <https://graz.pure.elsevier.com/de/publications/cardiac-triggering-based-on-locally-generated-pilot-tones-in-a-co>
- Schroeder L, Wetzl J, Maier A, Lauer L, Bollenbeck J, Fenchel M, et al. ISMRM 2016 Singapore, Abstract #410: A Novel Method for Contact-Free Cardiac Synchronization Using the Pilot Tone Navigator.
- Bacher, M. SCMR 2020 Orlando, FL, USA, co-workshop. [Not accessible online].
- Falcão MBL, Di Sopra L, Ma L, Bacher M, Yerly J, Speier P, et al. Pilot tone navigation for respiratory and cardiac motion-resolved free-running 5D flow MRI. *Magn Reson Med*. 2022;87(2):718-732.
- Chen C, Liu Y, Simonetti OP, Tong M, Jin N, Bacher M, et al. Cardiac and respiratory motion extraction for MRI using Pilot Tone-a patient study. *arXiv:2202.00055 [eess.SP]*.
- Inventors: Huang YT, Zhang QY, Li ZB. Using eigenvector algorithm to reduce RF interference in respiration or heartbeat detection. CN112415453-A. Publication: 2021-02-26.
- Pan Y, Varghese J, Jin N, Hayes C, Speier P, Ahmad R, et al. ISMRM 2022 London, UK, Abstract #4770: Validation of Beat Sensor Cardiac Triggering against ECG Cardiac Triggering in both Volunteer and Patient Cohorts.
- Hayes C, Huang YT, Rick M, Kroeker R, Bacher M, Pan Y, et al. ISMRM 2022 London, UK, Abstract #4786: Multi-center evaluation of the novel Beat Sensor Cardiac triggering technology.
- Lin K, Sarnari R, Speier P, Hayes C, Davids R, Carr JC, et al. Pilot Tone-Triggered MRI for Quantitative Assessment of Cardiac Function, Motion, and Structure. *Invest Radiol*. 2022. doi: 10.1097/RLI.0000000000000922. Online ahead of print. PMID: 36070525.
- Schroeder L, Wetzl J, Maier A, Rehner R, Fenchel M, Speier P. ISMRM 2016 Singapore, Abstract #3103: Two-Dimensional Respiratory-Motion Characterization for Continuous MR Measurements Using Pilot Tone Navigation.
- Speier P, Bacher M, Bollenbeck J, Fenchel M, Kober T. ISMRM 2018 Paris, Abstract #4101: Separation And Quantification Of Head Motion Modes By Pilot Tone Measurements.

- 33 Moskalenko YE. Utilization of superhigh frequencies in biological investigations. Biophysics (USSR) (English translation). 1958;3:619–26. [Only second hand knowledge! We have not been able to get a copy of the original article yet.]
- 34 Tarjan PP, McFee R. Electrodeless measurements of the effective resistivity of the human torso and head by magnetic induction. IEEE Trans Biomed Eng. 1968;15(4):266–78.
- 35 Buikman D, Helzel T, Röschmann P. The rf coil as a sensitive motion detector for magnetic resonance imaging. Magn Reson Imaging. 1988;6(3):281–9.
- 36 Graesslin I, Stahl H, Nehrke K, Harvey P, Smink J, Mens G, et al. An alternative concept for non-sequence interfering, contact-free respiration monitoring. In: Proceedings of the 17th Annual Meeting of ISMRM, Honolulu, HI, USA. 2009:753.
- 37 Jaeschke S, Robson MD, Hess AT. Cardiac gating using scattering of an 8-channel parallel transmit coil at 7T. Magn Reson Med. 2018;80(2):633–640.
- 38 Anand S, Lustig M. ISMRM 2021 online, Abstract #0568: Beat Pilot Tone: Exploiting Preamplifier Intermodulation of UHF/SHF RF for Improved Motion Sensitivity over Pilot Tone Navigators.
- 39 Hyvärinen A. Fast and Robust Fixed-Point Algorithms for Independent Component Analysis. IEEE Trans Neural Netw. 1999;10(3):626–634.
- 40 Spincemaille P, Nguyen TD, Prince MR, Wang Y. Kalman filtering for real-time navigator processing. Magn Reson Med. 2008;60(1):158–168.
- 41 Vahle T, Bacher M, Rigie D, Fenchel M, Speier P, Bollenbeck J, et al. Respiratory Motion Detection and Correction for MR Using the Pilot Tone: Applications for MR and Simultaneous PET/MR Examinations. Invest Radiol. 2020;55(3):153–159.



Contact

Peter Speier, Ph.D.
Cardiovascular Application Development
SHS DI MR RCT CLS CARD
Allee am Roethelheimpark 2
91052 Erlangen
Germany
peter.speier@siemens-healthineers.com

Advertisement



Watch as BioMatrix Beat Sensor developers Peter Speier, Mario Bacher, Carmel Hayes, and Manuela Rick explain the various stages of the development.



Visit us at:

[www.siemens-healthineers.com/magnetic-resonance-imaging/
clinical-specialities/cardiovascular-mri](https://www.siemens-healthineers.com/magnetic-resonance-imaging/clinical-specialities/cardiovascular-mri)

Meet Siemens Healthineers

Siemens Healthineers: Our brand name embodies the pioneering spirit and engineering expertise that is unique in the healthcare industry. The people working for Siemens Healthineers are totally committed to the company they work for, and are passionate about their technology. In this section we introduce you to colleagues from all over the world – people who put their hearts into what they do.

Katie Grant, Ph.D.

Katie is a passionate leader who enjoys working with others to make things happen. She is currently Senior Director for MR Marketing and Sales Operations in North America. After earning her Ph.D., Katie worked for Mayo Clinic and the Department of Defense in high-speed electronics prototype development. She also worked as a liaison to physicians working on integrating these technologies into advanced medicine. After five years, the opportunity arose to join Siemens Healthineers as a collaboration manager in the CT business, which was a dream job that combined her strengths and interests. Katie spent ten years in the CT business, working across various parts of the organization to drive innovation and partnerships with customers, both nationally and globally. Katie then moved on to lead the NAM MR R&D collaboration team of over 55 scientists. After spending 12 years in R&D collaborations, she switched to the commercial side of the business to learn more about internal operations within a large sales and marketing organization. Katie earned a bachelor's degree in physics from Miami University, a Ph.D. in biomedical engineering from Mayo Clinic, and is a principal key expert. She is an inventor on 17 granted patents and has published over 35 papers. Katie lives in Minnesota, USA, with her husband and two daughters.



How did you first come into contact with MRI?

I first learned about MRI as a physics student studying electromagnetics. Having had a CT scan for a sports injury when I was younger, I was intrigued by cross-sectional imaging and found MRI to be incredibly interesting. I wanted to understand how and why it worked. I went on to start my Ph.D. in MRI and biomedical engineering at Mayo Clinic, which led to even more interesting opportunities that stretched beyond MRI. I ended up writing a thesis on neurophysiology of the neuromuscular junction, using confocal and transmission electron microscopy. That was a far cry from CT or MR. About five years after I finished my Ph.D., a friend asked me to consider joining the CT team at Siemens Healthineers – I haven't looked back since!

What do you find motivating about your job?

That I get to solve problems that are meaningful and impact people around the world. There always seems to be new challenges in MRI, in every aspect of the business. But I cannot say that without acknowledging what a big impact my colleagues and our customers make on me every day. I have been very fortunate to work with incredible people throughout my tenure at Siemens Healthineers. I remain motivated and enjoy solving problems because I get to do so alongside really intelligent, thoughtful, and fun people who share a passion to do and be the best, for the sake of the patient.

What are the biggest challenges in your job?

As with any job, there are a multitude of challenges, but a crucial underlying challenge is communication. There are so many different stakeholders involved in projects, each with different viewpoints, personalities, and hurdles to overcome. It can be a real challenge to get everyone involved to have the same understanding of what needs to be accomplished. It can be a lot of work and sometimes painful, but solid communication is critical to our overall success. I have also found this to be the most rewarding aspect of my work, as it allows me to get to know a lot of people across the company and learn not only about their roles and challenges, but also about them as individuals. Excellent communication is also what helps us stay at the cutting edge of innovation. In order to solve complex problems, we need to understand the concerns and challenges of our customers and be able to translate this to the engineering teams – and vice versa. It is really exciting to be on this blurry edge where physics, medicine, and engineering intersect.

What are the most important developments in healthcare?

I feel the most important developments in healthcare are the ones that improve the quality of a patient's life – which means they must have access to care. While artificial intelligence is an easy and perhaps obvious answer, there is so much more. The advances in connectivity and the

developments around digitalization of healthcare are also enabling more affordable, high-quality access worldwide. The ability to bring care to a patient, remotely check in on their health, and provide expert care in a remote area has grown significantly over the past few years. MAGNETOM Free.Max and MAGNETOM Viato.Mobile¹ coupled with syngo Virtual Cockpit are fantastic examples of how we are working on this challenge internally at Siemens Healthineers. Hopefully, we will continue to see the positive effects of these developments in the years to come.

¹Work in progress. MAGNETOM Viato.Mobile is still under development and not commercially available yet. Its future availability cannot be ensured.

What would you do if you could spend a month doing whatever you wanted?

There are so many places I would love to explore! I would travel with my family and spend as much time as possible outdoors hiking, skiing, and things like that. I'd also read as many books as possible. I've never visited South America, so that would be one of the first countries on my list. I'd also love to see Norway, as many of my ancestors were Norwegian.

Tom Hilbert, Ph.D.

Tom was born and raised in a small town in Thuringia, a state known as "the green heart of Germany." In 2007, he began his studies in biomedical engineering and medical computer science at the University of Applied Sciences in Stralsund. The city is on the Baltic coast and Tom developed a passion for sailing there.

During both an internship and a period spent writing his bachelor's thesis at the Lausanne-based Innovation Hub Switzerland run by Siemens Healthineers, Tom gained his first experiences with MR imaging. In 2011, he continued his education by studying medical computer science at Heidelberg University in Germany. During this time, he continued working at Siemens on improving MR methods and wrote his master's thesis at the company. In 2013, with the beginning of his dissertation at the École Polytechnique Fédérale de Lausanne (EPFL), he finally moved to Lausanne, the city at Lake Geneva which he still calls his home. His dissertation focused on quantitative imaging and how it can be translated into clinical routine. He continues to pursue these goals today by leading a Switzerland-wide team of scientists who work on topics related to MR image acquisition and reconstruction within the Swiss Siemens Healthineers Innovation Hub.



How did you first come into contact with MRI?

The first time I came into contact with MRI was during my internship in 2009. It was my first time joining Siemens Healthineers in Lausanne and I was tasked with simulating motion artifacts in MR images. I thought I knew a lot about MRI from my courses at university, but I soon realized we have only scratched the surface of MRI. Even now, more than 13 years later, I feel like I have so much left to learn and understand about MR physics and image reconstruction methods. This fascinated me so much that I have been working with the team in Lausanne ever since 2009, first in various projects to improve the performance of image analysis algorithms, and later diving deeper into the clockwork of sequences and image reconstruction with a focus on quantitative imaging.

What do you find motivating about your job?

The thing that gets me up in the morning and go to work is that we have a chance to make a difference with the methods and tools we are developing. Our goal is to help patients who are struggling with diseases we have not yet fully understood. Although our improvements to modern

healthcare are small and incremental, I believe we can make a difference for individuals in the future. So I find it very motivating to hear about clinical researchers classifying tumors with a new quantitative mapping technique, or a neuroradiologist finding cortical dysplasia in an epilepsy patient at 7T that they could not see at 3T.

What are the biggest challenges in your job?

I have had to learn to deal with two main frustrations in my job. The first concerns limited resources. We get to meet many scientists and partners of Siemens Healthineers, and they all have great ideas about how we might improve patient care in the future. Unfortunately, we cannot work on every exciting idea – we can only focus on some of them, since the day only has 24 hours. The second is delayed gratification. It can take years for an idea to become a product that can actually help patients. That's because we want to develop methods with scientific rigor and provide robust, validated, and well-tested tools. This rather lengthy process is important for evidence-based medicine, but can become frustrating on a personal level.

What are the most important developments in healthcare?

One of the most important developments, especially in my field of quantitative imaging, is translating scientific methods into clinical routine. As well as finding ways of quantifying microstructural information and seeing how they relate to diagnoses and treatment monitoring, we also need to focus on making them easily useable in clinical workflows. The academic community does a great job of identifying and developing these new methods. In my opinion, the job of Siemens Healthineers is to use these new findings and make them accessible for patients today. This can be difficult, since they should not interrupt MR acquisition workflows by, e.g., lengthening acquisition times, but they should also decrease the workload for radiologists by minimizing the manual inputs required. Therefore, I will be focusing my efforts on acceleration methods and automatic analysis tools for quantitative imaging.

What would you do if you could spend a month doing whatever you wanted?

In our daily work, we have so many ideas that could have great potential to improve MRI methods. Unfortunately, we rarely manage to work on these ideas because we are already so busy with other projects. So if I could spend a month doing whatever I wanted professionally, I would use the time to focus on just one idea, uninterrupted and maybe with some colleagues, and develop it as far as we can in that time. Obviously, on the condition that none of the great ideas we are already working on are stagnating.

From a private point of view, if I could spend one month doing whatever I wanted, I would spend the time sailing. Ever since I lived on the Baltic coast, and now here in Lausanne on Lake Geneva, I've really enjoyed sports sailing. So I would take a small catamaran to hop from island to island somewhere warm, with no plans and just following the direction of the wind each day.

Get to know us



Eva Eberlein

Erlangen,
Germany



Kelvin Chow, Ph.D.

Chicago, USA



Emily Lucchese

Melbourne, Australia



Miguel Contreras

Santiago, Chile



Solenn Toupin, Ph.D.

Bordeaux,
France



Zhang Le, Ph.D.

Shenzhen,
China



Find more portraits
of our colleagues
around the world!

www.magnetomworld.siemens-healthineers.com/meet-siemens-healthineers

The entire editorial staff at Texas A&M University and Houston Methodist Hospital, Houston, TX, USA, and at Siemens Healthineers extends their appreciation to all the radiologists, technologists, physicists, experts, and scholars who donate their time and energy – without payment – in order to share their expertise with the readers of MAGNETOM Flash.

MAGNETOM Flash – Imprint

© 2023 by Siemens Healthcare GmbH,
All Rights Reserved

Publisher:

Siemens Healthcare GmbH
Magnetic Resonance,
Karl-Schall-Str. 6, D-91052 Erlangen, Germany

Editor-in-chief:

Antje Hellwich
(antje.hellwich@siemens-healthineers.com)

Guest Editor:

Roderic I. Pettigrew, Ph.D., M.D.
CEO of Engineering Health (EnHealth) and inaugural
dean, School of Engineering Medicine (EnMed) at
Texas A&M and Houston Methodist Hospital, Houston,
TX, USA

Editorial Board:

Jane Kilkeny; Kathrin El Nemer, M.D.;
Heiko Meyer, Ph.D.; Rebecca Ramb, Ph.D.;
Wellesley Were

Review Board:

André Fischer, Ph.D.; Daniel Fischer;
Christian Geppert, Ph.D.; Zahra Hosseini, Ph.D.;
Felix Müller-Witt; Gregor Thörmer, Ph.D.

Copy Editing:

Sheila Regan, Jen Metcalf, UNIWORKS,
www.uni-works.org
(with special thanks to Kylie Martin)

Layout:

Agentur Baumgärtner,
Friedrichstr. 4, D-90762 Fürth, Germany,
www.agentur-baumgaertner.com

PrePress and Image Editing, Production:

Clemens Ulrich, Paul Linssen,
Siemens Healthcare GmbH

Printer:

Schmidl & Rotaplan Druck GmbH,
Hofer Str. 1, D-93057 Regensburg, Germany

Note in accordance with § 33 Para.1 of the German Federal Data Protection Law: Despatch is made using an address file which is maintained with the aid of an automated data processing system.

MAGNETOM Flash is sent free of charge to Siemens Healthineers MR customers, qualified physicians, technologists, physicists and radiology departments throughout the world. It includes reports in the English language on magnetic resonance: diagnostic and therapeutic methods and their application as well as results and experience gained with corresponding systems and solutions. It introduces from case to case new principles and procedures and discusses their clinical potential. The statements and views of the authors in the individual contributions do not necessarily reflect the opinion of the publisher.

The information presented in these articles and case reports is for illustration only and is not intended to be relied upon by the reader for instruction as to the practice of medicine. Any health care practitioner reading this information is reminded that they must use their own learning, training and expertise in dealing with their individual patients. This material does not substitute for that duty and is not intended by Siemens Healthcare to be used for any purpose in that regard. The drugs and doses mentioned herein are consistent with the approval labeling for uses and/or indications of the drug. The treating physician bears the sole responsibility for the diagnosis and treatment of patients, including drugs and doses prescribed in connection with such use. The Operating Instructions must always be strictly followed when operating the MR system. The sources for the technical data are the corresponding data sheets. Results may vary.

Partial reproduction in printed form of individual contributions is permitted, provided the customary bibliographical data such as author's name and title of the contribution as well as year, issue number and pages of MAGNETOM Flash are named, but the editors request that two copies be sent to them. The written consent of the authors and publisher is required for the complete reprinting of an article.

We welcome your questions and comments about the editorial content of MAGNETOM Flash. Please contact us at
magnetomworld.team@siemens-healthineers.com

Manuscripts as well as suggestions, proposals and information are always welcome; they are carefully examined and submitted to the editorial board for attention. MAGNETOM Flash is not responsible for loss, damage, or any other injury to unsolicited manuscripts or other materials. We reserve the right to edit for clarity, accuracy, and space. Include your name, address, and phone number and send to the editors, address above.

MAGNETOM Flash is also available online:

www.siemens-healthineers.com/magnetom-world

Not for distribution in the US

On account of certain regional limitations of sales rights and service availability, we cannot guarantee that all products included in this brochure are available through the Siemens Healthineers sales organization worldwide. Availability and packaging may vary by country and is subject to change without prior notice. Some/All of the features and products described herein may not be available in the United States.

The information in this document contains general technical descriptions of specifications and options as well as standard and optional features which do not always have to be present in individual cases, and which may not be commercially available in all countries.

Due to regulatory reasons their future availability cannot be guaranteed. Please contact your local Siemens organization for further details.

Siemens Healthineers reserves the right to modify the design, packaging, specifications, and options described herein without prior notice. Please contact your local Siemens Healthineers sales representative for the most current information.

Note: Any technical data contained in this document may vary within defined tolerances. Original images always lose a certain amount of detail when reproduced.

Siemens Healthineers Headquarters

Siemens Healthcare GmbH
Henkestr. 127
91052 Erlangen, Germany
Phone: +49 9131 84-0
siemens-healthineers.com